Geological controls on gold mineralization in the Kukuluma Terrain, Geita Greenstone Belt, NW Tanzania

Thesis by

Shimba Daniel Kwelwa BSc, MSc UDSM (Tanzania)

for the degree of Doctor of Philosophy

in the College of Science and Engineering,

James Cook University, Australia

Original submission: December, 2016

Final submission: June, 2017

TABLE OF CONTENTS

CHAPTER 3.

THE STRUCTURAL HISTORY OF THE KUKULUMA AND MATANDANI DEPOSITS AND CONTROLS ON GOLD MINERALIZATION, GEITA GREENSTONE BELT, TANZANIA

CHAPTER 4.

THE PETROGENESIS OF THE NEOARCHEAN KUKULUMA INTRUSIVE COMPLEX, NW TANZANIA

STATEMENT OF ACCESS

I, undersigned, the author of this thesis, understand that James Cook University will make it available of use within the University Library, and by microfilm or other means, allow access to other users in other approved libraries.

All users consulting this thesis will have to sign the following statement:

In consulting this thesis, I agree not to copy closely or paraphrase it in whole or in part without the written consent of the author; and to make proper public written acknowledgement for any assistance that I have obtained from it.

Beyond this, I donot wish to place any restrictions on access to this thesis.

Shimba Daniel Kwelwa June, 2017

STATEMENT OF SOURCES

DECLARATION

I declare that this thesis is my own work and has not been submitted in any form for another degree or diploma at any other institution for tertiary education.

Information derived from published and unpublished work of others has been acknowledged in the text and a list of references has been given.

_____ _____

Shimba Daniel Kwelwa June, 2017

ELECTRONIC COPY

DECLARATION

I, the undersigned, the author of this thesis, declare that the electronic copy of this thesis provided to the James Cook University Library is an accurate copy of the print thesis submitted, within the limits of the technology available.

Shimba Daniel Kwelwa June, 2017

ACKNOWLEDGMENTS

Firstly, I would like to thank the Geita Gold Mine management for funding this study as well as giving me time to do my presentations and laboratory work at James Cook University in northern Queensland, Australia. James Cook University is thanked for providing me with a one year fee weaver through the Australia government research fund in order to finish-up my studies at the time there was an economic crisis within the company due to a sudden fall in the gold price.

My sincere appreciation goes to my university supervisors; Prof Paul Dirks, Dr Ioan Sanislav, Prof Thom Blenkinsop and Dr Yvonne Cook. This group provided me with tireless support during my entire course of study. Their boundless support and motivation inspired me to keep going regardless of the rough situations that I faced during the course of this study. Many thanks go to Mike Rubenach for the time that he dedicated to me for technical discussions on various sections of my thesis.

I would also like to thank the staff working at the Advanced Analytical Centre at James Cook University for providing me with technical assistance in terms of training in data collection using the current state-of the art technology machines. Just to mention a few, Dr Kelvin Blake is thanked for his support on electron microprobe and Dr Yi on the Laser Ablation machine.

On the mine site, the former geology manager Steve Robins and his management team are thanked for allowing me to do this study in a condusive environment. Craig Duvel, the current head of the geology department is thanked for allowing me to have another visit to James Cook University for six months in mid-2015 in order to finish-up my laboratory work and other university requirements that needed my physical presence. My exploration superintendent Hatari Mjinja and other members of the team are thanked for their tireless support during my study. It will be unfair if I will not acknowledge the maximum support that I got from a highly motivated team of field technicians such as Freeman Kaishe, Robert Alphonce, Mkama Kajeri and Msafiri Solonga just to mention a few. These guys worked really hard in this hilly and challenging terrain to make sure we accomplish what we planned for particular days in the field.

My former exploration manager Sergio L. Kolling is categorically thanked for inception of the project and his continuous technical support that he provided to me since I joined the company through the GGM-JCU the project. For sure, his tireless technical and motivational support even during the weekends and late hours in weekdays was fantastic and non-comparable. It is his technical support that has significantly helped me to build–up my technical capabilities in mineral exploration and geology as a whole.

Lastly, I would like to thank my family for their love, patience, inspiration, moral support and motivation that kept me strong even in times when I felt tired. Their motivation statements and specifically from my mother pushed me to keep going fearlessly even in difficult situations. It is for these reasons; I dedicate this work to my family.

CHAPTER 1

INTRODUCTION AND THESIS OUTLINE

1.1. SUMMARY

A general introduction to greenstone belt geology and Archaean gold mineralization is provided in which the broad parameters of different models for Archaean tectonic and mineralization processes are discussed. This is followed by an overview of the geology of the Tanzania craton, in which the general stratigraphy of the craton is introduced, after which the geological setting of the Sukumaland and Geita greenstone belts is introduced in more detail. These descriptions serve as general introductions to the structural history, intrusive history, geochemistry and geochronology of the Kukuluma area, as presented in chapters 3, 4 and 5. Following the introduction of the geological setting, the history of Geita Gold Mine will be presented together with a brief outline of the structure of this thesis.

1.2. ARCHITECTURE OF GREENSTONE BELTS AND GOLD MINERALIZATION

The Archaean greenstone belts are elongate structures composed of supracrustal units deformed in broadly synformal or keel-like shapes forming the younger units in most of the Archaean Cratons such as Zimbabwe, Yilgarn, Dharwar, Superior and Tanzania Craton (Chadwick et al., 2000; Percival et al., 2001; Jelsma and Dirks, 2002; Blewet et al., 2010; Czarnota et al., 2010; Manikyamba and Kerrich, 2012; Bèdard et al., 2013; Anhaeusser, 2014; Sanislav et al., 2014). The supracrustal units that form these greenstone belts are made

of bimodal metavolcanics intercalated with variable types of clastic sediments (Condie, 1994; deWit and Ashwal, 2006; Anhaeusser, 2014), which are surrounded and intruded by tonalite-trondhjemite-granodiorite (TTG) suites resulting in the formation of open, round antiforms, arches or domes shapes (Bouhallier et al., 1995 and Anhaeusser, 2014).

To date, various tectonic models have been proposed to explain the geometric configuration of these greenstone belts, but none of them have been satisfactory. These models include vertical tectonics involving density inversion and diapiric emplacement of mid- to lower-crustal melt into upper-crustal volcano-clastic sequences (e.g. Choukroune et al., 1995; Chardon et al., 1996; Collins et al., 1998; Bédard et al., 2003; Van Kranendonk, 2011) or horizontal tectonic processes involving low-angle subduction and crustal stacking, or core complex formation followed by late granite intrusions due to decompression melting (Polat et al., 1998; Bouhallier et al., 1995; Kloppenburg et al., 2001;Jelsma and Dirks, 2002;Blewett et al., 2004; 2010a; Kabete et al., 2012), with these processes being linked to early forms of plate tectonics, mantle plume activity or both (e.g. Moyen et al., 2006; Blewett et al., 2010a).

In line with this debate, over the past few decades, geochemists have been conducting a number of studies on the petrogenesis of the rocks of TTG or adakitic composition, which form the dominant chemical composition of the Archaean rock record (Taylor and Mclennan, 1995; Condie, 2005; Moyen, 2011; Moyen and Martin, 2012; Tatsumi, 2008; Hacker et al., 2015). The understanding of the tectonic models for greenstone belts formation become more important during the Late Archaean period when major shifts in the composition of the TTG suites are interpreted to reflect fundamental changes in global tectonics (e.g. Martin et al., 2010; Moyen and Martin, 2012). In this geochemical perspective, two models have been debated; a subduction–related model has been proposed as a suitable tectonic setting in the

formation of the adakites and sanukitoids (Martin, 1999; Polat and Kerrich, 2001; Manya et al., 2007; Manikyamba et al., 2007; Mohan et al., 2013; Kwelwa et al., 2013) like the horizontal tectonics model described by Windley (1995). Alternatively, a vertical tectonic model suggests that these "adakitic" rocks can form by melting thickened mafic lower crust (e.g. Atherton and Petford, 1993; Rudnick, 1995; Wang et al., 2005), or through the interaction of delaminated eclogitic lower crust with the underlying mantle (e.g. Bedard et al., 2003; Gao et al., 2004; Wang et al., 2005; Goss et al. 2011).

The structural set-up and lithological composition are the key drivers for the dominance of quartz vein or shear hosted gold deposits in greenstone belts. These deposits formed in structural settings near major shear zones and quartz veins (Groves et al., 1998; Goldfarb et al., 2005; Frimmel, 2008). Usually, these deposits are classified as orogenic by linking their formation to the accretionary processes that occurred during the late stages of cordilleran-type tectonics, where gold mineralization events correspond with shifts in the stress regime from a compressional to a transpressional or transtensional phase, and that suggests the existence of modern day plate tectonic during Archaean times (Kerrich et al., 2000; Goldfarb et al., 2001, 2005; Groves et al., 2003, 2006; Bierlein et al., 2006; Frimmel, 2008; Begg et al., 2009; Dirks et al., 2013; Sanislav et al., 2015, 2016). To the contrary, a some researchers propose an non-orogenic model for greenstone belt formation that involves vertical melt segregation above mantle plumes challenging the orogenic origin for the lode gold deposits (e.g. Bédard et al., 2014; Cook et al., 2015).

In many Archaean greenstone belts, the regional gold bearing structures are localized within particular tectonic domains with suitable geological settings involving terrain boundaries that act as first-order structures that control crustal-scale plumbing systems of mantle-derived magma and hydrothermal fluids (e.g. Ridley et al., 1996; Goldfarb et al., 2005; Phillips and Powell, 2010). The relationship between the regional structures, mantle –

derived magma and hydrothermal fluids in the formation of these deposits make the understanding of the timing of granitoid intrusion with respect to greenstone formation, structural configuration of the controlling structures, host-rock, and intrusive geochemistry to be important when targeting potential areas for gold mineralization on a terrain-scale.

Deposit-scale geology shows that the shear-hosted and lode-gold deposits are associated with a number of dilatant, brittle-ductile structures that occur as secondary features near major compressional or transpressional shear zones (Colvine et al., 1988; Groves et al., 1998; Tripp and Vearncombe, 2004; Dirks et al., 2009). These shear zones act as the main fluid pathways for the mineralizing fluids involving the repeated locking and reactivation of fault planes in response to fluid pressure changes similar to the fault valve model (Sibson, 2001, 2004). Apart from the major brittle – ductile shear zones, gold mineralization locally gets trapped in secondary structures including fracture arrays, breccia zones and fold hinges within more brittle lithologies (Robert et al., 1991; Groves et al., 2000; Sanislav et al., 2015). In these places, gold precipitation along the structural traps is facilitated by changes in physico-chemical conditions of the fluids that occur during interaction between the gold-bearing fluids with the wall-rock (e.g. Sanislav et al., 2015).

1.3. REGIONAL GEOLOGICAL FRAMEWORK

The supra-crustal stratigraphy of the Tanzania craton has been subdivided into three main units (Fig. 1.1). The Dodoman Supergroup is the oldest unit, and consists of high-grade mafic and felsic granulite with subordinate amounts of lower-grade schist and thin slivers of greenstone (Kabete et al., 2012). The Nyanzian Supergroup overlies the Dodoman Supergroup (e.g. Quennel et al., 1956; Gabert, 1990) and consists of a base dominated by mafic volcanic units (i.e. the Lower Nyanzian comprising amphibolite, pillow basalt, andesite and minor gabbro; Cook et al., 2015) dated at ~2823 Ma (Manya and Maboko, 2008; Cook et

al., 2015) overlain by units dominated by felsic volcanic and pyroclastic rocks inter-bedded with banded ironstone, chert, volcanoclastic sequences and immature turbiditic sediment (i.e. the Upper Nyanzian; Kuehn et al. 1990; Borg 1992; Borg and Shackelton 1997; Borg and Krogh 1999; Krapez, 2008).

The Kavirondian Supergroup rests unconformably on the Nyanzian Supergroup and consists of a folded clastic assemblage composed of conglomerate, quartzite, grit, sandstone and siltstone (Stockley, 1936; Harpum, 1970; Borg, 1992) deposited between ~2450 Ma and ~2762 Ma (Gabert, 1990; Chamberlain and Tosdale, 2007; Sanislav et al., 2015). Rocks of the Nyanzian and Kavirondian Supergroups in general have been metamorphosed to greenschist facies (Quennel et al., 1956). Locally, rocks record higher metamorphic grades along major shear zones near margins of greenstone sequences, and as a result of contact metamorphic processes (Borg and Shackleton, 1997).

The northern Tanzania Craton contains dispersed greenstone slivers that have been grouped into six greenstone belts (Fig. 1.1), all clustered around the margins of Lake Victoria, in a region commonly referred to as the Lake Victoria Gold Fields (Borg and Shackleton, 1997). These greenstone belts include the Nzega, Musoma-Mara, Iramba-Sekenke, Shinyanga-Malita, Kilimafedha and Sukumaland Greenstone Belts. Each of these greenstone belts consist of several disconnected greenstone domains that have been grouped based on stratigraphic correlations and geographic proximity; i.e. the various greenstone portions may not necessarily share a common geological history (e.g. Kabete et al., 2012; Cook et al., 2015). Kabete et al. (2012) proposed a terrane-based sub-division of the northern Tanzania Craton in which the greenstone belts are interpreted as separate terrains accreted across major lineaments (Fig. 1.1).

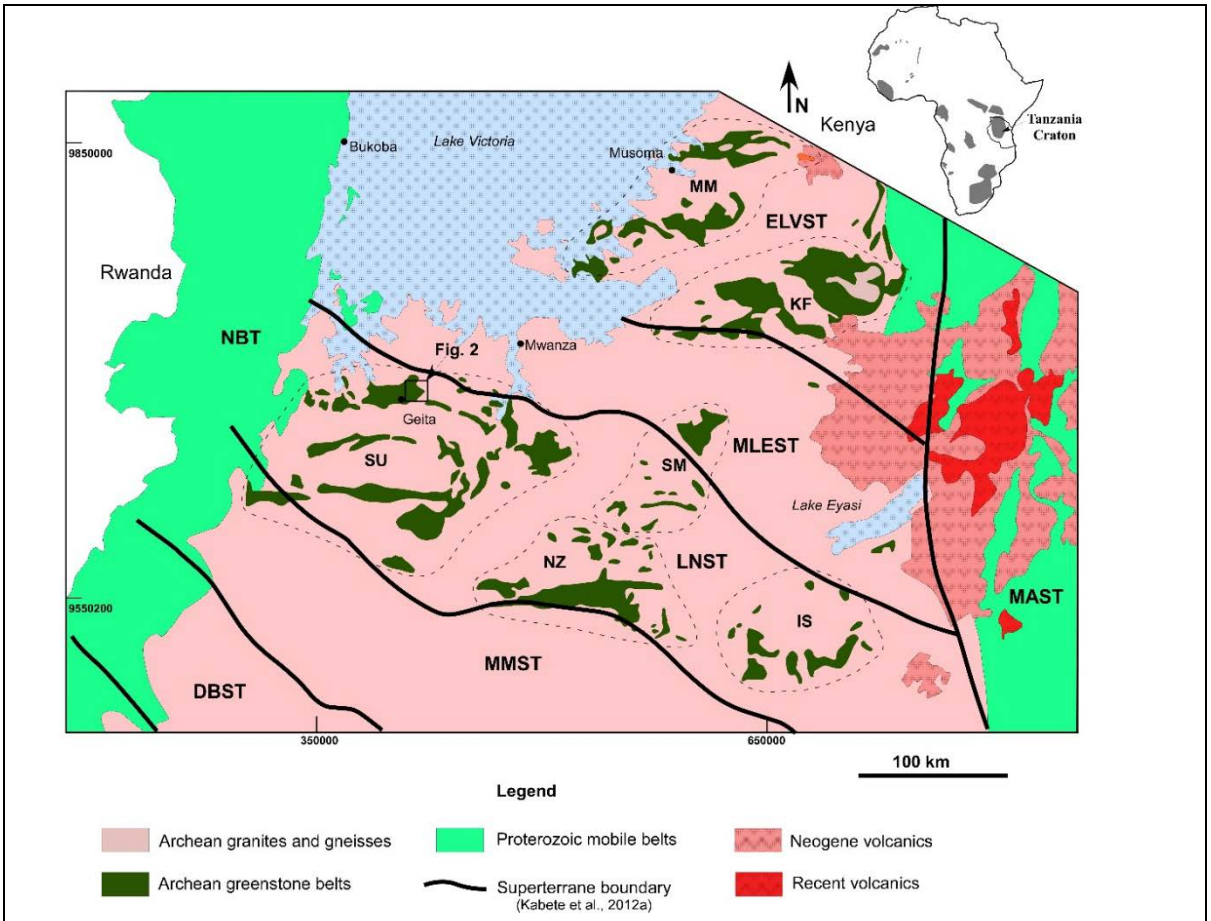

Figure 1.1. Geological map of the northern half of the Tanzania Craton showing the main geological and tectonic units in the craton. SU — Sukumalanad Greenstone Belt; NZ — Nzega Greenstone Belt; SM—Shinyanga-Malita Greenstone Belt; IS—Iramba-Sekenke Greenstone Belt; KF—Kilimafedha Greenstone Belt; MM—Musoma-Mara Greenstone Belt. Super-terrane boundaries are as proposed by Kabete et al. (2012): ELVST— East Lake Victoria; MLEST —Mwanza Lake Eyasi; LNST — Lake Nyanza; MMST —Moyowosi-Manyoni; DBST — Dodoma Basement; MAST — Mbulu-Masai; NBT — Nyakahura-Burigi. Inset map of Africa shows the location of Archaean blocks. The figure has been adapted from Sanislav et al. (2015). The insert shows the study area as shown in figure 1.2 previously shown as Fig.2.

1.3.1. The Sukumaland Greenstone Belt

Of the six greenstone belts, the Sukumaland Greenstone Belt hosts most of the world-class gold deposits including the Bulyanhulu, Geita Hill and Nyakanga deposits (Goldfarb et al., 2001; Bierlein et al., 2006, 2009). Borg et al. (1990) and Borg (1994) describe the

Sukumaland Greenstone Belt as an arcuate-shaped belt intruded by syn- to post-tectonic granitoid of TTG affinity, and divide the belt into an inner arc dominated by Lower Nyanzian, mafic volcanic rocks (Quennel et al., 1956; Borg, 1992; Borg and Shackleton, 1997) and an outer arc dominated by banded ironstone, felsic tuff and volcanoclastic sediment of the Upper Nyanzian (Fig. 1.1; Barth, 1990; Borg, 1992; Borg and Shackleton, 1997). However, abundant mafic units have been described from the outer arc (e.g. Manya and Maboko, 2008; Cook et al., 2015; Fig. 1.2), and sediments and felsic volcanic intercalations are common in the inner arc (e.g. Cloutier et al., 2005; Manya and Maboko, 2008). In addition, young ages have been obtained from rocks in the inner arc, and old ages from rocks in the outer arc (Borg and Krogh, 1999; Manya and Maboko, 2003; Chamberlain and Tosdal, 2007), all indicating that the subdivision into an inner and outer arc is an oversimplification of the greenstone stratigraphy in the area. Instead the Sukumaland Greenstone Belt probably comprises several distinct greenstone fragments separated by major shear zones and intrusives, which can be treated as greenstone belts in their own right (e.g. Cook et al., 2015). Because of the uncertainty with the definition of the Sukumaland Greenstone Belt, we prefer to adopt the terminology of Kuehn et al. (1990) and Sanislav et al. (2014) who use the name Geita Greenstone Belt to refer to the segment of greenstone units that host the Geita deposits.

1.3.2. The Geita Greenstone Belt (GGB)

The Geita Greenstone Belt (GGB, Fig. 1.2) forms an 80 x 25km large, generally east-west trending portion of mafic and felsic volcanic, volcanoclastic and sedimentary units, bounded to the south by a large, east-west trending shear zone that separates the belt from gneiss and mylonitic granitoid. To the north, east and west the greenstone lithologies are

intruded by late syn- to post-tectonic granitoid plutons dated at 2660-2620 Ma (Sanislav et al. 2014).

Age (Ma)	Error	Dating Method	Rock dated	Comments	Reference
2821	30	U-Pb zircon SHRIMP	pyroclastic tuff	SGB. Tulawaka;volcanism (pyroclastic tuff)	Chamberlain and Tosdal, 2007*; Kabete et al, 2012; Sanislav et al, 2014
2808	3	single zircon U-Pb	rhyolitic pyroclastic	Upper Nyanzian, SGB	Borg and Krogh, 1999*
2780	3	single zircon U-Pb	rhyolitic pyroclastic	Upper Nyanzian, SGB	Borg and Krogh, 1999*
2779	13	U-Pb zircon SHRIMP	felsic	SGB. Nyanzaga;volcanism (pyroclastic tuff)	Chamberlain and Tosdal, 2007*; Kabete et al, 2012; Sanislav et al, 2014
2771	15	U-Pb zircon SHRIMP	tuff layer	SGB. Nyamullilima, Geita; tuff interlayered with BIF	Chamberlain and Tosdal, 2007*; Kabete et al, 2012; Sanislav et al, 2015
2770	9	U-Pb zircon SHRIMP	rhyolite	SGB. Masabi, Mega Hill, within the Siga Hills area;	Chamberlain and Tosdal, 2007*; Kabete et al, 2012; Sanislav et al, 2014
2765	25	U-Pb zircon SHRIMP	tonalite	SGB. Kahama-Mwadui.	Chamberlain and Tosdal, 2007*; Kabete et al, 2012; Sanislav et al, 2014
2758	7	U-Pb zircon SHRIMP	diorite	SGB.Imweru. Magmatism	Chamberlain and Tosdal, 2007*; Kabete et al, 2012; Sanislav et al, 2014
2758	6	U-Pb zircon SHRIMP	diorite	SGB.Imweru. Magmatism	Chamberlain and Tosdal, 2007*; Kabete et al, 2012; Sanislav et al, 2014
2758	7	U-Pb zircon SHRIMP	diorite	SGB.Imweru. Magmatism	Chamberlain and Tosdal, 2007*; Kabete et al, 2012; Sanislav et al, 2014
2758	6	U-Pb zircon SHRIMP	diorite	SGB.Imweru. Magmatism	Chamberlain and Tosdal, 2007*; Kabete et al, 2012; Sanislav et al, 2014
2743	12	U-Pb zircon SHRIMP	diorite	SGB. Lubando. Magmatism	Chamberlain and Tosdal, 2007*; Kabete et al, 2012; Sanislav et al, 2014
2743	14	U-Pb zircon SHRIMP	gabbro	SGB. Lubando. Magmatism	Chamberlain and Tosdal, 2007*; Kabete et al, 2012; Sanislav et al, 2014
2743	12	U-Pb zircon SHRIMP	diorite	SGB. Lubando. Magmatism	Chamberlain and Tosdal, 2007*; Kabete et al, 2012; Sanislav et al, 2014
2743	14	U-Pb zircon SHRIMP	gabbro	SGB. Lubando. Magmatism	Chamberlain and Tosdal, 2007*; Kabete et al, 2012; Sanislav et al, 2014
2738	9	U-Pb zircon SHRIMP	tonalite	SGB.-Geita. Magmatism	Chamberlain and Tosdal, 2007*; Kabete et al, 2012; Sanislav et al, 2014
2738	9	U-Pb zircon SHRIMP	tonalite	SGB.-Geita. Magmatism	Chamberlain and Tosdal, 2007*; Kabete et al, 2012; Sanislav et al, 2014
2719	16	U-Pb zircon SHRIMP	dacites	SGB. Bulyanhulu. Volcanism (pyroclastic tuff)	Chamberlain and Tosdal, 2007*; Kabete et al, 2012; Sanislav et al, 2014
2710	10	U-Pb zircon SHRIMP	porphyry dyke	SGB. Bulyanhulu. Volcanism (minimum)	Chamberlain and Tosdal, 2007*; Kabete et al, 2012; Sanislav et al, 2014
2699	9	U-Pb zircon age	trachyandesite	old Geita mine; monzodiorite?	Borg and Krogh, 1999*
2698	12	U-Pb zircon SHRIMP	gneiss/TTG	SGB. Lubando. Deformation	Chamberlain and Tosdal, 2007*; Kabete et al, 2012; Sanislav et al, 2014
2698	12	U-Pb zircon SHRIMP	gneiss/TTG	SGB. Lubando. Deformation	Chamberlain and Tosdal, 2007*; Kabete et al, 2012; Sanislav et al, 2014
2697	10	U-Pb zircon SHRIMP	quartz porphyry	SGB. Geita. Volcanism (minimum)	Chamberlain and Tosdal, 2007*; Kabete et al, 2012; Sanislav et al, 2014
2695	18	U-Pb zircon SHRIMP	quartz-feldspar porphyry	SGB. Geita. Volcanism (minimum)	Chamberlain and Tosdal, 2007*; Kabete et al, 2012; Sanislav et al, 2014
2686	13	U-Pb zircon SHRIMP	lamprophyre	SGB. Geita. Au mineralization (minimum)	Chamberlain and Tosdal, 2007*; Kabete et al, 2012; Sanislav et al, 2014
2684	21	U-Pb zircon SHRIMP	feldspar porphyry	Nyankanga pit, Geita; volcanism	Chamberlain and Tosdal, 2007*; Kabete et al, 2012; Sanislav et al, 2014
2680	3	single zircon U-Pb	migmatitic gneiss	southern margin of SGB near Kahama;	Borg and Krogh, 1999*
2680	9	U-Pb zircon SHRIMP	granitoid	SGB.Kahama-Mwadui. Magmatism	Chamberlain and Tosdal, 2007*; Kabete et al, 2012; Sanislav et al, 2014
2670	21	U-Pb zircon SHRIMP	feldspar dyke	SGB. Biharamulo. Volcanism (minimum)	Chamberlain and Tosdal, 2007*; Kabete et al, 2012; Sanislav et al, 2014
2667	14	U-Pb zircon SHRIMP	feldspar porphyry dyke	SGB. Imweru. Volcanism (minimum)	Chamberlain and Tosdal, 2007*; Kabete et al, 2012; Sanislav et al, 2014
2666	8	U-Pb zircon SHRIMP	granitoid	SGB.Geita. deformation	Chamberlain and Tosdal, 2007*; Kabete et al, 2012; Sanislav et al, 2014
2666	8	U-Pb zircon SHRIMP	granitoid	SGB.Geita. deformation	Chamberlain and Tosdal, 2007*; Kabete et al, 2012; Sanislav et al, 2014
2661	14	U-Pb zircon LA-ICP-MS	granite	SGB. North of Geita. High-K granites	Sanislav et al 2014*
2656	11	U-Pb zircon SHRIMP	granitoid	SGB.Kahama-Mwadui. Magmatism	Chamberlain and Tosdal, 2007*; Kabete et al, 2012; Sanislav et al, 2014
2654	15	zircon U-Pb	flow banded rhyolite	SGB. lower Nyanzian from Kasubuya	Borg and Krogh, 1999*
2653	10	U-Pb zircon SHRIMP	granodiorite	SGB. Kasubuya;magmatism	Chamberlain and Tosdal, 2007*; Kabete et al, 2012; Sanislav et al, 2014
2652	10	U-Pb zircon LA-ICP-MS	high-k granite	SGB. North of Geita. High-K granites	Sanislav et al 2014*
2646	14	U-Pb zircon SHRIMP	high-k granite	SGB. Bukoli. Magmatism	Chamberlain and Tosdal, 2007*; Kabete et al, 2012; Sanislav et al, 2014
2644	3	zircon U-Pb	lamprophyre dyke	cross-cuts the ironstones at the Geita mine	Borg and Krogh, 1999*
2642	32	U-Pb zircon LA-ICP-MS	high-k granite	SGB. North of Geita. High-K granites	Sanislav et al 2014*
2634	41	U-Pb zircon LA-ICP-MS	high-k granite	SGB. North of Geita. High-K granites	Sanislav et al 2014*
2628	12	U-Pb zircon LA-ICP-MS	high-k granite	SGB. North of Geita. High-K granites	Sanislav et al 2014*
2623	15	U-Pb zircon LA-ICP-MS	high-k granite	SGB. North of Geita. High-K granites	Sanislav et al 2014*
2617	11	U-Pb zircon LA-ICP-MS	high-k granite	SGB. North of Geita. High-K granites	Sanislav et al 2014*
2717	12	U-Pb zircon LA-ICP-MS	crystal tuff	SGB. Kukuluma pit. Geita area	This study
2661	16	U-Pb zircon LA-ICP-MS	granodiorite dyke	SGB.Kukuluma pit. Geita area	This study
2658	15	U-Pb zircon LA-ICP-MS	granodiorite dyke	SGB.Kukuluma pit. Geita area	This study
2662	6	U-Pb zircon LA-ICP-MS	granodiorite intrusion	SGB. Kukuluma terrain. Geita area	This study
2651	14	U-Pb zircon LA-ICP-MS	granodiorite dyke	SGB. Matandani pit. Geita area	This study

Table 1.1. Summary of the existing zircon ages from the SGB.

The southern part of the GGB contains metabasalt with minor gabbro and a MORB-like affinity, yielding ages of ~ 2823 Ma (Manya and Maboko 2008; Cook et al., 2015). The remainder of the greenstone belt is dominated by meta-ironstone units intercalated with and overlain by turbiditic meta-sedimentary units and volcanoclastic beds older than 2699 ± 9 Ma (Borg and Krogh, 1999, Sanislav et al., 2015), and intruded by syn-tectonic igneous complexes of dioritic to tonalitic composition (e.g. Sanislav et al., 2015, 2016) with intrusives around Nyankanga and Geita Hill dated between 2686 ± 13 Ma and 2699 ± 9 Ma (U-Pb zircon; Borg and Krogh, 1999; Chamberlain and Tosdal 2007). A summary of all zircon ages from the GGB is presented in Table 1.1.

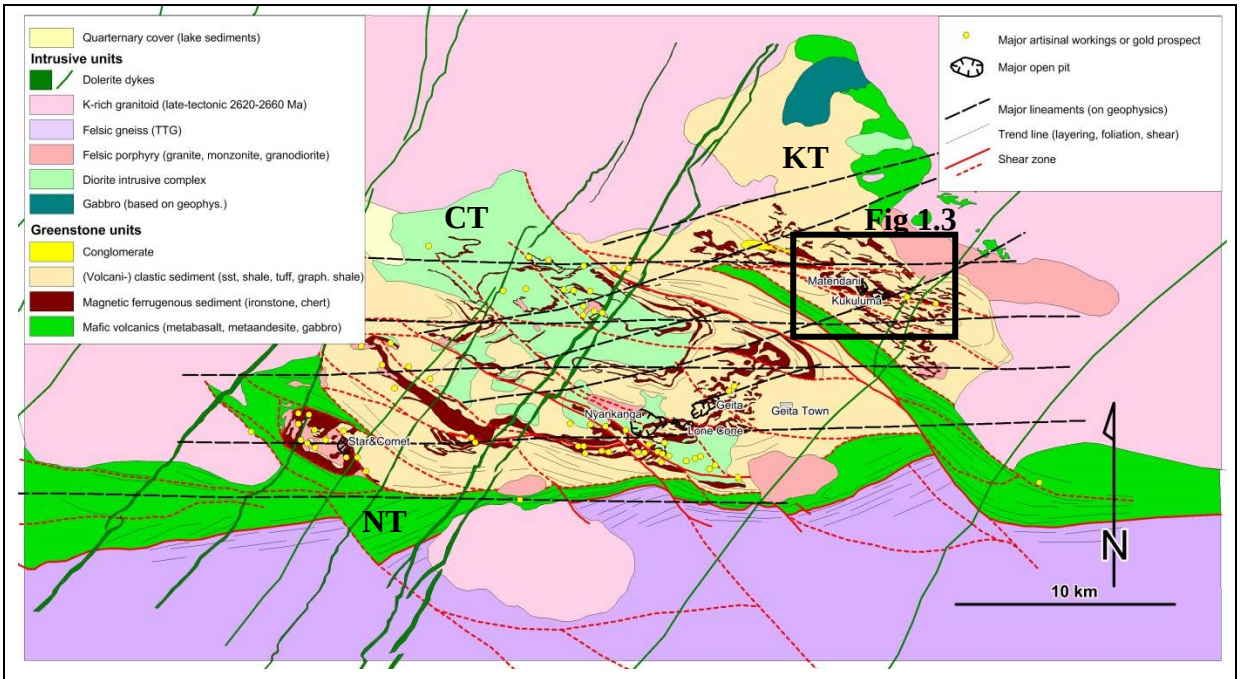

Figure 1.2. Geological map of the Geita Greenstone belt showing the distribution of the main lithological units, structures gold deposits in the area (modified from Sanislav et al., 2015). The insert shows the study area in figure 1.3. NT = Nyamulilima Terrain; CT = Central Terrain; KT = Kukuluma Terrain

Outcrop of the greenstone sequence is generally poor, with the exception of the meta-ironstone units that form steep hills and ridges along the length of the GGB. The meta-

ironstone units are exposed in three distinct northwest-southeast trending terrains separated by areas with little or no outcrop that are underlain by meta-sediments and characterized by major lineaments visible on aero-magnetic datasets and interpreted as large shear zones or terrain boundaries (Fig. 1.2). These terrains are the Nyamulilima terrain to the west, the Central terrain in the middle, and Kukuluma terrain to the east (Fig. 1.2). The Nyamulilima terrain contains three major gold deposits along a northwest-southeast trend (Ridge 8, Star & Comet and Roberts; Fig.1.2). The Central terrain contains at least seven major gold deposits with the three largest occurring along a northeast-southwest trend including the Geita Hill, Lone Cone and Nyankanga deposits (Sanislav et al., 2015, 2016). The Kukuluma terrain contains two major gold deposits and several exploration targets distributed along a westnorthwest to eastsoutheast trend (Figs 1.2 and 1.3), referred to in this paper as the Kukuluma Mineralized Trend. Two of these, the Matandani and Kukuluma deposits, were mined until 2007. The nearby deposits of Area 3 are undeveloped. The area around Matandani, Kukuluma and Area 3, within the central part of the Kukuluma Mineralized Trend, forms the focus of this study. No detailed geological work is available for the Kukuluma terrain apart from mine reports (Bansah et al., 2000; Porter, 2002; Skead, 2003).

1.3.3. Brief history of Geita Gold Mine and context of the study

The GGB hosts the Geita Gold Mine, which is a collection of gold deposits owned by Anglo Gold Ashanti. Over the past five years, the mine has been performing very well in terms of gold production. For example in 2015, Geita Gold Mine produced 476,880 ounces against the set target of 525,747 ounces at an average cut–off grade of 0.5g/t Au.

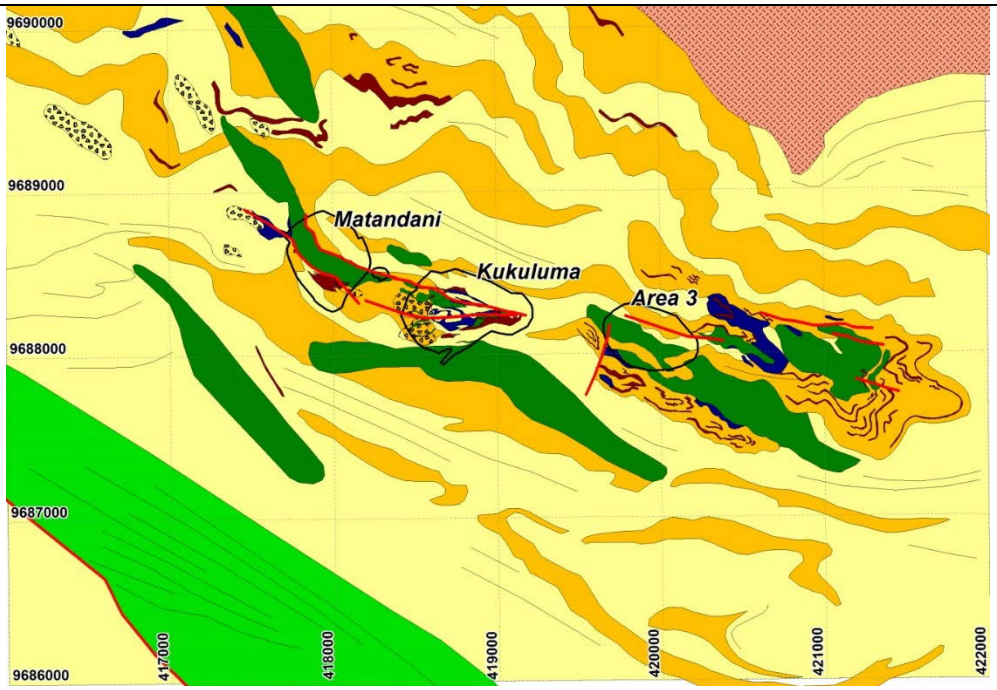

(a)

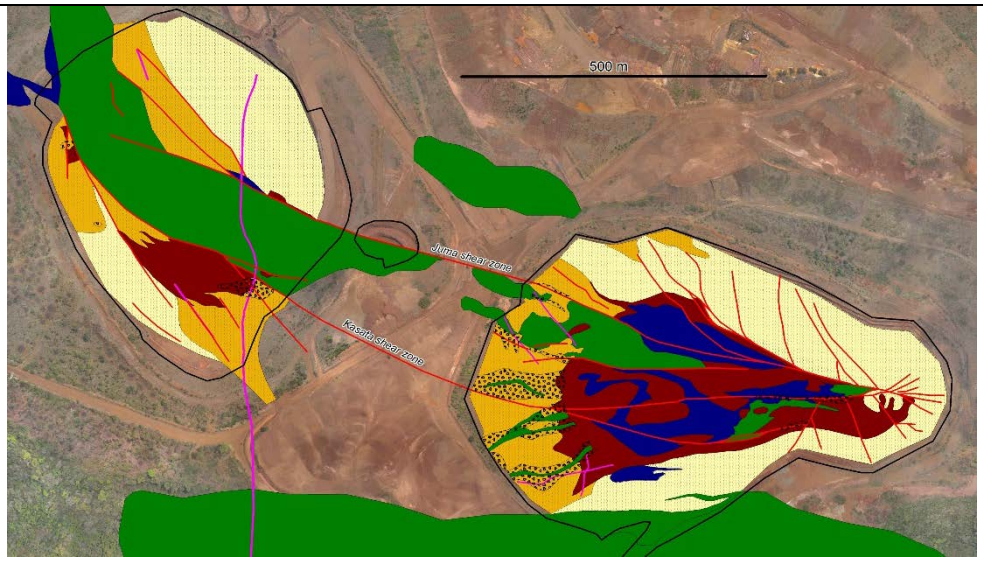

(b)

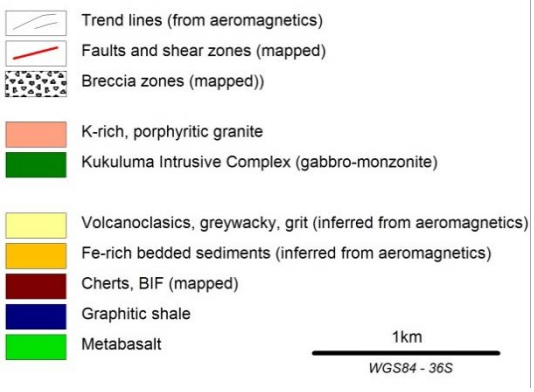

Figure 1.3. (a) Geological map of the central Kukuluma Terrain showing the position of the main gold deposits in the area. The distribution of the "Fe-rich bedded sediments" is derived from geophysics. (b) Geological map in the vicinity of the Matandani and Kukuluma pits.

Gold mineralization within the GGB was discovered by a german prospector in 1898 (GGM internal report). A follow up regional survey in the area was conducted in 1930 by a Kenyan Prospecting company, which resulted in a mine development in 1934-1936 at Geita Hill as an underground operation.

The mining operations closed in 1966 due to the drop in gold price and changes in the Tanzanian government policies on the mining sector. In 1994, Cluff Resources re-opened the exploration activities in the area and operated for two years before selling its shares to Ashanti in 1996. In 1998, Ashanti acquired SAMAX, which owned the Kukuluma Terrain. Continued exploration by Ashanti Company within the Geita Greenstone Belt resulted into the discovery and eventual opening of the Nyankanga world–class gold deposit as an open pit in 1999. In the year 2000, AngloGold acquired 50% of the Ashanti`s Geita Gold Mine shares, which resulted in the formation of the company known as AngloGold Ashanti. One year later, in 2001, the open pit mining commenced at Lone Cone, a deposit connecting Nyankanga and Geita Hill deposits. Mining started at Geita Hill deposit (currently known as Geita Hill West deposit) in 2004. Continued exploration activities in the Kukuluma Terrain led to the opening of the Kukuluma open pit in 2002 and the Matandani pit in 2005, which were eventually suspended in 2006 and 2007 respectively due to the refractory nature (high arsenopyrite content) of the ore. Mining in the Nyamullilima Terrain started in 2008 with the Star and Comet open pit. Currently the Star and Comet deposit operates as an underground mine.

The Kukuluma Terrain is one of the least studied parts of the GGB and there were no systematic studies conducted on the geology of the deposits. The terrain hosts three deposits (Matandani, Kukuluma, and Area 3 West) and two prospects (Central and South). The deposits are overlain by a few meters' thick regolith below which, the weathering profile is as

deep as 150 m. The intensity of oxidation and weathering led to gold redistribution by leaching up to 20m deep and supergene enrichment of gold near the base of the regolith (Bansah et al., 2000). The leaching and supergene enrichment phenomena are evidenced by the distribution of artisanal workings in the Kukuluma pit.

Historical exploration activities in 1994-1996 involved trenching of strong and weak soil anomalies in deeply weathered and leached rock within the Kukuluma-Matandani area, and gave a few results indicative of the potential existence of large ore bodies at depth. This was supported by free gold found in old artisanal workings.

Follow-up exploration drilling conducted in the area returned 2-3 g/t average values between 60-105 m depth at Kukuluma and a planar zone of gold enrichment was found between the base of the regolith and the top of fresh rock (Bansah et al., 2000). Mining conducted between 2002 and 2007 exposed the geology in the Matandani and Kukuluma pits. Since 2007 no exploration activities were conducted in this area until 2011, when AngloGold Ashanti resumed drilling for metallurgical testing. The aim was to investigate the feasibility of mining the arsenopyrite-rich ore and to test potential extensions both down-dip and along strike of the known orebodies in the individual deposits.

Internal mine reports (Skead, 2003; Bansah et al., 2000; Porter, 2002) proposed that gold mineralization in the Matandani and Kukuluma deposits is spatially linked to the major northwest-southeast trending, steeply dipping Juma and Kasata shears. At Kukuluma deposit, for example, the Juma shear zone locally cuts obliquely along limbs of a fold described by Skead (2003), whereas the Kasata shear intersects a fold hinge. In Area 3 West, gold mineralization occurs at the intersection of crosscutting northeast faults with northwest shears. The gold is associated with arsenopyrite in magnetite-rich bands or occurs with silicification and quartz veins at the sheared contact between the ironstones and felsic tuffs.

The mineralization is described as high grade over relatively narrow widths (e.g. *18.85g/t@6m, 13.9 g/t @8m* etc). The internal mine reports focused on the distribution of the gold mineralization within the mineralized zones only and therefore the overall geology of the area and the geological controls on gold mineralization remained unknown.

1.4. THESIS STRUCTURE

This thesis applies a multidisciplinary approach to better understand the geology of the Kukuluma Terrain and the geological controls on gold mineralization. I used a combination of field, computer and laboratory based techniques to help me constrain a variety of factors influencing the gold mineralization. This thesis is subdivided into 6 chapters with appendices as follows:

Chapter 1 is the introduction to the thesis study topic and the geological setting of the Tanzania craton and Geita Greenstone Belt. It also provides a brief history of the Geita Gold Mine.

Chapter 2 presents the methodologies followed in compiling the data sets presented in chapters 3, 4 and 5. I report on data collected from internal mine reports, regional and pit scale geological mapping, drill core logging, cross-section interpretations, and 3D modelling using Leapfrog (software version 3.1.1), and provide an overview of the methodologies used in the structural (chapter 3), geochemical (chapters 4 and 5) and geochronological (chapter 5) studies.

Chapter 3 presents the first detailed structural evolution history of the Kukuluma Terrain and discusses the structural controls on gold mineralization. The structural evolution of the area was developed based on overprinting relationships observed from detailed regional and

deposit-scale geological mapping, drill core logging and the review of historical datasets such as maps and geophysical images, the details of which are included in chapter 2. I use the relationships between the distribution of gold mineralization and different structures to place spatial and temporal correlation between the structural evolution and the mineralizing event. I also constrained the relative timing of dykes and intrusive rocks emplacement in relation to deformation and mineralization. This chapter has been prepared for publication.

Chapter 4 deals with the petrogenesis of the dykes and intrusive units within the Kukuluma Terrain. I present detailed petrographic descriptions of the igneous rocks and high quality major and trace element geochemical analyses. The igneous rocks that intruded the Kukuluma Terrain form three suites: a monzonite suite, a diorite suite, and a granodiorite suite. Because the three suites overlap in space and partly in time I grouped them into the Kukuluma Intrusive Complex. The monzonite and the diorite suites form a ~ northwest-southeast oriented body that runs through the middle of the Kukuluma Terrain and they are virtually undistinguishable in the field while the granodiorite suite occurs mostly as dykes with various orientations and locally form small intrusive bodies. The petrogenetic evolution of the igneous rocks is of particular importance, because of their close spatial relationship with the gold mineralization. It is also possible that fluids related to the emplacement of the igneous rocks may have played a role in gold mineralization. For example, the timing of emplacement and the geochemical characteristics of sanukitoid-type igneous rocks have been linked to gold mineralization in many Archaean gold deposits (Mikkola et al., 2014). This chapter has been submitted for publication.

Chapter 5 presents the first zircon ages and Hf isotope data from igneous rocks and sediments from the Kukuluma Terrain. The geochronological results are used to constrain the absolute timing of emplacement and deformation where possible. The results of zircon dating

made it possible to place a maximum mineralization age in the area. The detrital age data is used to understand the timing of sedimentation in the area, but also set up the timing on the beginning of deformation in the area. I used the Hf isotope data to better constrain the sources and to understand the processes of crustal growth in this part of the Tanzania Craton. This chapter has been submitted for publication.

Chapter 6 contains the conclusions of the thesis and provides recommendations for further work in the area.

Chapters 3, 4 and 5 have been written as papers to be submitted to international journals. Chapter 3 has been written using a similar structure as that used by Sanislav et al. (2015, 2016), and will be submitted to the African Journal of Earth Sciences or a similar journal. Chapter 4 in its current form has been submitted to Precambrian Research and is under review, Chapter 5 will be submitted to a suitable international journal. Because of this approach there is some overlap in materials presented in the various chapters. However, I have tried to minimize this overlap, by presenting the introductory geological setting only once (in Chapter 1), and by combining all methodological sections in Chapter 2.

CHAPTER 2

METHODS AND PROCEDURES USED IN MAPPING, CORE LOGGING AND 3-D MODELLING OF THE MATANDANI, KUKULUMA AND AREA 3 WEST DEPOSITS.

2. 1. INTRODUCTION

This chapter explains the methods and procedures that were followed during surface mapping, drill core logging, chip logging and the construction of the 3-D geological models for the Matandani, Kukuluma and Area 3 West deposits. These models and the associated maps and logs provide the basic datasets that underpin the geological (structural and intrusive) framework presented in chapter 3, and the geochemistry and geochronology work presented in chapters 4 and 5 respectively.

In conducting the mapping, logging and modelling, a number of challenges were encountered during the compilation of historical data sets, including: incomplete back-ground information (e.g. collar position for drill holes); cross-sections without coordinates; and geological maps for which projections were not known. In addition, the nomenclature used to describe lithologies in the company`s database did not always match the lithological names and codes used in historical reports.

This made it necessary to review large amounts of data (e.g. Table A2-1) in order to generate a consistent nomenclature and stratigraphy for the lithologies in the area (as presented in Chapter 3), by grouping related geological units and providing them with a proper lithological name based on petrological and geochemical work (as presented in

Chapter 4). The standardized geological nomenclature was than used to define stratigraphic subdivisions from which 3-D models were built.

2.2. METHODOLOGIES

2.2.1. Mapping

All mapping was done in UTM with information referenced to datum ARC1960, 36S. Surface geological mapping was conducted in open pits, along road cuts and river valleys using high-definition aerial photography and digital terrain models provided by GGM. In mapping, use was made of historical maps held in the GGM database, which were mostly compiled during the exploration phase for the mine in the 1990's and early 2000's (see Appendix A1). Because of poor outcrop, use was made of high-resolution geophysical images including airborne magnetics, radiometrics and surface EM (electromagnetics), to identify the aerial extent of mainly magnetic units (the cherts and ironstones) and structures (see Appendix A1).

All data and maps produced were scanned and georeferenced (UTM36S, Arc1960) in GIS ArcMap software (v. 10.3.1) and entered into the mine database. This information forms the basis for the geological maps presented in this theses (e.g. Fig.1.3).

2.2.2. Logging of diamond drill cores and rock chips.

Cross-sections, maps and 3-D models are largely based on the re-logging of drill core and rock chips that were collected in the early 2000`s and kept in the database, and the collection of new data from drill core obtained between January 2013 and early 2016. A total of 14600 drill holes were used in the reconstruction of the 3-D geology, spread across the three deposits (Fig.2.1a; Appendix A2).

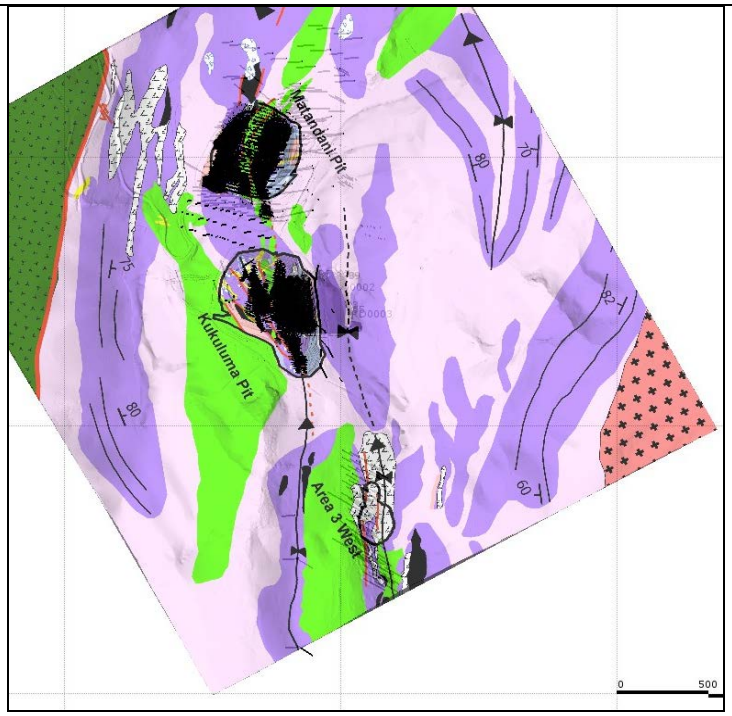

(a)

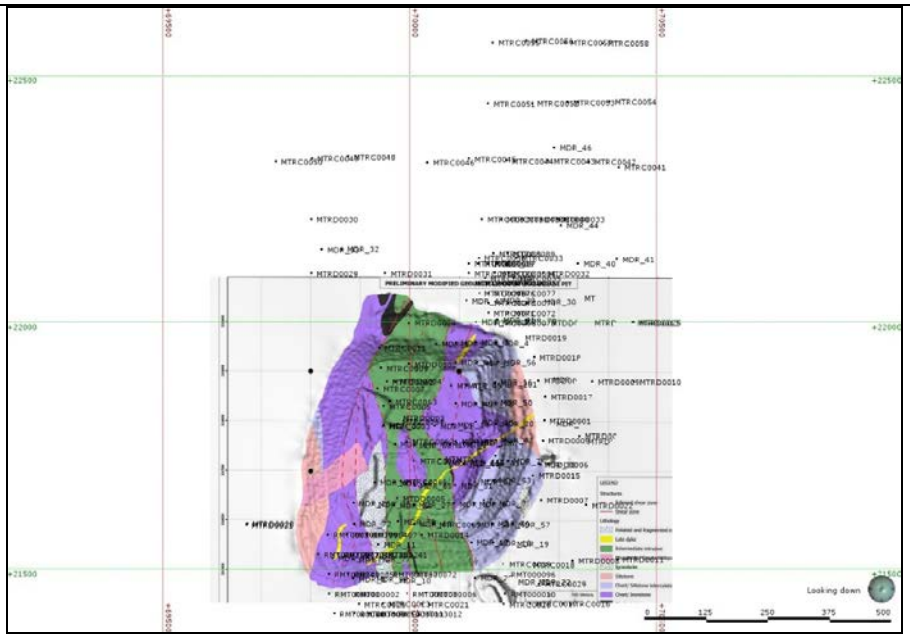

(b)

Figure. 2.1 (a) Regional geological map of the Kukuluma terrain showing the topography and spatial distribution of drill holes (black coloured dots) in Matandani, Kukuluma and Area 3 West deposits; (b) Distribution of drill holes around the Matandani deposit used in 3D-modelling. The image is taken looking north with reference to the Kukuluma Local Mine Grid (i.e. Local = UTM + 44.5degrees)

Of these, 11000 had been logged previously by Geita Gold Mine exploration geologists. The re-logging of drill cores and chips was done for 13000 drill holes as part of this study in order to get a consistent observational base from which to construct the surface

maps and cross-sections. Core logs with structural measurements and data on lithologies, alteration and ore-grade were entered into the GGM data base.

Each logged drill core was photographed following the GGM standard operating procedure for diamond drill core photography (Brayshaw, 2011). Specific areas of interest were selected and described in more detail to assist in geological interpretations. Rock chip samples obtained from percussion drilling were split for gold analysis. Sampling for logging and assays was done on a 1 m interval as per GGM standard chip sampling procedure. Gold assay results are taken as an average value within the sampled meter. The accurate logging of rock chips is difficult in the deeply weathered regolith, which can be up to ~100 m thick. To overcome rock identification problems, logging of the rock chips was done in an interactive manner with the logging of diamond drill cores that originated from nearby the percussion holes.

2.2.3. Rock types logged

Due to a lack of consistency in the historical logs, a standardized nomenclature was developed for the rock types encountered in the Kukuluma terrain. Note that historically there has been a great deal of variability in the way some of the units have been identified in drill core. The details of the standardized nomenclature based on the re-logging campaign versus the historical names in the database are summarized in Appendix A2, Table A2.1. A summary stratigraphy constructed from these drill cores is shown in figure 2.2.

2.2.4. Grade analysis/Assaying

During logging of drill cores, ore zones were first identified using visual indicators of mineralization including increased silicification and carbonate ± chlorite alteration, and fracture networks in-filled with pyrrhotite. High-grade zones are characterized by the

development of cubical arsenopyrite and the replacement of magnetite by pyrrhotite. In rock chips, mineralized zones are harder to identify, but they can be recognized based on the presence of highly silicified and sulphidized chips.

Once a mineralized zone has been identified, the core was cut, and half-core was assayed. In relatively barren zones, assay results were collected at sample intervals of 1 m. In well-mineralized zones, a standard sampling interval of 0.5 m has been used. Samples were assayed at the on-site SGS laboratory, and results entered in the data base and used to model ore envelopes. Envelopes were reconstructed in Leapfrog at a lower cut off of 0.5g/t. Higher grade envelopes were constructed at >1 g/t as required.

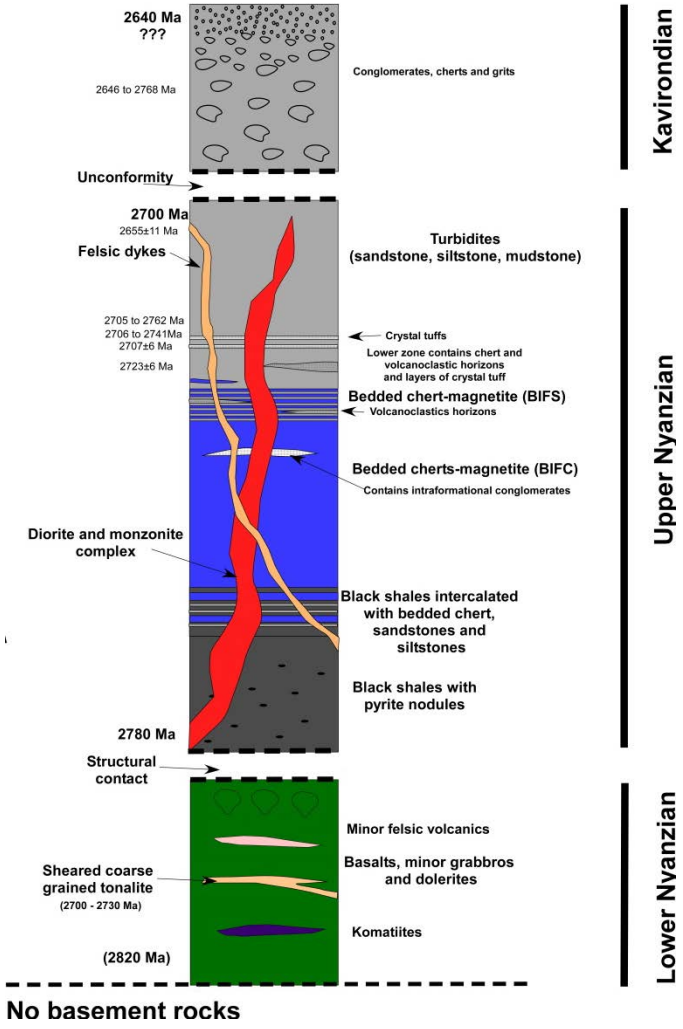

Figure 2.2. Summary stratigraphy for the Kukuluma terrain.

2.2.5. Leapfrog modeling

3-D models have been constructed from geological maps and cross-sections (Appendix A4). The cross sections were constructed from surface maps and drill cores. The most detailed 3-D model (i.e. the model based on the largest number of reconstructed sections) presented in this study is from the Matandani deposit (Appendix A5; Fig. A5.1), which has been the focus of exploration in recent years.

Geological modelling was done using Leapfrog Geo software (v. 3.1.1). In this project, a local UTM grid, called the Kukuluma Local Mine Grid (KLMG) was used for data input. This grid was constructed at a high angle to the expected envelope of the ore bodies. The relationship between the KLMG and the regional UTM grid (i.e. ARC1960, 36S) is as follows: KLMG = Arc 1960, 36s UTM + 44.5°.

Drillholes were drilled along the north-south line on the local grid, either plunging to the southwest or to the northeast at an approximate plunge of 65°. Drill spacing is variable. The locations of drill holes used in this study are shown in figure 2.1.

All datasets were imported into Leapfrog before modelling was done, including: drill hole data (collar position, down hole orientation survey, gold assay results and lithological units). Validation of the drill hole data was done by making sure that all data entry is consistent. All lithological units entered were grouped as shown in Table A2.1.

After all data was entered into Leapfrog, logging data was projected onto vertical section planes. These section planes were used as base maps for the drawing of cross sections. Cross sections were constructed along the north-south lines in the KLMG at intervals of 50-100m (Appendix A4; Fig. A4.1). In this context it is important to note that sections constructed during the earlier stages of this project (e.g. the Kukuluma sections; Fig.

A4.2b) did not fully capture all the deformational details, whereas later sections (e.g. some of the Matandani and Area 3 West sections; Fig. A4.2c) more faithfully reflect the complex fold interference patterns described in Chapter 3. Once hand-drawn sections were completed and cross checked by supervisors on the mine, the sections were scanned, digitized and imported into Leapfrog.

The cross sections have been used as the base information for constructing 3-D solids of lithological units and ore-envelopes in Leapfrog. The data in cross sections was augmented with drill core data obtained away from section lines. Results of the 3-D modelling for each of the ore bodies have been included in Appendix 5 (Figs A5.1, A5.2 and A5.3).

2.2.6. Methodology for fault kinematic analysis

Results of kinematic analysis for faults in the Kukuluma and Matandani pits have been presented in Chapter 3 (Figs 3.6 and 3.9). The methodologies on which the analyses are based are briefly summarized below. Kinematic data from faults can be used to reconstruct palaeo-stress fields (e.g. Angelier and Mechler, 1977). For this, information is required on the orientation of the fault plane, the slip direction visible as slickenlines, striations or gouge marks, and the sense of movement. Stress inversion techniques rely on the assumption that the slip direction coincides with the resolved shear stress on the fault plane, and that the set of faults used in the analysis, formed or were active in response to the same far field stress. Fault-slip data can be inverted to a reduced moment tensor with information on the direction of the principal stress axes with their relative size expressed as a stress ratio (Angelier, 1994; Delvaux and Sperner, 2003). This reduced stress tensor can be calculated using the P and T axes that bisect the fault plane and an auxiliary plane perpendicular to the fault, by using least-square minimization techniques of direction cosines (e.g. Marrett and Allmendinger, 1990) or iterative methods that test a variety of possible tensor solutions (e.g. Etchecopar et

al., 1981). Stress axes can also be determined graphically using the right dihedron method (Lisle, 1987; Delvaux and Sperner, 2003), which constrains the orientation of principal stress axes by determining the area of maximum overlap of compressional and extensional quadrants for a suite of faults.

In analyzing the fault-slip data, we have used a linked Bingham distribution tensor calculated with the programme FaultKinWin (Allmendinger, 2001, 2012) following methods described by Marrett and Allmendinger (1990), and Cladouhos and Allmendinger (1993). The FaultKinWin programme (Allmendinger, 2001) uses the distribution of P and T axes for a suite of faults to calculate a Bingham axial distribution based on a least squares minimization technique for direction cosines. In this technique, the dihedral angle between the fault plane and an auxiliary plane is 90º and bisected by P and T axes. The eigenvectors for the calculated Bingham axial distribution provide average orientations for the maximum, minimum and intermediate concentration direction of the P and T axes, and the eigenvalues provide a measure of the relative concentration, or distribution of P and T axes. These eigenvalues vary between -0.5 and +0.5, with maximum values reached when P and T axes are perfectly concentrated. Variations in the eigenvalues (ev) can be linked to the stress regime using the relative size of the normalized eigenvalues expressed in a ratio, Rev, (with Rev = [ev2-ev3]/[ev1-ev3]) (constrictional stress: Rev=1 with $ev_1 = ev_2$; plane stress: Rev =0.5 with ev2 = 0; flattening stress: Rev = 0 with $ev_2 = ev_3$). The FaultKinWin programme output is a plot of linked Bingham axes with eigenvalues and a related fault plane solution diagram displaying P and T quadrants in a manner similar to earthquake focal mechanisms (Figs 3.6 and 3.9 in Chapter 3).

Although stress analysis from fault slip data is widely applied, debate continues whether the obtained solutions represent a stress field or provide a measure of strain and strain rate (e.g. Molnar, 1983, Twiss and Unruh, 1998). Marrett and Allmendinger (1990)

and Allmendinger (2001), using FaultKinWin, prefer to interpret the fault plane solutions as an indicator of strain rather than stress. Here, the linked Bingham fault plane solution through FaultKinWin has been interpreted as an indication of the palaeo-stress field. In doing this we are aware of the various pitfalls. Faults, once formed, can interact in complex ways in response to an imposed stress-field due to scale-dependent strain partitioning, complex fault interactions, block rotations, inhomogeneities in the rock mass etc. (e.g. Twiss and Unruh, 1998). In spite of such limitations, the palaeo-stress analysis technique has been successfully applied in a wide variety of tectonic settings (e.g. Sperner et al., 2003; Dirks et al., 2009, 2013), and we believe that it does provide valuable insights in the tectonic controls on gold mineralization at Kukuluma.

Misfits in collected datasets may have resulted from observational errors, the mixing of unrelated data points or limitations in the approach used. They can also be due to non-uniform stress fields as a result of fracture interactions, anisotropies in the rock mass, block rotations or slip partitioning. In calculating a Bingham tensor solution using FaultKinWin all data points collected were included, and every measurement was given the same weight. It is stressed that throughout the analyses of datasets, few data points were incompatible with the final results, suggesting generally homogeneous data.

As a general rule, the results from the palaeo-stress analyses are best constrained for large data sets that combine fracture planes with different directions and movement sense. Thus, conjugate fracture sets, or Riedel, anti-Riedel and P-shear arrays provide good results more likely to be indicative of the regional palaeo-stress field, especially if the stress inversion is based on at least 15 fracture planes (Delvaux and Sperner, 2003; Sperner et al., 2003), whilst sites in which only few planes, or planes in a limited number of directions can be measured provide at best an indication only of the local palaeo-stress field, which may or may not conform with the regional results.

2.2.7. Methodology for major and trace element analyses

With respect major and trace element analyses as reported in Chapter 4, all geochemical analyses were performed at the Advanced Analytical Centre at James Cook University (JCU) on samples collected from drill cores. All samples were collected away from the mineralized zones to minimize the effect of alteration. Representative sample material was milled to a fine powder in a tungsten carbide ring mill. Major elements were analyzed by conventional X-ray fluorescence (XRF) using a Bruker-AXS S4 Pioneer XRF Spectrometer on fused beads. The fused beads consist of rock powders mixed with 12:22 borate flux (XRF Scientific Limited, Perth, Australia) at 1:8 sample to flux ratio that were fused to glass after heating to 1050 °C for 15 min in a F-M 4 Fusion Bead Casting Machine (Willunga, Australia).

For trace element analyses, chips of the fused beads were mounted into a standard epoxy puck and analyzed for a range of trace elements using a Geolas Pro 193 nm ArF Excimer laser ablation unit (Coherent) coupled to Varian 820 quadrupole ICP-MS. Helium was used as the carrier gas (0.8 l/min), which was subsequently mixed with Ar via a mixing bulb between the ablation cell and the ICP-MS to smooth the ablation signal. Laser energy density was set to 6 J/cm^2, and laser spot size and repetition rate were set to 120 μm and 10 Hz, respectively. Each fused bead was analyzed 3 times and average values are reported. The ICP-MS was tuned to ensure robust plasma conditions and low oxide production levels (≤ 0.5% ThO) with the plasma power set at 1.25 kW. NIST SRM 610 glass was used as a bracketed external standard using the standard reference values of Spandler et al. (2011). Data were quantified using Ca (as previously determined by XRF on the same fused bead) as the internal standard, and data were processed using the Glitter software (Van Achterbergh et al., 2001). To monitor precision and accuracy of the analyses, we analyzed Hawaiian basalt

reference glass (KL2-glass; n=21) as a secondary standard (Jochum et al., 2006). The precision for REE analyses by LA-ICP-MS is better than 5% (mostly <3%), and the accuracy is better than 6%, often <2%. The standard reference material NIST612 (n=11) was analyzed as a ternary standard. The precision for all the elements, besides Zn (3.5%) and Ge (~8.3 %,) is <2%, and <1% for REE. The accuracy for all the elements (standard reference concentrations taken from Spandler et al., 2011) is <3%. The only exceptions are Tb (6.5%), Ge (~8.3%), Sb (~9%), and Zn (~5.3%) where relatively large uncertainties in the NIST612 glass have to be taken into consideration. The results of the analyses are presented in Appendix 7.

2.2.8. Methodology for zircon dating

With respect the zircon dating presented in chapter 5, for each outcrop targeted for dating, 2-3 kilograms of sample was collected. The samples were split and the weathered surfaces were removed. The split fraction from each sample was milled with a tungsten carbide disc mill to a grain size of ≤ 500 μm. The 500 μm portion was run in water current on a Wilfley table, and the heavy mineral fraction was collected and subsequently run through a Frantz magnetic separator. The non-magnetic fraction was divided further using heavy liquids from which the heavy fraction was run again through a Frantz magnetic separator. Zircons were hand-picked from the non-magnetic fraction and mounted into epoxy resin blocks and polished to about half of their thickness; first with a 3 μm diamond paste than with a 1 μm diamond paste.

Before the analysis, all zircon grains were imaged using a Jeol JSM5410LV with attached cathodoluminescence detector to identify growth domains and inherited cores within the grains. U–Pb isotope analyses were obtained using a GeoLas 200 Excimer Laser Ablation System in a He ablation atmosphere, coupled to a Varian ICP-MS 820 series instrument.

Laser parameters during the analyses include a repetition rate of 10 Hz, spot size of 32 µm and energy of 6.0 J/cm^2. Analyses involved 30 seconds of background measurement (gas blank) followed by 35 seconds of acquisition of U-Pb isotope data. U–Pb fractionation was corrected using the GJ-1 (ID-TIMS $^{207}Pb/^{206}Pb$ age = 608.5 ± 0.4Ma (Jackson et al., 2004) as the primary standard. FC-1 zircons (ID-TIMS $^{207}Pb/^{206}Pb$ age = 1099.0 ± 0.6Ma (Paces and Miller, 1993) and the 91500 zircons (ID-TIMS $^{206}Pb/^{238}U$ age = 1062 ± 1Ma (Wiendenbeck et al., 1995) were used as secondary standards. Several zircon grains were excluded from analysis due to the metamict nature and small size of the grains. Analyses with high common Pb and/or significant discordance (>10%) were not included in the age calculations.

Data processing was done using the software package GLITTER^{TM} (Jackson et al., 2004), and the age calculations were made using Isoplot (Ludwig, 2003). Over the duration of this study the reported weighted average age (errors at 95% confidence) for GJ-1 is 602 ± 3 Ma for $^{206}Pb/^{238}U$ and the concordia age is 602 ± 3 Ma. FC-1 gave a weighted average age of 1100 ± 10 Ma for $^{207}Pb/^{206}Pb$ and 1099 ± 10 Ma for the concordia age. 91500 weighted average during the analyses was 1061 ± 6 Ma for $^{207}Pb/^{206}Pb$ and the concordia age was 1061± 7 Ma. $^{207}Pb/^{206}Pb$ grain ages are used in this study. Abundances of U and Th were measured using a NIST 610 glass standard in conjunction with internal standardization using the known stoichiometric abundance of Si in zircon. The data analyses for the various zircon standards used in this study are presented in Appendix 8.

2.2.9. Methodology for hafmium (Hf) data collection

For Hf isotope data acquisition the analytical protocols followed the procedures outlined in Kemp et al. (2009). The Hf isotope compositions were acquired with a Thermo-Scientific Neptune multi-collector ICP-MS attached to a Coherent GeoLas 193 nm ArF laser.

Each analysis was performed on the same area of the zircons that were previously dated by LA-ICP-MS or on the same CL defined growth domain. A 60 µm laser beam diameter was used at a 4Hz laser repetition rate. Standard zircons analyzed during the study were Mud Tank and FC1, the latter to check the isobaric interference corrections for Yb. The average $^{176}Hf/^{177}Hf$ and the 2 sigma errors during the analyses for the standards were: 0.282482 (±0.000004) for Mud Tank, and 0.282153 (±0.000005) for FC1. Epsilon Hf (ε_{Hf}) values were calculated using the present day chondritic values of $^{176}Hf/^{177}Hf_{CHUR\ (0)}$ =0.282785 and $^{176}Lu/^{177}Hf_{CHUR\ (0)}$ = 0.0336 (Bouvier et al., 2008). For this study, we adopted the ^{176}Lu decay constant of 1.867 X 10^{-5} m.y.$^{-1}$ proposed by Soderlund et al. (2004). The data analyses for the various zircon standards used in this study are presented in Appendix 8.

CHAPTER 3

THE STRUCTURAL HISTORY OF THE KUKULUMA AND MATANDANI DEPOSITS AND CONTROLS ON GOLD MINERALIZATION, GEITA GREENSTONE BELT, TANZANIA

3.1. SUMMARY

A series of westnorthwest trending gold deposits centred on the Kukuluma deposit occur over a ~5 km strike length in the eastern part of the Geita Greenstone Belt, northwest of Tanzania and are hosted within an Archaean meta-volcanosedimentary package dominated by ironstone. The deformation history in the area encompasses a series of ductile folding and shearing events (D_1-D_5) which formed at upper-greenschist to amphibolite facies conditions, simultaneous with the emplacement of monzonite-diorite-gabbro intrusions (the Kukuluma Intrusive Complex), and overprinted by a first generation of porphyritic dykes and sills. D_1 comprises a family of structures including boudins of primary bedding, layer-parallel chert veins and intrafolial folds in near-layer-parallel chert units interpreted as low-angle shear zones. D_2 folding is widespread, and coincides with the peak of regional metamorphism and the formation of a penetrative fabric that in many places is near parallel to the compositional layering. D_2 folds are closed to isoclinal and vary in scale from 1-500m, and are overprinted by 1-500 m scale D_3 folds, which form the dominant structures in the area. They consist of open to closed upright folds developed in fold domains separated by planar high strain zones or foliation domains where S_0, S_1, S_2 and S_3 have been transposed. D_2 and D_3 structures form complex, Type 2 fold interference patterns that affect the distribution of chert and ironstone units, which are the main host to gold mineralization. D_3 structures were refolded by near

vertical, D_4 gentle folds and D_5 low angle reverse faults and associated open, recumbent folds.

The earliest intrusions of the Kukuluma Igneous Complex were emplaced pre-D_3, with the main face of igneous activity occurring syn-D_3, resulting in the alignment of intrusive bodies with the axial plane of D_3 folds. Emplacement and crystallization of the intrusive bodies was associated with fluid release resulting in localized breccia development within the more brittle meta-ironstone lithologies. These events were followed by the development of east- to southeast-trending, steeply dipping, brittle-ductile shear zones (D_6) that formed along a westnorthwest corridor as a result of north-south compression. The D_6 shear zones are transected by at least one generation of later north-trending porphyry dykes, and have subsequently been reactivated (D_7) at brittle-ductile to brittle conditions as normal faults, mostly with a sinistral component of shear.

Gold mineralization within the Kukuluma area is late and spatially associated with D_6 shear zones along the steeply dipping contacts between diorite of the Kukuluma Intrusive Complex and iron-rich lithologies (mainly chert and bedded ironstone) conducive to the precipitation of sulphide and gold. The distribution of these lithologies is strongly affected by D_2-D_3 fold interference patterns, creating a discontinuous distribution of host lithologies in sectional planes. The complex D_2-D_3 fold architecture and breccia zones also created the micro-fracture networks and dilatant zones needed for fluid movement, with enhanced mineralization observed in areas of intense D_3 folding. Gold precipitation was accompanied by the replacement of magnetite by pyrrhotite and the growth of arsenopyrite, pyrite, stibnite and scheelite in fracture networks and as disseminations. Mineralisation overprints the late north-trending porphyry dykes, and is interpreted to be associated with D_7 faulting, in part by re-activating D_6 shear zones during northnortheast-southsouthwest extension.

3.2. INTRODUCTION: GREENSTONE BELTS AND GOLD MINERALIZATION

Archaean granite greenstone belts are elongate structures that consist of supracrustal units deformed in broadly synformal or keel-like shapes. They vary in composition from ultramafic to felsic metavolcanics, interbedded with clastic sediments that range from distal turbidite units to proximal, coarse-clastic conglomerate (e.g. Condie, 1994; Jelsma and Dirks, 2002; Anhaeusser, 2014). Greenstone belts are commonly bounded and cut by large intrusive complexes of tonalite-trondhjemite-granodiorite (TTG) composition that form open, rounded antiforms, arches or domes (Condie, 1994; Bouhallier et al., 1995; Jelsma and Dirks, 2002; Anhaeusser, 2014). Various tectonic models have been proposed to explain the characteristic geometry of granite-greenstone terrains including vertical tectonics involving density inversion and diapiric emplacement of mid- to lower-crustal melt into upper-crustal volcano-clastic sequences (e.g. Choukroune et al., 1995; Chardon et al., 1996; Collins et al., 1998; Bédard et al., 2003; Van Kranendonk, 2011), or horizontal tectonic processes involving low-angle subduction and crustal stacking, or core complex formation followed by late granite intrusions due to decompression melting (Polat et al., 1998; Bouhallier et al., 1995; Windley, 1995; Shackleton, 1995, Dirks and Jelsma, 1998, Jelsma and Dirks, 2002; Kloppenburg et al., 2001; Blewett et al., 2004; 2010b; Kabete et al., 2012), with these processes being linked to early forms of plate tectonics, mantle plume activity or both (e.g. Moyen et al., 2006; Blewett et al., 2010a,b).

Greenstone belts represent one of the principle settings for gold deposits, which are generally categorized as quartz lode or shear zone hosted deposits, considering their association with secondary structures near major shear zones and associated quartz veining (Groves et al., 1998; Goldfarb et al., 2005; Frimmel, 2008). Gold deposits forming in greenstone belts are commonly interpreted as orogenic gold deposits linked to accretionary processes in arc settings during the late stages of Cordilleran–type tectonics (e.g. Groves et

al.,1998; Bierlein et al., 2006, 2009), with gold mineralisation coinciding with change in the stress regime from a compressional to a trans-pressional or trans-tensional phase (e.g. Kerrich et al., 2000; Goldfarb et al., 2001,2005; Groves et al., 2003, 2006; Bierlein et al.,2006; Frimmel, 2008; Begg et al., 2009; Dirks et al., 2013; Sanislav et al., 2015, 2016). Linking Archaen lode or shear hosted deposits to orogenic processes would imply that modern plate tectonics, in some form would have occurred in the Archaen (e.g. Kabete et al., 2012; Groves and Santosh, 2015). With respect gold mineralization the sharp increase in the number of gold deposits during the Late Archaean has been used to illustrate the advent of plate-tectonics at that time (e.g. Goldfarb et al., 2001; Bierlein et al., 2006, 2009). In contrast, alternative tectonic models for greenstone belt formation that invoke vertical melt segregation above mantle plumes (e.g. Bédard et al., 2014; Cook et al., 2015), would imply that lode-gold deposits are not orogenic in origin.

Regionally, large gold systems are thought to be selectively developed in specific tectonic domains with suitable geological settings involving terrain boundaries, which act as first-order structures that control crustal-scale plumbing systems of mantle-derived magma and hydrothermal fluids (e.g. Ridley et al., 1996; Goldfarb et al., 2005; Leahy et al. 2005; Bierlein et al., 2006; Phillips and Powell, 2010). The timing of granitoid intrusion with respect greenstone formation, geometric orientation of controlling structures, and host-rock and intrusive geochemistry are major factors to be considered when targeting areas that are prospective for mineralization on a terrain-scale. Particular indicators for mineralisation can be the presence of late- to post-kinematic granitoids that act as proxies for the heat engines critical for driving gold mineralization (e.g. Phillips and Zhou, 1999).

On a mine- or camp-scale, shear-hosted, lode-gold deposits are associated with complex arrays of dilatant, brittle-ductile structures commonly interpreted to form as secondary features near compressional or transpressional shear zones (Colvine et al., 1988;

Robert et al., 1991; Groves et al., 1998; Cox et al., 2001; Tripp and Vearncombe, 2004; Dirks et al., 2009). Such shear zones are generally seen as the principle conduits for mineralizing fluids involving the repeated locking and reactivation of fault planes in response to fluid pressure fluctuations (i.e. the fault valve model of Sibson, 2001, 2004). Secondary structures include fracture arrays, breccia zones and fold hinges within more brittle lithologies (Robert et al., 1991; Ojala et al., 1993; Groves et al., 2000; Sanislav et al., 2015). The gold-bearing fluids interact with wall-rocks along structural traps where favourable changes in physico-chemical conditions lead to ore formation (e.g. Sanislav et al., 2015).

In the Tanzania Craton, many gold deposits were developed in the 1990's and early 2000's by re-opening and extending known historical workings. The Geita Greenstone Belt (GGB) in the northern part of the craton (Fig. 1.2) hosts a number of large (>1Moz) gold deposits spread along 25km of the greenstone belt. These deposits, include (from west to east) the Star & Comet, Nyankanga, Lone Cone, Geita Hill, Matandani and Kukuluma deposits , and are commonly referred to collectively as Geita mine (e.g. Bierlein et al. 2006). All of these deposits are largely hosted by meta-ironstone units near the intrusive contacts of monzonitic to dioritic bodies that intruded internal to the greenstone belt (e.g. Borg, 1994; Sanislav et al., 2015, 2016).

To date no detailed work has been published for the major deposits that occur in the eastern part of the GGB (Figs.1.2 and 1.3). These include the Matandani, Kukuluma and Area 3 deposits that collectively host several Moz of gold. In this chapter, a deformation model for the area around the Matandani and Kukuluma pits will be presented, based on detailed mapping, core logging in the pits and surrounding areas. The deformation model will be linked to the relative timing of intrusive units and gold mineralization, and forms the basis for geochemical and geochronological studies in the area (see Chapters 4 and 5). For background

to the general geology of the Tanzania Craton and geological setting of the Geita Greenstone Belt I refer to the introduction in Chapter 1.

3.3. PREVIOUS STRUCTURAL WORK

Initial models for the deformation history of the GGB and associated gold deposits did not move beyond a general scheme involving early upright folding (D_1), overprinted by a second folding event characterized by steeply plunging axes (D_2) and cut by later shear zones (D_3), with gold mineralization post-dating D_2 and utilizing regional-scale shear zones as fluid pathways (Booth, 1954a, b; Borg et al., 1990; Borg, 1992, 1994). Mine models in the early 2000's assumed that mineralised shear zones in the GGB were part of complex thrust stacks associated with horizontal shortening and stacking of the greenstone sequence with gold-mineralisation concentrating in dilatant zones along thrusts and near fold hinges (Painter, 2004). Subsequent mining has demonstrated that the structures associated with gold did not facilitate large-scale thrusting, but instead have complex deformation histories as shown for the Nyankanga and Geita Hill deposits (Sanislav et al., 2015, 2016). These deposits are centred on NW dipping reverse faults (D_6) that overprint a complexly sheared and folded (D_{1-5}) stack of meta-ironstone and chert, and were reactivated as (D_8) normal faults at the time of mineralization. Gold-deposition preferentially occurred along diorite-meta-ironstone contacts exploited by the shear system (Sanislav et al., 2015, 2016) after 2644 Ma (Borg and Krogh 1999), i.e. 40-50 Ma later than the formation of D_6 thrusts (Sanislav et al., 2016).

3.4. ROCK TYPES AND STRATIGRAPHY OF THE KUKULUMA TERRAIN

The Kukuluma terrain forms the eastern part of the GGB and is bounded to the west by a major northwest-trending shear zone, which juxtaposes lower greenschist facies meta-sediments of the Central terrain, with lower amphibolite facies mafic to ultramafic meta-

basalts of the Kukuluma terrain (Fig. 1.2; Cook et al. 2015). In this section, we provide brief descriptions of the lithological units and proposed stratigraphy as encountered along the Kukuluma Mineralized Trend in the central part of the Kukuluma terrain (Figs 1.3). A summary stratigraphic column is provided in Figure 2.2. Examples of the main lithological units are shown in Figure 3.1.

3.4.1. Volcano-sedimentary units

The sedimentary sequence in the central Kukuluma terrain is dominated by clastic sediments interbedded with chert beds of possibly tectonic origin (see below), magnetite-rich meta-ironstone units and volcanoclasic beds, which overlie mafic volcanics preserved along the western margin of the Kukuluma terrain (Figs 1.2, 2.2, 3.1). The base of the clastic sedimentary pile consists of a black, graphitic shale unit of undefined thickness (drill intersections indicate a minimum thickness of ~10m) that is well exposed at the bottom of Kukuluma pit. They are locally interlayered with chert and meta-ironstone beds (Figs 2.2, 3.1), and associated with pyrite and pyrrhotite nodules. The black shale unit transitions into a well-layered meta-ironstone unit, with a thickness that is variable as a result of structural attenuation, folding, transposition and tectonic duplication. The meta-ironstone unit is widely distributed across the central parts of the Kukuluma terrain (Fig. 1.3), and consists of regularly layered packages with magnetite-rich layers and selvages interlayered with more well-foliated shale beds and highly silicified, quartzose beds with a glassy appearance that are locally cherty (Fig. 3.1).

(a)

(b)

(c)

(d)

(e)

(f)

(g)

Figure 3.1. Examples of the main lithological units in the central Kukuluma terrain: (a) well-layered ironstone; (b) fragmental volcanoclastic unit; (c) intraformational conglomerate within the ironstone units, in which conglomerate clasts are mostly composed of angular chert fragments [drill core hole ID: MTRD0009 (458 - 461m)]; (d) black shale with remnants of pyrrhotite nodules; (e) turbiditic siltstone and sandstone showing graded bedding; (f) intrusive diorite with biotite after amphibole blasts elongated along S_3; (g) late felsic porphyry dyke.

Individual meta-ironstone beds vary in thickness from several mm's to several tens of cm. In some places, the unit contains thick beds of chert (up to 10m), that form prominent ridges (Fig. 1.3). The chert layers are locally discontinuous, possibly due to deformational processes (boudinaging and shearing), and may contain magnetite-rich layers that transition into chlorite-biotite-rich shale bands, with abundant grunerite along the contacts.

In places (e.g. in the northen wall of the Kukuluma pit) the meta-ironstone unit is intercalated with volcanoclastic units that include fragmental rocks with ignimbritic characteristics. These fragmental pyroclastic flow deposits are exposed in the Kukuluma area as two, northwest striking elongate bodies each ~350m long and 30m thick. They are layered and contain shards of silica-rich, glassy material with chilled margins embedded in a fine-grained, feldspar-rich matrix (Fig. 3.1).

In the Kukuluma-Matandani area, the magnetite-rich meta-ironstone unit transitions into meta-greywackes that comprise laminated shale- to sandstone units (Fig. 8) best exposed along the eastern and western walls of Matandani pit and the northeastern and southern walls of Kukuluma pit. The clastic meta-greywackes are well-bedded with a typical bed thickness of 5-15 cm and are interlayered with fine-grained meta-tuff beds and volcanoclastics. Sedimentary structures are well preserved within the meta-greywacke unit and include graded bedding (fining upward with partial Bouma sequences), low-angle cross bedding and scour marks, which provide younging indicators (Fig. 3.1e). Some of the thicker meta-sandstone units contain small, well-rounded chert pebbles or grit at their base. These graded beds are reminiscent of turbidites and are interbedded with several more massive, non-structured (i.e. no grading), matrix supported conglomerate beds that contain mostly angular chert clasts, <3cm in diameter embedded in a coarse, sand matrix. The sedimentary structures suggest that these beds were laid down on the proximal parts of a marine fan-delta system with input of immature sediment (e.g. Hofmann et al., 2001a). Younging directions confirm that the unit

underwent early isoclinal folding making it hard to estimate the original stratigraphic thickness. In Kukuluma pit the unit is underlain by a thick chert horizon associated with intense shear, isoclinal folding and numerous quartz veins, which is probably of tectonic origin (Figs 3.1a; 3.2a). The meta-greywacke unit is generally deeply weathered and has previously been described as felsic tuff (e.g. Skead, 2003).

3.5. THE HISTORY OF DEFORMATION AND INTRUSION IN THE CENTRAL KUKULUMA TERRAIN

The deformation events in the Kukuluma-Matandani area comprise an early group of penetrative structures involving overprinting folding, shearing and brecciation events, which occurred when the rocks mostly behaved in a ductile manner (D_1-D_5), and a later group of more localized structures as strain was partitioned into brittle-ductile shear zones, faults and joints (D_6-D_7). With respect gold mineralization, the former group of structures created the architecture that influenced the distribution of rock-types favorable for gold precipitation, whereas the latter group of structures more closely controlled fluid flow. Deformation events were accompanied by the emplacement of two separate diorite and monzonite suites that intruded syn-tectonically, and a granodiorite suite (mostly dykes) that intruded late syn-tectonically, which collectively form the Kukuluma Intrusive Complex (KIC; Chapter 4). The KIC probably formed as a result of intracrustal melting at the base of a thickened oceanic plateau, and may not have involved subduction (Chapter 4), similar to other volcanic units in the area (e.g. Cook et al., 2015). The intrusions of the KIC are spatially associated with breccia bodies along their intrusive margins with meta-ironstone units. Late-tectonic felsic porphyry dykes cross-cut all units. The deformation events have been summarized in Table 3.1. In describing the structural sequence, heavy reliance has been placed on the outcrops in the Kukuluma and Matandani pits, because outcrop outside of pits is limited.

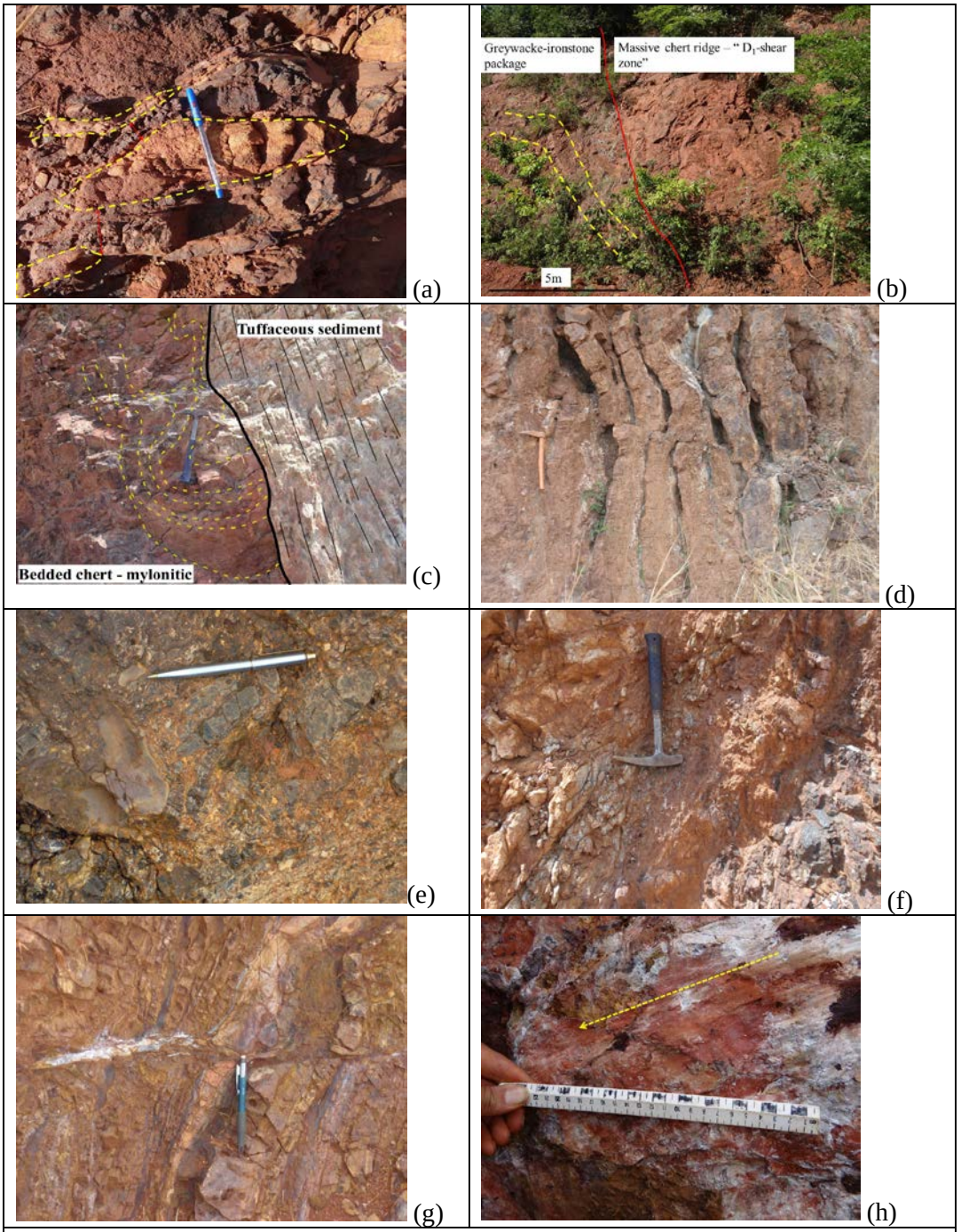

Figure 3.2. Examples of shear zones in the central Kukuluma terrain: (a) Closely spaced magnetite-bearing quartz veins that intruded along a D_1 shear zone (Kukuluma pit: 0417844-9687934); (b) Planar chert ridge cuts at a low-angle through primary bedding (Kukuluma pit: 417644-9687702). The chert is interpreted as a D1 shear zone; (c) Planar chert horizon in stratigraphy E of Area 3 (0420250-9688160). The chert parallels S_0 in the surrounding sediments, but internally the chert is strongly folded with a mylonitic appearance (S_1); (d) D_5 low-angle reverse fault and associated recumbent folding in chert (Kukuluma pit); (e) Cataclasite and tectonic breccia zone along D_6 shear zone where it truncates chert in Kukuluma pit; (f) D_6, Kasata shear in NW corner of Matandani pit; (g) D_7 fracture plane with (white) sericite and sulphide alteration in artisanal workings along W wall of Matandani pit; (h) D_7 fracture plane with (white) sericite and slickenlines indicative of normal-sinistral movement (Matandani pit).

Deformation event	Intrusive event (age)	Description	Mineralisation
D_{1a}		***Deposition of sedimentary sequence***	
D_{1b}		- Chert horizons with disharmonic folds - intrafolial folds - Local formation of S_0-parallel fabric, S_1	
D_2		- non-cylindrical folding on 1-500 m scale - Formation of penetrative S_0-parallel fabric, S_2	
	Start of emplacement of KIC: Diorite & Monzonite suites	- Sills, dykes and plugs of gabbro-diorite-monzonite	Mineralisation along diorite-ironstone contacts
D_3	continued emplacement of KIC : Diorite & Monzonite suites	- folding on 1-500 m scale with - plunge varies across F_2 fold limbs, - associated with a planar axial planar cleavage that dips steeply SW - High-strain foliation domains bound folded domains - Emplacement of KIC along D_3 axial planes; development of internal S_3 fabric - Extensive brecciation of D_2-D_3 folded ironstone near margins of KIC intrusions	Mineralisation linked to F_3 fold axial zones Mineralisation in fracture/breccia zones
D_4		- Open, cylindrical upright folding - Symmetric folds plunging steeply WNW - Limited S_4 fabric development	
D_5		- Open cylindrical recumbent folding - Associated with low angle reverse faults with small offsets (<10m)	
	continued emplacement of KIC : Granodiorite suite	- Felsic porphyry dykes truncate D_{1-4} folds	
D_6		- NW to WNW trending, steeply dipping, brittle ductile shear zones. - Dextral-reverse as a result of N-S compression - Form fracture networks overprinting D_3 folds and breccia zones - Near contacts between KIC and meta-sediments - Locally associated with tectonic breccia	D_6 shear zones are mineralised
	Emplacement of felsic dykes	- N trending felsic porphyry dyke	Mineralisation overprints dykes
D_7		- Normal faulting - Reactivation of D6 shears as sinistral normal faults	D_7 shear zones are mineralised
	Granitoids plutons 2620-2640 Ma[1]		

Table 3.1. Summary of deformation and intrusive events to affect the central Kukuluma terrain. [1] after Sanislav et al., (2013)

3.5.1. D1- bedding parallel shearing events

The well-layered, silicified meta-ironstone units locally preserve fine lamellae of foliated, para-concordant and anastomosing magnetite-rich horizons, that are associated with silicification and the formation of fine (<3mm thick) chert layers. This tectonic layering is concordant with, but overprints sedimentary bedding and results in a finely laminated sequence of rocks, with a complex compositional banding referred to as S_0/S_1 layering. S_0/S_1 has been folded around both D_2 and D_3 fold hinges confirming a D_1 origin for the composite layering. S_0/S_1 lithological banding is variably developed across the area and locally intensifies in layered packages, or units, up to 30m thick that are dominated by chert layers, which originated as, locally, slightly discordant planar units. A good example of this occurs along the access ramp into Kukuluma pit between 418900-9688150 and 418950-9688180 (all grid references in WGS84, zone 36S). In this zone, moving from southwest to northeast, a well-layered greywacke unit consisting of alternating graded, meta-sandstone-siltstone beds is intruded by dark-grey, planar quartz veins with a fine-grained chert-like appearance (Fig. 3.2a). The veins are largely parallel to layering, but locally transect each other and the primary compositional layering within the meta-greywacke units, and there parallelism with S_0 is in part due to rotational alignment as a result of flattening strain. Over a horizontal distance of about 15m the density of these intrusive veins increases from 2-3 veins per meter to over 20 veins per meter, as the rocks change from bedded meta-greywacke into a massive glassy chert unit. As the density of chert-like quartz veins increases, the wall rock greywacke becomes strongly silicified, and coarser grained sandstone beds are boudinaged, in which individual boudins display a clockwise rotation around a vertical axis. Where the boudinaging of primary layering becomes apparent, a layer-parallel fabric (S_1) has developed, and rare intrafolial folds and dextral shear bands occur. An L_1 mineral stretching lineation is locally preserved and plunges southwest at a shallow angle (~234/15). This lineation and the

asymmetry of shear bands and boudin trains suggests that the D_1 structural zone was a shear zone that accommodated top-to-northeast displacement, although the regional significance of such movement is undefined as a result of later deformation overprints. The fact that this zone is associated with boudinaging and extension of the host rock layering suggests an extensional origin. This chert-rich zone has been interpreted as a D_1 high-strain zone, or layer-parallel shear zone, marking a lithological boundary between meta-greywacke and meta-ironstone (Fig. 1.3).

Similar discordant chert horizons are common throughout the central Kukuluma terrain. In many places (e.g. Fig. 3.2b) they display abrupt boundaries, in which the chert layer transects the surrounding meta-ironstone or meta-greywacke units at a low angle. In other places the orientation of chert beds is parallel to layering within the wall rock (Fig. 3.2c). The chert beds are generally <5m wide, but may be as wide as 20-30m and display internal layering, similar to that described for Kukuluma pit (i.e. the layering may have a tectonic origin). It is common to find several generations of 0.1-1m scale, highly non-cylindrical, disharmonic folds inside the chert bands, whilst the surrounding sediments remain non-deformed (Fig. 3.2c). In places such folds assume sheath-like geometries within an ultra-fine-grained finely laminated, glassy fabric with mylonitic affinities (e.g. 420250-9688160).

On a regional scale, the chert bands form low ridge lines, and constitute the only exposure on the landscape. As a result they can be relatively easily mapped, and some can be traced for several kilometres (Fig. 1.3). Such chert horizons display large thickness variations along strike and in places bifurcate or merge to form anastomosing patterns. The chert bands are affected by all later folding events described below, and therefore must have formed early in the tectonic history of the Kukuluma terrain. Figure 10a shows a stereo plot of the poles to S0/S1 for the cenral Kukuluma terrain. The bedding orientation, although variable, shows a

consistent NW trend with steep dips that vary from 50° northeast to 50° southwest around vertical (Fig. 3.3a). The spread of data arises from fold overprints detailed below.

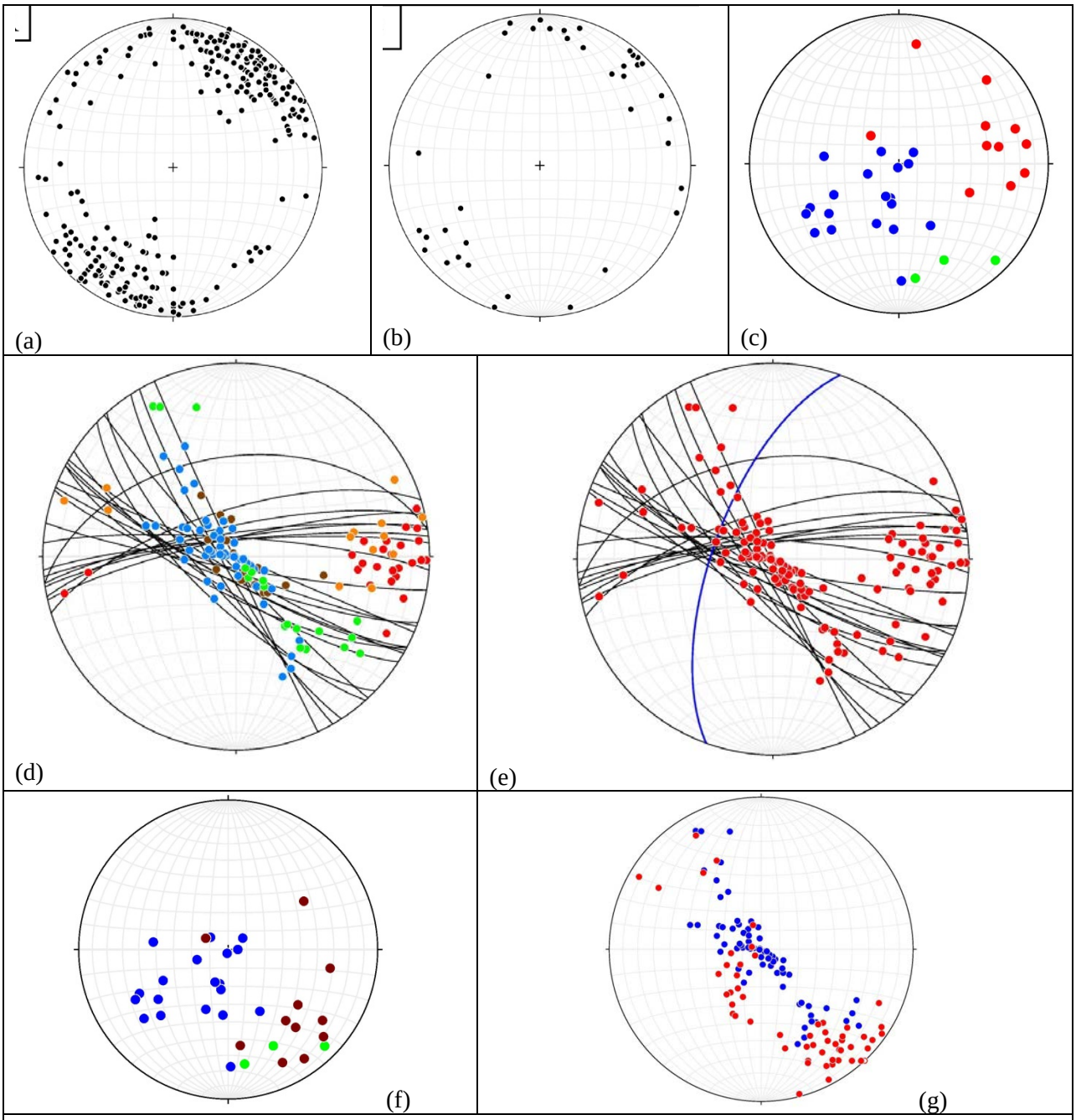

Figure 3.3. (a) Orientation of poles to S_0 (N=304); Orientation of poles to the intrusive diorite-sediment contacts as observed in drill core and the field (N=38); (c) Orientation of F_2 fold axes in Kukuluma and Matandani pits (N = 33). Colour coding of fold axes refers to domains in the pits: red = S ramp in Kukuluma pit; Blue = SW side in Matandani pit; green = NE side in Matandani pit; (d) Orientation of S_3, fold axial planes (great circles) and F_3 fold axes in Kukuluma and Matandani pits. Colour coding of fold axes refers to domains in the pits: red = S ramp in Kukuluma pit; orange = W ramp in Kukuluma pit; brown = NW wall in Kukuluma pit; Blue = SW side in Matandani pit; green = NE side in Matandani pit;

(e) Orientation of S_3, fold axial planes (great circles) and F_3 fold axes (red dots) in Kukuluma and Matandani pits. S_3 and F_3 are distributed in two clusters in either limb of D_4 folds. The orientation of the D_4 axial plane has been constructed from the distribution of the two clusters (i.e. S_4 equals the plane bisecting the obtuse angle = 290/65) Bingham stats for poles to the S_3 surfaces (N = 24):

Axis	*Eigenvalue*	*Trend*	*Plunge*
1.	*0.7885*	*019.8,*	*01.5*
2.	*0.1893*	*110.5,*	*24.5*
3.	*0.0222*	*286.5,*	*65.4*

(f) Orientation of F_2 fold axes in Kukuluma and Matandani pits in which the Kukuluma axes have been rotated clockwise by 50 degrees around an axes of 287/65, to remove the effects of D_4 open folding (i.e. the average orientations of S_3 in the S-wall of Kukuluma and SW part of Matandani have been rotated towards parallelism, by keeping the orientation of S_3 in Matandani fixed and by moving S_3 in Kukuluma). Colour coding of fold axes refers to domains in the pits: brown = rotated orientations along S ramp in Kukuluma pit; Blue = SW side in Matandani pit; green = NE side in Matandani pit; (g) Orientation of F_3 fold axes in Kukuluma and Matandani pits in which the Kukuluma axes have been rotated clockwise by 50 degrees around an axes of 287/65, to remove the effects of D_4 open folding (i.e. the average orientations of S3 in Kukuluma and Matandani have been brought into parallelism, by rotating Kukuluma data). Colour coding of fold axes refers to domains in the pits: red = rotated F_3 orientations in Kukuluma pit; Blue = F_3 orientations in Matandani pit.

In drill core, chert-rich laminated ironstone preserves an early layer-parallel fabric (S_1). Thin chert and sandstone layers are locally boudinaged, and small-scale, syn-sedimentary normal faults are common in laminated cherts and shales. These features suggest that D_1 events were associated with syn-sedimentary extension and normal faulting at the time of deposition of the volcano-sedimentary package.

3.5.2. D_2-D_3 folding and shearing

The composite S_1/S_0 fabric in the central Kukuluma terrain is folded, and locally sheared in response to D_2 and D_3 events (Figs 3.4, 3.5). In the Kukuluma and Matandani area this has resulted in locally complex D_2-D_3 interference folding of the volcano-sedimentary stratigraphy, including those units that preferentially host gold mineralization.

F_2 folds can be locally recognized on outcrop scale as tight to isoclinal folds that develop a penetrative axial planar cleavage in fine-grained shale. F_2 fold axes are highly variable in orientation (Fig. 3.3c). This variability is in part due to the non-cylindrical nature

of D_2 folds (similar to observations made in the Geita Hill area; Sanislav et al., 2016), which affects variability on outcrop scale, and partly results from later folding overprints causing more regional variability in the D_2 fold axes.

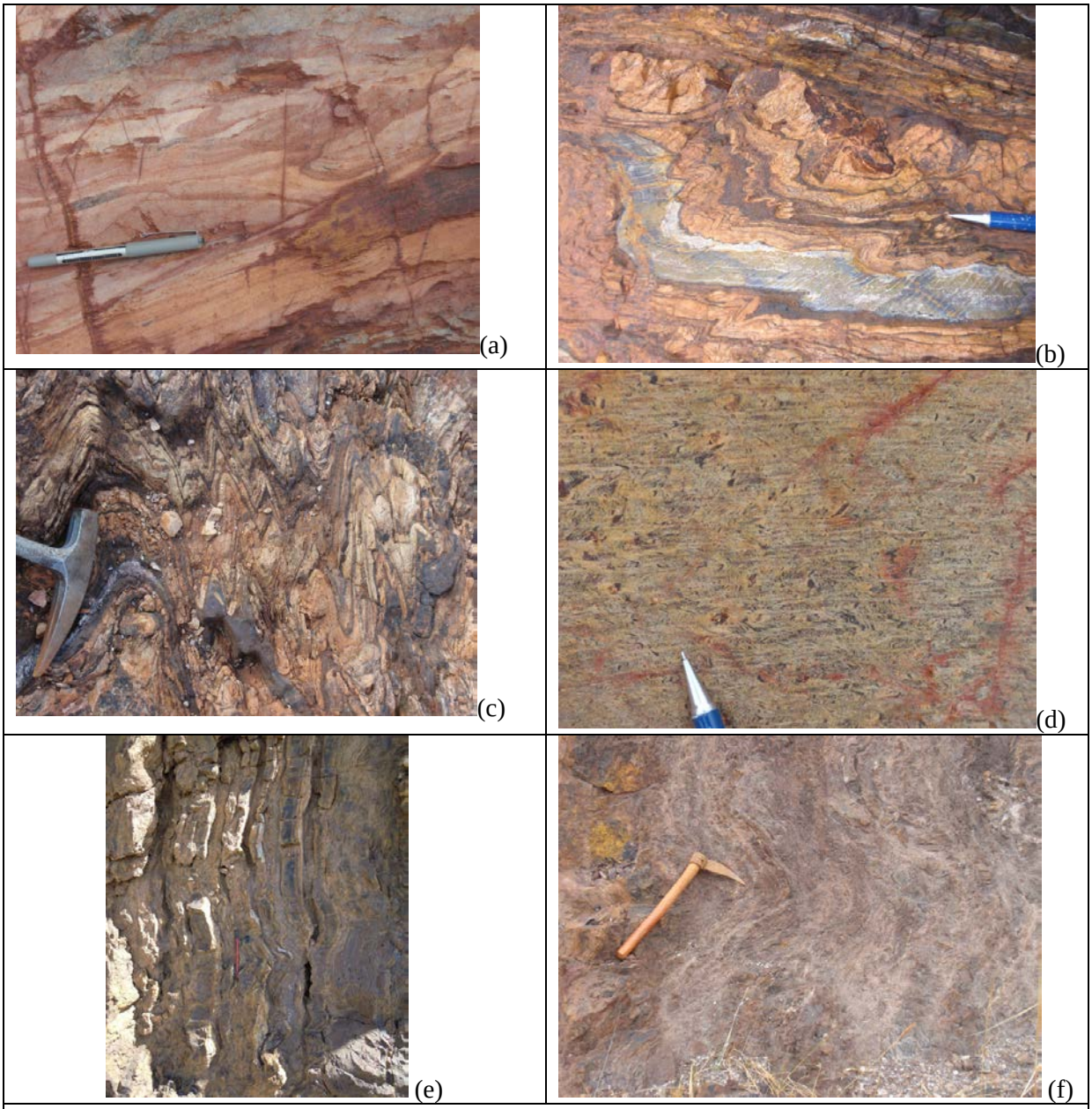

Figure 3.4. Examples of fold structures in the central Kukuluma terrain: (a) ductile, flame-like isoclinal folds in turbiditic greywacke interpreted as folding associated with fluidization during D_1; (b) D_3 folds in alternating shale and ironstone beds. Note well developed S_3 crenulation cleavage in shale horizons; (c) tight D_3 vertical folds in ironstone in SW Matandani pit; (d) close up of S_3 spaced crenulation cleavage in shale; (e) open recumbent D_5 folding in chert bands; (f) open D_5 folding along the margin of a felsic porphyry dyke affected by the D_5 folding.

In single outcrops where F_2-F_3 interference folding is well developed (e.g. Fig. 3.5), the orientation of F_2 fold axes can vary from near-parallelism with F_3 fold axes, to high angles to F_3 fold axes; a trend reflected in stereoplots of F_2 (Fig. 3.3). The existence of large-scale (>100m scale) D_2 folds is evident from the regional distribution patterns of chert ridges (Fig.1.3), and can also be inferred from the domainal distribution of D_3 fold axes orientations (Fig. 3.3) as explained below.

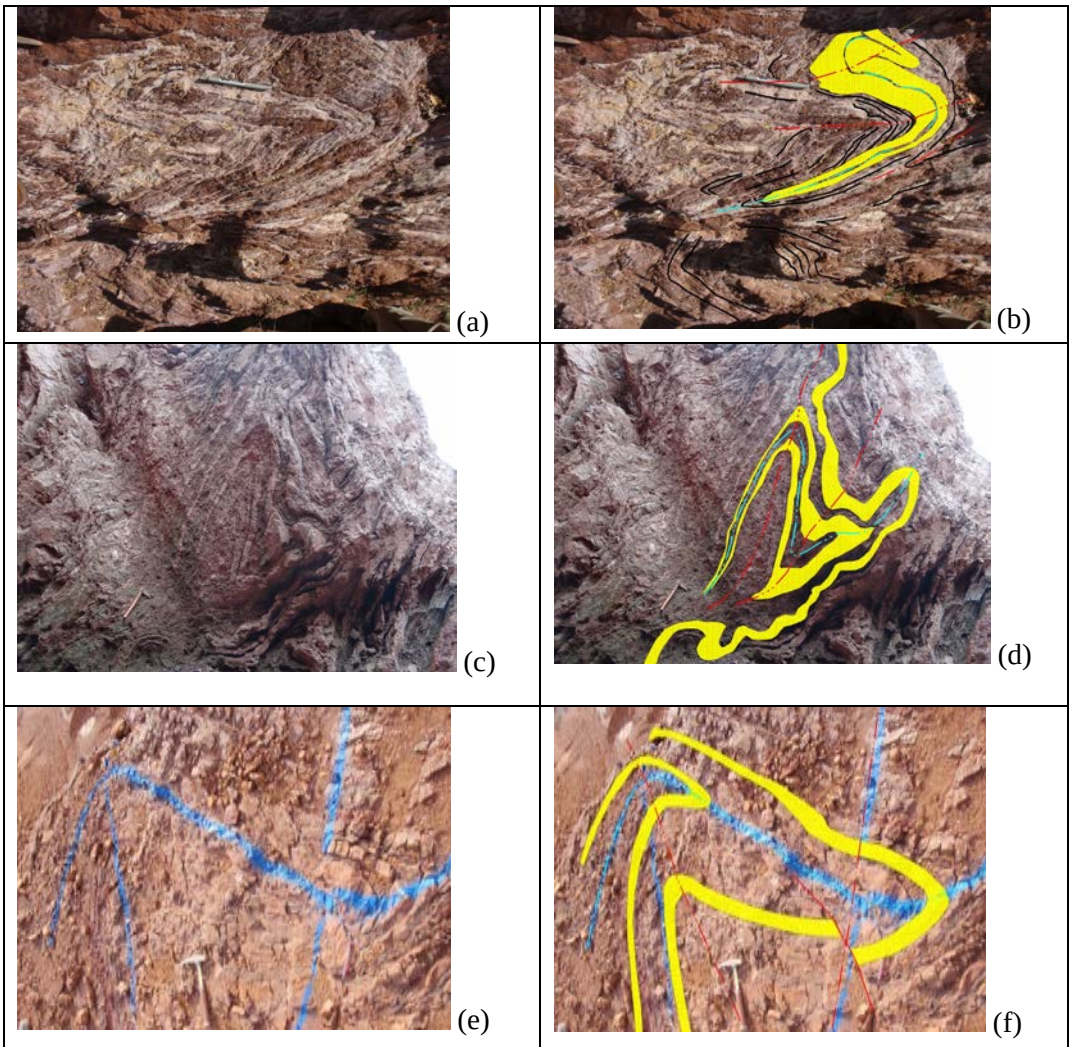

Figure 3.5. Examples of outcrop-scale D_2-D_3 fold interference patterns in the central Kukuluma terrain shown as annotated pairs. Marker layers have been highlighted in yellow; the D_2 fold axial trace is shown in light blue; the D_3 fold axial trace is shown in red. (a) & (b) horizontal view of fold pair along access road to Kukuluma pit; (c) & (d) vertical view of fold pair in erosion gully along the E face of Matandani pit; (e) & (f) horizontal view of fold pair on the upper benches in the SW corner of Matandani pit.

D_3 folds are common in the area and comprise upright to vertical folds that vary from open to near-isoclinal, with tightening of the folds occurring near planar high strain zones. The S_3 axial planar surface is generally near vertical and varies in trend from E-W to NW with orientations in the pits showing two clear maxima around 210/80 and 350/75 (Fig 10d). These variations in orientation of S_3 are the result of D_4 folding (discussed below). S_3 fold axial planar fabrics vary in character from well-developed closely spaced (<1mm) planar crenulation cleavages in shale domains (Fig. 3.4), to more widely spaced, fracture cleavages with a high degree of cleavage refraction in more competent silicified meta-ironstone beds with cleavage planes in folded chert units commonly decorated by thin quartz veinlets along the outside rims of folds indicative of buckle folding (Fossen, 2016).

F_3 fold axes orientations vary in a systematic manner across the pits as a result of D_2-D_3 fold interference (Fig. 3.3). Along the southern wall of the Kukuluma pit, F_3 fold axes generally plunge shallowly east (ave. F_3 = 091/17; Fig. 3.3d). This same orientation also occurs along the western ramp into Kukuluma pit, although the F_3 orientation locally rotates towards a shallow northwest plunge as a result of D_4 fold overprints. Towards the nothern wall of the Kukuluma pit, F_3 fold axes rotate to near-vertical (ave. F_3 = 287/83; Fig. 3.3d), with outcrop scale D_3 folds assuming vertical to steeply reclined orientations. The same vertical D_3 fold orientations also dominate outcrops in the area between Kukuluma and Matandani pits, and in the SW wall of Matandani pit (Fig. 3.3d).

Towards the northeastern wall of the Matandani pit, F_3 fold axes are more variable and rotate between a near vertical plunge and a gentle northwest-southeast plunge (Fig. 3.3d). This domainal distribution of F_3 fold axes across the pits is illustrated with a stereoplot in figure 3.3d. The bimodal distribution of F_3 fold axes along the S_3 axial planar surface, which itself maintains a relatively constant orientation, indicates that large-scale D_2 folds are present, with the hinge zone of one such fold trending in a general northeast direction along

the northwestern margin of Kukuluma pit, and a second possible hinge zone passing through Matandani pit. Before the occurrence of upright D_3 folding, these F_2 hinge zones would have separated a generally steeply north to northwest dipping S_0/S_1composite layering across the southern part of Matandani pit and the area between Matandani and Kukuluma pits, from generally shallow dipping layering in most of Kukuluma pit and the northern part of Matandani pit. This pattern suggests the presence of a 500 m scale, possibly southeast verging, asymmetric antiformal D_2 fold with a northwest dipping axial planar surface.

Outcrop scale vergences of D_3 folds vary across the pits, reflecting large-scale D_3 folding. Along the southern and western walls of Kukuluma pit, outcrop scale D_3 folds are generally asymmetric and verge north, whereas D_3 folds along the northern wall of the pit verge south. This means that Kukuluma pit is positioned in the centre of a 500m scale east to southeast trending, upright, closed D_3 fold and occurs together with Matandani pit along the hinge zone of a large-scale D_3 anticlinorium, which overprinted earlier reclined, non-cylindrical D_2 folds, which were tighter, but had developed at a similar scale.

D_2-D_3 fold interference patterns are common on outcrop-scale (e.g. 0418140-9688080; Fig. 3.5) and are generally of type 2, in which both F_2 fold hinges and S_2 axial planes have been folded by D_3 folds (Thiessen, 1986; Fossen, 2016). Interference patterns are characterized by crescent and hook shapes (Fig. 3.5) and locally converge to type 3 fold interference patterns where F_2 and F_3 fold hinges reach near-parallelism (Thiessen, 1986). The large-scale fold interference patterns described from the variable distribution of D_3 fold axes orientations can also be seen from the outcrop patterns of D_1 chert ridges around Area 3, where they locally preserve 500-800m scale type 2 fold interference patterns (Fig.1.3).

Locally the D_2-D_3 fold domains are truncated by planar foliation domains that are unaffected by D_2-D_3 folding, except for the presence of isoclinal intrafolial folds within the foliation, good examples can be seen along the southeastern wall of Matandani pit (e.g.

418180-9688300). These foliation domains trend in a northwest direction across the central Kukuluma terrain and are generally near-vertical. They are associated with a moderately to steeply west to northwest plunging mineral lineation that parallels the axes of intrafolial folds within the high strain domains. The layering in these foliation domains is composite in nature with $S_0/S_1/S_2/S_3$ all transposed and parallel to each other, and they developed at the same time as D_3 folding. The regional distribution of these D_3, high-strain zones cannot be assessed due to poor outcrop.

3.5.3. D_4 gentle upright folding

D_4 folds are gentle, cylindrical, upright folds with steep axial planes that warp S_3 (and earlier foliations) on a 0.5-1km scale. D_4 folds are not clearly visible in outcrop, but can be seen when tracing D_1 chert horizons or S_3 along strike; e.g. across Kulkuluma pit S_3 orientations change from steeply southwest dipping (ave. 210/80) in the northwestern corner of the pit to steeply north dipping (ave. 350/75) across the rest of the pit as a result of large-scale, D_4 folding with a steeply west plunging fold axes and northwest dipping fold axial plane (Fig. 3.3e). Similar open folding of D_3 structures is apparent across the area (Figs 1.3, 3.6, 3.7), with the fold axial trace of D_4 folds trending roughly northnortheast-southsouthwest. No penetrative S_4 fabric has developed, but where D_4 folds affect thick chert layers, e.g. around Area 3 West deposit a spaced northnortheast-trending fracturing can be observed in the hinge zones.

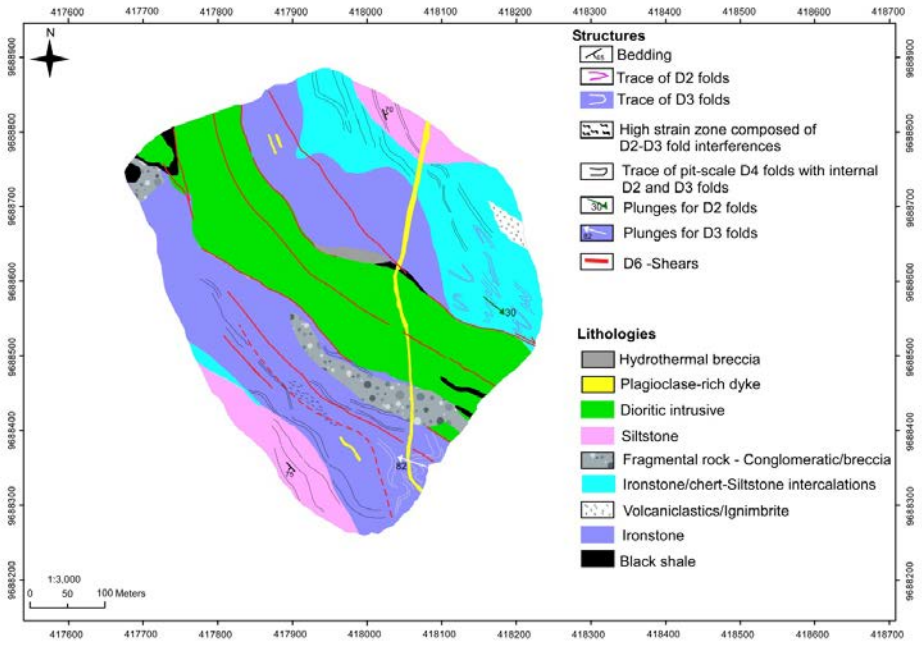

(a)

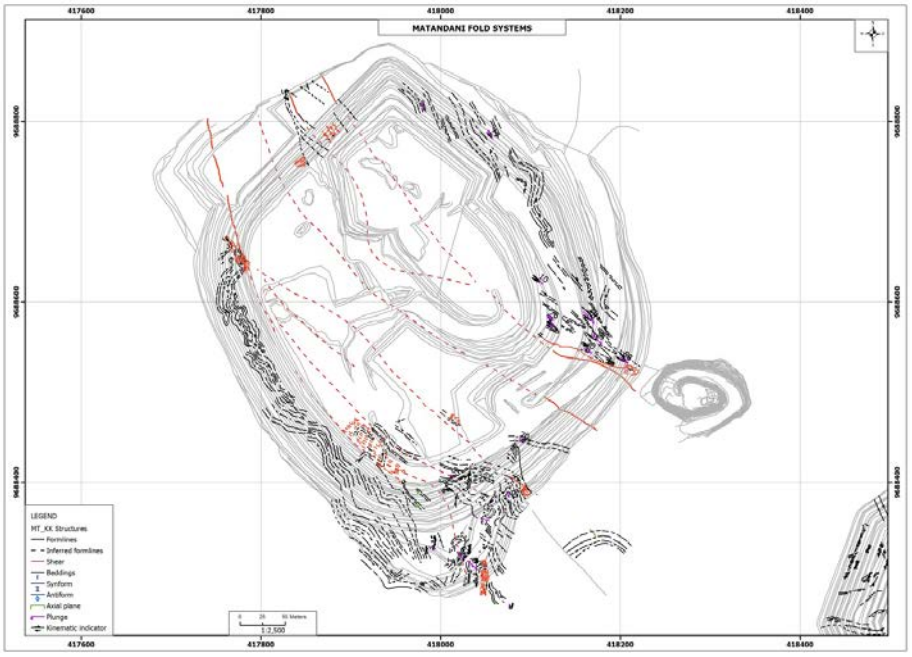

(b)

Figure 3.6. (a) 2015 version of geological map of Matandani pit. This version has been used for the construction of leap-frog models as explained in chapter 2, and has been updated with later mapping as shown in Figure 1.3. (b) Trend map of Matandani pit (2016 version) showing main folding events and shears.

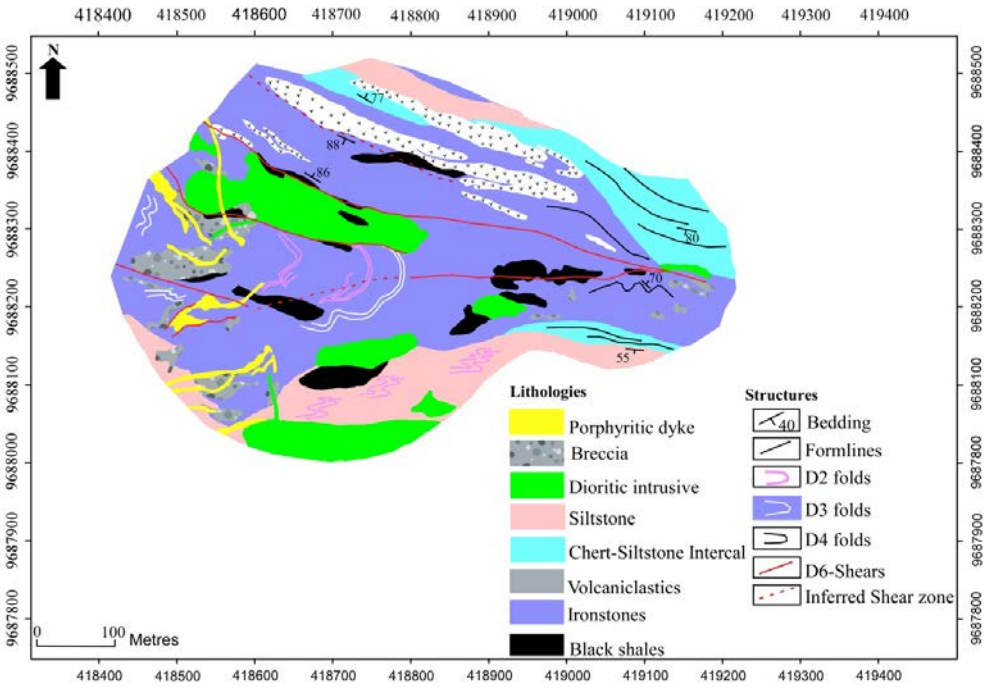

(a)

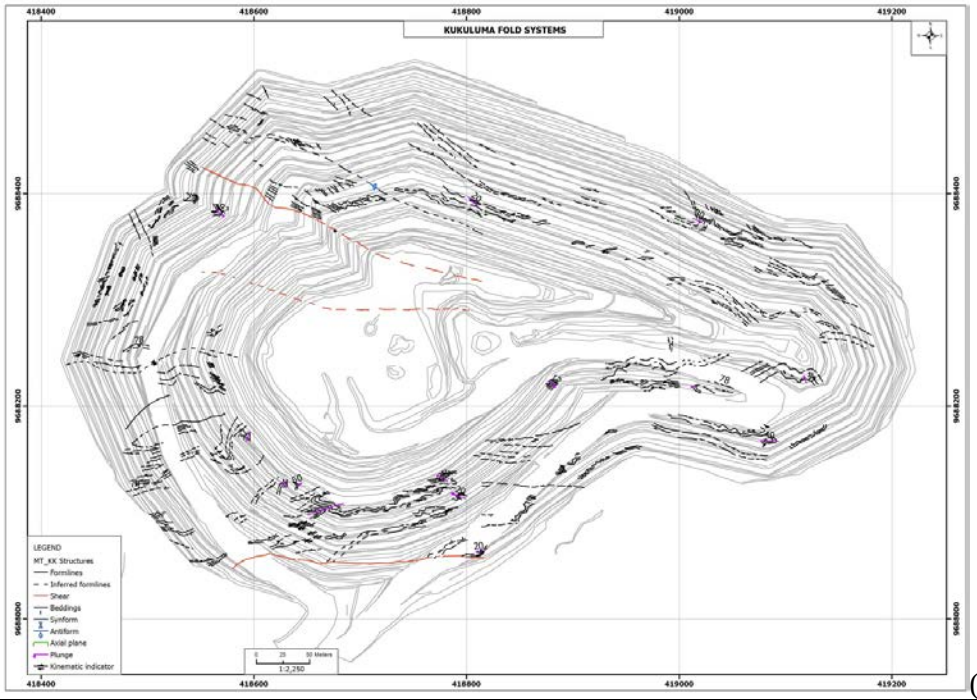

(b)

Figure 3.7. (a) 2015 version of geological map of Kukuluma pit. This version has been used for the construction of leap-frog models as explained in chapter 2, and has been updated with later mapping as shown in Figure 1.3. (b) Trend map of Kukuluma pit (2016 version) showing main folding events and shears.

3.5.4. D_5 recumbent folding and low-angle reverse faulting

D_5 involved localized low-angle reverse faulting and associated recumbent folding that is poorly visible in areas without good vertical exposure. Low-angle reverse fault planes

are best developed within the well-bedded ironstone units in the western side of Kukuluma pit. Fault planes vary in thickness from several mm to ~20cm, but are generally thin and discrete, and visible as thin grey clay zones that ramp up through the ironstone units. The larger (i.e. wider) fault zones generally dip gently north (around 000/20), but they locally vary in orientation and narrow secondary faults display more variable attitudes with S dipping orientations most common. These secondary faults locally steepen where fracture surfaces move in parallelism with bedding. Fault planes are hard to trace along strike partly because they are narrow, move in parallelism with bedding planes and are masked by breccia zones in ironstone units (see below), but also because their development is localized, with discrete fault planes having limited strike lengths before dissipating in networks of minor fractures. Displacements across the faults are indicative of reverse movements, although clear lineations on thrust planes have not been observed. Displacement of lithological contacts suggests that none of the fault zones accommodated displacements in access of ~10m with most faults accommodating significantly less.

Folding is common in spatial association with the fault planes. D_5 folds vary in scale from 0.1-5m and are generally open recumbent folds with near horizontal to shallowly dipping axial planar surfaces that parallel the low angle fault planes (Figs. 3.2d, 3.4e,f), and shallowly east or west plunging fold axes. In places the folds are asymmetric and have the appearance of drag folds associated with the faults (Fig. 3.2d). Elsewhere, D_5 folds form open corrugations in well-bedded meta-ironstone, with a widely spaced fracture cleavages (Fig. 3.4f).

3.5.5. D_6 brittle-ductile shear zones

A network of generally steeply dipping, northwest to westnorthwest trending shear zones can be traced along the Kukuluma Mineralised Trend. These D_6 shears cross cut the

folded sequence and have been linked to mineralization (e.g. Skead, 2003). In the Kukuluma and Matandani pits the system of D_6 shear zones is referred to as the Juma and Kasata shear zones (Figs 1.3b, 3.6, 3.7). In Area 3 similar west to northwest trending shear zones are targeted by artisanal gold miners, and can be seen in drill core, but poor outcrop prevents these shears from being mapped in detail.

The Juma shear zone can be traced along the entire length of the Kukuluma and Matandani pits, and also occurs within the small open pit between Kukuluma and Matandani (Fig. 1.3b). The shear zone is positioned along the westnorthwest to northwest trending northern contact of a major intrusive diorite sill belonging to the KIC (Figs 1.3b, 3.6, 3.7). Towards the eastern end of Kukuluma pit, the Juma shear, which trends towards 110°, terminates into a network of smaller moderately to steeply dipping fracture zones with variable trends (mainly northwest, northeast and east-west trending; Fig. 1.3b).

The Kasata shear zone can be traced through the centre of Kukuluma pit as a composite, steeply dipping, and generally west to westnorthwest trending fracture zone. In Matandani pit it re-appears in the southern corner of the pit as several westnorthwest trending, semi-parallel fracture zones that merge towards the northwestern part of the pit into a single northwest trending brittle-ductile shear zone that follows the contact of the same intrusive diorite bordering the Juma shear (Figs 1.3b, 3.6). In the eastern part of Kukuluma pit the Juma and Kasata shears merge across a complex network of mostly east-west trending fractures. In drill core from Area 3 a similar D_6 shear zone spatially associated with mineralization was observed along the contact of intrusive monzonite and sediment.

Individual shear planes vary in width from <1 cm to ~10 cm, with wider shear zones commonly accompanied by damage zones several meters in width that are associated with secondary jointing, brecciation, veining and silicic alteration. Where several shear planes are in close proximity to one another (e.g. in the southern corner of Matandani pit, or where the

Kasata and Juma shears merge in the eastern part of Kukuluma pit), up to 15m wide, extensively fractured and altered (strongly silicificied) domains occur. Where the shears transect micaceous schists, chlorite-muscovite shear bands have developed into S-C like fabrics (e.g. Fig. 3.2f). In meta-ironstone beds magnetite bands have localized strain and chlorite-magnetite-quartz segregations along foliation domains are apparent in which chert is reduced to mm-sized fragments. Brittle deformation structures (veins, breccia and cataclasite zones) are more common in portions where the shear zone cuts across massive, chert-rich meta-ironstone units (Fig. 3.2e). Lineations on the shear zones are visible as mineral alignments in foliation domains, and as striations and quartz rods in quartz-rich portions of the shears and along veins.

The orientation of the D_6 fracture zones associated with the Juma and Kasata shears as measured in the Kukuluma pit is shown in figure 3.8a. Here, four distinct shear orientations have been observed that are all interconnected. The dominant shear zones (i.e. the main strands of the Juma and Kasata shears) trend westnorthwest (020/80) with a gently northwest or southeast plunging lineation recording a dextral sense of movement with a reverse component. A prominent set of 2nd order shears trends more northwest with a steep southwest dip (ave. 235/75) and moderately south plunging lineation recording reverses dextral movements. A third set of steeply northnorthwest to northwest dipping shear zones (ave. 324/72) with moderately to steeply north plunging lineations record sinistral-reverse movements and a fourth set of steeply southerly dipping, east-west trending faults (ave. 175/76) hosts down dip lineations and a pure reverse (south over north) sense of movement (Fig. 3.8a). This network of shears is consistent with Y-shears (the Juma shear), Riedel shears (northwest trending set) and anti-Riedel shears (southwest trending set) within a wider dextral transpressional shear system (Fossen, 2016), that combines with high-angle reverse faults (the east-trending set). On a larger scale, the distribution of the main D_6 shear zones is

reminiscent of a right stepping en echelon array of westnorthwest to northwest trending shears within a more east-west trending shear envelope accommodating reverse dextral movement (Fig. 1.3).

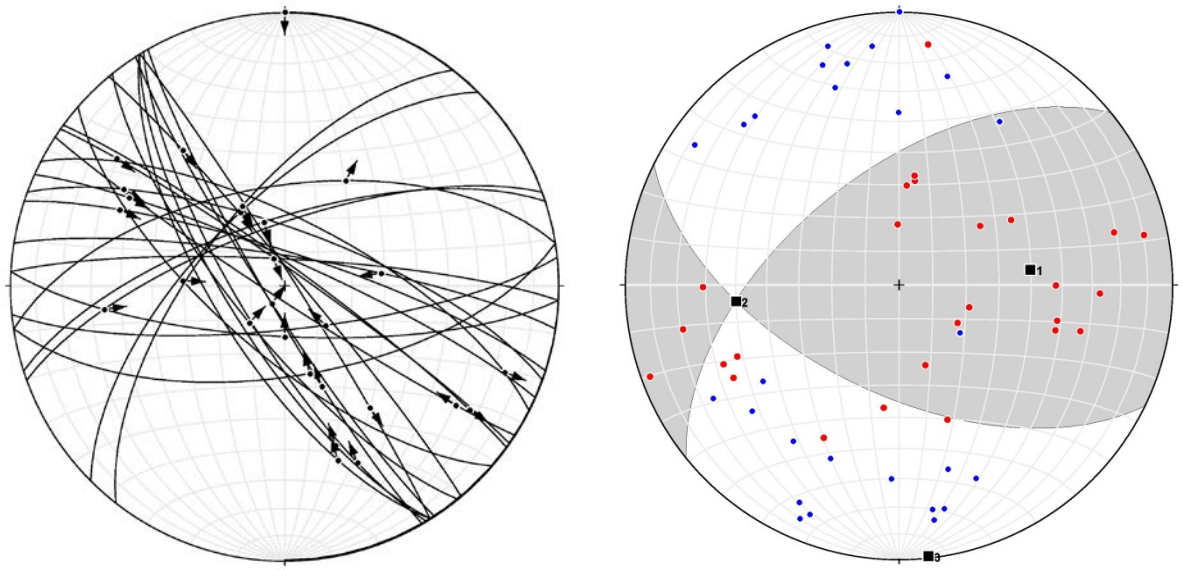

(a) (b)

Figure 3.8. *Orientation and palaeo-stress analysis for D_6 shear zones measured in Kukuluma and Matandani pits (N = 27). (a) plot of fault planes and lineations, arrows point in direction of movement of the hanging wall; (b) fault plane solution (Bingham matrix solution) for the measured D_6 faults (compression dihedron in white; tension dihedron in grey). P axes are shown in blue, T axes in red. The Bingham solution shows N-S compression with a near-horizontal σ_1, and a dispersed distribution of P and T axes, i.e. σ_2 and σ_3 are similar. Bingham solution:*

Axis	*Eigenvalue*	*Trend*	*Plunge*
1.	*0.1918*	*083.1,*	*50.2*
2.	*0.0419*	*264.5,*	*39.8*
3.	*0.2337*	*173.9,*	*00.7*

A paleo-stress analysis for the D_6 faults in Kukuluma and Matandani pits using Faultkin (Marrett and Allmendinger, 1990; Allmendinger et al., 2012; Chapter 2 for a description of the methodology) was performed on a total of 27 shear planes for which kinematic data was obtained (Fig. 3.8b). These shear zones are all part of the interconnected network of fractures that form the Juma and Kasata shear zones (Fig. 1.3), and hence it is assumed that they formed simultaneously in response to the same far field stress (see

appendix 1 for a more detailed discussion). In doing the analysis all shear planes were given the same weight. The results are shown in Fig. 3.8b, and indicate that the D_6 shear zones in the central Kukuluma terrain formed in response to horizontal, near north-south shortening in a plane strain to flattening strain environment (Rev = 0.35)

3.5.6. D_7 faulting

The D_6 shear zones are locally reactivated along mm-wide discrete fracture surfaces that are commonly slickensided, with slickenfibres defined by sericite. Reactivation of D_6 shear zones during D_7 is most clearly demonstrated in Matandani pit, where a north-trending porphyry dyke cuts through the D_6 shear zones, but is fractured and slightly displaced as a result of brittle reactivation of the D_6 shears. Where the D_7 faults cut the dyke, the dyke is mineralized. The D_7 shearing event on the westnorthwest to northwest trending shear zones is generally associated with discrete fracture planes containing variable lineation directions, but they record a consistently normal sense of movement, commonly with a sinistral component. D_7 reactivation planes of the Juma shear can be seen in the eastern corner of Kukuluma pit, where artisanal miners have excavated the high-grade mineralisation along the shear zone. Displacements on D_7 shear planes are small, i.e. in the order of centimeters.

Apart from reactivation of D_6 shear zones, narrow fracture zones attributed to D_7 occur in parts of the pits and in Area 3 (Figs 3.2g, h). Such fractures have the appearance of joints, and are locally paralleled by thin grey quartz stringers. They have only been observed, because they are targeted by artisanal miners who dig out the fracture planes, which are strongly mineralized. Good examples of such mineralized fracture arrays occur in Matandani pit.

In the western wall of Matandani pit, three 15-20m wide fracture zones occur to the west of the Kasata shear zone, within deeply weathered layered turbiditic meta-sediment and

ironstone. Each fracture zone comprises an interconnected network of variable orientated fractures within envelopes that trend roughly 290-110. The three fracture zones are arranged in an en echelon array along a northwest trend. Within each fracture zone, individual fractures have maximum strike lengths of several 10's of meters, but most are shorter in length.

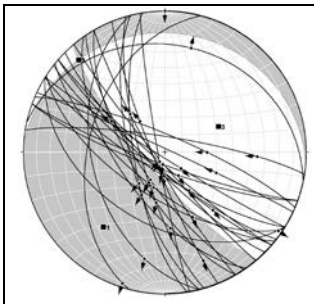

Axis	Eigenvalue	Trend	Plunge
1.	0.3361	217.8,	32.5
2.	0.0356	315.7,	12.2
3.	0.3717	063.5,	54.7

(a)

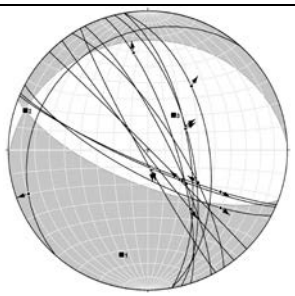

Axis	Eigenvalue	Trend	Plunge
1.	0.2589	194.3,	23.9
2.	0.0660	288.0,	08.3
3.	0.1929	035.8,	64.5

(b)

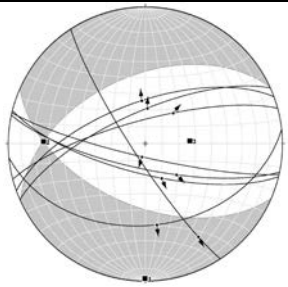

Axis	Eigenvalue	Trend	Plunge
1.	0.3299	180.3,	02.0
2.	0.0011	271.3,	26.4
3.	0.3288	086.2,	63.5

(c)

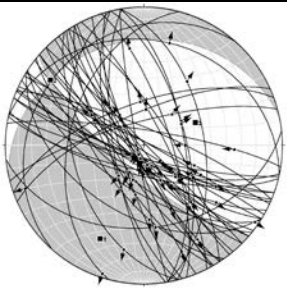

Axis	Eigenvalue	Trend	Plunge
1.	0.2856	205.2,	26.5
2.	0.0261	304.9,	18.7
3.	0.3117	065.9,	56.7

(d)

Figure 3.9. Orientation and palaeo-stress analysis for D_7 fracture arrays measured in Kukuluma and Matandani pits. For each area, the plot shows the fault planes as great circles and lineations as arrows that point in the direction of movement of the hanging wall; these are placed on top of the fault plane solution (Bingham matrix solution) for the measured D_7 faults (compression dihedron in white; tension dihedron in grey). The Bingham solutions for each data set are shown below the stereoplot. (a) W wall of Matandani pit (N = 30);(b) NE wall of Matandani pit (N = 13); (c) E wall of Kukuluma pit (N = 8); (d) all measurements from kukuluma and Matandani pits combined (N=51). All plots show N-S to NE-SW extension with a steep σ_1, and flat. σ_2 and σ_3 orientations.

The fractures are narrow (<3mm) and characterized by sericitic alteration (now mostly visible as white kaolinite staining) with disseminated sulphide growth (now mostly oxidized). Fracture planes preserve excellent slickenlines and shear sense indicators indicative of predominantly sinistral-normal movement (Fig. 3.2h).

Paleo-stress analyses for the D_7 fracture zones in Kululuma and Matandani pits using Faultkin (Marrett and Allmendinger, 1990; Allmendinger et al., 2012; appendix 1 for a description of the methodology) was performed on a total of 53 fracture planes for which kinematic data was obtained. These fractures are all part of interconnected fault zones targeted by artisanal workers, and hence it is assumed that they formed simultaneously in response to the same far field stress (see appendix 1 for a more detailed discussion). In doing the analysis all fracture planes were given the same weight. The results are shown in Fig. 3.9, and indicate that the D_7 shear zones in the central Kukuluma terrain formed in response to horizontal, NNE extension in a plane strain environment.

Similar fractures are also targeted by artisinal miners in Area 3, where many are decorated by stringers of thin (<1cm wide) grey quartz veins. The larger scale distribution of the D_7 faults, beyond the pit areas, is not clear, because the structures are extremely subtle and not exposed beyond the workings of artisanal miners. However, the structures are clearly targeted by artisanal miners and therefore important to mineralisation.

3.5.7. The emplacement of intrusions during deformation

Deformation events were accompanied by the emplacement of two separate suites of syn-tectonic intrusions, one gabbroic to dioritic, the second monzodioritic to monzonitic in composition, and a granodiorite suite that manifests itself as a first generation of porphyry dykes and sills. These intrusions are collectively called the Kukuluma Intrusive Complex (KIC; see Chapter 4) and they occur across the central part of the Kukuluma terrain where

they can be traced from the far eastern parts of Area 3 to northwest of Matandani pit (Fig. 1.3). They have been overprinted by a second generation of felsic porphyry dykes.

The monzonite and diorite suites of the KIC are dominated by equigranular, fine- to medium-grained, sheet-like bodies, stocks and plagioclase-rich porphyritic dykes of irregular thickness (e.g. northwestern corner of Kukuluma pit), which locally form interconnected networks that both transect and parallel bedding (Figs 1.3, 3.6, 3.7).

The granodiorite suite comprises thin (<2 m wide) dykes that occur in a variety of orientations (steeply dipping dykes with west, northnorthwest and north trends have been observed), with porphyritic textures in which rounded quartz augen and euhedral to subhedral feldspar crystals are embedded in a fine-grained felsic matrix (Fig. 3.1g).

The intrusive diorite and monzonite bodies of the KIC are weakly to moderately foliated as a result of D_3 deformation. In some places intrusive margins were folded during D_3 and vein systems internal to the intrusions are also (D_3) folded (e.g. 0418900-9687780). More commonly intrusions form sheet-like bodies that were emplaced along axial planar orientations of D_3 fold, with intrusive contacts cutting through (D_3) folded meta-sedimentary sequences, whilst foliations parallel to S_3 develop within the intrusions. In the southwestern part of Matandani pit, rafts of D_3 folded meta-ironstone occur within an intrusive diorite body that is foliated in an orientation parallel to S_3. Nowhere did we see diorite or monzonite intrusions being folded around D_2 structures, but the intrusions are affected by the large-scale warping caused by D_4. Plagioclase-rich porphyritic dykes of the diorite suite cut through the more massive diorite bodies, and are foliated. Where these dykes cut through meta-sediment and especially D_3 planar high strain zones, they can be slightly folded as a result of D_3. These relationships indicate that the diorite and monzonite suites were emplaced as a number of separate intrusions after D_2, but immediately before and during D_3 events.

The porphyritic granodiorite dykes of the KIC are not foliated and intrude into the diorite and monzonite bodies within Kukuluma and Matandani pits. They are overprinted by D5 reverse faults and recumbent folds.

A second generation of felsic porphyry dykes represented by a single, north-trending, 1-2m wide, porphyritic felsic dyke transects Matandani pit (Figs 1.3b, 3.6). The dyke has chilled margins and no internal fabric and cuts through D_1-D_6 structures. Where this dyke cuts through the Juma and Kasata shears it can be seen to transect D_6 fabrics. However, the dyke is cut by narrow fracture planes assigned to D_7, associated with slickensides, a sinistral normal sense of movement with limited displacement (<5cm) and alteration including sulphide growth and gold mineralization, i.e. the timing of emplacement of this dyke is post D_6, but pre D_7 and pre-mineralisation (Table 3.1).

3.5.8. Syn-tectonic brecciation events

Parts of the folded meta-sedimentary sequences in Kukuluma and Matandani pits were affected by brecciation processes. In Kukuluma pit, the breccia zones occur as elongated bodies, 5-50m thick covering the entire height of the pit wall that are largely restricted to the W wall of the pit. They occur within the strongly D_2-D_3 folded package of meta-ironstone units with clasts consisting mostly of chert embedded in a more micaceous and feldspar-rich matrix, in close spatial association with intrusive dykes and stocks of the KIC.In Matandani pit, extensive brecciation occurs in the southwestern part of the pit, within strongly D_2-D_3 folded meta-ironstone intercalated with micaceous and graphitic shale, and concentrated along the W contact of a diorite intrusion that transects the centre of the pit (Fig. 1.3b). Outside the open pits, a major breccia body (~100x50 m in size) has been recognized to the northwest of Matandani pit (Fig.1.3a), where it has also been intersected in drill core.

The relationship between the breccia bodies, and the various deformation and intrusive events is well preserved along the access ramp descending the western wall of Kukuluma pit. Here the breccia's vary form crackle breccias, in which breccia blocks have a close jig-saw fit, where the underlying folds and layering are preserved and still visible in a semi-coherent manner (Fig. 3.10a), to massive chaotic breccia in which the primary layering is no longer visible (Fig. 3.10b). The change form jigsaw breccia to chaotic breccia is gradational, and along the western wall of the pit, zones of more intense brecciation alternate with folded zones were brecciation is weak to absent. Zones that display both D_2 and D_3 folds are brecciated, with some of the brecciation appearing more intense near fold hinge zones, i.e. in areas where the S_3, axial planar fracture cleavage was more intensely developed. Although the breccia zones are highly silicic, intensive quartz veining or vein stockworks are largely absent, and the matrix to the breccia blocks is mostly made up of clay-rich micaceous material and smaller chert fragments.

Zones of brecciation show a close spatial relationship with meta-ironstone units and dykes belonging to the KIC, with breccia occurring along the margins of intrusive diorite-monzonite bodies, or with dykes intruding into breccia zones. In one location (0418636-9687782; Fig.3.10e-h) a porphyritic diorite dyke intruded into the breccia and displays highly irregular boundaries, involving a planar trail of irregular, blob-like intrusive bodies up to 2 m in size with indented boundaries and irregular protrusions and apophyses of dyke material emplaced into meta-ironstone breccia. This intrusive relationship suggests that the dyke was emplaced at the time the wall rocks had lost coherency, i.e. were 'fluidized' as a result of brecciation. In other words this dyke was emplaced at the same time as breccia formation.

(a)

(b)

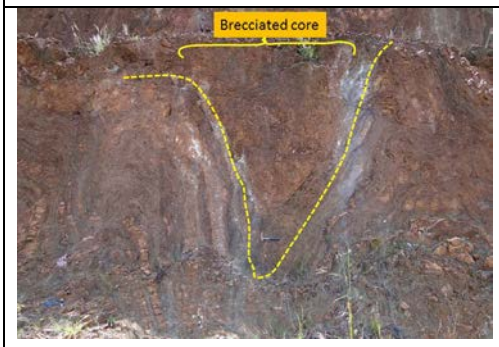

(c)

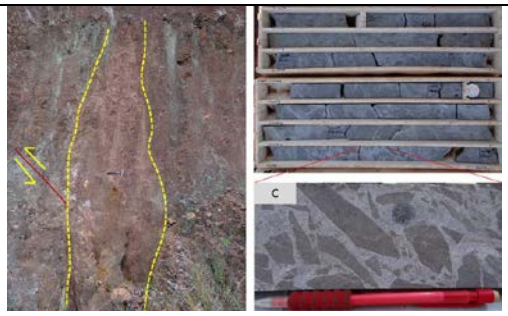

(d)

(e)

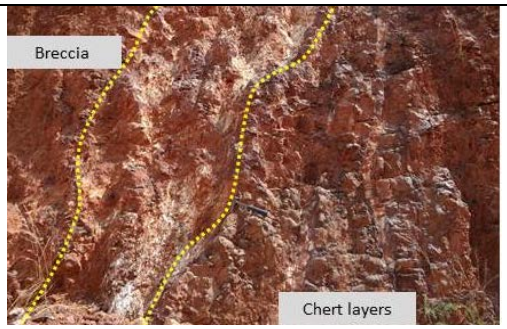

(g)

(g)

(h)

Figure 3.10. Examples of hydrothermal, syn-D3 breccia and intrusions in W wall of Kukuluma pit: (a) & (b) progressive brecciation in ironstons including a complexly folded zone with crackle breccia in which the original folded bedding is still visible (a) and more advanced brecciation in which individual clasts have moved, but remnants of underlying folds are visible (b); (c) layer-parallel breccia in the core of a D_3 fold (0418852-9688107); (d) fine-grained breccia pipe transecting folded ironstone/chert package (0418494-9688242). The inset shows hydrothermal breccia in a dioritic intrusive (drill hole ID: MTRD0005-588m); (e) to (h) relationship between diorite intrusion and breccia, suggesting emplacement into fluidized breccia with pepperite-like textures. (e) & (f), diorite dyke with highly irregular margins is emplaced into the breccia zone; (g) & (h) irregular blebs and fragments of diorite mixed within the breccia near the intrusive contacts of the dyke shown in (e) & (f).

In other places (e.g. 0418621-9687801), polymict breccias can be observed in which rare green, chlorite-actinolite-rich clasts of altered mafic origin, occur mixed with meta-ironstone clasts along zones that show no internal layering or structure and transect folded meta-ironstone beds. In such areas there is evidence for considerable movement between breccia clasts. In places the breccia bodies show a much higher degree of matrix material and a much smaller clast size along highly-altered, clay-rich planar zones that are reminiscent of fluid pathways in intrusive breccia pipes (Fig. 3.10d). One such zone (0418574-9687942; Fig.3.10d) cuts through an area of ironstone that was intensely folded during D_3. Directly adjacent to this zone, a strongly brecciated layer in sharp contact with non-brecciated meta-ironstone is folded around a D_3 fold (0418580-9688000; Fig. 3.10c) indicating that some brecciation pre-dates D_3 folding and is strata-bound, possibly even indicating a syn-sedimentary origin for this breccia. In Matandani pit a raft of crackle breccia in which brecciation overprints D_3 folds, is embedded within a diorite intrusion with an S_3 foliation. The relationship between the breccia zones and D_4 is not well developed within the pits, but the breccia zones are truncated by low angle reverse faults of D_5 origin and affected by D_5 recumbent folding. In areas where D_5 thrusts cut through the highly folded and fractured meta-ironstone units, brecciation also appears to occur in spatial association with the D_5 fault planes.

When considered together, it appears that the bulk of the breccia bodies in Kukuluma and Matandani pits formed immediately preceding or during D_3 at the same time as the emplacement of the diorite and monzonite bodies to which they are spatially linked. They are best developed in the chert-rich meta-ironstones affected by D_2-D_3 folds. The highly folded zones may have been conducive to breccia formation as a result of the pervasive S_3 fracture cleavage, which developed within the competent meta-ironstones during folding events.

Although most brecciation appears to have been in-situ brecciation of folded competent rock units, some 'streaming' of breccia blocks with pipe-like characteristics did occur. The field relationships indicate that this type of breccia probably formed as a result of the emplacement of the KIC during D_3 events, with D_3 folding, magma emplacement and hydrofracturing working in concert to break up the competent meta-ironstone units.

Apart from the hydrothermal breccia associated with the KIC, there are planar breccia zones or cataclasite zones associated with D_6 shear zones (Fig. 3.2e), and syn-sedimentary chert clast breccias (Fig. 3.1c). The D_6 breccia zones are limited in areal extent and restricted to places where D_6 shear zones transect thick chert beds. These breccia bodies are elongate and up to 2m wide and consist of laminated chert clasts embedded in a commonly sulfidic, iron-rich matrix, which weathers black.

Fragmental sedimentary rocks, probably of volcanoclastic origin, are also common as intercalations within the meta-greywackes, especially along the northern wall of Kukuluma pit (Figs 3.1b, c). These fragmental volcanoclasic rocks have the appearance of strata-bound, matrix supported breccia layers in which angular clasts and layer fragments of chert are embedded in a matrix of siltstone/sandstone rich in micas and feldspar. They differ from the hydrothermal breccia in the proportion of clasts to matrix, the fact that some display a degree of grading and the fact that they are stratabound. Some of these syn-sedimentary fragmental layers may also be affected by the later hydrothermal brecciation processes described above.

3.6. GOLD MINERALIZATION

The deposits of Kukuluma and Matandani occur on a deeply weathered erosional plateau that possibly formed part of the (Cretaceous) African Erosion Surface, and they are overlain by a thick regolith. Complete oxidation and weathering of all rock types occurs to depths of >100m, which influenced gold distribution with leaching of gold in the top 20m of

the regolith profile, and supergene enrichment of gold near the base of the regolith (Bansah et al. 2000) as evidenced by the distribution of artisanal workings in Kukuluma pit. The gold anomalies in Area 3 occur along the edge of the plateau, where the thick regolith has been largely removed by erosion.

Initial trenching of a weak soil anomaly in deeply weathered and leached rock in the Kukuluma-Matandani area gave few indications of the large ore bodies at depth, although, free “leaf” gold in old artisanal workings indicated gold was present. Exploration drilling revealed a general 2-3 g/t increase in mean grade between 60 and 105m depth at Kukuluma and a planar zone of gold enrichment between the base of the regolith and the top of fresh rock (Bansah et al., 2000). Mining of the oxidized ore zones took place between 2002-2007, but once primary mineralization in fresh rock was reached mining stopped due to the refractory nature of the ore (arsenopyrite-rich ore with locally abundant graphitic shale).

Gold mineralization along the Kukuluma Mineralized Trend is spatially related to D_6 shear zones, to competent iron-rich lithologies, including meta-ironstone and chert that are distributed in a complex manner due to D_2-D_3-D_4 fold interference, and to the margins of sheet-like intrusions of the KIC including gabbro, monzonite and diorite especially where these intrusions are in contact with ironstone (Fig. 3.11). High-grade mineralisation is also closely related to fracture networks of D_7 origin. The ore zones are generally tabular in shape with a northnorthwest strike and dips around vertical, parallel to the contact zones of intrusions (Fig. 3.11). In Kukuluma pit it was observed that mineralisation widens along the Juma shear where it cuts across the nose of an eastern plunging D_3 fold, and narrows again where the Juma shear runs oblique along the limbs of D_3 folds (Skead, 2003). A second ore zone in the pit occurs along the Kasata shear and is up to 50m wide, trending 290°, where the Kasata shear intersects a complex D_2-D_3 antiformal fold interference structure in meta-

ironstone; i.e. the presence of D_3 fold hinge zones appears to have affected the width of ore zones.

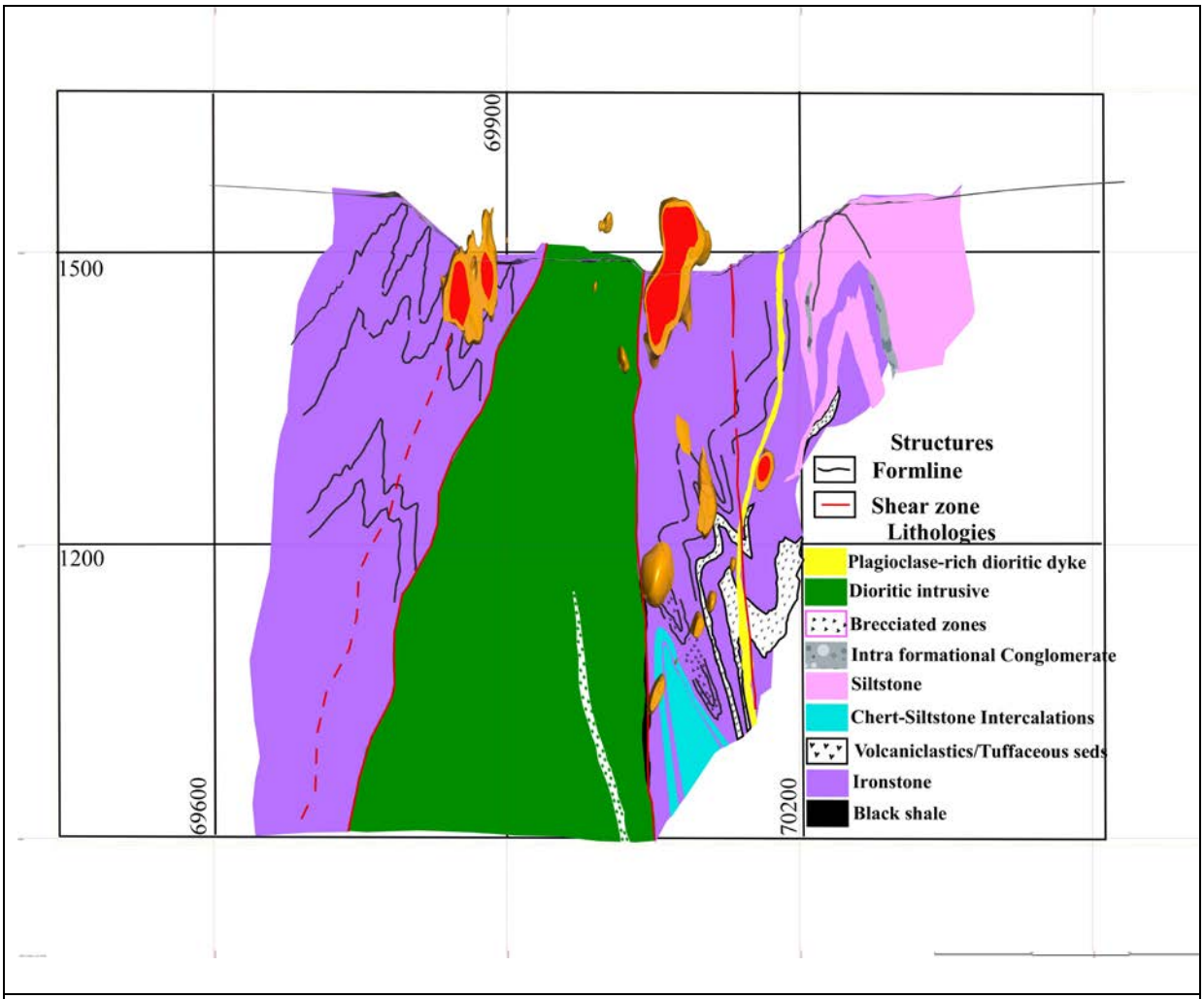

Figure 3.11. E-W cross-section through Matandani pit showing ore distribution along the margin of the Dioritic body as part of the Kukuluma Intrusive Complex. The cut- off grade of ore envelope is 0.5 ppm. The orange coloured ore envelope represents gold values 0.5-1 g/t Au whereas the one in red colour within the ore envelope represents gold grades > 1.0g/t Au.

Higher grade ore in the Matandani, Kukuluma and Area 3 deposits is normally found within meta-ironstone and chert units, with low-grade ore distributed over a larger range of lithologies (Table. 3.2, Fig. 3.12). For 30 diamond drill holes, representing a total length of 6094m from Matandani (2160m), Kukuluma (1787m) and Area 3 (2147m), which transect

the main ore zones, the total length of mineralized rock at grades of >0.1, >0.5, >1 and >5 ppm gold was measured as a function of rock type.

Deposit	grade	Chert	Ironstone	Volc	Seds	Bshale	Diorite	FP	Total
Matandani	>0.1 ppm Au (m)	**533.44**	**300.49**	**112.01**	**69.35**	**30.24**	**31.49**	**5.19**	**1082.21**
	>0.5 ppm Au (m)	**287.65**	**208.38**	**32.76**	**29.04**	**5.45**	**15.60**	**2.54**	**581.42**
	>1.0 ppm Au (m)	**193.59**	**174.70**	**20.04**	**18.64**	**1.50**	**15.60**	**0.00**	**424.07**
	>5.0 ppm Au (m)	**33.28**	**65.17**	**9.00**	**1.00**	**0.00**	**13.00**	**0.00**	**121.45**
Kukuluma	>0.1 ppm Au (m)	**175.79**	**283.07**	**73.07**	**92.11**	**17.97**	**40.47**	**0.00**	**682.48**
	>0.5 ppm Au (m)	**111.30**	**111.41**	**16.20**	**52.89**	**4.00**	**8.30**	**0.00**	**304.10**
	>1.0 ppm Au (m)	**86.65**	**45.98**	**3.00**	**41.75**	**3.00**	**4.30**	**0.00**	**184.68**
	>5.0 ppm Au (m)	**21.00**	**4.45**	**1.00**	**15.98**	**0.00**	**11.00**	**0.00**	**53.43**
Area 3 West	>0.1 ppm Au (m)	**127.75**	**265.34**	**49.86**	**7.00**	**17.35**	**17.00**	**0.00**	**484.30**
	>0.5 ppm Au (m)	**60.11**	**128.50**	**27.00**	**1.00**	**2.50**	**10.00**	**0.00**	**229.11**
	>1.0 ppm Au (m)	**37.36**	**93.34**	**12.70**	**0.00**	**0.00**	**4.00**	**0.00**	**147.40**
	>5.0 ppm Au (m)	**10.21**	**28.44**	**2.00**	**0.00**	**0.00**	**2.00**	**0.00**	**42.65**

(a)

Deposit	grade	Chert	Ironstone	Volc	Seds	Bshale	Diorite	FP	Total
Matandani	>0.1 ppm Au (%)	**49.29**	**27.77**	**10.35**	**6.41**	**2.79**	**2.91**	**0.48**	**100.00**
	>0.5 ppm Au (%)	**49.47**	**35.84**	**5.63**	**4.99**	**0.94**	**2.68**	**0.44**	**100.00**
	>1.0 ppm Au (%)	**45.65**	**41.20**	**4.73**	**4.40**	**0.35**	**3.68**	**0.00**	**100.00**
	>5.0 ppm Au (%)	**27.40**	**53.66**	**7.41**	**0.82**	**0.00**	**10.70**	**0.00**	**100.00**
Kukuluma	>0.1 ppm Au (%)	**25.76**	**41.48**	**10.71**	**13.50**	**2.63**	**5.93**	**0.00**	**100.00**
	>0.5 ppm Au (%)	**36.60**	**36.64**	**5.33**	**17.39**	**1.32**	**2.73**	**0.00**	**100.00**
	>1.0 ppm Au (%)	**46.92**	**24.90**	**1.62**	**22.61**	**1.62**	**2.33**	**0.00**	**100.00**
	>5.0 ppm Au (%)	**39.30**	**8.33**	**1.87**	**29.91**	**0.00**	**20.59**	**0.00**	**100.00**
Area 3 West	>0.1 ppm Au (%)	**26.38**	**54.79**	**10.30**	**1.45**	**3.58**	**3.51**	**0.00**	**100.00**
	>0.5 ppm Au (%)	**26.24**	**56.09**	**11.78**	**0.44**	**1.09**	**4.36**	**0.00**	**100.00**
	>1.0 ppm Au (%)	**25.35**	**63.32**	**8.62**	**0.00**	**0.00**	**2.71**	**0.00**	**100.00**
	>5.0 ppm Au (%)	**23.94**	**66.68**	**4.69**	**0.00**	**0.00**	**4.69**	**0.00**	**100.00**

(b)

Table 3.2. (a) Length of logged drill core expressed in meters, listed by grade and rock type for the Matandani, Kukuluma and Area 3 West deposits. (b) Length of logged drill core expressed in % of total, listed by grade and rock type for the Matandani, Kukuluma and Area 3 West deposits. The lithological units listed comprise the following: Chert = massively banded chert and highly silicified laminated sedimentary units; Ironstone = well bedded, silicified, magnetite-rich units including BIF. Transitional with chert; Volc = volcanoclastic units including agglomerate, fragmental tuff and ignimbrite; Seds = sediments comprising alternating siltstone-shale units with layers of coarser-grained sandstone, grit and rare conglomerate; Black shale = black shale; Diorite = monzonite, and diorite of the Kukuluma Intrusive Complex.

It was noted, that rocks were not always logged in the same manner, and that some rock types were not identified, so that some generalizations had to be made. Nevertheless, it is clear that all deposits show similar relationships between host lithology and ore grade, with >75% of high-grade material (>5ppm) hosted in grunerite-magnetite-chlorite-biotite-rich meta-ironstone and chert units (81% at Matandani, 73% at Kukuluma and 82% at Area 3; Fig. 3.12), which are commonly logged as chert-rich BIF or sedimentary BIF (Sanislav et al., 2016), suggesting a close relationship between mechanically competent, iron-rich lithologies and gold mineralisation. Significant high-grade mineralisation may also occur in sedimentary units (30% at Kukuluma) and diorite (11% at Matandani, 21% at Kukuluma and 5% at Area 3; Fig. 3.12).

The monzonite-diorite intrusions are generally mineralized to within ~3m from the contact with mineralized meta-ironstone, especially near zones were the margin is sheared and meta-ironstone xenoliths occur within the intrusions. At lower grades (<1ppm), other lithologies host some mineralization, but the bulk of the ore (~70-80%) continues to be hosted in the highly fractured, silicified meta-ironstone and chert lithologies (Fig. 3.12). Gold in fresh rock is fine-grained (<20 mμ) and occurs preferentially in silicified meta-iron stone units, within magnetite, pyrrhotite and arsenopyrite grains that are spatially associated with fibrous grunerite aggregates and pyrrhotite, pyrite and chlorite alteration (Fig. 3.13. Note, that grunerite is not restricted to ore zone, but is also a regional metamorphic mineral that is pervasive in meta-ironstone and formed during D_2-D_3 events. In mineralized zones magnetite is commonly replaced by pyrrhotite and arsenopyrite, pyrrhotite, pyrite, stibnite and scheelite occur in fracture networks and as disseminations. Silicification, chlorite-biotite alteration and minor veining characterize the ore zones more broadly. Arsenopyrite–pyrrhotite–magnetite–chlorite assemblages are dominant in highly brecciated chert units whereas pyrite is more

common where meta-ironstone is interbedded with shale units. The alteration assemblages affect intrusive units at or near the sheared contact zones (Fig. 3.11). Higher grades are recorded in areas where arsenopyrite is dominant and chlorite alteration less prominent. In highly mineralized zones gold is generally associated with a network of mm-scale micro-fractures that are in-filled with pyrrhotite and arsenopyrite (Fig.3.13), and that are best develop in the chert-rich layers of brecciated and folded meta-ironstone units. It is these fracture zones at that are also targeted on surface by artisanal miners, and they are probably the result of D_7 faulting.

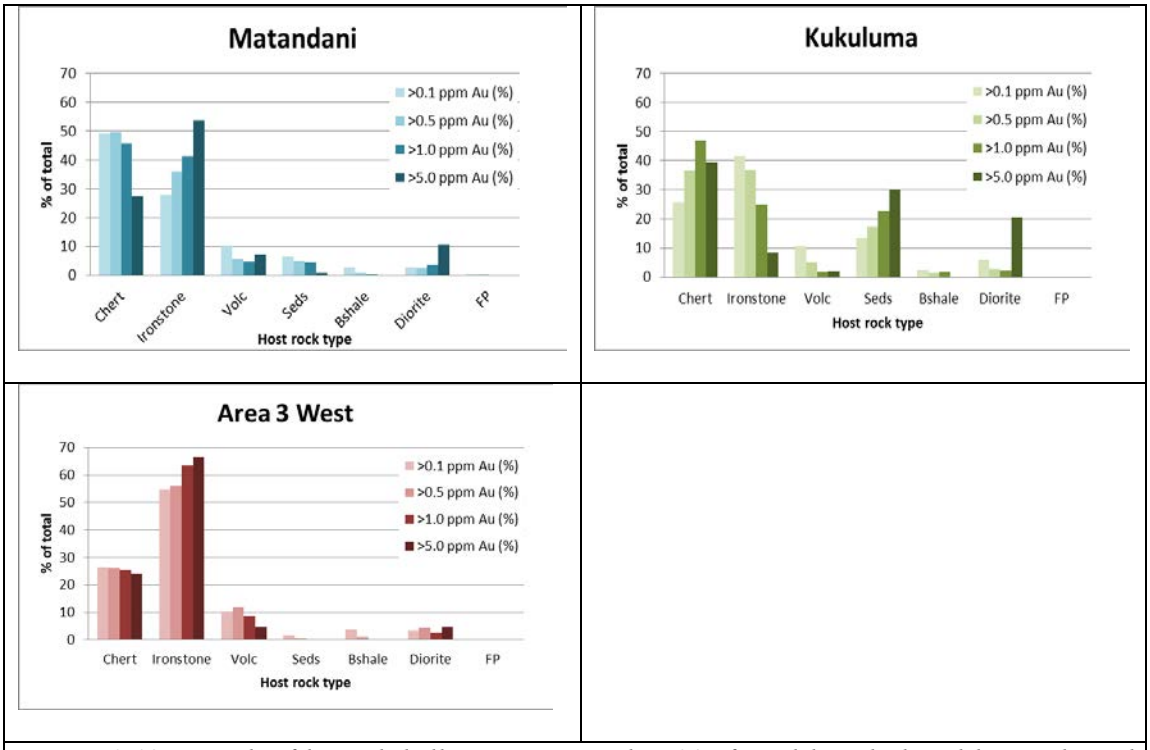

Figure 3.12. Length of logged drill core expressed in % of total length, listed by grade and rock type for the Matandani, Kukuluma and Area 3 West deposits. The plots are based on values listed in Table 2. The lithological units listed comprise the following: Chert = massively banded chert and highly silicified laminated sedimentary units; Ironstone = well bedded, silicified, magnetite-rich units including BIF. Transitional with chert; Volc = volcanoclastic units including agglomerate, fragmental tuff and ignimbrite; Seds = sediments comprising alternating siltstone-shale units with layers of coarser-grained sandstone, grit and rare conglomerate; Bshale = black shale; Diorite = monzonite, and diorite of the Kukuluma Intrusive Complex.

In places, hydrothermal breccia zones are mineralized (Fig.3.13c) where they are cut by D_6-shear zones, which themselves are associated with tectonic cataclasite or breccia zones infiltrated with sulphide (e.g. southern part of Matandani pit). Gold mineralization has also been observed in breccia zones that are not obviously (D_6) sheared, but that are close to shears and occur next to the contact with the diorite/monzonite intrusives. In such areas, intense micro-fracturing, probably of D_7 origin can be observed in drill core with progressive infill of pyrrhotite in fractures within the ore zone. The highly fractured zones represented by the D_3 fold hinges and breccia zones in chert and meta-ironstone would have acted as easy passageways for mineralizing fluids at the time of gold mineralization, which can happen away from D_6 shear zones.

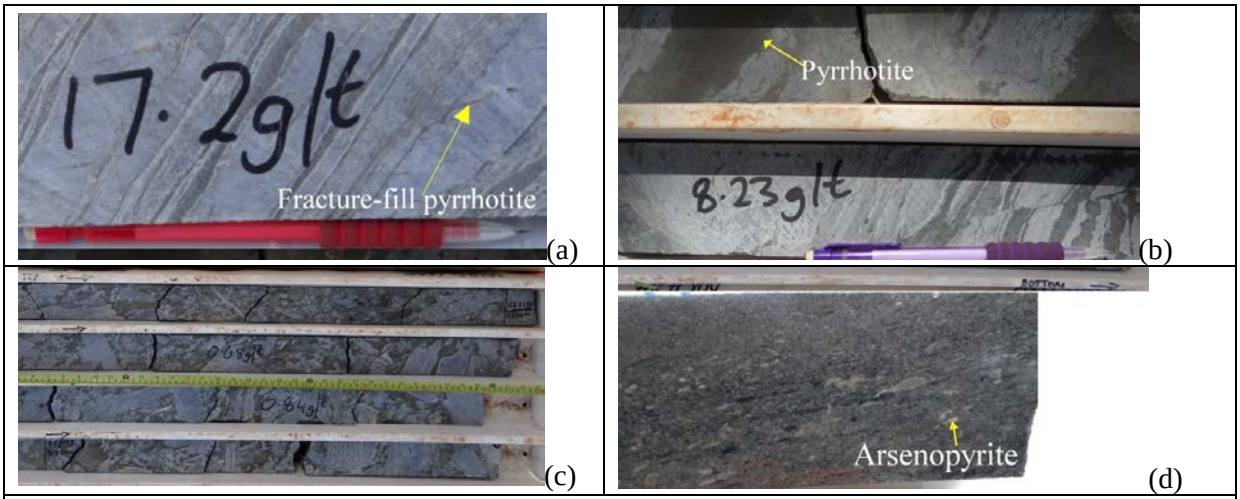

Figure 3.13. Examples of mineralised lithologies in the Matandani deposit and Kukuluma deposits: (a) laminated ironstone package with pyrrhotite mineralization along thin fractures; (b) ironstone with gold-rich pyrrhotite replacement of magnetite; (c) mineralized brecciated ironstone with a siliceous matrix affected by carbonate infill; (d) Strongly foliated mafic volcaniclastic unit with gold-rich arsenopyrite (21g/t Au).

3.7. DISCUSSION

3.7.1. Tectonic history of the central Kukuluma terrain.

A summary of the deformation, intrusive and mineralizing events encountered in the central Kukuluma terrain is presented in Table 3.1. Following deposition of the volcano-

sedimentary sequence at least 7 separate deformation events and 2 intrusive episodes have been identified. The ductile deformation events D_1-D_5 evolved from early layer-parallel shearing (D_1) possibly in response to syn-sedimentary extension, via a first episode of upright folding (D_2) and a second phase of distributed shearing and cylindrical upright folding with northwest trending axial planar surfaces (D_3) to a late stage of open vertical folding (D_4) and then recumbent folding and thrusting (D_5) in response to north-south shortening. This was followed by the development of a network of brittle-ductile shear zones recording dextral reverse movement on NW trending structures and sinistral reverse movement on southwest trending shears, consistent with continued north-south shortening (D_6; Fig. 3.8) and finally reactivation of the shears as normal faults (D_7; Fig. 3.9). Considering that both D_5 thrusts and D_6 shears are consistent with N-S shortening, both events could have formed progressively. Early deformation events were accompanied by the emplacement of the Kukuluma Intrusive Complex (KIC), with dykes, stocks and tabular plugs belonging to diorite and monzonite intrusions being emplaced during D_3, with earliest intrusions preceding D_3 folding, and latest intrusions intruding along D_3 fold axial planes, but still preserving an internal S_3 foliation. Porphyritic granodiorite dykes interpreted as a late felsic phase belonging to the KIC, intruded after D_5, but before the development of D_6 shear zones. A second generation of (north trending) felsic porphyry dykes was emplaced after D_6, but before D_7 and has been affected by D_7 normal faulting and alteration, which included gold mineralization (Table 3.1).

The deformation and intrusive sequence of events described for the central Kukuluma terrain (Table 3.1) is near-identical to the deformation-intrusive sequences obtained in the Nyankanga (Sanislav, 2015) and Geita Hill (Sanislav, 2016) deposits in the Central terrain, even though the latter occur across a major terrain boundary at somewhat lower peak metamorphic conditions (Fig. 1.2). Both areas record early D_1 events associated with chert formation along discordant zones, and $D_{2\text{-}4}$ events in both areas are near identical, with the

exception that structures in Nyankanga and Geita Hill are generally co-linear around a moderately northwest plunging lineation with fold interference patterns dominated by type 3 patterns, whereas D_{2-4} structures in the central Kukuluma terrain preserve a greater diversity in fold-axes orientation with type 2 interference folding being common. This suggests that the central Kukuluma terrain experienced lower strain, which is consistent with the excellent preservation of primary sedimentary structures in the area. Nevertheless, localized, planar D_3 high strain zones with northwest plunging lineations in which S_0, S_1, S_2 and S_3 fabrics have been transposed also occur in the central Kukuluma terrain where strain was partitioned on a 500-1000m scale in planar domains, enveloping fold domains, in a manner not dissimilar from foliation domains and microlithons described for crenulation cleavages in thin section (e.g. Passchier and Trouw, 2006), but on a much larger scale. The fold domains represent areas of relatively low D_3 strain where sedimentary structures and layering are clear and D_1, D_2 and D_3 folds are well exposed. In contrast planar domains, which look less deformed at first glance, actually represent areas of relatively high D_3 strain where all earlier fabrics have been transposed into a planar S_3 fabric. In the central Kukuluma terrain these zones vary in width from several metres up to50m, but elsewhere in the GGB, larger planar high strain zones have been recognized, especially along the S margin of the belt (Cook et al., 2015) where they are equated with major terrain boundaries (e.g. Kabete et al., 2012; Fig. 1.2).

The similarity in deformation histories for the Central and Kukuluma terrains suggests that the tectonic history for much of the GGB is similar, and that terrain boundaries internal to the GGB do not separate diverse domains as would be expected in accretionary terranes (e.g. Dirks et al., 2002; Blewett et al., 2010b; Kabete et al., 2012a), at least not at the scale of the GGB. It is common in many greenstone terrains that early, layer-parallel shear zones (D_1) are overprinted by later, more upright folding events (D_{2-4}), which resulted in the formation of synformal or keel-like geometries (e.g. Peterson and Zaleski, 1999; Hofmann et

al., 2003; de Witt et al., 2011; Bedard et al., 2013; Lin and Beakhouse, 2013); i.e. the GGB does not vary significantly from many other greenstone terrains and its tectonic history may reflect greenstone tectonics more broadly.

D_5 events in the Kukuluma area are more clearly developed than at Geita Hill or Nyankanga (Sanislav et al., 2015, 2016); with recumbent folding showing a clear relationship with low-angle reverse faults. Such structures are common in many greenstone belts, and may have resulted from the rise of diapirs and consequent steepening of the margins of the greenstone belt (e.g. Jelsma et al. 1996; Lin and Beakhouse 2013).

D_6 brittle-ductile shears along the Kukuluma Mineralised Trend correlate to the N-dipping sinistral thrust zones in Nyankanga and Geita Hill; they are identical in metamorphic grade (and association with gold) and only vary in orientation and dominant shear sense, but both are consistent with north-south shortening (Sanislav et al., 2016). In the Kukuluma and Matandani pits, the network of D_6 shear zones share a common, steeply westnorthwest plunging (Fig. 3.6) intersection lineation that more-or-less parallels D_4 fold axes, a dominant cluster of D_3 fold axes (Fig. 3.3e) and the mineral elongation lineation in D_3 high strain zones. This co-linearity of deformation features was also noted in the Geita Hill deposit (Sanislav et al., 2016) where mineralization followed the same general trend, and it has been interpreted to reflect a co-genetic relationship of D_2-D_6 events linked to the same large-scale accretionary processes (Sanislav et al., 2015, 2016).

Later reactivation of D_6 shears in Geita Hill and Nyankanga involved several events including strike-slip and normal movements grouped as $D_{7\text{-}8}$ events, whilst in the central Kukuluma terrain these events are grouped as D_7 with normal movement being dominant, These D_7 events resulted from northnortheast extension and they can be linked to gold mineralization. In a similar way, the KIC correlates in composition and relative timing with the Nyankanga Intrusive Complex (Sanislav et al., 2014; Chapter 4), and both areas show

evidence of igneous events associated with felsic dykes and lamprophyres after D_6 and before D_7.

Considering the close correlation between the two terrains it is suggested that following Sanislav et al. (2015), D_{1-6} events in the Kukuluma terrain occurred at the same time as D_{1-6} events at Geita Hill, i.e. between 2700 and 2680 Ma including the emplacement of the KIC. In the Nyankanga deposit, quartz porphyry dykes dated at 2689 ± 11 Ma (Chamberlain and Tosdal 2007; Sanislav et al., 2015) truncate D_6 shear zones, which suggests that D_6 (and D_5) events represent the retrograde, waning stages immediately following accretionary D_{1-4} events. Using a similar comparison, emplacement of the late porphyry dyke, D_7 normal faulting and mineralization occurred later (probably <2650 Ma) and coincided with emplacement of 2620-2660 Ma granitoids to the east, north and west of the GGB (Sanislav et al. 2014). This deformation and intrusive framework has been tested with zircon geochronology presented in chapter 5.

3.7.2. The nature of D_1 events.

D_1 chert ridges in the central Kukuluma terrain form prominent structures and can be linked to quartz veining, display low angle truncations with S_0, preserve internal disharmonic folding of a well-developed early fabric, and show bifurcation of quartz ridges. These tectonic characteristics suggest that many of the chert ridges in the area originated as low angle shear zones during D_1 (e.g. Hofmann et al., 2001a, 2001b, 2003; Dirks et al., 2002), rather than exhalative deposits associated with ironstone formation in the original volcano-sedimentary pile (e.g. Borg and Rittenauer 2000; Krapez et al. 2003). Similar tectonic chert units decorating early low-angle shear zones have been described from other greenstone belts (e.g. Zegers et al., 1996; deWit and Ashwal, 1997; Hofmann et al., 2003; Dirks et al., 2003, 2009; Weinberg and van der Borgh, 2008), and have been equated to low-angle shear zones

that either accommodated stratigraphic duplication of the greenstone sequence (e.g. deRonde and deWit, 1994; Hofmann et al., 2001a) or extension (e.g. Zegers et al., 1996; Kloppenburg et al., 2001). It is noted that on a regional scale, stratigraphic duplications of the greenstone sequences appear absent, which could suggest that the D_1 structures in the Kukuluma terrain represent low-angle detachment zones that facilitated basin development in which the greenstone sequences accumulated (e.g. Zegers et al., 1996; Kloppenburg et al., 2001). Given that at least some of the cherts originated as layer-parallel quartz veins that intruded in large numbers, and that layering at the time of D_1 was probably sub-horizontal (i.e. D_1 events predated all upright folding events), it would indicate that the D_1 cherts formed close to surface (i.e. at a level where regional fluid pressures would allow the emplacement of horizontal quartz veins across large areas). This would suggest that basinal fluids, possibly of diagenetic origin, were channeled along these structures during early stages of burial, in a manner similar to that described for the Neo-Proterozoic, Belingwe Greenstone Belt in Zimbabwe (e.g. Hofmann et al. 2001b, 2003). Syn-sedimentary extensional structures and chert formation have been described from the Geita-Nyankanga area (Krapez, 2008), which is consistent with this interpretation.

3.7.3. Controls on gold mineralization

Spatially, gold mineralization within the Kukuluma Mineralized Trend is closely associated with D_6-D_7-shear zones where they utilize the contact zone between diorite intrusions of the KIC and magnetite-rich, meta-ironstone units within the surrounding volcano sedimentary package (Fig. 3.11). High-grade mineralisation is also closely associated with networks of extensional D_7 fractures. Ore zones occur almost entirely within the meta-ironstone units, and differ in this respect from mineralisation in Nyankanga and Geita Hill, where diorite of the Nyankanga Intrusive Complex is widely mineralised, be it at a lower

grade (Borg et al., 1990; Borg, 1994; Sanislav, 2015). The ore zones widen where D_6-D_7 shear zones traverse intensely folded and highly brecciated areas, with D_3 fold axial zones and syn-D_3 hydrothermal breccia zones near KIC intrusive margins especially conducive to the infiltration of mineralising fluids along pre-existing micro-fracture networks. However, this relationship only holds where mineralised D_6 shear zones are in close proximity to the folded and brecciated areas; i.e. brecciation of meta-ironstone units in itself does not guarantee gold mineralisation. These relationships indicate that the D_6-D_7 shear zones along the Kukuluma Mineralised Trend acted as upper-crustal channel ways for the mineralising fluids, facilitating the infiltration into fractured zones offered by the strongly folded and brecciated meta-ironstones (e.g. Robert et al., 1991; Cox et al., 2001). In this context it is also important to note that the distribution of the ironstones is highly complex as a result of D_2-D_3-D_4 fold interference, and, therefore, that the intersection zones of D_2-D_3-D_4 folded ironstones and D_6-D_7 shears is highly discontinuous, which contributes to the distributed nature of the ore zones in the area. Earlier reports (e.g. Skead, 2003) argued that mineralisation was controlled by the Juma and Kasata shears, and that their apparent displacement between Kukuluma and Matandani pits was the result of later E-W sinistral faults.

A similar east-west fault was assumed to have displaced the southern end of the Juma shear to account for mineralisation in Area 3 to the east. Pit exposure, now shows that the Juma and Kasata shears anastomose and change in orientation from west-trending to northwest trending, with no evidence of offsets by later east-west faults. Likewise the eastern tip of the Juma fault displays a complex fault splay, characteristic for fault tips or terminations (Fossen, 2016), with no evidence of displacement by cross cutting faults. Thus, the spaced distribution of mineralisation from Area 3 West, via Kukuluma to Matandani should be understood in terms of an en echelon array along a westnorthwest trending

corridor, rather than a continuous northwest trending ore zone displaced by later east-west faults.

The close spatial relationship of gold with meta-ironstone and the intrusive margins of the KIC indicate a litho-chemical control on mineralisation with sulphidization of the magnetite-rich units being particularly important. It is, therefore, assumed that much of the gold entered the system as sulphur complexes, which destabilised upon contact with magnetite-rich rocks (e.g. Seward, 1973; 1991; Kerrich, 1989; Shernberger and Barnes, 1989; McCuaig and Kerrich, 1998; Likhoidov et al., 2007; Sanislav et al., 2015). Compared to other major deposits in the GGB, mineralisation along the Kukuluma Mineralised Trend is more pyrrhotite-arsenopyrite rich, which may reflect a combination of higher metamorphic grade and host-rock control.

In terms of timing of gold mineralisation in the Kukuluma terrain, reference again must be made to the similarity of the geological history between Geita Hill, and Kukuluma and Matandani. Similar to Kukuluma and Matandani, mineralisation at Nyankanga is spatially linked to D_6 reverse faults that formed prior to ~2685Ma (Chamberlain and Tosdale, 2007; Sanislav et al., 2015). However, the mineralising event is late-tectonic and associated with normal fault reactivation of the older reverse faults (i.e. D_8 at Nyankanga and Geita Hill; Sanislav, 2015, 2016; D_7 at Matandani-Kukuluma; Table 1). The mineralising events post-date an intrusive event dated at Geita Hill at 2644 Ma (Borg and Krogh 1999). By analogy, the mineralisation along the Kukuluma Mineralised Trend, which truncates the late north-trending porphyry dyke in Matandani, is similarly late-tectonic and associated with extension of the older D_6 structures (see also Chapter 5). Thus, whilst the ore-body geometries are entirely controlled by deformational structures and lithological distributions that formed during the early (i.e. 2700-2680 Ma) stages of evolution of the GGB, the actual mineralising events probably occurred much later when fluids, possibly linked to a deeper igneous source,

were pumped into the dilatant zones during extension. In this context it is important to note that the ore zones in Kukuluma and Matandani pits widen, where the D_6 shear zones display s-like bends (from northwest to west to northwest trending). Such S-bends would be constraining bends (Fossen, 2016) during D_6 dextral reverse faulting, but during D_7 the faults were reactivated to accommodate sinistral-normal movement, meaning that the S-bends would be areas of maximum dilatancy.

In review papers on gold mineralisation the Geita mine is commonly classified as a Neoarchean, BIF-hosted, orogenic gold deposit (e.g. Goldfarb et al., 2001, 2005; Groves et al., 2006; Bierlein et al., 2006, 2009) related to subduction-accretion systems with all mafic sequences deposited in a subduction-back arc environment (Kabete et al., 2012). Cook et al. (2015) and Sanislav et al. (2015, 2016) showed that this interpretation needs adjustment. They argue that, rather than forming in a classic orogenic setting, mineralization entered the greenstone belt during an extensional phase concomitant with the emplacement of widespread TTG granites (Sanislav et al., 2014), ~40-50 Ma after compressional deformation and accretion of the greenstone sequence. Cook et al. (2015) showed that the mafic-intermediate volcanics in the GGB could have evolved from melt segregation of depleted mantle below thick oceanic plateaus away from subduction systems and accretionary margins, and that the greenstone sequence may in fact have never experienced accretion-subduction processes as postulated by Kabete et al., 2012. If so, this would further invalidate a traditional orogenic setting for the gold deposits in the GGB (Goldfarb et al., 2001).

3.8. CONCLUSIONS

Detailed mapping of the central part of the Kukuluma terrain in the E GGB shows that the deformation-intrusive history of the area (Table 3.1) is near identical to the geological history of the Central terrain which hosts the world class Nyankanga and Geita Hill deposits.

This similarity occurs across major structural boundaries, and suggests that the geological history of much of the GGB is similar, with an early compressional-accretionary phase (D_{2-6}) between 2700-2680Ma associated with the emplacement of internal intrusions of the KIC, and a later extensional phase (D_7) associated with a second generation of intrusions, and gold mineralisation.

The geometry of the ore bodies at Kukuluma and Matandani is controlled by the distribution of magnetite-rich meta-ironstone, near the margins of monzonite-diorite bodies of the KIC where they are cut by D_6-D_7 shear zones. High-grade mineralisation is enhanced by pre-existing breccia zones and D_3 fold hinges characterised by a high density of micro-fracturing. The actual mineralising events may have happened late (<2650 Ma), during D_7 extensional reactivation of some D_6 shear zones, and the formation of broader D_7 deformation zones.

CHAPTER 4

THE PETROGENESIS OF THE NEOARCHEAN KUKULUMA INTRUSIVE COMPLEX, NW TANZANIA*

**This chapter has been submitted to Precambrian Research as: S. D. Kwelwa, I. V. Sanislav, P. H. G. M. Dirks, T. Blenkinsop, S. L. Kolling, 2017 etc.*

4.1. SUMMARY

Kukuluma Intrusive Complex (KIC) is an intermediate to felsic, late Archean igneous complex that intruded the Geita Greenstone Belt of northwest of Tanzania. The KIC consists of two separate diorite and monzonite suites that intruded syn-tectonically, and a granodiorite suite (mostly dykes) that intruded late syn-tectonically. The monzonite and the diorite suites have low silica content ($SiO_2 \leq 62$ wt %), moderate Mg# ($Mg\#_{average}$ = 49), high Sr/Y ($Sr/Y_{average}$ = 79) and high La/Yb ($La/Yb_{average}$ = 56) ratios, and strongly fractionated chondrite normalized (La_n/Yb_n = 9 to 69) REE patterns. Their moderate Ni ($Ni_{average}$= 50 ppm), Cr ($Cr_{average}$= 85 ppm), variable Cr/Ni ratio (0.65-3.56) and low TiO_2 ($TiO_{2average}$= 0.5 wt%) indicate little to no interaction with the peridotitic mantle. For most major elements (Al_2O_3, FeO_t, Na_2O, TiO_2 and P_2O_5) the monzonite and the diorite suites display sub parallel trends for the same SiO_2 content indicating they represent distinct melts. Intrusions belonging to the diorite suite have high Na_2O ($Na_2O_{average}$ = 4.2 wt %), Dy/Yb_n ($Dy/Yb_{n\text{-}average}$ = 1.6), a positive Sr anomaly and uncorrelated Nb/La and Zr/Sm ratios suggesting derivation from partial melting of garnet-bearing amphibolite in which plagioclase was not stable. Intrusions belonging to the monzonite suite have higher Na_2O ($Na2O_{average}$ = 5.61 wt %), Dy/Yb_n ($Dy/Yb_{n\text{-}average}$ = 2.21), a negative Sr anomaly and correlated Nb/La and Zr/Sm ratios

consistent with derivation from partial melting of eclogite with residual rutile. Small variations in the Th/U ratio and near chondritic/MORB average values ($Th/U_{monzonite}$ = 3.65; $Th/U_{diorite}$ = 2.92) are inconsistent with a subducting slab signature, and it is proposed that the monzonite and the diorite suites of the KIC formed by partial melting of the lower mafic crust of an oceanic plateau.

The granodiorite suite has lower Mg# ($Mg\#_{average}$ = 41), moderately fractionated REE, low Sr/Y ($Sr/Y_{average}$ = 20), La/Yb ($La/Yb_{average}$ = 15), Dy/Yb_n ($DyYb_{n\text{-}average}$= 1.24) and small negative Eu anomalies suggesting derivation from partial melting of amphibolite and plagioclase fractionation. Near-MORB Th/U ($Th/U_{average}$ = 2.92) and Zr/Sm ($Zr/Sm_{average}$ = 30.21) ratios are consistent with intracrustal melting of amphibolite.

4.2. INTRODUCTION

The geochemical signature of intermediate to felsic rocks with fractionated REE patterns and high Sr/Y and La/Yb ratios has been interpreted to indicate melt derivation from a subducted slab at amphibolite to eclogite facies conditions (Defant and Drummond, 1990; Drummond and Defant, 1990). Their particular geochemical signature, including a high Mg# (molecular (Mg/Mg+Fe) x100) and enriched large-ion lithophile elements (LILE) were interpreted to represent different degrees of interaction between slab melts and mantle peridotite in the mantle wedge (e.g. Kay, 1978; Tatsumi and Ishizaka, 1981; Shirey and Hanson, 1984; Stern et al., 1989; Defant and Drummond, 1990; Drummond and Defant, 1990; Tatsumi, 2006; Moyen, 2009; Castillo, 2012). Arc rocks with similar geochemical signatures, including andesite, dacite, sodic rhyolite and their plutonic equivalents, were grouped under the term “adakites” by Defant and Drummond (1990) implying they share a specific petrogenetic history, namely, melting of the mantle wedge induced by fluids and/or

melts from the subducted slab. Another class of rocks sharing similar petrogenetic processes (e.g. melting of mantle peridotite metasomatised by subduction fluids/melts) and geochemically similar to adakites includes the high-Mg andesites or sanukitoids (e.g. Tatsumi and Ishizaka, 1981; Shirey and Hanson, 1984; Tatsumi, 2006; Tatsumi, 2008), and the crustal contaminated sanukitoids of South India described as "Closepet-type" granites (Jayanada et al., 1995).

The important message contained in the original definition of adakites and sanukitoids was that the metasomatised mantle wedge is the primary source for these magmas, and the slab derived fluids/melts are just the metasomatic agents, thus imparting a subduction signature. Martin et al. (2005) subdivided adakites into two groups, low-silica adakites (LSA) and high-silica adakites (HSA), corresponding to distinct petrogenetic processes. In this subdivision the LSA are equivalent to sanukitoids and their petrogenesis involves melting of subduction modified peridotite as originally proposed by Defant and Drummond (1990). On the other hand, the HSA are proposed to be analogues of the late Archean tonalite-trondhjemite-granodiorite (TTG) magmas and derived from partial melts of subducted basaltic crust in the garnet stability field, which reacted with peridotite during ascent (Martin et al., 2005). Archean rocks with an "adakitic" geochemical signature have been used to argue in favour of a plate tectonics regime in the Archean (e.g. Martin, 1999; Polat and Kerrich, 2001; Manya et al., 2007; Manykyamba et al., 2007; Mohan et al., 2013; Kwelwa et al., 2013).

However, alternative models propose that rocks with an "adakitic' signature can form by fractional crystallization in the garnet stability field (e.g. Kamber et al., 2002; Macpherson et al., 2006; Richard and Kerrich, 2007; Rooney et al., 2011), by melting thickened mafic lower crust (e.g. Atherton and Petford, 1993; Rudnick, 1995; Wang et al., 2005), or through

the interaction of delaminated eclogitic lower crust with the underlying mantle (e.g. Bedard et al., 2003; Tuloch and Kimbrough, 2003; Gao et al., 2004; Wang et al., 2005; Goss et al. 2011). Since most of the continental crust was formed in the Archean (e.g. Taylor and Mclennan, 1995; Tatsumi, 2008; Hacker et al., 2015) and the Archean rock record is dominated by rocks with an adakite-like (TTG's; e.g. Condie, 2005; Moyen, 2011; Moyen and Martin, 2012) geochemical signature, understanding the petrogenetic processes that resulted in the formation of rocks with an adakitic signature in the Archean is essential. This is particularly important for the late Archean period when major shifts in the composition of the TTG suites are interpreted to reflect fundamental changes in global tectonics (e.g. Condie, 2005; Martin et al., 2010; Moyen and Martin, 2012; Condie, 2014). In this contribution we present major and trace element geochemical data from the Kukuluma Intrusive Complex (KIC) that intruded the NeoArchean Geita Greenstone Belt of NW Tanzania and discuss the petrogenesis and tectonic setting of the KIC. For background to the general geology of the Tanzania Craton and geological setting of the Geita Greenstone Belt I refer to the introduction in Chapter 1.

4.3. THE KUKULUMA INTRUSIVE COMPLEX

The Kukuluma Intrusive Complex (KIC) consists of a series of northwest trending intermediate to felsic igneous rocks (Fig. 1.3) that intruded the folded sequence of the Upper Nyanzian sediments. Three major gold deposits, Matandani, Kukuluma and Area 3 West, occur along the contact between the KIC and the sediments (Fig. 1.3). The KIC is dominated by equigranular, fine- to medium-grained and locally porphyritic, intermediate intrusives (Fig. 4.1) and subordinate felsic (Fig. 4.1) porphyritic dykes.

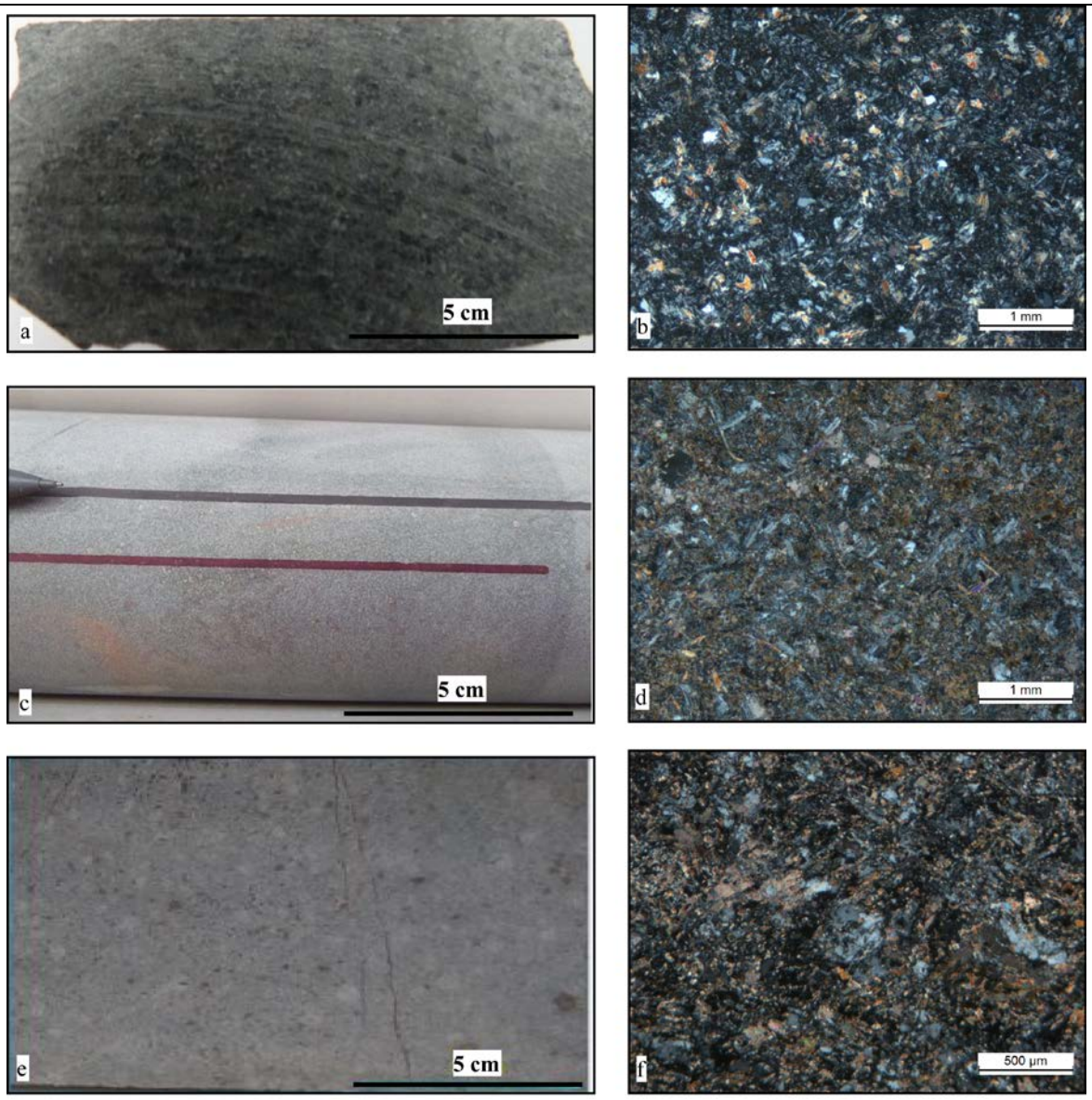

Figure 4.1. Photomicrographs showing the three main rock types found in the KIC. a and b) Medium grained diorite; the mineralogy is dominated by amphibole (mostly actinolite) and plagioclase with minor quartz. c and d) Medium grained monzonite; the mineralogy is dominated plagioclase, k-feldspar, biotite and amphibole with minor quartz. The diorite and monzonite have been deformed and metamorphosed to greenschist facies. As a result amphibole and pyroxene have been partly replaced by actinolite. Note that the feldspars in both rock types are not altered to sericite and appear fresh under microscope suggesting that the samples have not been significantly affected by hydrothermal alteration. e and f) Photographs of a porphyritic granodiorite dyke. Note that the feldspars from the granodiorite have been partly replaced by sericite but appear mostly fresh under microscope. Small amounts of carbonate and chlorite, disseminated or as microveins are present in all samples.

The intermediate intrusive bodies are weakly to moderately foliated, indicating syn-D_3 emplacement (using the deformation scheme of Sanislav et al., 2015). The mineralogy is dominated by plagioclase (30-45 %), amphibole (30-40 %), alkali-feldspar (5-25 %), biotite (5-15%) pyroxene (5-10%) and quartz (5-20%). Based on the mineralogical composition the intermediate intrusives of the KIC can be separated into a diorite suite (gabbro-diorite and diorite; Figs 4.3a and b) and a monzonite suite (monzodiorite and monzonite; Figs 4.1c and d). The feldspars are only partly sericitized (Figs. 4.1b and d) while some of the mafic minerals are partly replaced by metamorphic actinolite. Accessory minerals include apatite, magnetite and rutile. Minor chlorite and carbonate are present as disseminated minerals, partly replacing the mafic minerals or along veins.

The felsic porphyritic dykes (Figs 4.1e and f) show a narrower variation in their mineralogical composition. Their mineralogy is dominated by quartz (15-40 %), plagioclase (50-70%), K-feldspar (5-40%), biotite (5-15%) and amphibole (1-10%). Based on their mineralogical composition the felsic phase of the KIC varies between granodiorite and tonalite. The plagioclase is partly sericitized and the mafic minerals are partly replaced by chlorite.

4.4. ALTERATION AND ELEMENT MOBILITY

The KIC rocks are deformed, metamorphosed and locally overprinted by hydrothermal alteration related to the three gold deposits located along its margins. The top 100 meters of the intrusive complex is highly weathered so that all samples were collected from diamond drill holes that intercepted the intrusive complex at more than 400 meters below the surface. Petrographic examination of the samples revealed minor carbonate and chlorite alteration indicating that the samples have been hydrated and carbonated. The loss of ignition (LOI)

values of up to 5.5% confirms the petrographic observations and requires that all samples be screened for element mobility.

To test the element mobility for the KIC samples we used only the monzonite and diorite suites, because the higher number of samples allows compositional variations induced by post-magmatic alteration to be identified more easily. Na, K, Rb and Sr are all easily mobilised during low-temperature hydrothermal alteration and metamorphism. The post-magmatic disturbance of Na, K, Rb and Sr by hydrothermal alteration and metamorphism can be tested by plotting their concentration against the LOI values. A lack of correlation indicates little or no significant disturbance while well-correlated trends indicate significant disturbance and mobility. The lack of any correlation between these elements and the LOI values (Fig. 4.2) combined with their coherent behaviour on other geochemical plots suggests that the post-magmatic alteration did not significantly mobilised these elements and they can be used for petrogenetic interpretations. In general REE and HFSE are considered immobile during hydrothermal alteration and greenschist facies metamorphism but situations where the REE were mobile have been documented (e.g. Wood et al., 1976; Condie et al., 1977); with the LREE considered to be more mobile than the HREE (Sun and Nesbit, 1978). To test the mobility of the REE from the KIC rocks, we plotted the concentration of La against Zr (Fig. 4.2e), and to test the mobility of the HFSE we plotted the concentration of Nb against Zr (Fig. 4.2f).

The strong positive correlation that exists between these elements in combination with the coherent behaviour of the REE and HFSE on chondrite and primitive mantle normalised plots indicate that these elements most probably retained their original concentrations. The ratio of highly incompatible elements such as Th and U should be near chondritic ($Th/U_{chondrite}$= 3.63; Sun and McDonough, 1989) unless disturbed by alteration processes

when U is mobile under oxidizing conditions. The average Th/U ratio of all KIC rocks ($Th/U_{monzonite}$=3.65; $Th/U_{diorite}$= 2.92; $Th/U_{granodiorite}$= 2.92) is near chondritic suggesting little to no mobility of these elements during hydrothermal alteration and metamorphism.

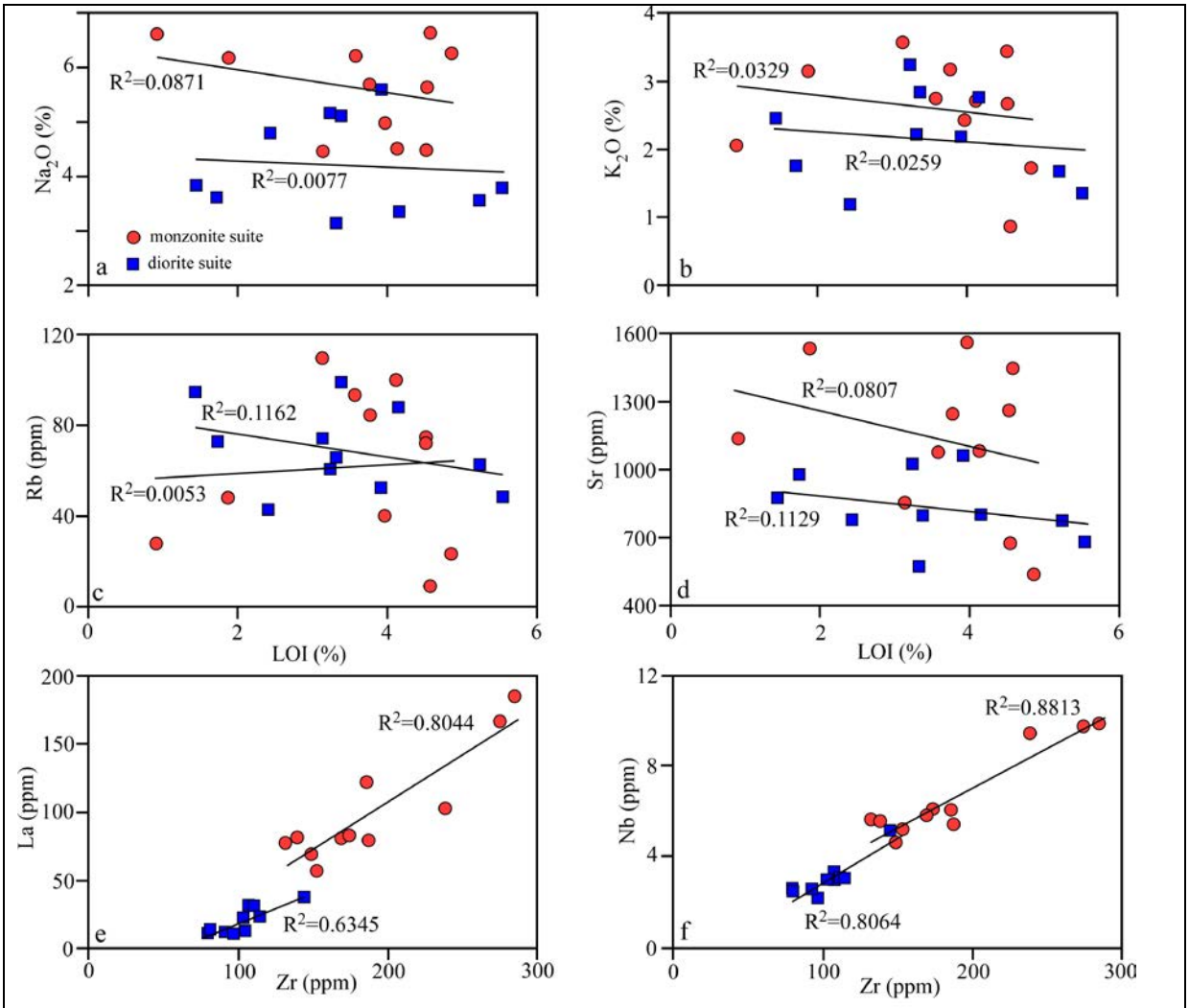

Figure 4.2. Series of diagrams showing that although the rocks of the KIC have been hydrated and carbonated, as indicated by the petrography and LOI values, their major and trace element composition was very little disturbed. Diagrams a and b show that there is no correlation between the concentration of two of the most mobile major elements, Na_2O and K_2O, and the LOI values. The same pattern is observed in c and d where the concentration of two of the most mobile trace elements, Rb and Sr, are plotted against the LOI values suggesting that most likely the concentration of these elements is close to their initial values. The mobility of REE and HFSE was tested by plotting the values of La (e) and Nb (f) against Zr, a highly immobile element. The good correlations suggest that these elements were most likely immobile during post-magmatic alteration and metamorphism.

4.5. THE GEOCHEMISTRY OF THE KIC

The geochemical composition of the KIC (Tables A7.1-A7.3; Fig. 4.3) is characterised by: intermediate SiO_2 (59.17 wt %), moderate #mg (0.47), high Al_2O_3 and FeO (15.83 wt% and 5.66 wt% respectively) and moderate MgO (2.78 wt %). The K_2O/Na_2O ratio is less than 1 (0.70) and $CaO+Na_2O$ is more than 8 (8.82%). The Y content is low (14.5 ppm) and Sr is high (765 ppm) with an average Sr/Y ratio of 59. The HREE are depleted relative to the LREE with an average La/Yb ratio of 42 and the Cr content is moderately high (62 ppm). The chondrite normalized REE pattern (Fig. 4.4) show fractionated patterns while the primitive mantle normalized multi-element patterns show negative Nb and Ti anomalies and a general enrichment in the large ion lithophile elements (LILE).

4.5.1. The Monzonite suite

The geochemical composition of rocks that belong to the monzonite suite (Fig. 4.3; Table A7.1) from the KIC is characterized by intermediate SiO_2 (51.7- 62.1 wt%), FeO (3-9 wt%), MgO (2.5-5.6wt%) and CaO (3.8-7 wt%), moderate K_2O (0.9-3.6 wt%), high Al_2O_3 (14.4-16.5 wt%) and Na_2O (4.5-6.6 wt%) and low TiO_2 (0.4-0.6 wt%). They have high $CaO+Na_2O$ (8.6-12.9), high Sr (537-1563 ppm) and high LREE (La_n = 241-777; the subscript "n" refers to chondrite normalized). These features combined with a low K_2O/Na_2O ratio (0.1-0.8), low Y (11-30 ppm), low HREE (Yb_n = 4-11) and high Sr/Y and La/Yb ratios (30-119 and 67-102 respectively) indicate that the monzonite suite has geochemical characteristics similar to adakites, sanukitoids and Closepet-type granite. Martin et al (2005) suggested that less differentiated sanukitoids (SiO_2<62 wt %) are similar to LSA and Closepet-type granite. However, rocks that belong to the monzonite suite from the KIC have, on average, higher Y, Yb and La/Yb than the LSA, higher #mg, Sr, Cr, Sr/Y and La/Yb than

the Closepet-type granite, and higher La/Yb than the average sanukitoid. At the same time the monzonite suite has lower TiO_2, #mg, Sr, Cr, Ni and Sr/Y than the LSA, lower TiO_2, Y, Yb than the Closepet-type granite and lower Cr compared to the average sanukitoid.

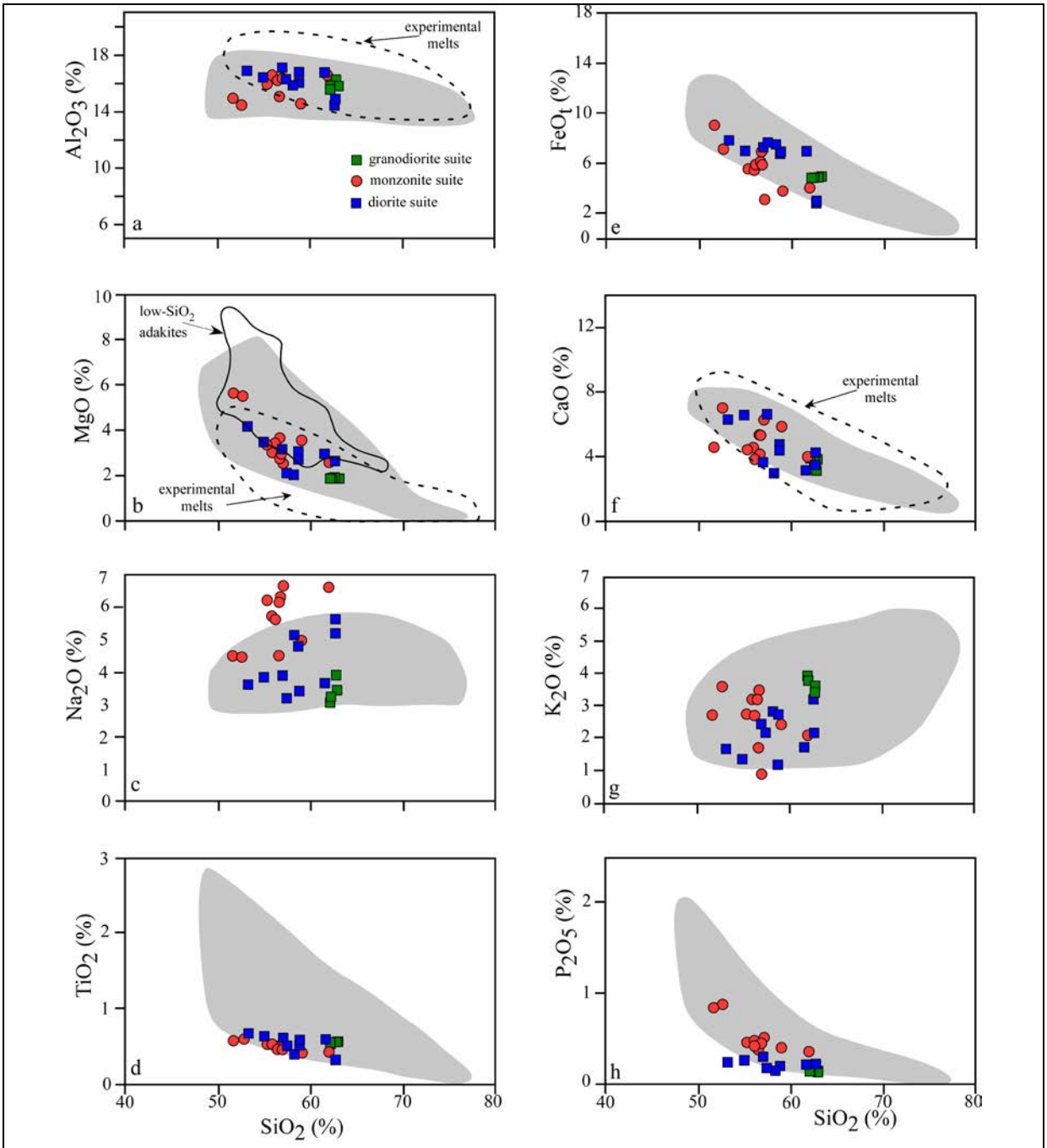

Figure 4.3. Major elements variation diagrams for the KIC. The grey area shows the field of sanukitoids from Martin et al., (2010). The field of LSA (continuous line in Figure 5b) is from Castillo (2012) and the field of basaltic experimental melts is from Rollison (1997) and Martin et al., (2005).

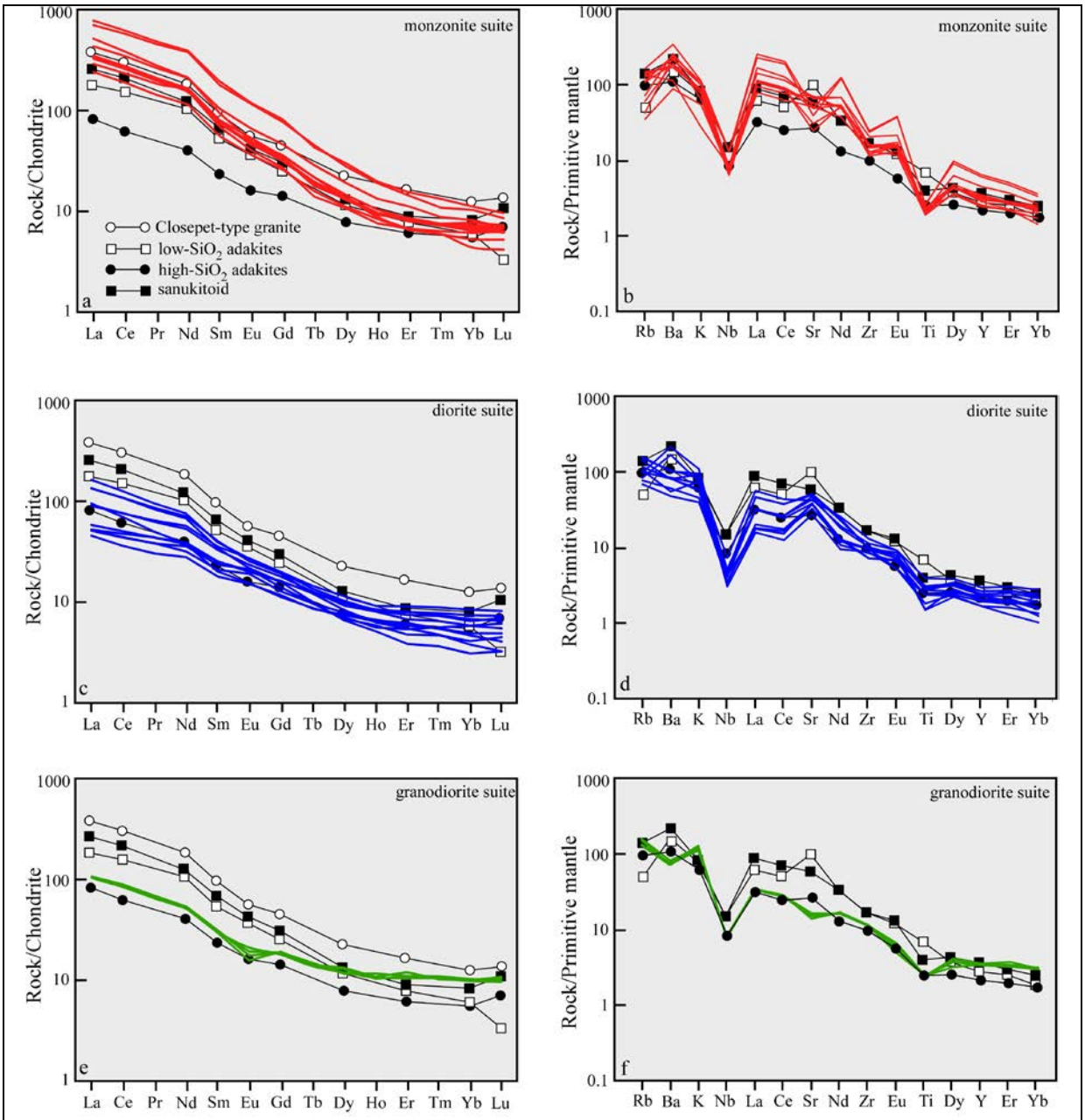

Figure 4.4. Chondrite normalized REE diagrams (a, c and e) and primitive mantle normalized trace element diagrams (b, d and f) for the KIC rocks. Also shown is the average of LSA, HSA, sanukitoids and Closepet-type granite from Martin et al., (2005).

The chondrite normalized REE pattern (Fig. 4.4a) of monzonite suite rocks is subparallel to the pattern from average LSA, sanukitoid and Closepet-type granite and shows the strong LREE enrichment characteristic for these type of rocks. When plotted on a primitive mantle normalized multielement diagram (Fig. 4.4b) the monzonite suite shows strong negative anomalies for Nb and Ti, and moderate negative anomalies for Zr and Sr. Their pattern is subparallel to that of the LSA, sanukitoids and Closepet-type granite. Notable differences are the positive Sr anomaly for the LSA, the lack of a Sr anomaly in sanukitoids and the lack of a negative Zr anomaly in LSA, sanukitoids and Closepet-type granite.

4.5.2. The Diorite suite

Rocks that belong to the diorite suite (Fig. 4.3; Table A7.2) have similar SiO_2 (53-63 wt %) contents compared to monzonite suite rocks with slightly higher Al_2O3 (14.4-17.1 wt %), FeO (2.8-7.8 wt %), and TiO_2 (0.3-0.7 wt %), and slightly lower Na_2O (3.1-5.6 wt %), K_2O (1.2-3.2 wt %) and P_2O_5 (0.1-0.3 wt %). These values combined with K_2O/Na_2O ~ 0.54, $CaO+Na_2O$ ~ 8, low Y (7.5-11.9 ppm), low HREE (Yb_n = 3-7.4) and high Sr (572-1062 ppm), Cr (49-98.5 ppm) and LREE (La_n= 45-161) suggest that the diorite suite also shares geochemical features with sanukitoid, adakite and Closepet-type granite. The average composition of rocks from the diorite suite is similar to the average composition of HSA except for lower SiO_2 (58.6 vs 64.8), higher FeO (6.39 vs. 4.27), higher Cr (75 vs 41) and higher Sr/Y (85 vs 56).

The chondrite normalized REE pattern (Fig. 4.4c) is similar to the average HSA and subparallel to, but at lower concentrations than the average LSA, sanukitoid and Closepet-type granite. On a primitive mantle normalized multi-element diagram (Fig. 4.4d) diorite suite rocks show a pronounced negative Nb anomalies, moderately negative Ti anomalies and moderately positive Sr anomalies, all of which are also typical for LSA. The overall pattern is

similar to that of HSA, except for the positive Sr anomaly, and is subparallel to the average pattern of LSA, sanukitoid and Closepet-type granite but at lower concentrations.

4.5.3. The Granodiorite suite

Four samples from the KIC were classified as granodiorites. Although the samples were collected a few hundred meters apart their major and trace element composition is almost identical (Fig. 4.3; Table A7.3). They have moderate SiO_2 (av. 62.5 wt %), low FeO (av. 4.9 wt %), MgO (av. 1.9 wt %), CaO (av. 3.7 wt %) and high K_2O (av. 3.67 wt %) when compared to rocks from the monzonite and the diorite suite. Their K_2O/Na_2O ratio is high (av. 1.1), $CaO+Na_2O$ is low (av. 7.4), Y is low (av. 16.4), HREE are low (Yb_n = 9.7), LREE are moderately high (La_n= 100), and Sr and Cr content are relatively high (332 and 21 ppm respectively). The lower Sr content (< 400 ppm), a Sr/Y ratio of less than 40 and a La/Yb ratio of less than 20 suggest that the granodiorites cannot be considered to have an adakite-like signature sensu Defant and Drummont (1990). However, as pointed out by Moyen (2009), HSA can have a Sr/Y ratio as low as 20.

On a chondrite normalized REE diagram (Fig. 4.4e) the granodiorites display a subparallel trend to that of the HSA but they plot at higher concentrations. They also show a weak negative Eu anomaly indicative of plagioclase fractionation. On a primitive mantle normalized multi-element diagram (Fig. 4.4f) their pattern is similar to that of the HSA, except that they have a weak negative Sr anomaly while the HSA have a weak positive Sr anomaly.

4.6. PETROGENESIS OF THE KIC

4.6.1. Relative timing of emplacement

There is no age data available for the rocks forming the KIC. However, field evidence may help constrain their relative timing of emplacement. The KIC occurs as a series of intrusive bodies subparallel to the northwest-southeast trending regional fabric (Fig. 1.3). The diorite and the monzonite suite rocks contain a weakly to well-developed foliation that is subparallel to the axial planar surface of regional D_3 folds (Sanislav et al., 2015, 2016) indicating coeval and syntectonic emplacement. The granodiorite suite rocks are not foliated suggesting that their emplacement postdates the emplacement of the diorite and the monzonite suite. Felsic dykes similar in composition to the granodiorite suite outcrop in the Kukuluma and Matandani deposits where they crosscut the folded sequence and are crosscut by brittle ductile shear zones. Borg and Krogh (1999) obtained a single zircon age of 2699±9 Ma from a diorite dyke subparallel to the banded ironstones from the Geita Hill deposit interpreted to indicate the minimum sedimentation age for the Upper Nyanzian sequence in the Geita area. The deformed sequence is intruded and truncated by the 2660-2620 Ma high-K granites (Sanislav et al., 2014). This constrains the timing of emplacement for the KIC between 2700 Ma and 2660 Ma.

4.6.2. Depth and source of melts

Fractionated REE patterns (Fig. 4.4), high Sr/Y and La/Yb ratios (Figs. 4.5a and b), and low Y and Yb contents suggest that garnet was present as a fractionating or residual phase in the melt. However, high Sr/Y and La/Yb ratios can also reflect an enriched source (Moyen, 2009), can be produced by the fractionation of amphibole, and by the delayed crystallization of plagioclase in hydrous mafic magmas (Castillo, 2012), while fractionated REE patterns may result from amphibole fractionation (e.g. Romick et al., 1992; Richards

and Kerrich 2007). Continental crust has high Sr/Y and La/Yb ratios, therefore, melting of continental crust and/or mixing with continental crust may impart high Sr/Y and La/Yb to their derivative melts. The low SiO_2 and moderate Mg# of the KIC rocks suggest a mafic to ultramafic source and preclude any significant contribution from felsic rocks. In mafic melts fractionation of amphibole may increase the La/Yb ratio of the residual melt, but the REE pattern will not develop a strongly concave shape. As magma becomes more dacitic the hornblende REE distribution coefficients increase and magmas develop concave REE patterns and high La/Yb ratios (Romick et al., 1992). So the net effect of amphibole and plagioclase fractionation is an increase in La/Yb and decrease in Dy/Yb (Moyen, 2009) while garnet fractionation or partial melting with residual garnet will effectively increase the Dy/Yb ratio in the melt (e.g. Macpherson et al., 2006; Davidson et al., 2007). Kelemen et al. (2003) proposed that melts with a clear garnet (eclogite) signature should have Dy/Yb_n ratios ≥ 1.5. All samples of the monzonite suite and the majority of the diorite suite samples have $Dy/Yb_n > 1.5$ (Fig. 4.5c) suggesting that their high Sr/Y and La/Yb ratios are related to deep melting. Eclogite melts reacting with the mantle (Kelemen et al., 2003) would effectively decrease both the Dy/Yb and the La/Yb ratios (Fig. 4.5d) of the initial melt. Therefore, a lack of eclogite melting signature in some of the samples (i.e. the granodiorite suite) does not automatically rule out their derivation from eclogite/garnet-bearing melts. Moreover, plagioclase crystallization can decrease Sr/Y ratios and increase Y concentrations. Thus, a deep melting signature (based on this ratio) can be erased by large degrees of plagioclase fractionation (e.g. Richard and Kerrich, 2007).

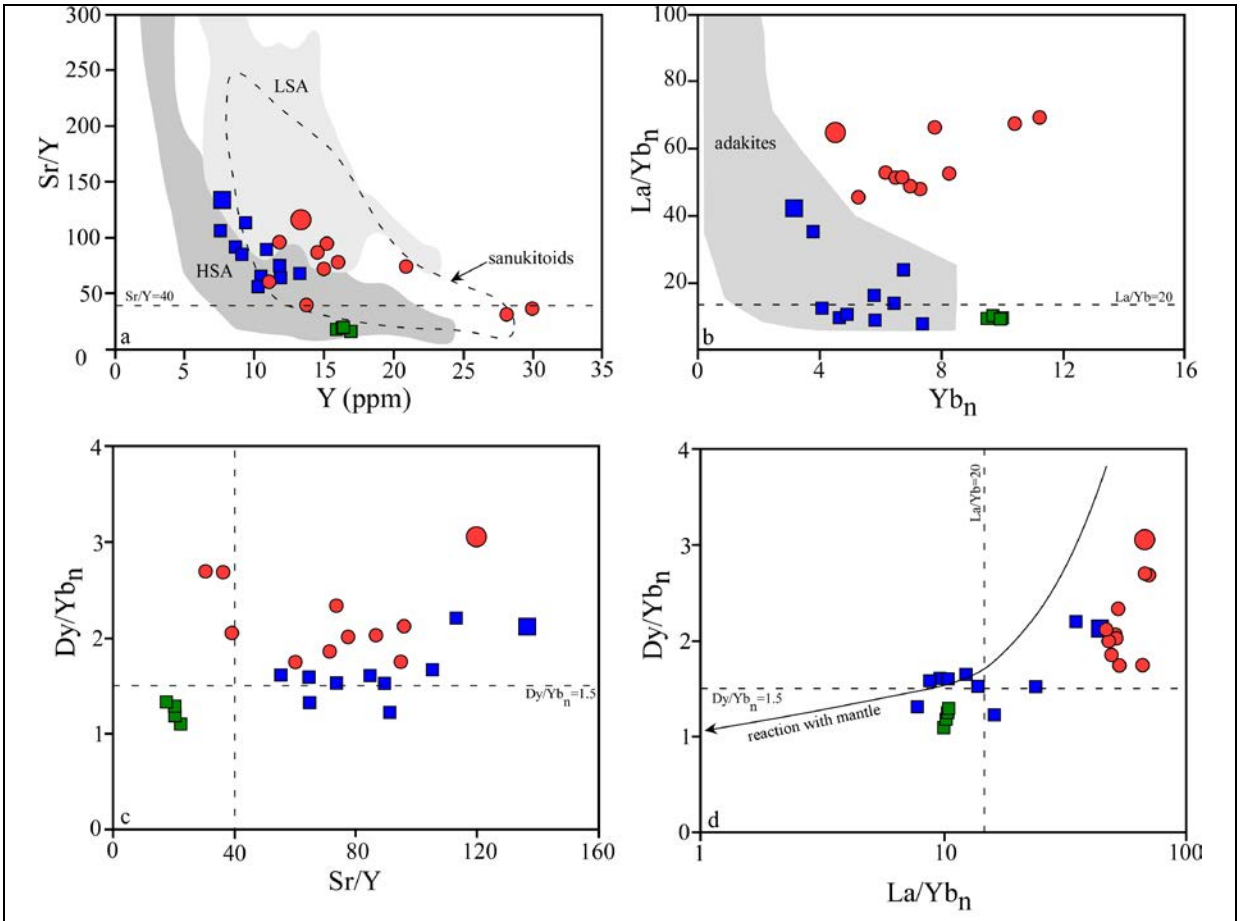

Figure 4.5. Sr/Y vs Y (a) and La/Yb$_n$ vs Yb$_n$ (b) diagrams for the KIC samples. The field of LSA (ligh grey) and HSA (darker grey) in (a) is from Castillo (2012) and the field of sanukitoids (dashed line) is from Martin et al., (2005). The field of adakites in (b) is from Moyen and Martin (2012). The diagrams in (c) and (d) show that the samples that have high Sr/Y (c) and La/Yb$_n$ ratios (d) also have high Dy/Yb$_n$ ratio indicative of high pressure melting. The large square (diorite suite) and the large circle (monzonite suite) show the samples with the highest Mg# which also have the Sr/Y, La/Yb$_n$ and Dy/Yb$_n$ ratios. The line with arrow in (d) shows that the interaction of eclogitic melts with the mantle peridotite leads to a decrease in the La/Yb and Dy/Yb ratios in the melt (Kelemen et al., 2003). Green = granodiorite suite; red = monzonite suite; blue = diorite suite.

The major element variation diagrams show that for the same SiO_2 content (Fig. 4.3), the diorite and the monzonite suites display subparallel trends for most of the elements. It is particularly obvious for Al_2O_3, FeO_t, Na_2O, TiO_2 and P_2O_5. Assuming that the two suites were derived from rocks having a similar composition this subparallel evolution of the major elements cannot be explained by magma mixing or by fractional crystallization alone and

requires melting at different pressures. For example, the Al_2O_3 content of melts becomes depleted with increasing pressure at the same degree of partial melting (e.g. Hirose and Kushiro, 1993). The negative correlation between SiO_2 and Al_2O_3 (Fig. 4.3a) in the diorite suite may indicate garnet fractionation or residual garnet, which will effectively reduce Al_2O_3 with increasing SiO_2 in the melt (Macpherson et al., 2006; Davidson et al., 2007). The positive correlation observed in the monzonite suite may indicate that garnet was consumed during melting. The monzonite suite rocks tend to have higher Na_2O at the same CaO (Fig. 4.6a) compared to the diorite suite rocks. This can also indicate a higher pressure during melting as Na_2O becomes more compatible in clinopyroxene at higher pressure (e.g. Kogiso et al., 2004).

On chondrite normalized diagrams (Fig. 4.4) the REE patterns for the two suites are subparallel, but the LREE elements are more fractionated for the monzonite suite compared to the diorite suite. This is also illustrated by much higher La/Yb_n and Dy/Yb_n ratios (Fig. 4.5) suggesting that rocks belonging to the monzonite suite may represent deeper melts compared to rocks from the diorite suite. Their primitive mantle normalized trace element patterns (Fig. 4.4) are also sub-parallel, with the notable difference that the diorite suite rocks have a positive Sr anomaly while the monzonite suite rocks have negative Sr and Zr anomalies. The presence of a significant positive Sr anomaly in the diorite suite cannot be explained by melting or crystallization unless plagioclase is involved. The lack of any correlation between the Sr/Sr* and the MgO (Fig. 4.6b) excludes fractionation. Thus, a plagioclase-rich component is required in the melt source region. Alternatively, interaction of the melt with a plagioclase-rich region (assimilation) will produce a similar effect. However, assimilation will result in a large decrease in FeO_t and a large increase in Al_2O_3 with

decreasing MgO (e.g. Peterson et al., 2014), which is not the case here. Therefore assimilation can be excluded.

The only viable explanation is that the positive Sr anomaly is related to the source rock. We propose that the diorite suite was formed by melting of garnet-bearing amphibolite and plagioclase was completely transferred into the melt, leaving behind a Sr-depleted (relative to Ce and Nd) residue of garnet-clinopyroxene-rutile eclogite. Further melting of the eclogite with residual rutile produced the monzonite suite with negative Sr and Zr anomalies. Zr and Hf have similar chemical properties and should not fractionate from each other in geological processes; i.e. their ratio should be chondritic in all earth materials (e.g. Zr/Hf=~36.3; Sun and McDounough, 1989). The diorite suite has an average Zr/Hf ratio of 36.8 (Fig. 4.6c), which is similar to the chondritic value, but the monzonite suite has an average Zr/Hf ratio of 42.7 (Fig. 4.6c), which exceeds the chondritic value suggesting that these elements were fractionated from each other.

Experimental data on amphibole/melt partition coefficients (e.g. Foley et al., 2002; Tiepolo et al., 2007) have shown that amphibole can fractionate most HFSE causing negative Ti and Nb anomalies, but only high-Mg amphibole can fractionate Zr from Hf. The ability of garnet to fractionate Zr from Hf is dependent on pressure and MgO content (e.g. Green et al., 2000; van Westrenen et al., 1999). The only mineral able to effectively fractionate HFSE from each other is rutile (Stalder et al., 1998; Foley et al., 2000). If rutile was the residual phase, the Nb/La and Zr/Sm ratios of the melt will correlate positively (Münker et al., 2004), but if high-Mg amphibole was the residual phase the melt ratios of these elements will correlate negatively. The monzonite suite shows a clear positive correlation between Nb/La and Zr/Sm (Fig. 4.6d) implying residual rutile. However, the diorite suite shows no correlation between these two ratios. Rutile cannot coexist with basaltic melts arising from

the partial melting of peridotite (e.g. Ryerson and Watson, 1987; Woodhead et al., 1993; Thirlwall et al., 1994) because it reacts with the olivine to form orthopyroxene and ilmenite. Thus, the most likely source for the monzonite suite is rutile-bearing, garnet-clinopyroxene eclogite.

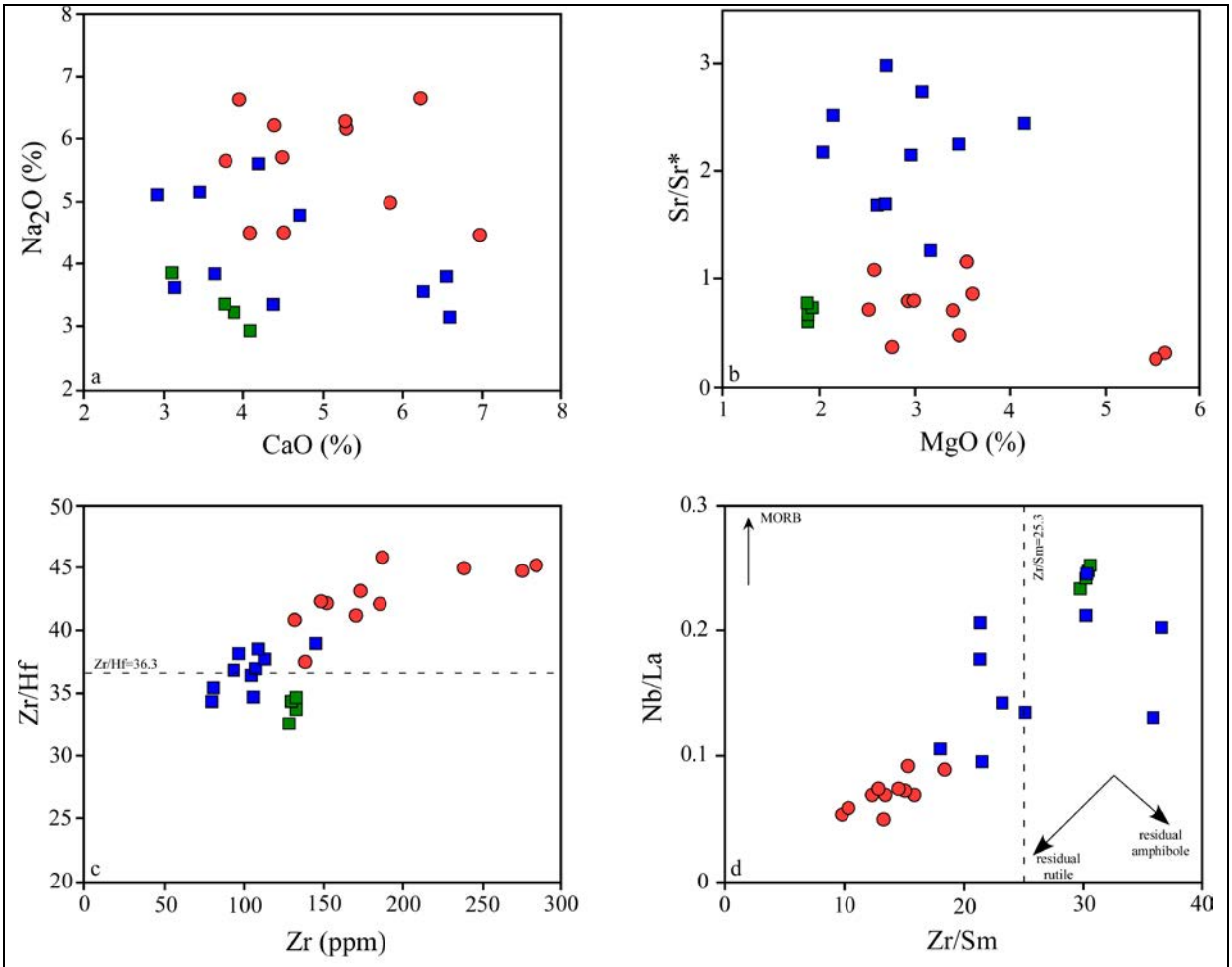

Figure 4.6. Diagram (a) showing that at similar CaO values the monzonite suite has higher Na_2O, which may reflect clinopyroxene in the source and melting at higher pressure. (b) The lack of correlation between the MgO and the Sr/Sr suggest that the Sr anomaly is not the result of plagioclase fractionation. (c) Shows that Zr and Hf are fractionated from each other in the monzonite suite which we attribute to residual rutile. The effect of residual rutile is shown in (d) where the positive correlation between Nb/La and Zr/Sm ratios is indicative of residual rutile (Münker et al., 2004). The dashed lines in (c) and (d) shows the chondritic ratios for the respective elements while the arrows in (d) show the effect of residual rutile (positive correlation) vs the effect of residual high-Mg amphibole (negative correlation). Green = granodiorite suite; red = monzonite suite; blue = diorite suite.*

4.6.3. Melt - mantle interaction

The low SiO_2 content, average Mg numbers, and relatively high Ni and Cr concentrations indicate that the source rocks for the KIC must be mafic or ultramafic. Their intermediate composition ($SiO_2 \leq 62$ wt %) suggests that fractionation played a minor role in their petrogenesis and they are close to primary magmas. From this point of view the rocks of the KIC resemble LSA and sanukitoid. However, there are some important differences. Firstly, at the same SiO_2 content the rocks of the KIC have much lower MgO compared to LSA and sanukitoid (Fig. 4.3b). Secondly, the rocks of the KIC overlap the field of mafic experimental melts (Figs 4.1a,b and f) while the LSA plot above it, and the sanukitoids overlap it but only for low MgO concentrations. Because of their low SiO_2, high Mg numbers and high Cr and Ni concentrations, the LSA and the sanukitoids are commonly interpreted to have formed by partial melting of mantle peridotite metasomatised by felsic melts (e.g. Shirey and Hanson, 1984; Rapp et al., 1999; Martin et al., 2005). The rocks of the KIC have lower Mg numbers (at the same SiO_2 content) and much lower Cr, Ni, Sr, K, Rb and Nb concentrations compared to the LSA and the sanukitoids (Fig. 4.7 and Tables A7.1-A7.3). The difference between KIC rocks and the LSA is clearly illustrated in figure 4.7 where the composition of KIC rocks overlaps the composition of the HSA, and closely resembles the composition of experimental melts of basalt (Figs. 4.5a and b).

On the K vs Rb diagram (Fig. 4.7a) some of the LSA plot subparallel to the y-axis suggesting high K/Rb ratios, which were interpreted to reflect Rb depletion by selective melting of metasomatic amphibole in a peridotite source (e.g. Martin et al., 2005 and references therein). However, in the absence of metasomatism, both peridotite and basaltic melts result in K/Rb ratios much lower than average oceanic basalt (K/Rb=1071; Sun and McDonough, 1989). High Sr contents can reflect deep melting at pressures above the

plagioclase stability field, melting of a source that was already high in Sr, and/or melt interaction with high-Sr geological materials (e.g. Moyen, 2009). Given the low SiO_2 ($\leq$ 62 wt %) of the KIC samples, their source rock must have been mafic or ultramafic.

Experimental melting of basalt produced liquids with up to 1000 ppm Sr (Fig. 4.7b), but to achieve the high Sr observed in LSA, interaction with mantle peridotite is required (e.g. Martin et al., 2005). Rocks from the diorite and granodiorite suites plot within the fields of basaltic melts and HSA (Fig. 4.7b), while some of the samples from the monzonite suite plot at higher Sr values (~1500 ppm) within the field of LSA, which may indicate some level of interaction with mantle peridotite. However, if the source of the KIC rocks was mafic lower crust (Sr = 348 ppm; Rudnick and Gao, 2003; Sr = 289 ppm; Hacker et al., 2015) rather than an average oceanic basalt (Sr = 90 ppm; Sun and Mcdonough, 1989), than high Sr values observed in the monzonite suite do not necessary require interaction with peridotite mantle. Maybe the most useful ratio to use when separating melts derived from partial melting of metasomatised mantle peridotite (LSA) and melts derived by partial melting of mafic rocks (HSA) is the Cr/Ni ratio (Fig. 4.7c; Martin et al., 2005). The Cr/Ni ratio for KIC samples (Fig. 4.7c) is clearly distinct from that of the LSA and overlaps the field of the HSA suggesting a mafic source and minimum interaction with the mantle. The lack of correlation between the Cr/Ni ratio and the Mg# (Fig. 4.7d) suggests that the Cr/Ni ratio of the KIC samples is a source characteristic and not dependent on fractionation.

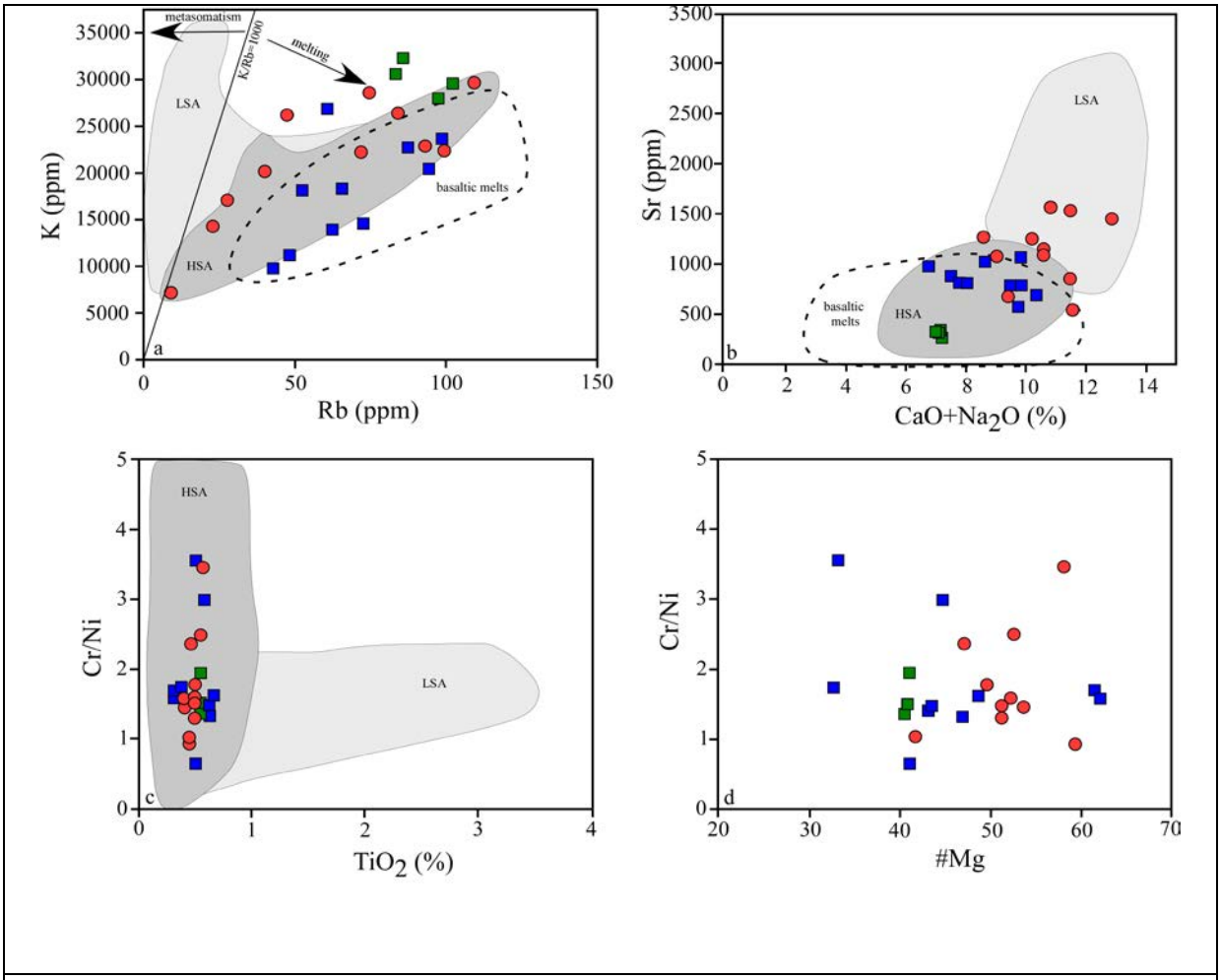

Figure 4.7. Diagrams showing the compositional differences between LSA and HSA on K vs Rb (a), Sr vs CaO+Na2O (b) and Cr/Ni vs TiO2 (c) compiled by Martin et al., (2005). In (a) the continuous line shows the average K/Rb ratio in MORB (Sun and McDonough, 1989) while the arrows show the effect of metasomatism, which increases the ratio and the effect of partial melting, which decreases the ratio. In all three diagrams the KIC samples resemble more the HSA than the LSA and mostly overlap the field of experimental basaltic melts. The diagram in (d) show that there is no correlation between the Cr/Ni ratio and the Mg# indicating that the Cr/Ni ratio in the KIC samples is a source characteristic rather than the result of fractionation. Green = granodiorite suite; red = monzonite suite; blue = diorite suite.

4.6.4. Tectonic setting

The rocks of the KIC have major and trace element signatures similar to "adakitic' rocks. Although the original description of adakites (e.g. Defant and Drummond, 1990) specifically indicates that their geochemical signature is derived from partial melting of a subducted slab, it is clear now that high Sr/Y and La/Yb ratios alone cannot be used to

unequivocally indicate a subduction setting (e.g. Moyen, 2009; Castillo, 2012), and rocks with “adakitic” signature can form in different tectonic settings as well. The KIC was emplaced syn-tectonically along axial planar surfaces of upright regional folds suggesting a period of crustal thickening. The age data from the northern half of the Tanzania Craton (e.g. Kabete et al., 2012; Sanislav et al., 2014) suggest that growth of this part of the craton started at ~ 2820 Ma with extensive tholeiitic mafic volcanism (e.g. Manya and Maboko, 2003, 2008; Cook et al., 2015) followed by a period dominated by the intrusion of diorite and TTG and completed with the intrusion of the 2620-2660 Ma high-K granites (Sanislav et al., 2014). Thus, the KIC was emplaced during the transition period from higher depth TTG magmas to shallower depth high-K magmas.

Cook et al. (2015) proposed that the ~ 2820 Ma mafic volcanics (Kiziba Formation) that form the base of the stratigraphic sequence (Lower Nyanzian) in the Sukumaland Greenstone Belt were emplaced in an oceanic plateau like setting. However, it is unclear at the moment whether or not the Upper Nyanzian sediments (intruded by the KIC) were deposit on top of the Kiziba Formation or the two units were tectonically juxtaposed. In the Geita region the contact between the two units is structural (Cook et al., 2015), but there appears to be evidence that the Geita Greenstone Belt is underlain by the mafic rocks of the Kiziba Formation suggesting that crustal growth in this part of Tanzania occurred by partial melting and maturation of an oceanic plateau by lower crustal delamination/modification (e.g. Vlaar et al., 1994; Zegers and van Keken, 2001; Bedard, 2006; Bedard et al., 2013; Cook et al., 2015). Chiaradia (2015) showed that there is a strong correlation between the Sr/Y and MgO of recent arc magmatism and the upper plate thickness indicating that source processes (slab melting, slab melt-mantle interactions) do not play a major role in the generation of high Sr/Y signatures. This implies that high Sr/Y occurs at lower MgO

contents, suggesting that thicker crust favours magma evolution at deeper levels, thus Sr/Y increases steadily with magmatic differentiation (Fig. 4.8a). In contrast, Archean rocks show a sudden increase of the Sr/Y ratio between ~2.5 and ~0.5 wt% MgO (Fig. 4.8a) suggesting that, as opposed to modern arc lava, source processes control the Sr/Y ratio of Archean rocks (Chiaradia, 2015). Source processes may include partial melting in the garnet stability field of subducted mafic crust or partial melting of delaminated lower mafic crust.

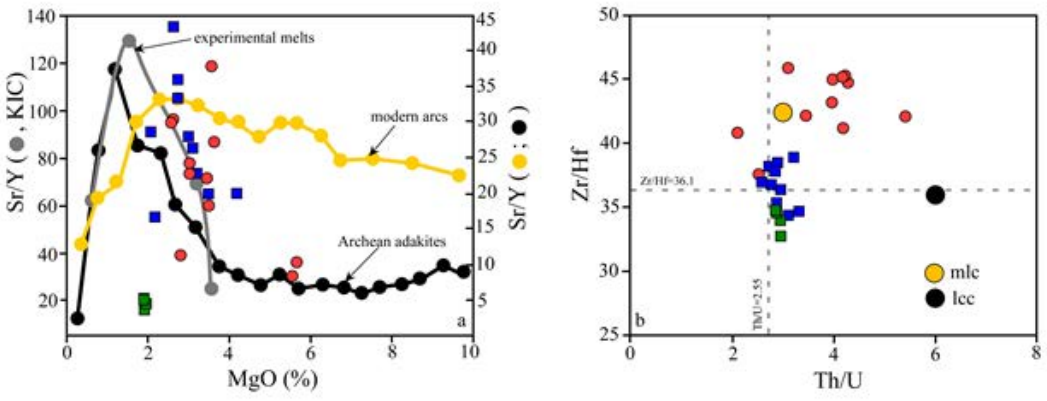

Figure 4.8. Diagram showing the variation of the Sr/Y ratio with MgO in modern arcs, Archean adakites and experimental melts from Chiaradia (2015). Chiaradia (2015) showed that in the modern arcs the Sr/Y ratio is a function of crustal thickness and the gradual increase of the Sr/Y ratio with increased crustal thickness also correlates with decreasing MgO suggesting that the Sr/Y ratio in modern arcs better reflects intracrustal processes than source characteristics. The sudden increase in Sr/Y ratios at low MgO in Archean adakites is similar to the data obtained for experimental basaltic melts and is consistent with partial melting of the lower mafic crust in the Archean. The KIC samples have Sr/Y and MgO values similar to the experimental basaltic melts and the Archean adakites suggesting lower mafic crust melting. The diagram in (b) shows that the diorite and the granodiorite suite have near MORB/chondritic Zr/Hf and Th/U ratios while the monzonite suite has Zr/Hf ratios similar to the mafic end member (mlc) of the lower crust (Hacker et al, 2015) and the Th/U ratio varies between the mafic end member of the lower crust and the lower continental crust values of Rudnick and Gao (2003). However, the Th/U ratios in all samples are near chondritic suggesting that Th and U were not fractionated from each other as required by a subduction environment. Green = granodiorite suite; red = monzonite suite; blue = diorite suite.

To investigate a possible subduction component in the generation of the KIC rocks we use Th/U vs Zr/Hf ratios. Given the highly incompatible behaviour of Th and U, normal

magmatic processes cannot significantly fractionate these elements from each other. U and Th are easily fractionated during surface processes because of the higher mobility of U during weathering and under oxidizing conditions. Seafloor alteration and addition of slab fluids will lower the Th/U ratio while dehydration and addition of sediment melts will increase the Th/U ratio (e.g. Bebout, 2007). Figure 4.8b shows that the diorite and the granodiorite suites have almost MORB-like Th/U and Zr/Hf ratios, thus precluding a subduction component. The monzonite suite has higher Zr/Hf ratios due to residual rutile (see above) and the Th/U ratio varies between the values for the lower mafic crust end-member of Hacker et al. (2015) and the values for the average lower continental crust of Rudnick and Gao (2003). Overall, the KIC shows a very narrow variation in Th/U ratios, which is more consistent with partial melting of the mafic lower crust than partial melting of a subducted oceanic crust.

4.7. CONCLUSIONS

In general Archean igneous rocks with adakite-like signature were interpreted to indicate a subduction setting. We have shown that although the rocks of the KIC can be easily classified as “adakites”, detail screening of their composition revealed important differences. Given the recognition that rocks with adakite-like signature can form in a variety of tectonic settings from non-unique petrogenetic processes, requires a re-examination of the existing Archean datasets. Higher Archean geothermal gradients would have favoured the development of thicker lithospheric roots and partial to complete eclogitization of the mafic lower crust; the removal of the eclogitised crust would favour partial melting of the thickened lower crust to generate adakite-like rocks. This scenario is similar to the interpretation of the post-tectonic adakite-like rocks from the Tibetan Plateau with the main difference that the KIC is syn-tectonic. Alternatively, KIC formed by partial melting of eclogitised mafic lower crust of an Archean oceanic plateau.

CHAPTER 5

ZIRCON U-Pb AGES AND Hf ISOTOPE DATA FROM THE KUKULUMA TERRAIN OF THE GEITA GREENSTONE BELT, TANZANIA CRATON: IMPLICATIONS FOR THE DEFORMATION HISTORY, SUPRACRUSTAL STRATIGRAPHY, CRUSTAL GROWTH AND TIMING OF GOLD MINERALIZATION

5.1. SUMMARY

The Geita Greenstone Belt is a late Archean greenstone belt located in the Tanzania Craton, trends approximately east-west and can be subdivided into three northwest-southeast trending terrains: the Kukuluma Terrain to the east, the Central Terrain in the middle and the Nyamullilima Terrain in the west. The Kukuluma Terrain forms a northwest-southeast trending zone of complexly deformed sediments, intruded by the Kukuluma Intrusive Complex which contains an early-syntectonic diorite-monzonite suite and a late-syntectonic granodiorite suite. Three gold deposits (Matandani, Kukuluma and Area 3West) are found along the contact between the Kukuluma Intrusive Complex and the sediments. A crystal tuff layer from the Kukuluma deposits returned an age of 2717±12 Ma which can be used to constrain maximum sedimentation age in the area. Two granodiorite dykes from the same

deposit and a small granodiorite intrusion found along a road cut yielded zircon ages of 2667±17 Ma, 2661±16 Ma and 2663±11 Ma respectively. One mineralized granodiorite dyke from the Matandani deposit has an age of 2651±14 Ma which can be used to constrain the maximum age of the gold mineralization in the area.

The 2717 Ma crystal tuff has zircon grains with suprachondritic $^{176}Hf/^{177}Hf$ ratios (0.28108 to 0.28111 at 2717 Ma) and positive (+1.6 to +2.6) εHf values indicating derivation from juvenile mafic crust. Two of the granodiorite samples have suprachondritic $^{176}Hf/^{177}Hf$ ratios (avg. 0.28106 and 0.28107 at 2663 and 2651 Ma respectively) and nearly chondritic εHf values (avg. -0.5 and -0.3 respectively). The other two granodiorite samples have chondritic $^{176}Hf/^{177}Hf$ ratios (avg. 0.28104 and 0.28103 at 2667 and 2661 Ma respectively) and slightly negative εHf values (avg. -1.1 and -1.5 respectively). The new zircon age and isotope data suggest that the igneous activity in the Kukuluma Terrain involves a significant juvenile component and occurred within the 2720 to 2620 Ma period which is the main period of crustal growth in the northern half of the Tanzania Craton.

5.2. INTRODUCTION

The architecture of many late Archean cratons such as the Zimbabwe Craton (Kusky, 1998; Jelsma and Dirks, 2002), the Yilgarn Craton (Blewet et al., 2010; Czarnota et al., 2010), the Dharwar Craton (Chadwick et al., 2000; Manikyamba and Kerrich, 2012) or the Superior Province (Percival et al., 2001; Bèdard et al., 2013) is commonly described in terms of a series of terranes assembled along major crustal-scale shear zones. In general, the assembly contains a core of older terrane fragments against which, younger terranes have been juxtaposed in a linear manner, commonly interpreted to indicate terrane accretion

analogous to modern day plate tectonic processes (e.g. Zeh et al., 2009; Blewet et al., 2010; Kabete et al., 2012a). Alternative tectonic scenarios include accretion of basaltic plateaus against proto-cratons along dominantly oblique strike-slip shear zones (Bedard et al., 2013) or inversion of intracontinental rift systems sited above mantle plumes (Hayman et al., 2015).

The tectonic architecture of the Tanzania Craton was initially (e.g. Harpum, 1970; Gabert, 1990; Kuehn et al, 1990) interpreted in terms of a basement unit, the Dodoman Basement Complex, on top of which younger units (the greenstone belts), such as the Nyanzian and the Kavirondian, were thrusted in a process comparable to continental arc tectonics. This interpretation was based mainly on the degree of tectonism described from the above units. The Dodoman Basement Complex comprises mainly high-grade metamorphic rocks including gneiss, migmatite and granulite that formed under mid- to lower crustal conditions, while the Nyanzian and Kavirondian units comprise mainly lower amphibolite to greenschist facies metavolcanics and metasediments.

Borg and Shackleton (1997) proposed that the geology of the Nyanzian and the Kavirondian units that occur in the northern half of the Tanzania Craton is distinct from the gneisses and granulites of the Dodoman Basement Complex that occur to the south and must be treated as a separate tectonic granite-greenstone domain. They subdivided the supra-crustal units in this part of the craton into six individual greenstone belts (Fig. 1.1) of which the Sukumaland Greenstone Belt is the largest. This interpretation was later confirmed when the first U-Pb zircon dating (Borg and Krogh, 1999) was performed on different units from the Sukumaland Greenstone Belt and it became evident that the gneisses and the migmatites, previously considered basement units, were in part younger that the overlying volcanics and sediments.

Subsequent, more extensive U-Pb zircon dating (Manya et al., 2006; Chamberlain and Tosdal, 2007; Mtoro et al., 2009; Kabete et al., 2012b; Sanislav et al., 2014) revealed that in

the northern half of the Tanzania Craton it is common for the 'basement' the gneiss, granite intrusions and felsic volcanics incorporated in the greenstone sequence to yield ages that are younger than or similar to the ages obtained from the mafic metavolcanics (dated at ~ 2820 Ma; Manya and Maboko, 2003; Manya and Maboko, 2008; Cook et al., 2015), attributed to the lower Nyanzian units. Following these new findings, the greenstone belts were interpreted to have formed in arc-like settings (e.g Manya and Maboko, 2003; Manya and Maboko, 2008; Mtoro et al., 2009; Mshiu and Maboko, 2012), to represent lateral accretion of exotic terranes (Kabete et al., 2012a) or to be reminiscent of oceanic plateaus (Cook et al., 2015). Thus, different parts of the northern half of the Tanzania Craton record specific geological histories. Manya et al. (2006) proposed that is unlikely that all the greenstone belts in the Tanzania Craton belong to the Nyanzian Supergroup and the geology of each greenstone belt should be treated individually.

Moreover, each of the six greenstone belts (Fig. 1.1) shows a highly fragmented map pattern. For example, the SGB is made of at least 15 individual greenstone fragments. It is unclear how much of this fragmentation is tectonic in nature, related to the intrusion of plutons or just a consequence of poor outcrop exposure. The lack of detailed studies on most of the greenstone fragments makes it difficult to assess whether they share a common geological history or not. The Geita Greenstone Belt (GGB; Fig. 1.2; Sanislav et al., 2014) is one of the largest and the best studied greenstone fragment that occurs within the SGB. It contains stratigraphic elements that can be related to the original description (e.g. Stockley, 1936; Quennel et al., 1956; Harpum, 1970) of the Nyanzian and the Kavirondian successions; a lower mafic unit, overlain by intercalations of shales, ironstones, sandstones, siltstones, mudstones and volcanoclastics which are unconformably overlain by quartzitic conglomerates and grits (Sanislav et al., 2015; Cook et al., 2015). In this contribution, we present U-Pb zircon ages and Hf isotope data from tuffaceous sediments, granodiorite dykes

and intrusions from the GGB and discuss their significance in terms of field relationships, timing of gold mineralization, implications for the stratigraphic relationships and for the crustal growth in the Tanzania Craton. For background to the general geology of the Tanzania Craton and geological setting of the Geita Greenstone Belt I refer to the introduction in Chapter 1.

5.3. PREVIOUS GEOCHRONOLOGY IN THE SUKUMALAND GREENSTONE BELT

The oldest reported zircon ages from the Sukumaland Greenstone Belt (SGB) are from pyroclastic tuffs and range in age from 2821 Ma to 2770 Ma (Table 1.1; Borg and Krogh, 1999; Chamberlain and Tosdal, 2007). The oldest zircon age of 2821±30 Ma comes from an altered ash layer of intermediate composition derived from the Tulawaka gold deposit (Chamberlain and Tosdal, 2007), which is located approximately 50 km southwest of Geita. From the southern part of the SGB, near Kahama, Borg and Krogh (1999) reported zircon ages of 2808±3 Ma and 2780±Ma from pyroclastic tuffs of rhyolitic composition. Similar zircon ages of 2779±13 Ma and 2770±9 Ma (Chamberlain and Tosdal, 2007) from pyroclastic tuffs of rhyolitic composition were reported from the Nyanzaga area about 100 km east of Geita. From the Nyamullima Terrain in the western part of the GGB a tuff layer interbedded with banded ironstones was dated at 2771±15 Ma (Chamberlain and Tosdal., 2007). The next oldest set of zircon ages was obtained from suites of intrusive rocks of dioritic and tonalitic composition that range in age between 2765 Ma and 2738 Ma (Chamberlain and Tosdal, 2007). The oldest age at 2765±25 Ma comes from a tonalite intrusion near Kahama. The remaining ages come mostly from the Lubando and Imweru areas, west of Geita, where diorite to gabbro-diorite intrusions that were emplaced into the

mafic volcanics yield ages ranging between 2758 and 2743 Ma. From the GGB two identical tonalite ages of ~ 2738 Ma are reported by Chamberlain and Tosdal (2007). One of the tonalites intruded the Kiziba Formation in the southern part of the greenstone belt while the other one intruded into the Nyamullilima Terrain. Field observations indicate that the former is strongly deformed; the latter tonalite intrusion could not be identified in the field.

From Bulyanhulu a pyroclastic felsic tuff was dated at 2719±16 Ma and interpreted to indicate a maximum age for volcanic activity in the area while a felsic porphyry dyke dated at 2710±10 Ma was interpreted to indicate the minimum age for the volcanism (Chamberlain and Tosdal, 2007). At Geita Hill a monzodiorite that cuts the ironstones at a low angle and locally follows the stratigraphy was dated at 2699±9 Ma and interpreted to constrain the age of deposition of the ironstones to before 2700 Ma (Borg and Krogh, 1999). From northwest of the Nyankanga deposit, chloritic and feldspathic sandstones contain detrital zircons which, returned homogenous ages of 2702±8 Ma, 2699±8 Ma and 2687±16 Ma (Chamberlain and Tosdal, 2007). From the Nyankanga deposit a diorite dyke was dated at 2698±14 Ma and two felsic porphyries and a lamprophyre yielded ages between 2693 and 2686 Ma (Chamberlain and Tosdal, 2007). The felsic porphyries were interpreted to represent a minimum age for volcanic activity in the area, while the mineralized lamprophyre dyke was interpreted to provide a maximum age constrain on the mineralization. The age of mineralisation has been further constrained by (Borg and Krogh, 1999) who obtained a zircon age of 2644±3 Ma for a deformed and mineralized lamprophyre dyke from the Geita Hill deposit. This age has been interpreted to provide a maximum age for the gold mineralization.

From the southern margin of the SGB, Borg and Krogh (1999) report two identical migmatitic gneiss ages of 2680 ± 3 Ma, which, showed that the gneisses that outcrop in the region do not belong to the Dodoman Supergroup and cannot form the basement to the greenstone sequence. From the same area, near Kahama, Chamberlain and Tosdal (2007)

reported a consistent granitoid age of 2680 ± 9 Ma.

Two felsic porphyry dykes that intruded near Imweru and Biharamulo, west of the GGB, were dated at 2670±21 Ma and 2667±14 Ma respectively, and were interpreted to provide an estimate for the minimum age of volcanism in the area (Chamberlain and Tosdal, 2007). From S of the GGB, near Samena Hill, and from the granites that crop out north of the GGB, Chamberlain and Tosdal (2007) reported two identical ages of 2666±8 Ma. Sanislav et al., (2014) reported a series of ages ranging from 2661±14 Ma to 2617±11 Ma from the high-K granites that crop out in the northern part of the GGB. Similar ages with the high-K granites, were reported from across the SGB, by Chamberlain and Tosdal (2007), including from the Nyankanga deposits (2653±35 Ma), the Kahama area (2656±11 Ma), Kasubuya (2653±10 Ma) and Bukoli (2646±14 Ma). A flow banded rhyolite from near Bulyanhulu dates at 2654±15 Ma and was interpreted to indicate an Upper Nyanzian sedimentation age.

5.4. NEW ZIRCON AGES FROM THE KUKULUMA TERRAIN

5.4.1. Samples and field relationships

Five samples were dated by LA-ICP-MS at the Advance Analytical Centre at James Cook University. Samples were collected from volcanoclastic sediments, intrusive units belonging to the Kukuluma Intrusive Complex (KIC) and from late-intrusive, feldspar porphyry dykes and intrusions in and around Matandani and Kukuluma pits (Fig. 5.1). The samples from the KIC contained no zircons or had a very low zircon yield and could not be dated. From five samples including a crystal tuff, three felsic porphyries and a felsic intrusion enough zircon grains were separated to obtain an age.

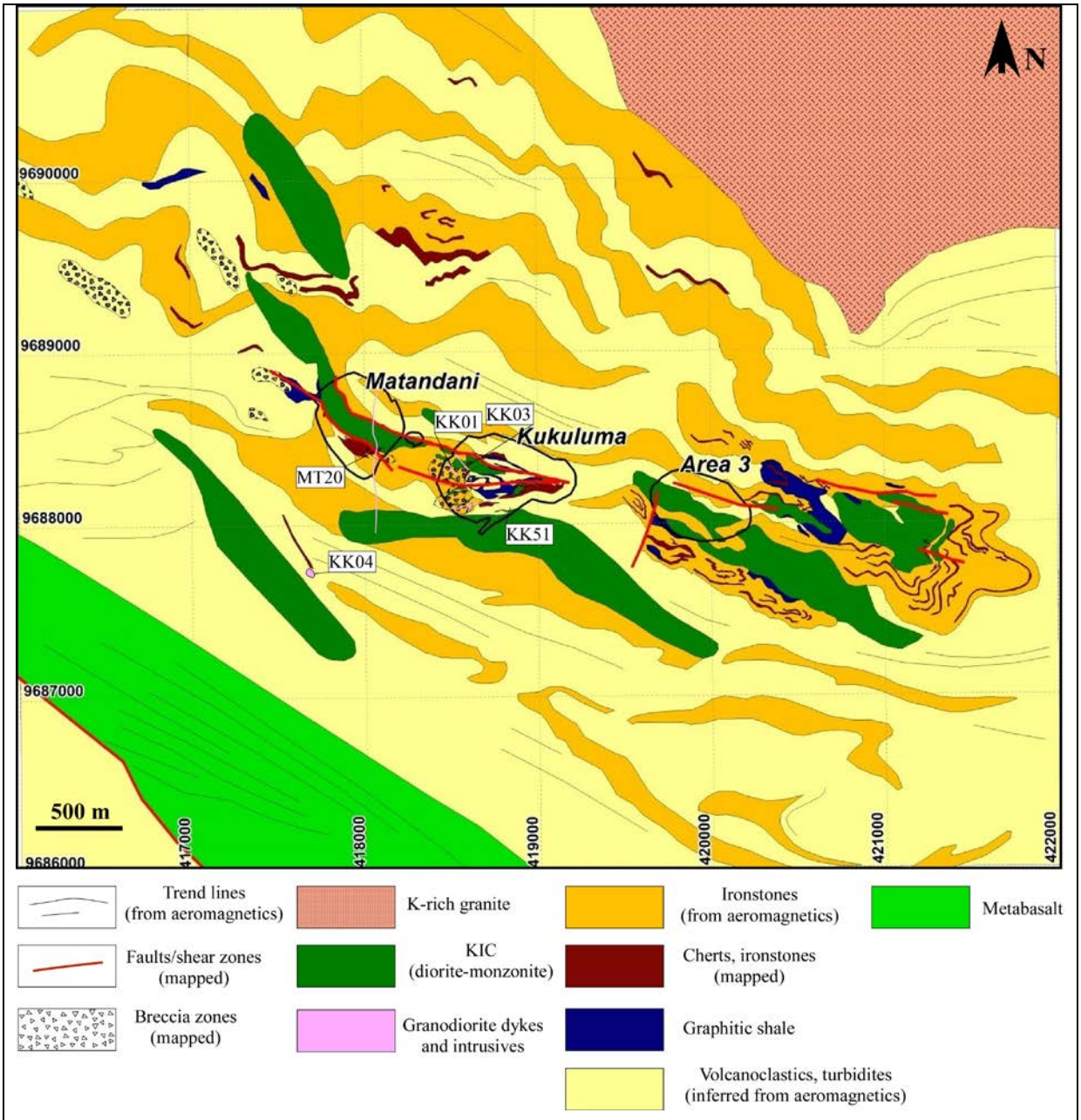

Figure 5.1. Geological map of the Kukuluma Terrain showing samples location.

5.4.1.1. Sample KK51 – crystal tuff

This sample was collected from the haul road that descends into Kukuluma pit, along the southern wall of the pit (Fig. 5.1), where a succession of well-bedded sediments intercalated with volcanoclastics is exposed. Sample KK51 was collected from a layer of crystal tuff interbedded with sandstone, siltstone and mudstone (Fig. 5.2). The sequence on

this side of the pit is dominated by tight D_3 folds with sub-vertical axial planes and shallowly plunging fold axes (for more detail see Chapter 3). This part of the stratigraphy is interpreted to represent the upper part of the Nyanzian. The crystal tuff layer is approximately 5 to 7 cm thick and contains a high amount of visible feldspar crystals that are up to 2 millimetres in diameter and are embedded in a fine-grained matrix. The feldspar phenocrysts and the matrix have been completely altered to sericite. Small quartz grains (~20%) are visible under the hand lens. No lithic fragments were identified and the layer appears to be compositionally homogenous.

5.4.2.2. Sample KK01 – granodiorite dyke.

A dyke of granodioritic composition (see Chapter 4) is approximately 1.5 metres (Fig. 5.2) wide and is well exposed in the western part of Kukuluma pit (Fig. 5.1). The dyke trends approximately northwest-southeast and cuts across D_2-D_3 fold interference patterns that are well developed in this part of the pit. The dyke also transects the hydrothermal breccia zones that developed along the margins of intrusive diorite-monzonite bodies belonging to the Kukuluma Intrusive Complex (KIC) and intrusions of the KIC itself. The dyke is exposed along the entire height of the western wall of Kukuluma pit and appears to be gently folded by open recumbent folds of D_5 origin. Although the relationship with D_4 folding is unclear; the relative age of emplacement of this dyke occurred at some point between D_3 and D_5. The dyke has been intersected in drill cores where its composition could be better assessed. It is composed of 40% quartz, 35% plagioclase, 20% k-feldspar and ~ 5% mafics (mostly hornblende), and has been classified as granodiorite. There is a visible decrease in grain size at the contact with the brecciated ironstones indicating chilled margins.

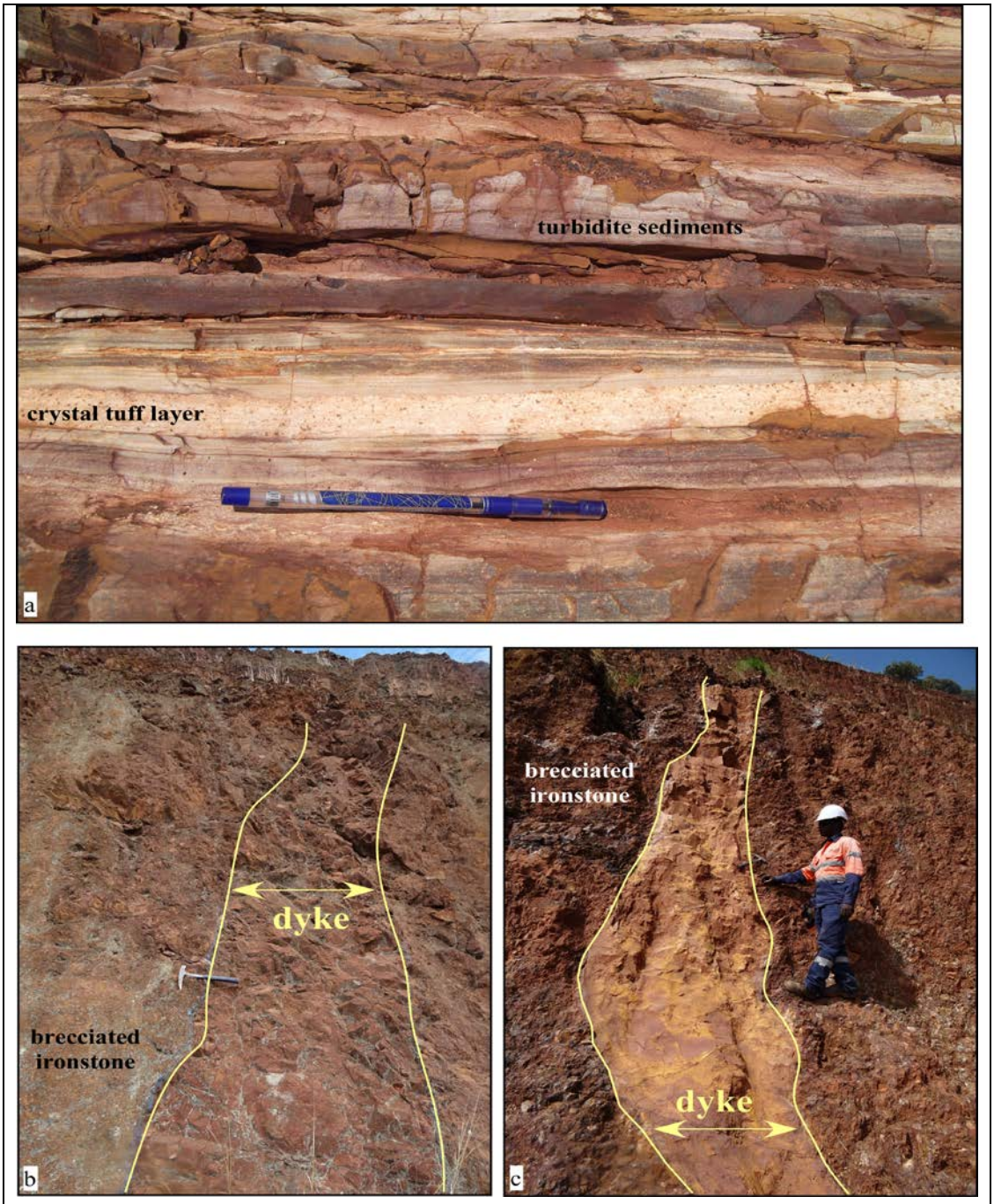

Figure 5.2. Photographs showing field relationships fro samples KK51(a) KK01 (b) KK03 (c).The crystal tuff layer (a) is interlayered with well-bedded immature sandstone, siltstone and mudstone.The dikes are weathered but the massive igneous texture is well preserved. These dikes cut across folded and brecciated ironstones.

5.4.2.3. Sample KK03 – granodiorite dyke.

A second dyke of granodioritic composition is well exposed along the W wall of

Kukuluma pit (Fig. 5.1). It is about 1 metre thick (Fig. 5.2c) and trends approximately northwest-southeast. The dyke is porphyritic and highly weathered, but altered feldspar and mafic phenocrysts (hornblende) can still be identified. In fresh drill core its mineralogical composition is near-identical to KK01 above, but it lacks chilled margins. The dyke transects D_3 folds, hydrothermal breccia zones and the KIC, and the dyke has been displaced by D_6 shear zones that run along the margins of the KIC. It's relative time of emplacement is therefore similar to KK01.

5.4.2.4. Sample KK04 –granodiorite intrusion.

A small granodiorite intrusion (Fig. 5.1) crops out in a road cutting along the Kukuluma access road (Fig. 5.3). In this outcrop, well layered sediments intruded by diorite dykes and sills are affected by D_3 and D_4 folds. A penetrative S_3 cleavage is preserved in mudstones and the diorite sills. The granodiorite intrusion is massive and cuts across the layering and the quartz-diorite dykes, but it was affected by a D_6 shear zone which developed along its contact; i.e. the timing of emplacement of this granodiorite body is similar to the timing of the granodiorite dykes described above. The granodiorite is coarse grained, equigranular and is composed of quartz (30-40%), plagioclase (30-40%), k-feldspar (20-30%) and mafics (less than 10%).

5.4.2.5. Sample MT20 – granodiorite dyke.

A granodiorite dyke cuts across the Matandani deposit along a north-south trend, and the dyke can be traced outside the pit to the Kukuluma access road 300m to the south (Fig. 5.1). The dyke is up to 3 metres thick (Fig. 5.4), grey in colour and partly weathered. It contains large plagioclase phenocrysts (~40%), small quartz grains (~30%), altered fine

grained k-feldspar (~25%) and a small amount of altered biotite (~5 %). In fresh samples collected from drill core minor sulfide and iron oxide can also be seen.

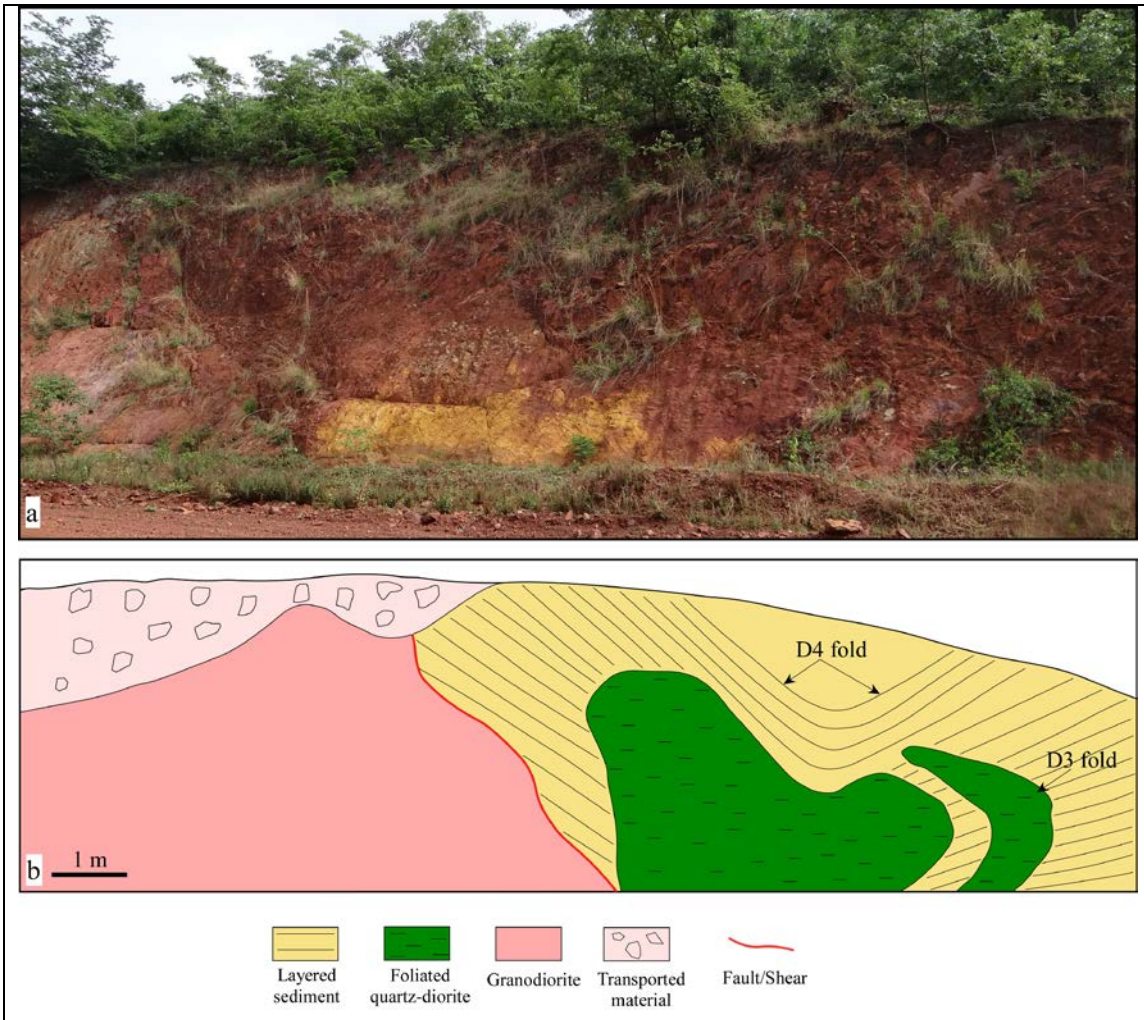

Figure 5.3. Photograph and outcrop sketch showing the field relationships for sample KK04.

In the pit the dyke cuts across the D_2-D_3 interference fold pattern and has not been affected by D_4 and D_5 folding. It cuts the diorite – monzonite suite as part of the KIC and the tectonic breccias found on in the SW corner of the pit. Along the Eastern diorite-Ironstone contact, both the dyke and the ironstone ± other sediments are locally (~3m thick zone of shearing) overprinted by the D_6 shear zone (Figs A4.1a and 1.3b). Within this sheared zone, the groundmass and the plagioclase phenocrysts display are clear preferential orientation

parallel to the orientation of the D_6-shear zone. However, a number of the fractures are identified within the ironstones and few in the granodiriote dike, which attributed to D_7 reactivations along the D_6 shear zone. These fractures did not accommodate visible displacement of the dyke, but this sheared part of the dyke does contain low grade mineralization. The relative timing of emplacement of this dyke therefore occurred prior to D_6 and D_7.

Figure 5.4. Photograph showing the field relationship for sample MT20. This dyke cuts across tight D2-D3 folds, the KIC and overprinted by the D6 shear zones.

5.5. RESULTS

5.5.1. Geochronology

5.5.1.1. Sample KK51-crystal tuff

Nine of the zircon grains analysed from sample KK-51 yielded analyses with 10% or less discordance (Table 5.1). The zircon grains are euhedral in shape, luminescent and have

concentric zoning without any evidence of relict cores or rim overgrowths (Fig. 5.5). All zircon grains from this sample show similar cathodoluminescence images suggesting a population derived from the same volcanic source.

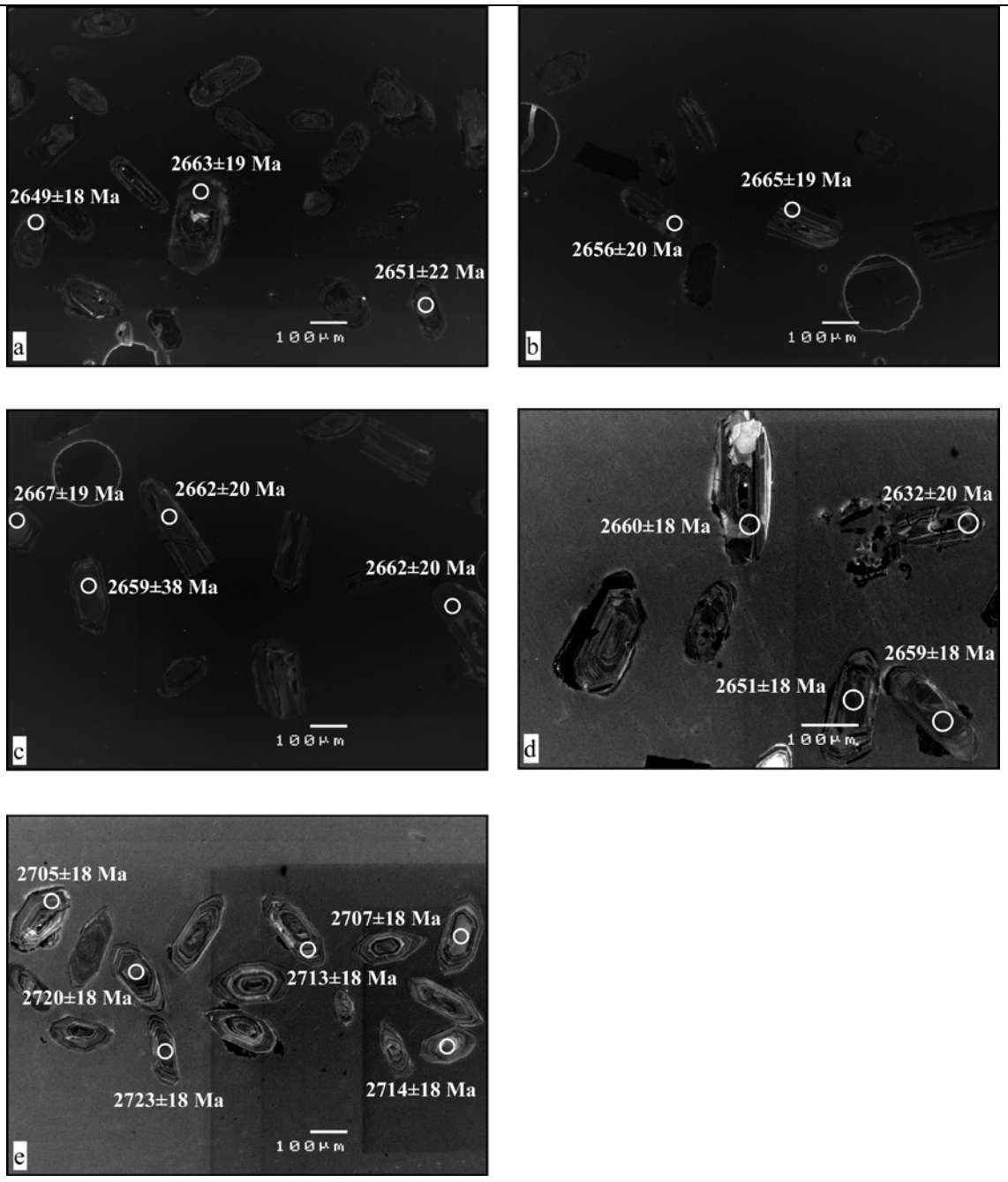

Figure 5.5. Cathodoluminescence images of zircon grains from sample KK51 (a), KK01 (b), KK03 (c), KK04 (d) and MT20 (e).

Analysis	$^{238}U/^{206}Pb$	Error (1σ)	$^{207}Pb/^{206}Pb$	Error (1σ)	$^{207}Pb/^{235}U$	Error (1σ)	$^{206}Pb/^{238}U$	Error (1σ)	Rho	Age (Ma) $^{207}Pb/^{206}Pb$	Error (1σ)	Age (Ma) $^{206}Pb/^{238}U$	Error (1σ)	Discordance (%)
KK51-01	1.824	0.018	0.186	0.002	14.042	0.149	0.548	0.005	0.94	2705	18	2818	23	-4
KK51-02	2.168	0.022	0.187	0.002	11.876	0.125	0.461	0.005	0.95	2713	18	2445	20	10
KK51-03	1.863	0.019	0.187	0.002	13.818	0.146	0.537	0.005	0.94	2713	18	2770	22	-2
KK51-04	1.886	0.019	0.186	0.002	13.594	0.144	0.53	0.005	0.94	2707	18	2743	22	-1
KK51-05	2.166	0.021	0.187	0.002	11.915	0.125	0.462	0.004	0.93	2718	18	2447	20	10
KK51-09	2.146	0.021	0.188	0.002	12.063	0.125	0.466	0.004	0.93	2723	18	2466	20	9
KK51-06	2.089	0.021	0.187	0.002	12.371	0.13	0.479	0.005	0.94	2720	18	2522	21	7
KK51-07	2.069	0.02	0.19	0.002	12.656	0.133	0.483	0.005	0.92	2742	18	2542	20	7
KK51-08	1.837	0.018	0.187	0.002	14.023	0.145	0.545	0.005	0.94	2714	18	2802	22	-3

Table 5.1. Analytical results and calculated ages for sample KK51.

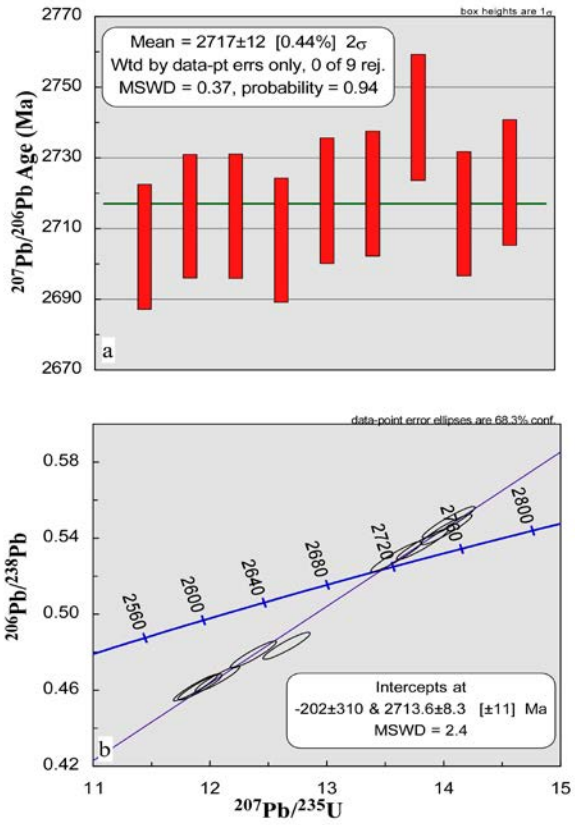

Figure 5.6. Diagrams showing the $^{207}Pb/^{206}Pb$ weighted average age (a) and the concordia age (b) for sample KK51.

The $^{207}Pb/^{206}Pb$ ages vary from 2742±18 Ma to 2705±18 Ma with a weighted average age of 2717±12 Ma (Fig. 5.6a). These ages are similar within error and can be considered to belong to the same age population. The upper concordia age for these zircon grains is 2714±8 Ma (Fig. 5.6b) which is similar within error to the weighted average $^{207}Pb/^{206}Pb$ age.

5.5.1.2. Sample KK01-granodiorite dyke

This sample contained many zircon grains of different shapes and sizes, and only nine zircon grains returned nearly concordant analyses (≤6% discordance; Table 5.2). The zircon grains have low luminescence and some grains contain relict cores with a rim overgrowth

(Fig. 5.5). In most cases the relict cores have very low luminescence and are surrounded by a thin line with high luminescence which separates the cores from a rim overgrowth. The relict cores contain high common lead and no reliable age could be calculated while the rim overgrowths were in most situations too thin to be analysed by laser ablation except one grain that contained a rim overgrowth large enough to be analysed (Fig. 5.5).

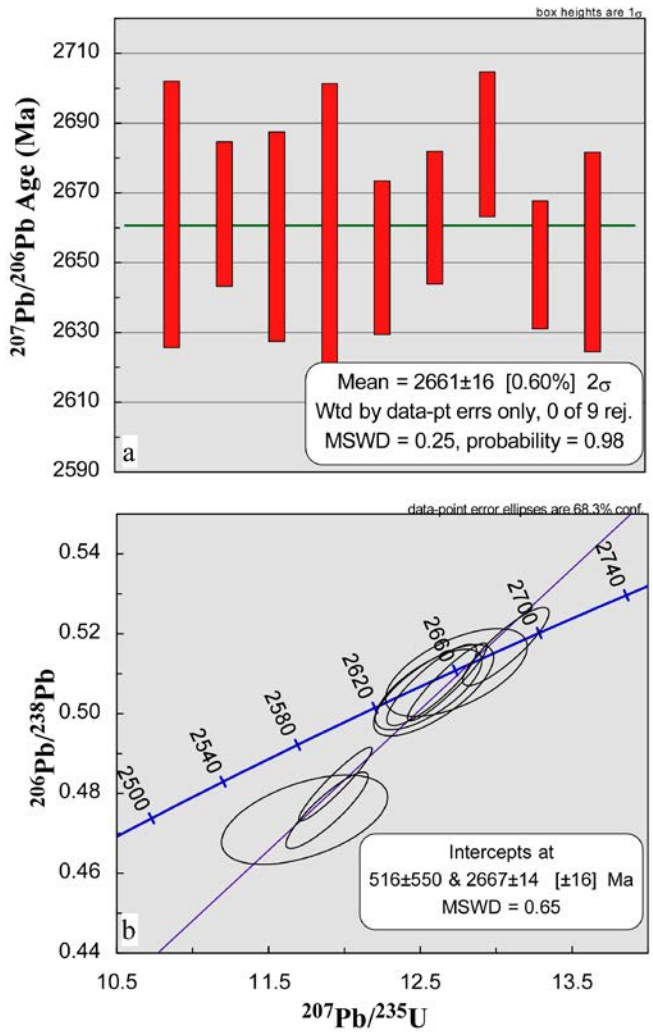

Figure 5.7. Diagrams showing the 207Pb/206Pb weighted average age (a) and the concordia age (b) for sample KK01.

This rim overgrowth returned a nearly concordant analysis with a $^{207}Pb/^{206}Pb$ age of 2663±19 Ma. The remaining analyses were performed on zircon grains with low luminescence having a faint concentric zoning with no evidence of relict cores or rim overgrowths. Their $^{207}Pb/^{206}Pb$ ages vary between 2684±21 Ma and 2649±18 Ma. The $^{207}Pb/^{206}Pb$ weighted average age for all nine analyses is 2661±16 Ma (Fig. 5.7a) which is similar within error to the concordia age of 2667±14 Ma (Fig. 5.7b).

Analysis	$^{238}U/^{206}Pb$	Error (1σ)	$^{207}Pb/^{206}Pb$	Error (1σ)	$^{207}Pb/^{235}U$	Error (1σ)	$^{206}Pb/^{238}U$	Error (1σ)	Rho	Age (Ma) $^{207}Pb/^{206}Pb$	Error (1σ)	Age (Ma) $^{206}Pb/^{238}U$	Error (1σ)	Discordance (%)
KK01-01	1.960	0.028	0.181	0.004	12.738	0.308	0.510	0.007	0.59	2664	38	2658	31	0
KK01-02	2.102	0.028	0.181	0.002	11.886	0.179	0.476	0.006	0.88	2664	21	2509	28	6
KK01-03	1.977	0.030	0.180	0.003	12.588	0.261	0.506	0.008	0.72	2657	30	2639	32	1
KK01-04	2.112	0.033	0.180	0.006	11.738	0.361	0.473	0.007	0.51	2651	50	2499	32	6
KK01-05	1.972	0.026	0.180	0.002	12.576	0.196	0.507	0.007	0.85	2651	22	2645	29	0
KK01-06	1.969	0.025	0.181	0.002	12.678	0.173	0.508	0.006	0.93	2663	19	2648	27	1
KK01-07	1.935	0.024	0.183	0.002	13.064	0.187	0.517	0.006	0.87	2684	21	2686	27	0
KK01-08	2.073	0.026	0.180	0.002	11.941	0.159	0.482	0.006	0.95	2649	18	2538	26	4
KK01-09	1.976	0.026	0.180	0.003	12.554	0.232	0.506	0.007	0.71	2653	29	2640	29	1

Table 5.2. Table showing the analytical results and the calculated ages for sample KK01

5.5.1.3. Sample KK03-granodiorite dyke

This sample had a low zircon yield, with only ten zircon grains separated. However, six grains returned nearly concordant (≤6% discordance; Table 5.3) analyses so that age calculations could be performed. The zircon grains vary in shape from short and stubby to elongated grains, and they have low luminescence with a vague concentric zoning (Fig. 5.5). No relict cores or rim overgrowths were observed. The $^{207}Pb/^{206}Pb$ age of the nearly concordant zircon grains varies between 2687±19 Ma and 2656±20 Ma with an average weighted age of 2667±17 Ma (Fig. 5.8a). The concordia upper intercept age for this sample is 2658±15 Ma (Fig. 5.8b).

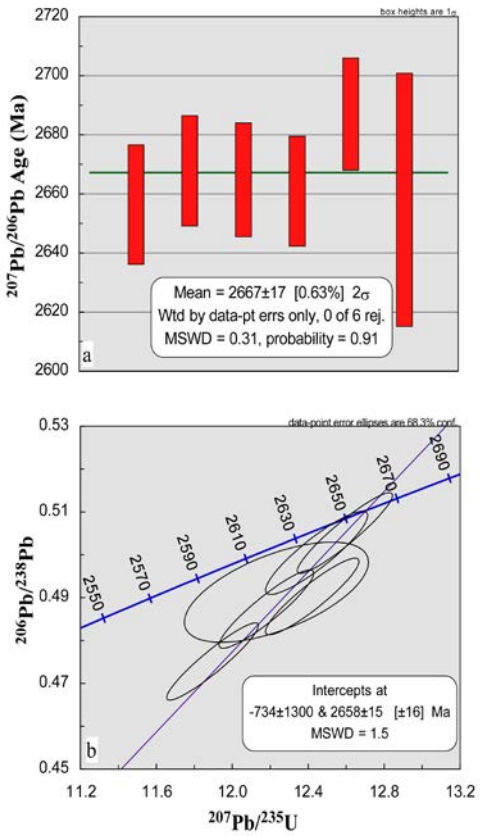

Figure 5.8. Diagrams showing the 207Pb/206Pb weighted average age (a) and the concordia age (b) for sample KK03.

Analysis	^{238}U/^{206}Pb	Error (1σ)	^{207}Pb/^{206}Pb	Error (1σ)	^{207}Pb/^{235}U	Error (1σ)	^{206}Pb/^{238}U	Error (1σ)	Rho	Age (Ma) ^{207}Pb/^{206}Pb	Error (1σ)	Age (Ma) ^{206}Pb/^{238}U	Error (1σ)	Discordance (%)
KK03-01	1.998	0.026	0.180	0.002	12.444	0.178	0.500	0.006	0.90	2656	20	2616	27	2
KK03-02	2.105	0.026	0.182	0.002	11.896	0.159	0.475	0.006	0.93	2668	19	2506	26	6
KK03-03	2.052	0.025	0.181	0.002	12.179	0.164	0.487	0.006	0.92	2665	19	2559	26	4
KK03-04	1.980	0.024	0.181	0.002	12.593	0.166	0.505	0.006	0.93	2661	19	2636	27	1
KK03-05	2.040	0.025	0.184	0.002	12.421	0.163	0.490	0.006	0.92	2687	19	2572	25	4
KK03-06	2.036	0.032	0.181	0.005	12.232	0.320	0.491	0.008	0.60	2658	43	2576	33	3

Table 5.3. Table showing the analytical results and the calculated ages for sample KK03.

5.5.1.4. Sample KK04-granodiorite intrusion

Sample KK04 had a very good zircon yield so that a large number of zircon grains could be analysed (Table 5.4).

Analysis	$^{238}U/^{206}Pb$	Error (1σ)	$^{207}Pb/^{206}Pb$	Error (1σ)	$^{207}Pb/^{235}U$	Error (1σ)	$^{206}Pb/^{238}U$	Error (1σ)	Rho	Age (Ma) $^{207}Pb/^{206}Pb$	Error (1σ)	Age (Ma) $^{206}Pb/^{238}U$	Error (1σ)	Discordance (%)
KK04-01	1.926	0.023	0.179	0.002	12.843	0.168	0.519	0.006	0.926	2648	19	2696	27	-2
KK04-02	1.928	0.023	0.182	0.002	13.015	0.169	0.519	0.006	0.935	2671	19	2694	27	-1
KK04-03	1.997	0.024	0.180	0.002	12.424	0.163	0.501	0.006	0.927	2653	19	2617	26	1
KK04-04	1.959	0.023	0.181	0.002	12.768	0.165	0.510	0.006	0.920	2666	19	2658	26	0
KK04-05	2.152	0.031	0.180	0.005	11.495	0.295	0.465	0.007	0.553	2651	42	2460	29	7
KK04-06	1.948	0.026	0.182	0.002	12.878	0.193	0.513	0.007	0.880	2672	21	2671	29	0
KK04-07	1.941	0.024	0.182	0.002	12.895	0.170	0.515	0.006	0.922	2667	19	2679	27	0
KK04-08	1.954	0.025	0.181	0.003	12.774	0.197	0.512	0.007	0.835	2664	23	2664	28	0
KK04-09	1.956	0.025	0.181	0.002	12.739	0.193	0.511	0.007	0.850	2661	22	2662	28	0
KK04-10	1.984	0.025	0.181	0.003	12.567	0.194	0.504	0.006	0.801	2661	24	2631	27	1
KK04-11	2.095	0.025	0.181	0.002	11.918	0.158	0.477	0.006	0.899	2662	20	2516	25	5
KK04-12	2.083	0.027	0.181	0.003	11.971	0.224	0.480	0.006	0.683	2661	30	2528	27	5
KK04-13	2.130	0.029	0.181	0.004	11.701	0.272	0.469	0.006	0.589	2659	38	2481	28	7
KK04-14	2.039	0.025	0.182	0.002	12.270	0.160	0.490	0.006	0.927	2667	19	2572	26	4
KK04-15	2.031	0.027	0.181	0.003	12.284	0.197	0.492	0.006	0.823	2663	24	2581	28	3
KK04-16	2.211	0.032	0.182	0.003	11.319	0.213	0.452	0.007	0.774	2668	28	2405	29	10

Table 5.4. Table showing the analytical results and the calculated ages for sample KK04.

The zircon grains are euhedral to subhedral and vary in shape from elongated needle-like grains to short and stubby grains. They are low luminescence with a vague concentric zoning (Fig. 5.5). A few grains contain small relict cores with very low luminescence surrounded by an overgrowth rim. These cores were too small to be analysed. One rim overgrowth analyses returned a $^{207}Pb/^{206}Pb$ age of 2662±20 Ma. The remaining analyses returned $^{207}Pb/^{206}Pb$ ages between 2671±21 Ma and 2648±19 Ma with a weighted average age of 2663±11 Ma (Fig. 5.9a) and an almost identical upper concordia intercept age of 2662±9 Ma (Fig. 5.9b).

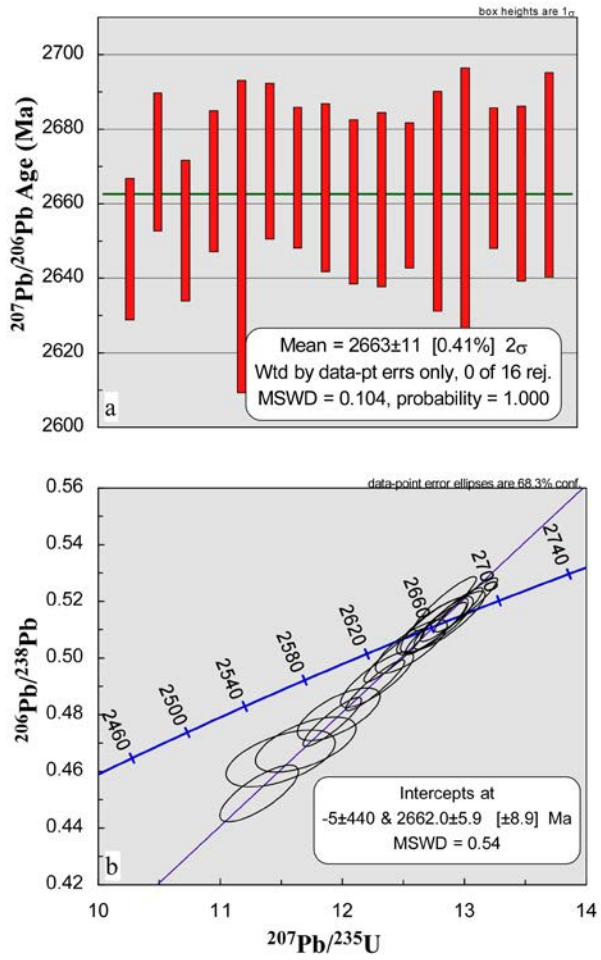

Figure 5.9. Diagrams showing the $^{207}Pb/^{206}Pb$ weighted average age (a) and the concordia age (b) for sample KK04.

5.5.1.5. Sample MT20-granodiorite dyke

Seven of the zircon grains analysed from these samples returned nearly concordant ages (≤5% discordance; Table 5.5). The zircon grains are euhedral with a prismatic shape and medium luminescence. Most zircon grains show a well-developed concentric zoning but several grains have more complex luminescence patterns (Fig. 5.5). Although, a few zircon grains contained evidence of relict cores they were too small to be dated. The $^{207}Pb/^{206}Pb$ ages of the zircon grains vary between 2660±19 Ma and 2632±20 Ma with a weighted average age

of 2651±14 Ma (Fig. 5.10a) and an almost identical upper concordia age of 2650±8 Ma (Fig. 5.10b).

Analysis	$^{238}U/^{206}Pb$	Error (1σ)	$^{207}Pb/^{206}Pb$	Error (1σ)	$^{207}Pb/^{235}U$	Error (1σ)	$^{206}Pb/^{238}U$	Error (1σ)	Rho	Age (Ma) $^{207}Pb/^{206}Pb$	Error (1σ)	Age (Ma) $^{206}Pb/^{238}U$	Error (1σ)	Discordance (%)
MT20-01	1.845	0.018	0.180	0.002	13.454	0.158	0.542	0.005	0.84	2654	20	2791	22	-5
MT20-02	1.884	0.019	0.180	0.002	13.161	0.146	0.531	0.005	0.90	2651	19	2745	22	-4
MT20-03	2.011	0.021	0.178	0.002	12.195	0.144	0.497	0.005	0.86	2632	20	2602	22	1
MT20-04	1.981	0.019	0.181	0.002	12.575	0.130	0.505	0.005	0.92	2660	18	2634	21	1
MT20-05	1.893	0.018	0.181	0.002	13.159	0.133	0.528	0.005	0.93	2659	18	2735	21	-3
MT20-06	1.855	0.018	0.180	0.002	13.364	0.136	0.539	0.005	0.93	2651	18	2780	22	-5
MT20-07	2.004	0.019	0.179	0.002	12.323	0.144	0.499	0.005	0.83	2645	20	2610	21	1

Table 5.5. Table showing the analytical results and the calculated ages for sample MT20.

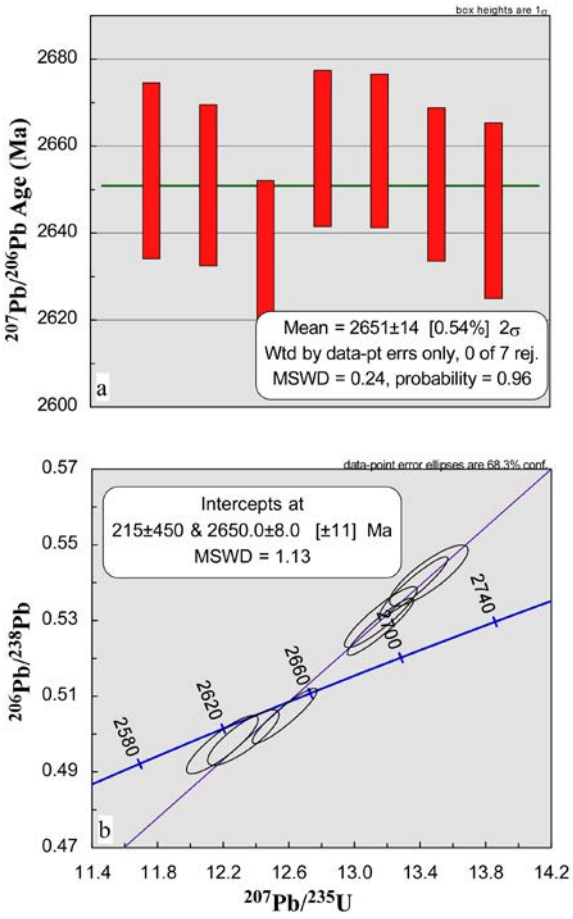

Figure 5.10. Diagrams showing the $^{207}Pb/^{206}Pb$ weighted average age (a) and the concordia age (b) for sample MT20.

5.5.2. Lu-Hf zircon results

Hafnium isotope data is presented in Table 5.6 and Figure 5.11. All analysed zircon grains have very low $^{176}Lu/^{177}Hf$ ratios, ranging from 0.00029 to 0.00233, suggesting that following the time of zircon crystallization the $^{176}Hf/^{177}Hf$ ratio of zircon changed little, but the εHf values changed significantly due to the increase of the chondritic $^{176}Hf/^{177}Hf$ ratio over time. The zircon grains from the granodiorite samples have similar Hf isotope compositions with nearly chondritic $^{176}Hf/^{177}Hf_i$ ratios (Fig. 5.11a) and small εHf variations (Fig. 5.11b). Sample KK01 shows 4 epsilon units variation, sample KK03 shows 2.2 epsilon units variation, sample KK04 shows only 1 epsilon unit variation and sample MT20 shows 1.4 epsilon units variation between different grains.

Analyses	$^{176}Lu/^{177}Hf$	1 σ	$^{176}Hf/^{177}Hf$	1 σ	$^{176}Hf/^{177}Hf_i$	2 σ	εHf_0	εHf_i	2 σ
				KK01					
KK01-01	0.000629	0.000031	0.280993	0.000022	0.280961	0.000022	-63.4	-4.0	0.8
KK01-02	0.000850	0.000035	0.281082	0.000010	0.281039	0.000010	-60.2	-1.2	0.3
KK01-03	0.001280	0.000015	0.281080	0.000017	0.281015	0.000017	-60.3	-2.1	0.6
KK01-04	0.000932	0.000013	0.281096	0.000007	0.281048	0.000007	-59.7	-0.9	0.3
KK01-05	0.000294	0.000003	0.281080	0.000007	0.281065	0.000007	-60.3	-0.3	0.2
KK01-06	0.000363	0.000003	0.281091	0.000007	0.281073	0.000007	-59.9	0.0	0.2
KK01-07	0.000687	0.000008	0.281066	0.000010	0.281031	0.000010	-60.8	-1.5	0.4
KK01-08	0.001858	0.000076	0.281105	0.000012	0.281011	0.000012	-59.4	-2.2	0.4
				KK03					
KK03-1	0.000527	0.000002	0.281091	0.000008	0.281065	0.000008	-59.9	-0.4	0.3
KK03-2	0.000373	0.000004	0.281083	0.000009	0.281064	0.000009	-60.2	-0.4	0.3
KK03-3	0.000469	0.000007	0.281064	0.000010	0.281040	0.000010	-60.9	-1.3	0.3
KK03-4	0.001171	0.000025	0.281085	0.000017	0.281025	0.000017	-60.1	-1.8	0.6
KK03-5	0.001248	0.000029	0.281067	0.000041	0.281004	0.000041	-60.7	-2.6	1.5
				KK04					

KK04-1	0.000397	0.000013	0.281062	0.000007	0.281042	0.000007	-60.9	-1.1	0.3
KK04-2	0.001456	0.000028	0.281125	0.000011	0.281051	0.000011	-58.7	-0.8	0.4
KK04-3	0.001469	0.000042	0.281124	0.000012	0.281049	0.000012	-58.7	-0.8	0.4
KK04-4	0.000824	0.000015	0.281107	0.000010	0.281065	0.000010	-59.3	-0.3	0.4
KK04-5	0.000581	0.000018	0.281079	0.000008	0.281049	0.000008	-60.3	-0.8	0.3
KK04-6	0.000543	0.000004	0.281070	0.000008	0.281043	0.000008	-60.6	-1.0	0.3
KK04-7	0.000871	0.000011	0.281126	0.000008	0.281081	0.000008	-58.7	0.3	0.3
KK04-8	0.000850	0.000006	0.281113	0.000009	0.281070	0.000009	-59.1	-0.1	0.3
KK04-9	0.000850	0.000006	0.281113	0.000009	0.281070	0.000009	-59.1	-0.1	0.3
				MT20					
MT20-1	0.000468	0.000018	0.281093	0.000009	0.281069	0.000009	-59.8	-0.4	0.3
MT20-2	0.002329	0.000062	0.281197	0.000016	0.281079	0.000016	-56.2	0.0	0.6
MT20-3	0.001047	0.000020	0.281148	0.000011	0.281095	0.000011	-57.9	0.5	0.4
MT20-4	0.001183	0.000021	0.281132	0.000013	0.281072	0.000013	-58.5	-0.3	0.5
MT20-5	0.000452	0.000002	0.281095	0.000007	0.281072	0.000007	-59.8	-0.3	0.2
MT20-6	0.000857	0.000010	0.281098	0.000009	0.281055	0.000009	-59.7	-0.9	0.3
MT20-7	0.000644	0.000006	0.281101	0.000009	0.281068	0.000009	-59.5	-0.4	0.3
				KK51					
KK51-1	0.000914	0.000012	0.281130	0.000009	0.281083	0.000009	-58.5	1.6	0.3
KK51-2	0.000970	0.000005	0.281161	0.000008	0.281111	0.000008	-57.4	2.6	0.3
KK51-3	0.001115	0.000009	0.281153	0.000009	0.281095	0.000009	-57.7	2.1	0.3
KK51-4	0.001076	0.000013	0.281147	0.000010	0.281091	0.000010	-57.9	1.9	0.4
KK51-5	0.000448	0.000009	0.281126	0.000008	0.281103	0.000008	-58.7	2.4	0.3
KK51-6	0.000805	0.000005	0.281136	0.000010	0.281094	0.000010	-58.3	2.0	0.4
KK51-7	0.000840	0.000007	0.281140	0.000007	0.281096	0.000007	-58.2	2.1	0.2

Table 5.6. Table showing the Hf isotope data for the zircon grains analysed in this study.

Overall, the granodiorite samples have a uniform Hf isotope composition with mean $^{176}Hf/^{177}Hf$ ratios of between 0.28107 and 0.28103, and mean εHf values that range from -0.3 to -1.5. The larger spread in Hf isotope composition and the lower εHf values observed in sample KK01could be attributed to the presence of relict cores and possibly to some degree

of crustal contamination experienced by this sample.

The zircon grains separated from the crystal tuff sample have suprachondritic $^{176}Hf/^{177}Hf_i$ ratios and positive εHf values. This sample also shows very limited variation in Hf isotope compositions between different grains with a maximum of one epsilon unit difference between analyses.

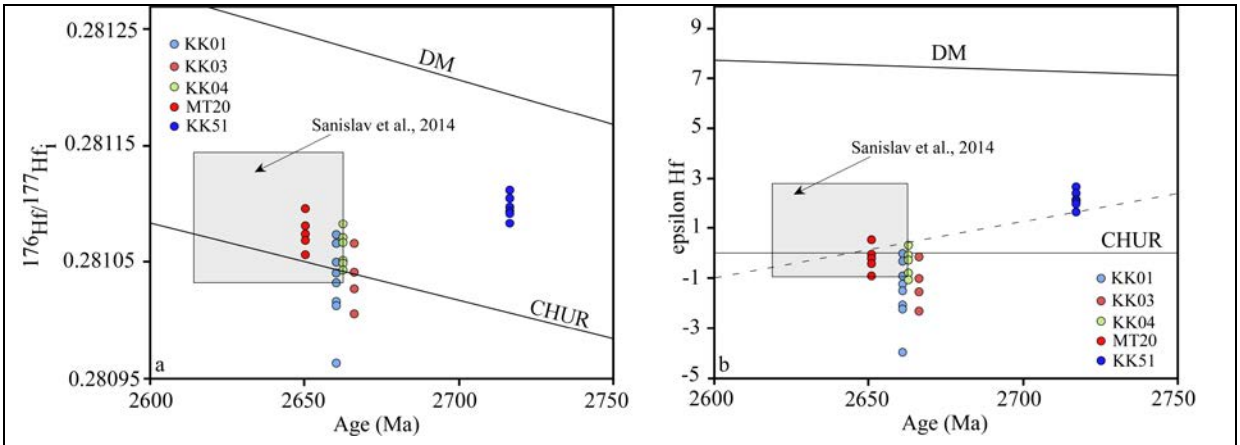

Figure 5.11. Diagrams showing the initial 176Hf/177Hf ratios (a) and the εHf values (b) vs. the 207Pb/206Pb age of the zircon grains analysed in this study. The shaded areas show the range in Hf isotopic composition for the 2660-2620 Ma high-K granites (Sanislav et al., 2014).

5.6. DISCUSSION

5.6.1. Implications for the deformation history

The Kukuluma Terrain and the Central Terrain share a similar deformation history suggesting that the entire GGB was deformed during the same period. The 2717±12 Ma crystal tuff layer from the Kukuluma pit is interbedded and deformed together with the turbiditic sediments and the ironstones. At the Geita Hill pit in the Central Terrain a trachyandesite dyke dated by Borg and Korgh (1999) at 2699±9 Ma was interpreted by Sanislav et al. (2015) to be one of the monzodiorite dykes that intruded and was folded during D_2 and/or D_3 events. The intrusion of the KIC is most likely synchronous with the

intrusion of the diorite dykes in the Central Terrain since both the KIC and the diorite dykes are affected by the D_3 deformation. The granodiorite dykes (samples KK01 and KK03) from the Kukuluma pit and the small granodiorite intrusion (sample KK04) along the Kukuluma access road were emplaced around 2660 Ma.

The 2662±6 Ma granodiorite (KK04) intrusion found along the Kukuluma access road cuts across the D_4 fold hinges, the 2661±16 Ma (KK01) granodiorite dyke from the western wall of the Kukuluma deposit is affected by D_5 sub-horizontal folding while the 2658±15 Ma (KK03) granodiorite dyke from the same side of the deposit is affected by D_6 shearing. These field relationships suggest that the granodiorites were emplaced after D_4, possibly during D_5 and before D_6 deformation. The 2651±14 Ma granodiorite dyke from the Matandani pit (MT 20) that cuts across the diorite –ironstone contact on both the western and eastern is locally overprinted by shear fabrics. The fact that, shear fabrics cut along the intersection of diorite-ironstone contact that is cut by the dike, suggests that, the D_6-shear zone overprints the emplacement of this dike. Also, the occurrence of the shear fractures in both the ironstones and the dike might be interpreted to be associated with reactivation of the D_6-shear zone by D_7-shear zone. By comparison, the 2658±15 Ma (sample KK03) granodiorite dyke from the Kukuluma pit is clearly displaced by the D_6 shear zones.

5.6.2. Implications for the supracrustal stratigraphy

The 2717±12 Ma crystal tuff layer is interbedded with turbiditic sediments and overlies the banded ironstones. The banded ironstones and the turbiditic sediments are in general interpreted to overlie the mafic volcanics of the Kiziba Formation (e.g. Manya and Maboko, 2008; Sanislav et al., 2015; Cook et al., 2015). The whole rock Sm-Nd model ages (Manya and Maboko, 2003; Manya and Maboko, 2008; Cook et al., 2015) indicate that the mafic volcanics were erupted around 2820 Ma, thus forming the oldest identified horizon in the

stratigraphy. In the southern part of the GGB where the mafic volcanics are well exposed the contact between the mafic volcanics and the upper part of the stratigraphy is structural (Cook et al., 2015); the metamorphic grade changes from amphibolite facies to lower greenschist facies in less than fifty meters.

It is unclear whether this structural contact follows an initial unconformity thus, opening the possibility of a sedimentation gap between the eruption of the mafic volcanics and the deposition of the ironstones and the related sediments. It is even less clear whether stratigraphic horizons can be correlated across the GGB or for that purpose across the much larger SGB. For example, the ironstone horizons are the most ubiquitous units across the entire region, have the best surface exposure and a clear geophysical signature but, correlating them across the region is not a straight forward exercise. In the Central Terrain chloritic and feldspathic sandstones that overly the ironstones yielded zircon ages between 2702 and 2687 Ma (Chamberlain and Tosdal, 2007); the field relationships indicate a continuous transition from the ironstones to the sandstones suggesting that the ironstones and the sandstones belong to the same sedimentary cycle.

However, in the Nyamullima Terrain (Fig. 1.2), in the western part of the GGB, a tuff horizon interbedded with the ironstones was dated at 2771±15 Ma (Chamberlain and Tosdal, 2007; Table 1.1) indicating ironstone deposition as early as 2770 Ma. Even though, the 2717 Ma crystal tuff layer overlies the ironstones in the Kukuluma Terrain, the ironstone units are interbedded with tuffaceous sediments and show a gradual transition into turbiditic sediments interlayered with volcanoclastics suggesting a continuous sedimentation history. Thus, it is possible, the ironstones, the turbidites and the interlayered volcanoclastics form a continuous unit in the Kukuluma Terrain and possibly the Central Terrain while the ironstones from the Nyamullima Terrain belong to a separate and maybe older stratigraphic horizon. Further evidence for an older ironstone stratigraphic horizon comes from the Nyanzaga area (Fig.

1.1), east of the GGB where Chamberlain and Tosdal (2007) reported a 2779±13 Ma age for pyroclastic tuffs overlaying the ironstone units (Table 1.1). Pyroclastic flows from near Kahama, the southern part of the SGB, have ages of 2808±6 Ma and 2780±3 Ma (Borg and Krogh, 1999) respectively, also pointing towards an early period of volcanism and sedimentation. Although, the stratigraphic age relationships are poorly constrained, the few available ages point towards the possibility of basin development over a considerable timespan or towards the existence of discrete sedimentation episodes in different basins. Both scenarios require testing in the field and systematic dating of selected stratigraphic horizons.

5.6.3. Timing of gold mineralization

The gold mineralization is spatially related with the D_6 shear zones which were reactivated during D_7 as normal faults (see Chapter 3). The granodirote dike cuts across the diorite-ironstone contact at Matandani pit (MT 20). The intersection between the diorite – irosntone contact and the granodiorite dike is overprinted by the D_6-shear zone that runs along the diorite-irosntone contact. The fact that the D_6-shear zone overprints both the diorite, ironstone and the dike suggests that, the emplacement of the dike pre-dated the D_6-shear zone. In addition, gold mineralization occurs in spatial association with the D_6-shear zone that utilizes the contact between the diorite and Ironstones. In the mineralized zones, the D_6-shear zones are interpreted to be reactivated by the D_7-shear fractures occuring as fracture networks observed in both the dike and the ironstones. Therefore, the 2651±14 Ma age from the Matandani pit granodiorite dike can be used to define a maximum age for the timing of gold mineralization in the area.

The 2651±14 Ma age of this dyke is similar within error to the 2644±3 Ma age (Borg and Krogh, 1999) of the mineralized lamprophyre dyke from the Geita Hill deposit suggesting that gold mineralization in the Central Terrain and the Kukuluma Terrain may

have occurred at about the same time. The gold mineralization in the Matandani pit consists of two sub-parallel mineralisation envelopes occurring on both sides of the KIC. This dyke is overprinted by both the eastern and western mineralization envelopes. This is evidenced by the localised shearing of the granodiriote observed along the diorite –ironstone contact. It is along this sheared zone where relatively low grade gold mineralization is recorded. However, away from the sheared diorite-ironstone contact, no shear fabrics are observed within the Granodiorite dyke. This strongly suggests that, gold mineralization within this area post-dates the emplacement of the granodiorite dikes.

5.6.4. Implications for crustal growth

Four episodes of crustal growth can be recognised in the SGB based on the available zircon ages (Fig. 5.12; Table 1.1). The earliest episode is represented by the extrusion of the ~2820 Ma mafic volcanics (Manya and Maboko, 2003; Manya and Maboko, 2008; Cook et al., 2015) and the associated intermediate volcanics. This is followed between 2780 Ma and 2740 Ma (Fig. 5.12) by a period dominated by the emplacement of igneous rocks of intermediate composition. A relatively continuous period occurred between 2720 Ma and 2620 Ma, over which magmatism transitions from mainly TTG and diorite in the early stages to the more evolved high-K granites in the later stages. This prolonged period can be subdivided into a TTG dominated period (2720-2660 Ma) and a high-K granite dominated period (2660-2620 Ma). The GGB appears to comprise elements of all the periods of crustal growth with the mafic volcanics being abundant in the southern part of the greenstone belt (Cook et al., 2015), 2770 Ma tuffs occurring in the Nyamullilima Terrain (Chamberlain and Tosdal, 2007) and ~ 2700 Ma diorite and TTG occurring all over the greenstone belt (Sanislav et al., 2015; 2016). The eastern, northern and western side of the greenstone belt are dominated by the 2660 to 2620 ma high-K granites (Sanislav et al., 2014).

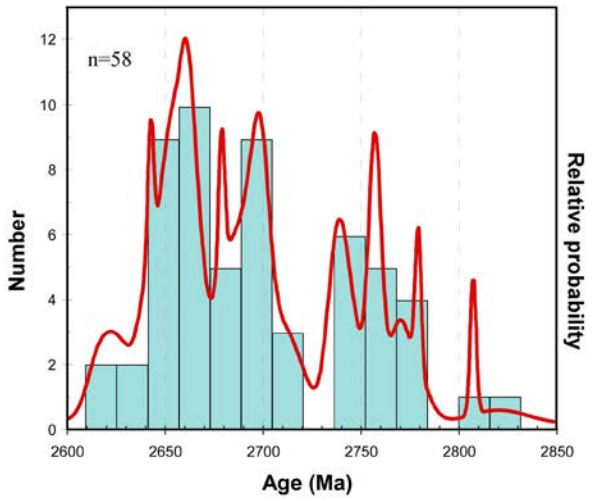

Figure 5.12. Probability density diagram showing the distribution of the zircon ages in the Sukumaland Greenstone Belt. Three main periods of crustal growth can be recognised. However, the 2720-2620 Ma period can be separated into a TTG dominated period (2720-2660 Ma) and a high-K granite dominated period (2660-2620 Ma).

This study presents the first zircon age data for the Kukuluma Terrain. This new dataset indicates that the Kukuluma Terrain was mainly affected by the 2720 to 2620 Ma episode of crustal growth. The 2717±12 Ma crystal tuff was most likely derived from igneous rocks of intermediate or primitive TTG composition as indicated by positive εHf values and suprachondritic $^{176}Hf/^{177}Hf_i$ ratios (Fig. 5.11). This was followed by the intrusion of the diorite and monzonite phase of the KIC most probably between 2700 and 2680 Ma by comparison with the Nyankanga Intrusive Complex from the Central Terrain (Sanislav et al., 2015; Chapter 3). It is worth noting that the igneous activity in the Kukuluma Terrain follows a similar pattern with the igneous activity in the Central Terrain. That is, an early phase dominated by intrusives of dioritic to monzonitic composition followed by a series of dykes of granodioritic composition (Sanislav et al., 2015; 2016).

In the Kukuluma Terrain, the granodiorite phase appears to consistently return ages between 2665 and 2650 Ma marking the transition to the more evolved 2660 to 2620 Ma

high-K granites that are wide spread around the margin of the greenstone belt. The nearly chondritic Hf isotope composition of the granodiorites requires a juvenile source for these rocks, most likely of mafic composition which experienced very little interaction with felsic crust. Two samples (KK04 and MT20) have almost identical Hf signatures and basically fall within the chondritic evolution line. The other two samples (KK01 and KK03) have εHf values as low as -4 which, can be explained by the assimilation of some sediment during emplacement. However, their average isotopic signature is still nearly chondritic requiring an important juvenile component in their source. Their geochemical signature (Chapter 4) is consistent with intracrustal partial melting of amphibolite. The Hf signature of the granodiorites is almost identical to the Hf signature of the similarly aged high-K granites which also have nearly chondritic affinities indicating crustal growth from a juvenile source, most probably of mafic to intermediate composition. The lack of a significant sub-chondritic component in the isotopic signature of zircons precludes any involvement of older felsic crust and the narrow compositional range indicates that little mixing or contamination occurred.

5.7. CONCLUSIONS

- The emplacement of the diorite and monzonite suites of the KIC may have occurred between ~2700-2680 Ma.
- The 2717 Ma age of the crystal tuff layer from the Kukuluma pit provides a maximum sedimentation age for this part of the greenstone belt. The crystal tuff layer is part of a volcanoclastic sequence that overlaies the ironstone and forms the top of the Nyanzian stratigraphy. It is possible that more than one ironstone horizons exist in the GGB.
- The 2650 Ma age of the mineralized granodiorite dyke from Matandani pit can be used to constrain the maximum age of the mineralization in the Kukuluma Terrain. This age is similar to the maximum mineralization age (2644 Ma; Borg and Krogh,

1999) proposed for the mineralization in the Central Terrain. It is likely that gold mineralization in the GGB occurred synchronously.

- Geochrological evidence suggests that Kukuluma Terrain was subjected to three phases of crustal growth: pre-2700 Ma sedimentation in a volcanically active region, the emplacement of the diorite, monzonite and granodiorite suites between ~2700 Ma and 2660 Ma and finally the emplacement of the high-K granites along the margins of the GGB.
- Hf isotopes suggest that magmatism and volcanism have a juvenile character.

CHAPTER 6

CONCLUSIONS

A large amount of research has been conducted in the past five decades with the aim of better understanding the geological controls on gold mineralization for the Archaean greenstone-hosted gold deposits. Most of these researches were focused on deposits from Western Australia, Canada, South Africa, India, Brazil, and China. However, the past two decades have seen a constant increase of research activity on the Archean gold deposits from Tanzania Craton. This thesis presents for the first time the geology of a mineralized terrain, the Kukuluma Terrain, from the Geita Greenstone Belt. The Kukuluma Terrain contains three gold deposits and a few prospects making it one of the highest prospective terrains in the Geita Greenstone Belt. In this thesis, I used several techniques to study the geology of the Kukuluma Terrain to create a better understanding of the controls on gold mineralization. These techniques involved: geological mapping, geochemistry (XRF for major elements and LA-ICP-MS for trace elements) (LA-ICP-MS), geochronology (LA-ICP-MS dating of zircon grains), isotopes (Hf isotopes in zircon grains), interpretation of geophysical datasets and 3D-modelling of key geological features.

In Chapter 2 of the thesis I presented the methods and the data I used as a foundation for the following chapters. The aim of this chapter was to show how 3D-geological models for the Matandani, Kukuluma and Area 3 West deposits were constructed from surface mapping, drill core logging, chip logging, cross-section interpretations and modeling. As a result, a standardized nomenclature (Table A2.1) of lithologies was established that led to the generation of a coherent geological framework for the area. Shapes and geometries of various

lithologies were established using cross-sections generated from individual deposits. The relative timing relationships of various lithological units were established using various techniques such as cross-cutting relationships and younging indicators. These observations form the basis for material presented in chapters 3, 4 and 5. In this chapter, I have also presented the methodologies and laboratory set-ups used for structural analyses (presented in Chapter 3), geochemical analyses (presented in Chapters 4 and 5) and geochronology (presented in Chapter 5).

In Chapter 3 of this thesis, I presented the detailed deformation and intrusive history of the Kukuluma Terrain (Table 3.1). The Geita Greenstone Belt can be subdivided into three NW-SE trending terrains: Kukuluma Terrain, Central Terrain, and the Nyamullilima Terrain. There is no published data for the Nyamullilima Terrain (except a few internal mine reports), but the geology of the Central Terrain has been discussed in a few papers over the last two decades (e.g. Borg, 1994; Sanislav et al., 2015; 2016). In this study I have showed that the Kukuluma Terrain experienced a complex deformation and intrusive history (Chapter 3) with multiple folding events (D_2 to D_5 deformation) and shearing (D_6 deformation) related to a compressional-accretionary phase followed by normal faulting (D_7 deformation) during the waning stages of Archean deformation. The Kukuluma terrain was intruded by monzonite, diorite and granodiorite forming the Kukuluma Intrusive Complex. The monzonite and the diorite phase intruded early during D_3 deformation while the granodiorite phase intruded mainly as dykes during later deformation events.

Overall, the deformation and intrusive pattern in the Kukuluma Terrain is similar to the deformation and the intrusive pattern described from other parts (e.g. Borg, 1994; Sanislav et al., 2015; 2016) of the Geita Greenstone Belt suggesting that the entire greenstone belt experienced a similar deformation and intrusive history. Gold mineralization is spatially

linked to the diorite-ironstone contact that is overprinted by the D_6-shear zone, hydrothermally brecciated hinge zones of D_3-folds and by the D_7-normal reactivation of earlier structures.

In Chapter 4 of the thesis I presented the major and trace element geochemistry of the Kukuluma Intrusive Complex and discussed the petrogenesis of the monzonite, diorite and the granodiorite suites. The major and trace element geochemistry of the Kukuluma Intrusive Complex such as low SiO_2 and relatively high MgO indicate their derivation from partial melting of mafic or ultramafic sources. The trace element geochemistry of the diorite and the monzonite suites resembles adakite rocks but it lacks a clear mantle or slab signature suggesting that they formed most likely by lower crustal melting of eclogite, while the granodiorite phase formed by partial melting of amphibolite. This indicates that crustal growth in this part of Tanzania did not occur by modern day like plate tectonic processes but involved a rather different tectonic setting mechanism specific for the Archean period.

In Chapter 5 of this thesis I presented new U-Pb zircon ages and Hf isotope data from tuffaceous sediments and from granodiorite dykes and I discussed the findings in relation to deformation history, timing of sedimentation, timing of mineralization and implications for crustal growth in Tanzania Craton. The sedimentation age of the volcano-sedimentary units within the Kukuluma terrain is proposed to be as old as ~2717Ma based on the crystal tuff age which interbands with ironstones. This sedimentation age is close to the 2702 Ma and 2687 Ma zircon ages reported from the feldspathic sandstone units interbedded with the ironstones in the Central Terrain. This similarity in the sedimentation ages between the two terrains appeals for re-assessment of the timing of the formation of this terrain bounding structure and its role if any in the sedimentation processes. In addition, the larger difference showed by the 2771 Ma tuffaceous sediments interbedded with ironstones from the

Nyamulilima Terrain indicates a more complex stratigraphic relationship over the GGB. This may indicate that ironstones were deposited more than once in GGB. Alternatively, the sedimentation processes were controlled by isolated volcanic activities in smaller basins that formed within the Geita Greenstone Belt.

It is likely that the diorite and monzonite suite of the KIC were intruded about the same time with the Nyankanga Intrusive Complex from the Central Terrain. That is indicated by similar composition, by the age of sediments they intruded into and by the age of later felsic porphyries that cut across these intermediate intrusive complexes. Thus, the KIC intruded sometime between 2700 Ma and 2670 Ma.

Using the existing zircon geochronology and the new U-Pb zircon ages and Hf isotopes presented in this thesis I proposed that the evolution of the Kukuluma Terrain fits within the general pattern of crustal growth observed in this part of the Tanzania Craton. The Kukuluma Terrain records prior to 2700 Ma a period dominated by volcanism and sedimentation; this period was followed by the main accretionary processes and the emplacement between ~ 2700 Ma and 2650 Ma of the intermediate phase of the KIC and the granodiorite dykes. The last period that affected the Kukuluma Terrain coincides with the emplacement of the 2660 Ma to 2620 Ma high-K granites around its north-eastern margin. The Hf isotopes in zircon indicate that the sediments and the granodiorite dykes were derived from a juvenile source and there are no indications of older crust being involved in the petrogenesis of these rocks. These conclusions fit very well with the interpreted petrogenesis of the granodiorite dikes (see Chapter 4) which, were interpreted to have formed by intracrustal partial melting of a juvenile amphibolite source. The maximum age for gold mineralization within the Kukuluma Terrain could be constrained to ~2650 Ma based on the crosscutting relationship of a mineralized granodiorite dyke from the Matandani pit.

This study has demonstrated that, the gold mineralization in the Kukuluma terrain occurred late during the tectonic evolution of the Geita Greenstone Belt. The Kukuluma Terrain experienced a complex deformation and intrusive history that created a favorable structural geometry, which under the right conditions trapped the gold from mineralized fluids. The late timing of gold suggests a potential link to the emplacement of the high-K granites and important contributions from fluids derived from melting/crystallization of crustally derived magmas. However, at the moment there is no clear evidence for a genetic link between gold and the high-K granites. This could be a topic for further studies since there may be implications for exploration. The isotope data supports a juvenile character for the Kukuluma Terrain typical for many Archean gold provinces worldwide.

The ironstones are the main hosts for gold mineralization. They are complexly folded and disrupted by shear zones and intrusives. Better understanding of their distribution and geometry at the terrain scale should be major focus for further exploration work. The contact between the KIC and the sediments is the next important control on gold distribution and further studies/exploration should focus on understanding its undercover extent. The relationship between the folded pattern and the KIC is also an important factor. It appears that mineralization preferentially occurs in zones of complex D_2-D_3 interference pattern located in bends of the KIC created by the D_4 and cut across by D_6 and D_7 shear zones. It appears that gold mineralization occurs along ~ east-west oriented structural corridors that intersect the dominant N-W structural trend. These ~east-west corridors manifest as steeply dipping fracture zones recording a normal component of movement. These corridors are visible in the geophysics, the open pits and mined by artisanal miners. Field mapping should further investigate their potential.

The emplacement of the granodiorite dykes and intrusives appears to “just” predate the gold mineralization. The composition and timing of some of these dykes and intrusives was touched upon in this thesis but, field evidence suggests that their composition and timing is more diverse compared to what has been presented here. The possibility of a link between this intrusive phase and gold should be further investigated. A detailed study on the alteration paragenesis and the alteration signature of the mineralizing fluids is missing. This has enormous implications for exploration, metallurgy and the understanding of mineralization therefore such a study is highly recommended.

REFERENCES

Allmendinger, R.W., 2012. StereoWin for Windows. (www.geo.cornell.edu/geology/faculty/RWA/programs.html).

Allmendinger, R.W., 2001. FaultKinWin, Version 1.1: a program for analyzing fault slip data for Windows™. (www.geo.cornell.edu/geology/faculty/RWA/programs.html).

Angelier, J., 1994. Fault slip analysis and palaeostress reconstruction, in: Hancock, P.L. (Ed.), Continental Deformation. Oxford, Pergamon, Oxford, pp. 101-120.

Angelier, J., Mechler, P., 1977. Sur une méthode graphique de recherche des contraintes principales également utilisable en tectonique et en séismologie: la méthode des dièdres droits. Bulletin de la Société Géologique de France 7, 1309-1318.

Anhaeusser, C.R., 2014. Archaean greenstone belts and associated granitic rocks-A review. Journal of African Earth Sciences 100,684-732

Atherton, M.P., Petford, N., 1993. Generation of sodium-rich magmas from newly underplated basaltic crust. Nature 362, 144-146.

Bansah, D., Chase, R., Davidson, A., Michael, H., Skead, M., Stuart, H., 2000. The Geita and Kukuluma mineralised trends, Lake Victoria Goldfield, Tanzania ore body characteristics and project planning. 4th International Mining Geology Conference, Coolum, Queensland, 14–17 May 2000.

Barth, H., 1990. Explanatory Notes on the 1:500 000: Provisional Geological Map of the lake Victoria Goldfields, Tanzania. Geologisches JahrbuchReihe B, Regional GeologieAusland Heft 72.

Bebout, G.E., 2007. Metamorphic chemical geodynamics of subduction zones. Earth and Planetary Science Letters 260, 373-393.

Bedard, J.H., 2006. A catalytic delamination-driven model for coupled genesis of Archaean crust and sub-continental lithospheric mantle. Geochimica et Cosmochimica Acta 70, 1188-1214.

Bedard, J.H., Harris, L.B., 2014. Neo-archaean disaggregation and re-assembly of the Superior Craton. Geology 42, 951-954.

Bedard, J.H., Harris, L.B., Thurston, P.C., 2013. The hunting of the snArc. Precambrian Research 229, 20-48

Bedard, J.H., Brouillette, P., Madore, L., Berclaz, A., 2003. Archaean cratonization and deformation in the northern Superior Province, Canada: an evaluation of plate tectonic vs vertical tectonic models. Precambrian Research 127, 61–87.

Begg, G.C., Griffin, W.L., Natapov, L.M., O'Reilly, S.Y., Grand, S.P., O'Neill, C.J., Hronsky, J.M.A., Djomani, D.Y., Swain, C.J., Deen, T., Bowden, P., 2009. The lithospheric architecture of Africa: seismic tomography, mantle petrology and tectonic evolution. Geosphere 5, 23–50.

Bierlein, F.P., Groves, D.I., Cawood, P.A., 2009. Metallogeny of accretionary orogens- the connection between lithospheric processes and metal endowment. Ore Geol. Rev.36, 282–292.

Bierlein, F.P., Groves, D.I., Goldfarb, R.J., Dubé, B., 2006. Lithospheric controls on the formation of provinces hosting giant orogenic gold deposits. Miner. Deposita 40, 874–886.

Blewett R.S., Czarnota K., Henson P.A., 2010a, Structural-event framework for the eastern Yilgarn craton, Western Australia, and its implications for orogenic gold: Precambrian Research 183, p. 203–229

Blewett, R.S., Henson, P.A., Roy, I.G., Champion, D.C., Cassidy, K.F., 2010b. Scale integrated architecture of the world-class gold mineral systems of the Archean eastern Yilgarn Craton. Precambrian Res. 183, 230–250.

Blewett, R.S., Shevchenko, S., Bell, B., 2004. The North Pole Dome: a non-diapiric dome in the Archaean Pilbara Craton, Western Australia. Precambrian Research 133, 105–120.

Booth, J.K., 1954b. A note on the structural geology of the Geita Mine. - Rec. Geol. Surv. Tanganyika 1, (1951), 20-21(1954).

Borg, G., 1994. The Geita gold deposit in NW Tanzania. Geology, ore petrography geochemistry and timing events. Geol. Jb. D100, 545–595.

Borg, G., 1992. New aspects on the lithostratigraphy and evolution of the Siga Hills, an Archaean granite-greenstone terrain in NW-Tanzania. Zeitschrift fur Angewandte Geologie 38, 89-93.

Borg, G., Rittenauer, A., 2000. Syn- and epigenetic sulphides in Archean BIFs of NW-Tanzania and their significance to gold mineralization. In: Rammlmair (ed) Applied mineralogy. Balkema, Rotterdam, pp 263–266

Borg. G., Krogh, T., 1999. Isotopic age data of single zircons from the Archaean Sukumaland Greenstone Belt, Tanzania. Journal of African Earth Sciences 29, 301-312.

Borg, G., Shackleton, R.M., 1997. The Tanzania and NE-Zaire Cratons. In: de Wit, M.J., Ashwal, L.D. (Eds.), Greenstone Belts. Oxford University Press, Oxford, pp. 608–619.

Borg, G., Lyatuu, D.R., Rammlmair, D., 1990. Genetic aspects of the Geita and Jubilee reef, Archean BIF-hosted gold deposits, Tanzania. Geol. Rundsch. 79, 355–371.

Bouhallier, H., Chardon, D., Choukroune, P., 1995. Strain patterns in Archaean dome-and-basin structures: the Dharwar craton (Kamataka, South India). Earth and Planetary Science Letters 135, 57–75.

Bouvier, A., Vervoort, J.D., & Patchett, P.J., 2008. The Lu–Hf and Sm–Nd isotopic composition of CHUR: Constraints from unequilibrated chondrites and implications for the bulk composition of terrestrial planets. Earth and Planetary Science Letters, 273, 48–57.

Brayshaw, M., Kolling, S.L., 2012. Standardized graphic log paper used in drill core logging. Geita Gold Mine.Internal document.

Castillo, P. R., 2012. Adakite petrogenesis. Lithos 134-135, 304-316.

Chadwick, B., Vasudev, V.N., Hegde G.V. 2000. The Dharwar Craton, southern India,interpreted as the result of Late Archean oblique convergence. Precambrian Research 99, 91–111.

Chamberlain, C.M., Tosdal, R.M., 2007. U–Pb geochronology of the Lake Victoria Greenstone Terrane, Tanzania. Mineral Deposit Research Unit The University of British Columbia (Research Program on World-class Gold Deposits and Advanced Exploration Projects Owned and/or Joint Ventured to Barrick Gold, Placer Dome, Anglogold-Ashanti, Resolute Mining NL as Main Sponsors.

Chardon, D., Choukroune, P., Jayananda, M., 1996. Strain patterns, decollement and incipient sagducted greenstone terrains in the Archaean Dharwar craton (south India). Journal of Structural Geology 18, 991–1004.

Chiaradia, M., 2015. Crustal thickness control on Sr/Y signatures of recent arc magmas: an Earth scale perspective. Scientific Reports 5, 8115.

Choukroune, P., Bouhallier, H., Arndt, N.T., 1995. Soft lithosphere during periods of Archaean crustal growth or crustal reworking. In: Coward, M.P., Ries, A.C. (Eds.), Early Precambrian Processes. Geological Society of London Special Publication, vol. 95, pp. 67–86.

Cladouhos, T.T., Allmendinger, R.W., 1993. Finite strain and rotation from fault slip data. Journal of Structural Geology 15, 771-784.

Cloutier, J., Stevenson, R. K., Bardoux, M., 2005. Nd isotopic, petrologic and geochemical investigation of the Tulawaka East gold deposit, Tanzania Craton. Precambrian Research 139, 147-163.

Collins, W.J., Van Kranendonk, M.J., Teyssier, C., 1998. Partial convective overturn of Archaean crust in the east Pilbara Craton, Western Australia: driving mechanisms and tectonic implications. Journal of Structural Geology 20, 1405–1424.

Colvine, A.C., Fyon, J.A., Heather, K.B., Marmont, S., Smith, P.M., Troop, D.G., 1988. Archaean lode gold deposits in Ontario. Ontario Geological Survey, Ontario, Canada. Miscellaneous Paper 139, pp. 136.

Condie, K. C., 1994. Greenstones through time. In: Condie, K. C (Ed.), Archaean Crustal Evolution. Elsevier, Amsterdam.

Condie, K.C., 2005. TTGs and adakites: are they both slab melts? Lithos 80, 33–44.

Condie, K.C., 2014. Growth of continental crust: a balance between preservation and recycling. Mineral. Mag. 78, 623–637.

Condie, K.C., Viljoen, M.J., and Kable, E.D.J., 1977. Effects of alteration on element distributions in Archaean tholeiites from the Barberton greenstone belt, South Africa. Contributions to Mineralogy and Petrology 64, 75-89.

Cook, Y.A., Sanislav, I.V., Hammerli, J., Blenkinsop, T.G., Dirks, P.H.G., 2015. A primitive mantle source for the Neoarchean mafic rocks from the Tanzania Craton. Geoscience Frontiers, 7, 911-926.

Cox, S.F., Knackstedt, M.A., Braun, J., 2001. Principles of structural control on permeability and fluid flow in hydrothermal systems. In: Richards, J.P., Tosdal, R.M. (Eds.), Structural Controls on Ore Genesis. Reviews in Economic Geology, 14. Society of Economic Geologists, Boulder, Colorado, pp. 1–25.

Czarnota K., Champion D.C., Goscombe B., Blewett R.S., Cassidy K.F., Henson P.A.,Groenewald P.B., 2010, Geodynamics of the eastern Yilgarn craton: Precambrian Research, v. 183, no. 2, p. 175–220.

Davidson, J., Turner, S., Handley, H., Macpherson, C., Dosseto, A., 2007. Amphibole “sponge” in arc crust? Geology 35, 787–790.

de Ronde, E.J., de Wit, M.J., 1994. The tectonic history of the Barberton greenstone belt South Africa: 490 million years of Archaean crustal evolution. Tectonics 13, 983–1005.

de Wit, M.J., Furnes, H., Robins, B., 2011. Geology and tectonostratigraphy of the Onverwacht Suite, Barberton Greenstone Belt, South Africa. Precambrian Res 186:1–27

de Wit, M.J., Ashwal, L.D., 1997. Greenstone Belts. Oxford University Press, Oxford,

Defant, M.J., Drummond, M.S., 1990. Derivation of some modern arc magmas by melting of young subducted lithosphere. Nature 347, 662–665.

Delvaux, D., Sperner, B., 2003. New aspects of tectonic stress inversion with reference to the TENSOR programme, in: Nieuwland, D.A. (Ed.), New insights into structural interpretation and modelling. Geological Society of London, Special Publication, 212, 75-100.

Dirks, P.H.G.M., Charlesworth, E.G., Munyai, M.R., Wormald, R.J., 2013. Stress analyses, post-orogenic extension and 3.01 Ga gold mineralization in the Barberton Greenstone Belt, South Africa. Precambrian Res 226,157–184.

Dirks, P.H.G.M., Charlesworth, E.G., Munyai, M.R., 2009. Cratonic extension and Archaean - gold mineralisation in the Sheba-Fairview mine, Barberton Greenstone Belt, South Africa. South African Journal of Geology 112, 291–316

Dirks, P.H.G.M., Jelsma, H.A., Hofmann, A., 2002. Accretion of an Archean greenstone belt in the Midlands of Zimbabwe. Journal of Structural Geology 24, 1707–1727.

Dirks, P.H.G.M., Jelsma, H.A., 1998. Horizontal accretion and stabilization of the Zimbabwe Craton. Geology 26, 11–14.

Drummond, M.S., Defant, M.J., 1990. A model for trondhjemite–tonalite–dacite genesis and crustal growth via slab melting: Archaean to modern comparisons. Journal of Geophysical Research 95, 21503-21521.

Etchecopar, A., Vasseur, G., Daignie`res, M., 1981. An inverse problem in microtectonics for the determination of stress tensors from fault striation analysis. Journal of Structural Geology 3, 51–65.

Foley, S., Tiepolo, M., Vannucci, R., 2002. Growth of early continental crust controlled by melting of amphibolite in subduction zones. Nature 417, 837– 840.

Foley, S.F., Barth, M.G., Jenner, G.A., 2000. Rutile/melt partition coefficients for trace elements and an assessment of the influence of rutile on the trace element characteristics of subduction zone magmas. Geochim. Cosmochim. Acta 64, 933–938.

Fossen, 2016. Structural geology. Cambridge University Press, Cambridge, 524pp

Frimmel, H.E., 2008. Earth's continental crustal gold endowment. Earth Planet. Sci. Lett. 267, 45–55.

Gabert, G., 1990. Lithostratigraphic and tectonic setting of gold mineralization in the Archaean Cratons of Tanzania and Uganda, East Africa. Precambrian Research 46, 59–69.

Gao, S., Rudnick, R.L., Yuan, H.L., Liu, X.M., Liu, Y.S., Xu, W.L., Lin, W.L., Ayerss, J., Wang, X.C., Wang, Q.H., 2004. Recycling lower continental crust in the North China craton. Nature 432, 892–897.

Goldfarb, R.J., Baker, T., Dubé, B., Groves, D.I., Hart, C.J.R., Gosselin, P., 2005. Distribution, character and genesis of gold deposits in metamorphic terranes. Econ. Geol. 100th Anniv. Vol. 407–450.

Goldfarb, R.J., Groves, D.I., Gardoll, S., 2001. Orogenic gold and geologic time: a global synthesis. Ore Geol. Rev. 18, 1–75.

Goss, A.R., Kay, S.M., Mpodozis, C., 2011. The geochemistry of a dying continental arc: the Incapillo Caldera and Dome Complex of the southernmost Central Andean Volcanic Zone (28°S). Contributions to Mineralogy and Petrology 161, 101-128.

Green, T.H., Blundy, J.D., Adam, J., Yaxley, G.M., 2000. SIMS determination of trace element partition coefficients between garnet, clinopyroxene and hydrous basaltic liquids at 2 – 7.5 GPa and 1080–1200 °C. Lithos 53, 165– 187.

Groves, D.I., Santosh, M., 2015. Province-scale commonalities of some world-class gold deposits: Implications for mineral exploration. Geoscience Frontiers, 6, 389-399.

Groves, D.I., Vielreicher, R.M., Goldfarb, R.J., Condie, K.C., 2006. Controls on the heterogeneous distribution of mineral deposits through time. In: McDonald, I., Boyce, A.J., Butler, I.B., Herrington, R.J., Polya, D.A. (Eds.), Mineral Deposits and Earth Evolution: Geol. Soc., London Spec. Pub., 248.

Groves, D.I., Goldfarb, R.J., Robert, F., Hart, C.J.R., 2003. Gold deposits in metamorphic belts: overview of current understanding, outstanding problems, future research, and exploration significance. Econ. Geol. 98, 1–29.

Groves, D.I., Goldfarb, R.J., Knox-Robinson, C.M., Ojala, J., Gardoll, S., Yun, G., Holyland,P., 2000. Late-kinematic timing of orogenic gold deposits and significance for computer-based exploration techniques with emphasis on the Yilgarn block, Western Australia. Ore Geol. Rev. 17, 1–38.

Groves, D.I., Goldfarb, R.J., Gebre-Mariam, M., Hagemann, S.G., Robert, F., 1998. Orogenic gold deposits: a proposed classification in the context of their crustal distribution and relationship to other gold deposit types. Ore Geology Reviews 13, 7–27.

Hacker, B.R., Kelemen, P.B., Behn, M.D., 2015. Continental lower crust. Annual Review of Earth and Planetary Sciences 43, 167–205.

Harpum, J.R., 1970. Summary of the geology of Tanzania: structure and geotectonics of the Precambrian. Tanzania Geol. Surv. Mem. 1 Part V, 58 pp.

Hayman, P. C., Thébaud, N., Pawley, M. J., Barnes, S. J., Cas, R. A. F., Amelin, Y., Pegg, I., 2015. Evolution of a ~2.7Ga large igneous province: A volcanological, geochemical and geochronological study of the Agnew Greenstone Belt, and new regional correlations for the Kalgoorlie Terrane (Yilgarn Craton, Western Australia). Precambrian Research 270, 334-368

Hirose K, Kushiro I. 1993. Partial melting of dry peridotites at high pressures: determination of compositions of melts segregated from peridotite using aggregates of diamond. Earth Planet. Sci. Lett. 114, 477–89.

Hofmann, A., Dirks, P.H.G.M. and Jelsma, H.A., 2001a. Late Archaean foreland basin deposits, Belingwe greenstone belt, Zimbabwe. Sedimentary Geology, 141-142, 131-168.

Hofmann, A., Dirks, P.H.G.M. and Jelsma, H.A., 2001b. Horizontal tectonic deformation geometries in a late Archaean sedimentary sequence, Belingwe greenstone belt, Zimbabwe. Tectonics, 20, 909-932.

Jackson, S.E., Pearson, N.J., Griffin, W.L., Belousova, E.A., 2004. The application of laser ablation-inductively coupled plasma-mass spectrometry to in situ U-Pb zircon geochronology. Chemical Geology 211, 47–69.

Jayananda, M., Martin, H., Peucat, J.J., Mahabaleswar, B., 1995. Late Archaean crust-mantle interactions in the Closepet granite, Southern India: evidence from Sr–Nd isotopes, major and trace element geochemistry. Contributions to Mineralogy and Petrology 119, 314–29.

Jelsma, H.A., Dirks, P.H.G.M., 2002. Neoarchaean tectonic evolution of the Zimbabwe Craton. In: C.M.R. Fowler, C. Ebinger and C.J. Hawkesworth (Editors), The Early Earth: Physical, Chemical and Biological Development. Geological Society of London Special Publication, 199, 183–211.

Jelsma, H.A., Vinyu, M.L., Valbracht, P.J., Davies, G.R., Wijbrans, J.R., Verdurmen, E.A.T., 1996. Constraints on Archaean crustal evolution of the Zimbabwe Craton: a U-Pb zircon, Sm-Nd and Pb-Pb whole-rock isotope study. Contrib Mineralogy Petrology 124,55–70

Jochum, K.P., Stoll, B., Herwig, K., et al., 2006. MPI-DING reference glasses for in situ microanalysis: new reference values for element concentrations and isotope ratios. Geochemistry, Geophysics, Geosystems 7.

Kabete, J.M., Groves, D.I., McNaughton, N.J., Mruma, A.H., 2012a. A new tectonic and temporal framework for the Tanzanian Shield: implications for gold metallogeny and undiscovered endowment. Ore Geology Reviews 48, 88–124.

Kabete, J.M., McNaughton, N.J., Groves, D.I., Mruma, A.H., 2012b. Reconnaissance SHRIMP U–Pb zircon geochronology of the Tanzania Craton: Evidence for Neoarchean granitoid–greenstone belts in the Central Tanzania Region and the Southern East African Orogen. Precambrian Research 216 – 219, 232– 266.

Kamber, B.S., Ewart, A., Collerson, K.D., Bruce, M.C., McDonald, G.D., 2002. Fluid-mobile trace element constraints on the role of slab melting and implications for Archean crustal growth models. Contributions to Mineralogy and Petrology 144, 38–56

Kay, R.W., 1978. Aleutian magnesian andesites: melts from subducted Pacific Ocean crust. Journal of Volcanology and Geothermal Research 4, 117–132.

Kelemen, P.B., K. Hanghøj, and A.R. Greene 2003. One view of the geochemistry of subduction-related magmatic arcs with an emphasis on primitive andesite and lower crust, in The Crust, (R.L. Rudnick, ed.), Vol. 3, Treatise on Geochemistry, (H.D. Holland and K.K. Turekian, eds.), Elsevier-Pergamon, Oxford, 593-659,

Kemp, A. I. S., Foster, G. L., Schersten, A., Whitehouse, M. J., Darling, J., Storey, C., 2009. Concurrent Pb–Hf isotope analysis of zircon by laser ablation multi-collector ICP-MS, with implications for the crustal evolution of Greenland and Himalayas. *Chem. Geol*. 261, doi:10.1016/j.chemgeo.2008.1006.1019.

Kerrich, R., 1989. Shear zone hosted mesothermal gold deposits; a review of geochemical evidence on the source of fluids and solute, In J. T.Bursnall (Editor), Mineralization and Shear zones. Geological association of Canada. Short Course Notes, 6,129 - 197.

Kerrich, R., Goldfarb, R.J., Groves, D.I., Garwin, S., 2000. The geodynamics of world-class gold deposits: characteristics, space-time distribution, and origins. In: Hagemann, S.G., Brown, P.E. (Eds.), Gold in 2000. Reviews in Economic Geology, 13. Society of Economic Geologists, Boulder, Colorado, pp. 501–551

Kloppenburg, A., White, S.H., Zegers, T.E., 2001. Structural evolution of the Warrawoona Greenstone Belt and adjoining granitoid complexes, Pilbara Craton, Australia: implications for Archaean tectonic processes. Precambrian Research 112, 107–147.

Kogiso T., Hirschmann M.M., Petermann M., 2004. High-pressure partial melting of mafic lithologies in the mantle. Journal of Petrology 45, 2407-2422.

Krapez, B., 2008. Stratigraphic analysis of the Geita Mine Sequence. Geita GoldMine internal report — unpublished.

Krapez, B., Barley, ME., Pickard, A.L., 2003. Hydrothermal and resedimented origins of the precursor sediments to banded iron formations: sedimentological evidence from the early.Palaeoproterozoic Brockman Supersequence of Western Australia. Sedimentology 50, 979–1011.

Kuehn, S., Ogola, J., Sango, P., 1990. Regional setting and nature of gold mineralization in Tanzania and southwest Kenya. Precambrian Research 46, 71-82.

Kusky, T.M., 1998. Tectonic setting and terrane accretion of the Archean Zimbabwe Craton. Geology, 26, 163–166.

Kwelwa, S., Manya, S., Vos, I.M.A., 2013. Geochemistry and petrogenesis of intrusions of the Golden Pride gold deposit in the Nzega Greenstone Belt, Tanzania. African Journal of Earth Sciences, 86, 53-64.

Leahy, A., Barnicoat, A.C., Foster, R.P., Lawrence, S.R., Napier, R.W., 2005. Geodynamic processes that control the global distribution of gold deposits. In: McDonald, I., Boyce, I., Butler, I.B., Herrington, R.J., Polya, D.A. (Eds.), Mineral Deposits and Earth Evolution: Geol. Soc. London, Spec. Publ., 248, pp. 119–132.

Likhoidov, G.G., Plyusnina, L.P., Shcheka, Zh.A., 2007. The behavior of gold during listvenitization: experimental and theoretical simulation. Dokl. Earth Sci. 415, 723–726.

Lin. S., Beakhouse, G.P., 2013. Synchronous vertical and horizontal tectonism at late stages of Archean cratonization and genesis of Hemlo gold deposit, Superior craton, Ontario, Canada. Geology 41, 359–362.

Lisle, R. J., 1987. Principal stress orientations from faults: an additional constraint. Annales Tectonic 1, 155-158.

Ludwig, K.R., 2003. User's Manual for Isoplot 3.00. A Geochronological Toolkit for Microsoft Excel. Berkley Geochronology Centre Special Publication No.4.

Macpherson, C.G., Dreher, S.T., Thirwall, M.F., 2006. Adakites without slab melting: high pressure processing of basaltic island arc magma, Mindanao, the Philippines. Earth and Planetary Science Letters 243, 581–593.

Manikyamba C., Kerrich R. 2012. Eastern Dharwar Craton, India: continental lithosphere growth by accretion of diverse plume and arc terranes. Geoscience Frontiers 3, 225–240.

Manikyamba, C., Kerrich, R., Khanna, T.C., Subba Rao, D.V., 2007. Geochemistry of adakites and rhyolites from the Neoarchaean Gadwal greenstone belt, Eastern Dharwar craton India: implications for sources and geodynamic setting. Canadian Journal of Earth Sciences 44, 1517–1535.

Manya, S., Kobayashi, K., Maboko, M.A.H., Nakamura, E., 2006. Ion microprobe zircon U-Pb dating of the late Archean metavolcanics and associated granites of the Musoma-Mara Greenstone Belt, Northeast Tanzania: Implications for the geological evolution of the Tanzanian Craton. Journal of African Earth Sciences 45, 355-366.

Manya, S., Maboko, M. A. H., 2003. Dating basaltic volcanism in the Neoarchaean Sukumaland Greenstone Belt of the Tanzania Craton using the Sm–Nd method: implications for the geological evolution of the Tanzania Craton. Precambrian Research 121, 35-45.

Manya, S., Maboko, M.A.H., 2008. Geochemistry of the Neoarchean mafic volcanic rocks of the Geita area, NW Tanzania: implications for stratigraphical relationships in the Sukumaland Greenstone belt. Journal of African Earth Sciences 52, 152–160.

Manya, S., Maboko, M.A.H., Nakamura, E., 2007. Geochemistry of high-Mg andesite and associated adakitic rocks in the Musoma-Mara greenstone belt, northern Tanzania: possible evidence for Neoarchaean ridge subduction?''. Precambrian Research 159, 241–259.

Marrett, R. A., Allmendinger, R.W., 1990. Kinematic analysis of fault-slip data. Journal of Structural Geology 12, 973-986.

Martin, H., 1999. The adakitic magmas: modern analogues of Archaean granitoids. Lithos 46 (3), 411–429.

Martin, H., Moyen, J.F., Rapp, R.P., 2010. The sanukitoid series: magmatism at the Archaean-Proterozoic transition. Earth and Environmental Science. Transactions of the Royal Society of Edinburgh 100 (1–2), 15–33.

Martin, H., Smithies, R.H., Rapp, R., Moyen, J.F., Champion, D., 2005. An overview of adakite, tonalite–trondhjemite–granodiorite (TTG), and sanukitoid: relationships and some implications for crustal evolution. Lithos 79, 1–24.

McCuiag, T.C., Kerrich, R., 1998. P-T-t-deformation-fluid characteristics of lode gold deposits: evidence from alteration systematic. Ore Geology Reviews12, 381 - 453.

Mikkola, P., Heilimo, S., Huhma, H., 2014. Relationships between Sanukitoids and crust-derived melts and their implications for the diversity of Neo-archaean granitoids: A case study from Surmansuo and nearby areas, Eastern Finland. Bulletin of Geological Society of Finland, 86, 23-40.

Mohan, M.R., Piercey, S.J., Kamber, B.S., Sarma, D.S., 2013. Subduction related tectonic evolution of the Neoarchean eastern Dharwar Craton, southern India: new geochemical and isotopic constraints. Precambrian Research 227, 204–226.

Molnar, P., 1983. Average regional strain due to slip on numerous faults of different orientations. Journal of Geophysical Research 88, 6430-6432.

Moyen, J. F., 2011. The composite Archaean grey gneisses: petrological significance, and evidence for a non-unique tectonic setting for Archaean crustal growth. Lithos 123, 21-36.

Moyen, J.-F., 2009. High Sr/Y and La/Yb ratios: The meaning of the “adakitic signature”. Lithos 112, 556–574.

Moyen, J.-F., Martin, H., 2012. Forty years of TTG research. Lithos 148, 312–336

Moyen, J.F., Stevens, G., Kisters, A.F.M., 2006. Record of mid-Archaean subduction from metamorphism in the Barberton terrain, South Africa. Nature 442, 559–562.

Mshiu, E.E., and Maboko, M.A.H., 2012. Geochemistry and petrogenesis of the late Archaean high-K granites in the southern Musoma-Mara Greenstone Belt: Their influence in evolution of Archaean Tanzania Craton. Journal of African Earth Sciences 66, 1-12.

Mtoro, M., Maboko, M.A.H., Manya, S., 2009. Geochemistry and geochronology of the bimodal volcanic rocks of the Suguti area in the southern part of the Musoma-Mara Greenstone Belt, Northern Tanzania. Precambrian research 174, 241-257.

Munker, C, Worner, G., Yogodzinski, G., Churikova, T., 2004. Behaviour of high field strength elements in subduction zones: constraints from Kamchatka–Aleutian arc lavas. Earth and Planetary Science Letters. 224, 275– 293

Ojala, J.V., Ridley, J.R., Groves, D.I., Hall, G.C., 1993. The Granny Smith gold deposit: the role of heterogeneous stress distribution at an irregular granitoid contact in a greenschist facies terrane. Miner. Deposita 28, 409–419.

Paces, J.B., Miller, J.D., 1993. Precise U–Pb ages of the Duluth Complex and related mafic intrusions, northeastern Minnesota: geochronological insights to physical, petrogenetic, paleomagnetic, and tectonomagmatic processes associated with the 1.1 Ga midcontinent rift system. Journal of Geophysical Research 98, 13997–14013.

Painter, M., 2004. Mineralization and structural architecture of the Geita Hill Shear Zone. Geita Gold Mine Internal Report.

Passchier, C. W., Trouw, R. A. J., 2006. Microtectonics, 2nd ed. Springer-verlag, New York, Berlin, Heidelberg, 362pp.

Percival, J.A., Stern, R.A., Skulski, T., 2001. Crustal growth through successive arc magmatism: reconnaissance U–Pb SHRIMP data from the northeastern Superior Province, Canada. Precambrian Research 109, 203–238.

Peterson, M. E.,A. E. Saal,E. Nakamura,H. Kitagawa,M. D. Kurz, and A. M., Koleszar., 2014.Origin of the “ghost plagioclase” signature in Galapagos melt inclusions: New evidence from Pb isotopes.Journal of Petrology, 55, 2193–2216.

Peterson, V.L., Zaleski, E., 1999. Structural history of the Manitouwadge greenstone belt and its volcanogenic Cu-Zn massive sulphide deposits, Wawa subprovince, south-central Superior Province. Can J Earth Sci 36,605–625

Phillips, G.N., Powell, R., 2010. Formation of gold deposits: a metamorphic devolatilization model. J. Metamorph. Geol. 28, 689–718.

Phillips, G.N., Zhou, T., 1999. Gold-only deposits and Archean granite. Soc. Econ. Geol. Newsl. 37 April 1999.

Polat, A., Kerrich, R., 2001. Magnesian andesites, Nb-enriched basalt–andesites, and adakites from late-Archean 2.7 Ga Wawa greenstone belts, Superior Province, Canada: implications for late Archean subduction zone petrogenetic processes. Contributions to Mineralogy and Petrology 141 (1), 36–52.

Polat, A., Kerrich, R., Wyman, D.A., 1998. The late Archean Schreiber–Hemlo and White River–Dayohessarah greenstone belts, Superior Province: collages of oceanic plateaus, oceanic arcs, and subduction–accretion complexes. Tectonophysics, 289, 295-326.

Porter, C.W.P., 2002. Structural analysis and target generation Kukuluma-Matandani Area, Geita Greenstone Belt, Tanzania. Internal company report.

Quennell, A.M., McKinley, A.C.M., Aiken, W.G., 1956. Summary of the geology of Tanganyika: introduction and stratigraphy. Tanganyika Geol. Surv. Mem. 1 (Pt. 1) 264 pp.

Rapp, R.P., Shimizu, N., Norman, M.D., Applegate, G.S., 1999. Reaction between slab-derived melts and peridotite in the mantle wedge: experimental constraints at 3.8 GPa. Chemical Geology 160, 335–356.

Richards, J. P., Kerrich, R., 2007. Adakite-like rocks: their diverse origins and questionable role in metallogenesis. Economic Geology 102, 537–576.

Ridley, J.R., Mikucki, E.J., Groves, D.I., 1996. Archaean lode gold deposit: fluid-flow and chemical evolution in vertically extensive hydrothermal systems. Ore Geology Reviews, 10, 279-293.

Robert, F., Sheahan, P.A., Green, S.B., 1991. Greenstone Gold and Crustal Evolution. Publication of the Mineral Deposits Division, Geological Association of Canada, pp. 1–252.

Romick, J.D., Kay, S.M., Kay, R.M., 1992. The influence of amphibole fractionation on the evolution of calc-alkaline andesite and dacite tephra from the central Aleutians, Alaska. Contributions to Mineralogy and Petrology 112, 101–118.

Rooney, T.O., Franceschi, P., Hall, C.M., 2011. Water-saturated magmas in the Panama Canal region: a precursor to adakite-like magma generation? Contributions to Mineralogy and Petrology 161, 373-388.

Rudnick, R. L., Gao S., 2003. Composition of the continental crust. See Holland & Turekian 2003, pp. 1–64

Rudnick, R.L., 1995. Making continental crust. Nature 378, 573–578.

Ryerson, F. J., Watson, E. B., 1987. Rutile saturation in magmas: Implications for Ti–Nb–Ta depletion in island-arc basalts. Earth and Planetary Science Letters 86, 225–239.

Sanislav, I. V., Brayshaw, M., Kolling, S. L., Dirks, P. H. G. M., Cook, Y. A. and Blenkinsop, T., 2016. The structural history and mineralization controls of the world-class Geita Hill gold deposit, Geita Greenstone Belt, Tanzania. Mineralium Deposita (10.1007/s00126-016-0660-1)

Sanislav, I.V., Kolling, S.L., Brayshaw, M., Cook, Y.A., Dirks, P.H.G.M., Blenkinsop, T.G., Mturi, M.I., Ruhega, R., 2015. The geology of the giant Nyankanga gold deposit, Geita Greenstone Belt, Tanzania. Ore Geology Reviews 69, 1-16.

Sanislav, I.V., Wormald, R.J., Dirks, P.H.G.M., Blenkinsop, T.G., Salamba, L., Joseph, D., 2014. Zircon U–Pb ages and Lu–Hf isotope systematics from late-tectonic granites, Geita greenstone belt: implications for crustal growth of the Tanzania craton. Precambrian Res. 242, 187–204.

Seward, T. M., 1991. The hydrothermal geochemistry of gold, In: Foster, R. P. (Ed), Gold Metallogeny and exploration. Blackie, pp 37 - 62.

Seward, T.M., 1973. Thio complexes of gold and the transport of gold in hydrothermal ore solutions. Geochim. Cosmochim. Acta 37, 379–399.

Shackleton, R.M., 1995. Tectonic evolution of greenstone belts. In: Coward, M.E., Ries, A.C. (Eds.), Early Precambrian Processes, Special Publications 95. Geological Society, London, pp. 53–65.

Shenberger, D. M., Barnes. H. L., 1989.Solubility of gold in aqueous sulphide solutions from 150 to 350^0C. Geochim.Cosmochim.Acta 53, 269 - 278.

Shirey, S. B., Hanson, G. N., 1984. Mantle derived Archaean monzodiorites and trachyandesites. Nature 310, 222–4.

Sibson, R.H., 2001. Principles of structural control on permeability and fluid flow in hydrothermal systems. In: Richards, J.P., Tosdal, R.M. (Eds.), Structural Controls on Ore Genesis. Reviews in Economic Geology, 14. Society of Economic Geologists, Boulder, Colorado, pp. 25–50.

Sibson, R.H., 2004. Controls on maximum fluid overpressure defining conditions for mesozonal mineralization. Journal of Structural Geology 26, 1127–1136.

Skead, M.B., 2003. Geology and Structure of the Kukuluma Deposit, Geita Greenstone Belt, Tanzania. Company confidential report.

Soderlund, U., Patchett, P.J., Vervoort, J.D., Isachsen, C.E., 2004. The 176Lu decay constant determined by Lu–Hf and U–Pb isotope systematics of Precambrian mafic intrusions. Earth Planet. Sci. Lett. 219, 311–324.

Spandler, C., Pettke, T., Rubatto, D., 2011. Internal and external fluid sources for eclogite-facies veins in the Monviso meta-ophiolite, Western Alps: Implications for fluid flow in subduction zones. Journal of Petrology 52, 1207–1236.

Sperner, B., Müller, B., Heidbach, O., Delvaux D., Reinecker, J., Fuchs, K., 2003. Tectonic stress in the Earth's crust: advances in the world stress map project. in: Nieuwland, D.A. (Ed.), New insights into structural interpretation and modelling. Geological Society of London Special Publication 212, 101-116.

Stalder, R., Foley, S.F., Brey, G.P., Horn, I., 1998. Mineral aqueous fluid partitioning of trace elements at 900-1200 degrees C and 3.0-5.7 GPa: New experimental data for garnet, clinopyroxene, and rutile, and implications for mantle metasomatism. Geochimica et Cosmochimica Acta 62, 1781-1801.

Stern, R. A., Hanson, G. N., Shirey S. B., 1989. Petrogenesis of mantle-derived, LILE-enriched Archaean monzodiorites and trachyandesites (sanukitoids) in southwestern Superior Province. Canadian Journal of Earth Sciences, 26, 168- 171.

Stockley, G.M., 1936. Geology of the south and south-western region of Musoma District. Tanganyika Geol. Surv. Short Pap., 13.

Sun, S. S., McDonough, W. F., 1989. Chemical and isotopic systematics of oceanic basalts: implications for mantle composition and processes. In: Saunders, A.D., Norry, M.J. (Eds.), Magmatism in the Ocean Basins. Geol. Soc. London, London, pp. 313–345.

Sun, Shen-SU., Nesbitt, R.W., 1978. Petrogenesis of Archaean ultrabasic and basic volcanics: evidence from the rare earth elements. Contributions to Mineralogy and Petrology 65, 301-325.

Tatsumi, Y, and Ishizaka, K., 1981. Existence of andesitic primary magma: An example from Southwest Japan. Earth and Planet Science Letters 53, 124-130.

Tatsumi, Y., 2006. High-Mg Andesites in the Setouchi Volcanic Belt, Southwestern Japan: Analogy to Archean Magmatism and Continental Crust Formation? Annu Rev Earth Planet Sci, 34, 467—499.

Tatsumi, Y., 2008. Making continental crust: the sanukitoid connection. Chinese Science Bulletin 53 (11), 1620–1633.

Taylor, S. R. and McLennan, S. M., 1995. The Geochemical Evolution of the Continental Crust Reviews of Geophysics 22-2, 241-265.

Thiessen, R. L., 1986. Two-dimensional refold interference patterns. J. Struct. Geol. 8, 563-573.

Thirlwall M. F., Smith T. E., Graham A. M., Theodorou N., HollingsbP., Davidson J. P., and Arculus R. J., 1994. High field strength element anomalies in arc lavas: source or process? Journal of Petrology 35, 819–838.

Tiepolo, M., Oberti, R., Zanetti, A., Vannucci, R., Foley, S., 2007. Trace-element partitioning between amphibole and silicate melt. In: Hawthorne, F.C., Oberti, R., Ventura, G.D., Mottana, A. (Eds.), Amphiboles: Crystal Chemistry, Occurrence, and Health Issues: Mineralogical Society of America and Geochemical Society, Reviews in Mineralogy and Geochemistry, 67, pp. 417–452.

Tripp, G.I., Vearncombe, J.R., 2004. Fault/fracture density and mineralization: a contouring method for targeting in gold exploration. Journal of Structural Geology 26, 1087–1108.

Tulloch, A.J., Kimbrough, D.L., 2003. Paired plutonic belts in convergent margins and the development of high Sr/Y magmatism: Peninsular Ranges batholith of Baja- California and Median batholith of New Zealand. Geological Society of America Special Paper 374, 1–21.

Twiss, R.J., Unruh, J.R., 1998. Analysis of fault slip inversions: Do they constrain stress or strain rate? Journal of Geophysical Research 101, 8335-8361.

van Achterbergh E., Ryan C.G., Jackson S.E., Griffin, W.L., 2001. Data reduction software for LA-ICP-MS. In: Sylvester P (ed) Laser-ablation-ICPMS in the earth sciences: principles and applications. Mineralogical Association of Canada, Short Course 29, pp 239–243.

van Kranendonk, M.J., 2011. Cool greenstone drips and the role of partial convective overturn in Barberton Greenstone Belt evolution. Journal of African Earth Sciences 60, 346–352.

van Westeren, W., Blundy, J., Wood, B., 1999. Crystal-chemical controls on trace element partitioning between garnet and anhydrous silicate melt. American Mineralogist 84, 838–847.

Vlaar, N.J., van Keken, P.E., van den Berg, A.P., 1994. Cooling of the Earth in the Archaean: Earth and Planetary Science Letters, v. 121, p. 1–18.

Wang, Q., McDermott, F., Xu, J.F., Bellon, H., Zhu, Y. T., 2005. Cenozoic K-rich adakitic volcanic rocks in the Hohxil area, northern Tibet: lower-crustal melting in an intracontinental setting. Geology 33, 465–468.

Weinberg, R.F., van der Borgh, P., 2008. Extension and gold mineralization in the Archaean Kalgoorlie Terrane, Yilgarn Craton. Precambrian Res 161, 77–88

Wiedenbeck, M., Allé, P., Corfu, F., Griffin, W.L., Meier, M., Oberli, F., von Quadt, A., Roddick, J.C., and Spiegel, W., 1995. Three natural zircon standards for U-Th-Pb, Lu-Hf, trace element and REE analyses. Geostandards Newsletter, 19, 1-23.

Wiedenbeck, M., Allé, P., Corfu, F., Griffin, W.L., Meier, M., Oberli, F., von Quadt, A., Roddick, J.C., Spiegel, W., 1995. Three natural zircon standards for U-Th-Pb, Lu-Hf, trace element and REE analyses. Geostandards Newsletter, 19, 1-23

Windley, B.F., 1995. The Evolving Continents, 3rd ed. John Wiley, Chester, 526 pp.

Wood, D.A., Gibson, I.L., Thompson, R.N., 1976. Elemental mobility during zeolite facies metamorphism of the Tertiary basalts of eastern Iceland. Contributions to Mineralogy and Petrology 55, 241-254.

Woodhead J., Eggins S., Gamble J., 1993. High field strength and transition element systematics in island arc and back-arc basin basalts: Evidence for multi-phase extraction and a depleted mantle wedge. Earth Planet. Sci. Lett. 114**,** 491–504.

Zegers, T.E., van Keken, P.E., 2001. Middle Archean continent formation by crustal delamination. Geology 29, 1083–108.

Zegers, T.E., White, S.H., de Keyzer, M. and Dirks, P.H.G.M., 1996. Extensional structures during deposition of the 3460 Ma Warrawoona Group in the eastern Pilbara Craton, Western Australia. Precambrian Research 80, 89-105

Zeh, A., Gerdes, A., Barton, J.M., Jr., 2009. Archean accretion and crustal evolution of the Kalahari Craton—the zircon age and Hf isotope record of granitic rocks from Barberton/Swaziland to the Francistown Arc. Journal of Petrology 50, 933–966.

APPENDICES

Appendix 1. Map resources used

In the course of this study the following historical maps were used in the construction of figures, stratigraphic columns and sections:

Previous regional geological mapping conducted in the Matandani-Kukuluma area;

a) Mapping done during the initial exploration phase with maps held in the Geita Gold Mine database;
    (1) Geological map compiled by Hatari Mjinja in 2006
    (2) Geological map compiled by Hatari Mjinja in 2005
    (3) Geological map compiled by Hatari Mjinja in 2004
    (4) Geological map compiled by Hatari Mjinja in 2003
b) Geological mapping done during the PhD by contractor staff;
    (1) Geological map of the Kukuluma access road compiled by Tom Blenkinsop in 2011.
    (2) Geological map of the Matandani pit compiled by Ioan Sanislav in 2011
    (3) Geological map of the Kukuluma pit compiled by Ioan Sanislav in 2011
    (4) Geological map of the Kukuluma pit compiled by Mathew Brayshaw in 2013
    (5) Geological map of the Kukuluma pit compiled by Paul Dirks in 2011
c) Regional geological mapping of the Kukuluma terrain including Matandani and Kukuluma pits by Shimba Kwelwa in the period from 2013-2014.

Geophysical datasets used in the compilation of the geological map for the Kukuluma terrain include:

(a) U (red) –Th (blue) – K (white) radiometric map.
(b) Aeromagnetic map (xcal_amf_avg1) showing the iron-rich lithologies as magnetic highs

Examples of various map types are displayed in Figure A1.1

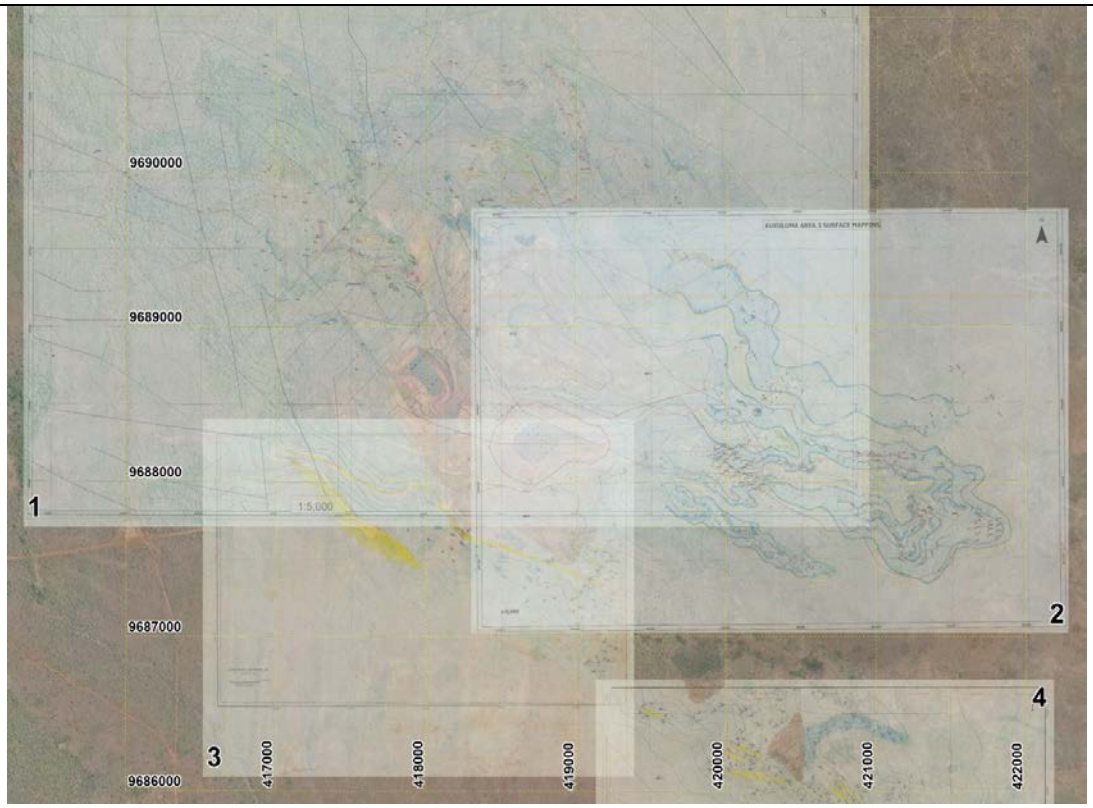
9690000
9689000
9688000
9687000
9686000
417000
418000
419000
420000
421000
422000
1
2
3
4

(a)

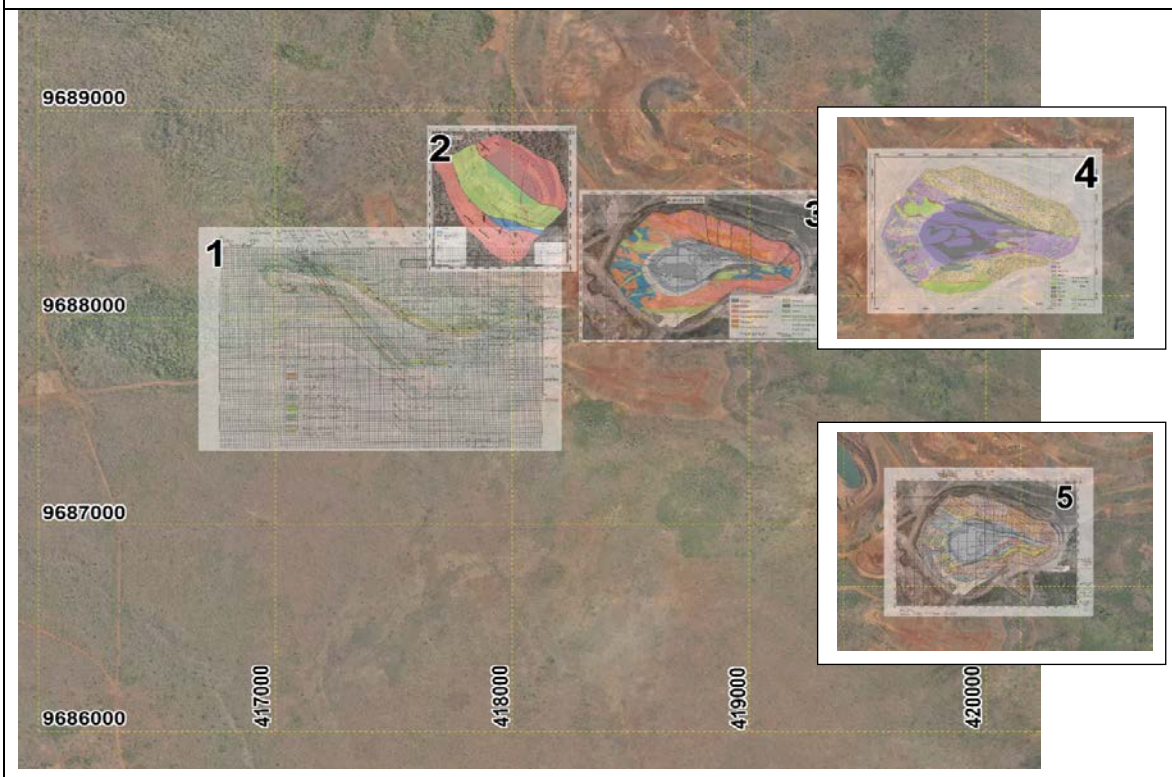
9689000
9688000
9687000
9686000
417000
418000
419000
420000
1
2
3
4
5

(b)

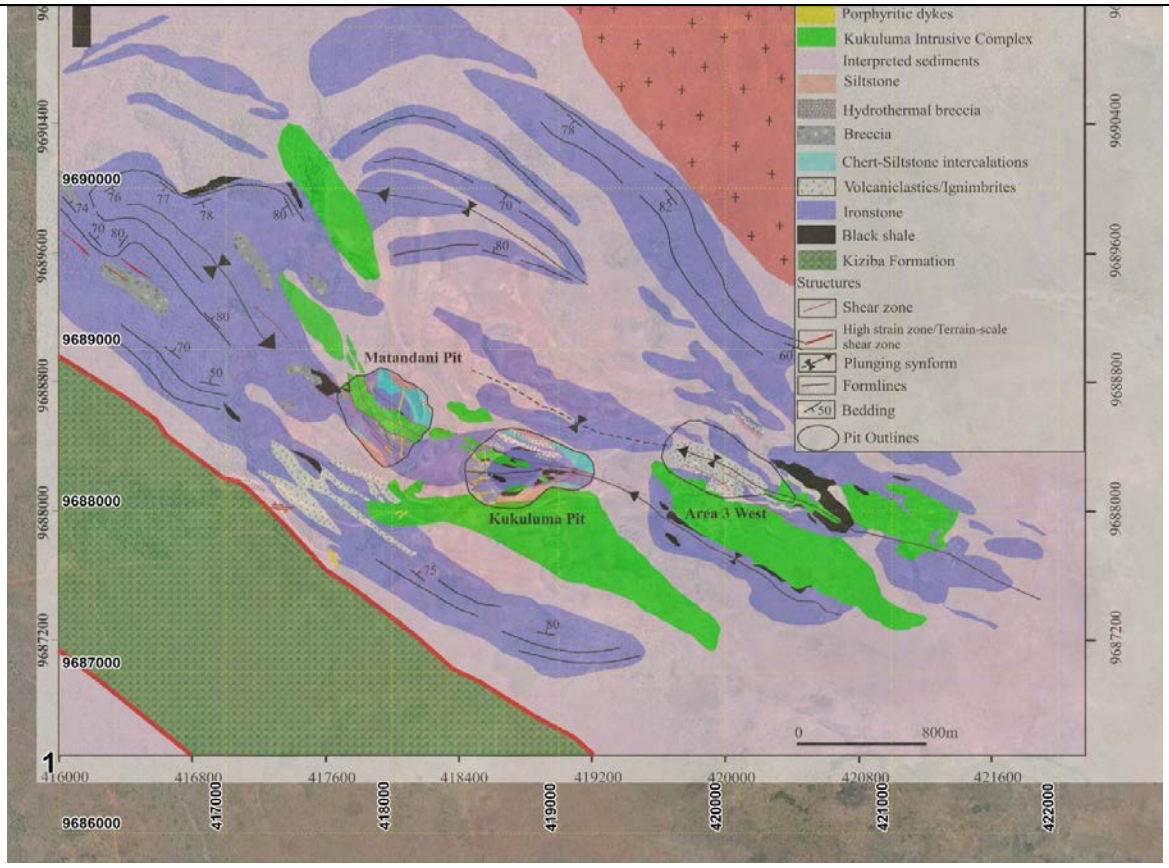
Porphyritic dykes
Kukuluma Intrusive Complex
Interpreted sediments
Siltstone
Hydrothermal breccia
Breccia
Chert-Siltstone intercalations
Volcaniclastics/Ignimbrites
Ironstone
Black shale
Kiziba Formation
Structures
Shear zone
High strain zone/Terrain-scale shear zone
Plunging synform
Formlines
Bedding
Pit Outlines
Matandani Pit
Kukuluma Pit
Area 3 West
0
800m
1
9690000
9689000
9688000
9687000
9686000
416000
416800
417600
418400
419200
420000
420800
421600
417000
418000
419000
420000
421000
422000

(c)

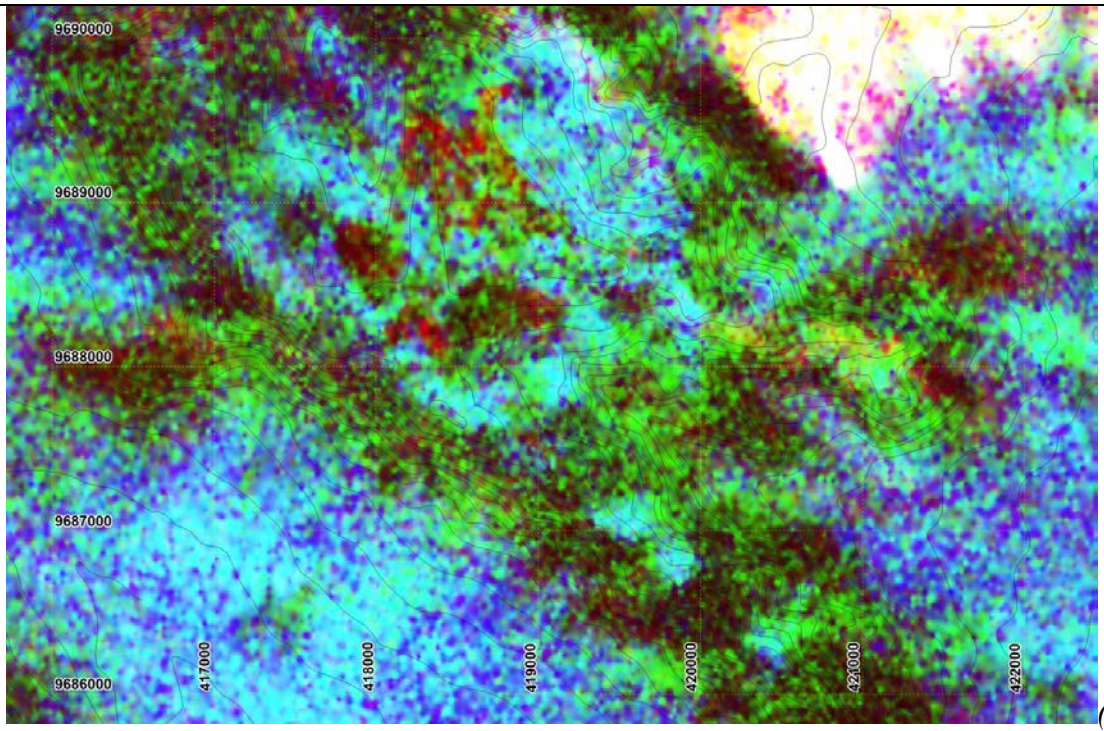
9690000
9689000
9688000
9687000
9686000
417000
418000
419000
420000
421000
422000

(d)

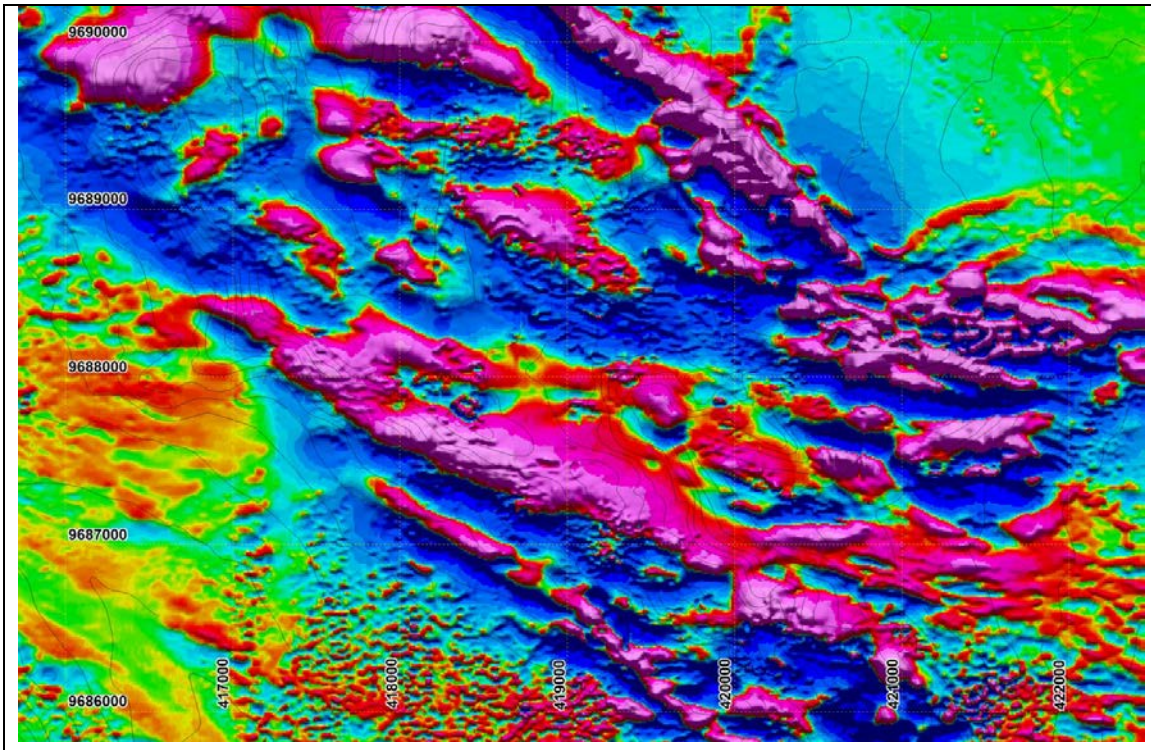

(e)

Figure A1.1. Examples of various types of maps used in the compilation of data presented in this thesis. (a) historical map coverage across the area of interest; (b) and (c) maps of Matendai and Kukuluma pits produced during this study; (d)radiometric map across the area; (e) aeromagneti map across the area.

Using these various data sets together with new mapping and drill core logging, the following geological maps were produced during this study (e.g. Figs 1.3a and b).

1. A regional geological map of the Kukuluma terrain compiled from historical mapping, drill core information, geophysical datasets and mapping by Shimba Kwelwa in 2013-2015 (Fig.1.3a).
2. Detailed geological map of the Matandani and Kukuluma pits compiled from historical mapping, drill core information and mapping by Shimba Kwelwa in 2013-2015 (Fig. 1.3b).

Appendix 2. Comparison of new stratigraphic units with historical log data

Based on analyses of lithological units in drill hole, the stratigraphy can be condensed into 5 volcano-sedimentary units and 4 main types of intrusive lithologies. Summaries for these various lithologies and comparisons to their historical names and logging codes are presented in Table A2.1.

Historical names/ codes	Standardized nomenclature and descriptions	Thickness in drill cores(m)
VOLCANO-SEDIMENTARY UNITS		
• Black shale with arsenopyrite nodules (BSHAsP), • Graphitic black shale (BSHG), Pyritic black shale nodules (BSHP), • Black shale with pyrrhotite nodules (BSHPr), • Carbonaceous pelite (CP), Carbonaceous shales (CSH or SHC), • Graphitic shale (SHG), • Pyritic black shales (SHPN) • Shale (SH)	**Black shale** • Very fine grained, dark coloured rock. • Sometimes contains pyrrhotite ± pyrite nodules, which are syn-sedimentary or early-diagenetic features. • Occurs near the stratigraphic base of the volcano-sedimentary units.	Few cm -14m
• Banded Iron Formation (BIF), • BIF-Chemical (BIFC), • Oxide Facies BIF (BIFO), • BIF Undefined (BI) • BIF-Sedimentary (BIFS). • Chert (CH)	**Ironstone** • Dominated by variable thicknesses of chert-magnetite interbands, ~15-30cm thick, with local thinner mudstone/shale units. • Chlorite and grunerite do occur on the margins between chert and magnetite or chert and chloritic mudstone layers. • Intra-formational conglomerates are observed within the Ironstones having dominantly chert ± mudstone clasts in a chloritised siltstone and /or mudstones matrix. These conglomeratic units occur as intraformational units, layer-parallel to the Ironstones. The clasts within them are randomly oriented whereas their boundaries are clearly layer parallel to Ironstone. Their thicknesses range from 3cm-53m as observed in the drill cores. • Variable breccia zones are observed within the ironstones ranging from hydrothermal breccia associated with replacement textures with vein – networks, that cut the layering randomly. Some of the breccia zones are a result of reactivation of early intra-formational conglomerates associated with the emplacement of the intrusives and some are related to the hinge zones of the fold systems. Likewise, the thicknesses of this breccia vary from 1m – 30m thick. **Chert** • These occur as relatively thinner layers or massive to banded highly silicified laminated sedimentary units. Normally interbedded with ironstones.	Few cm – 70m
• Acidic tuff (AT),	**Volcaniclastics**	Few cm – 66m

• Agglomerates (AG), • Crystal tuff (CT), • Intermediate tuff (IT), • Intermediate Undifferentiated (IM) and • Lithic tuff (LT)	• Fine–medium grained intermediate to felsic, layered unit. • Composed of cherty-like fragments or glassy-shards possessing reaction rim-like structures. • The shapes of the fragments are variable raging from angular, sub-rounded to ellipsoidal. • Occassional chert layering parallel to the volcaniclastic layers is observed. • The volcaniclastic package includes ignimbrites and tuffaceous sediments. • Occurs interbanded with Ironstone.	
• BIF-Sedimentary (BIFS), • Greywacke (GWAC|), • Meta-Sandstones (MetaSS), • Meta-psammite (Metapsammite) • sandstones (SS).	**Intercalated Chert-Siltstone** • The package is associated with interlayered chert and siltstone units. • The individual thicknesses of the chert layers and siltstone are variable ranging from 3cm – 30cm. • In places, relatively narrow zones composed of greywacke and mudstone are found to be intercalated with this package. • Intense grunerite and chlorite alteration are visible in the siltstone unit.	Few cm- 37m
• Siltstones (ST), • Meta-siltstones (MetaST), • sandstone units (SS) • mudstone units (MSS).	**Siltstone** • These are fine-grained sedimentary units with local occurrences of sandstone. • The unit occurs interlayered with chert-siltstone intercalations where the boundary between the two is gradational.	Few cm – 190m
INTRUSIVE UNITS		
• Andesite (AN), • Dacite (DA), • Diorite (DI), • Dolerite (DL), • Intermediate Tuff (IT), • Acidic tuff (AT), • Intermediate undifferentiated (IM) • Sandstones (SS).	**Diorite-Monzonite ± Tonalite** • Medium- to fine-grained, intermediate coloured unit. • Composed of plagioclases and hornblendes. Occassional occurrence of a Tonalite in Area 3 West with an increased amount of quartz phenocrysts in it. However, an exact cross-cutting relationship with the Diorite is not recognized in the drill cores. The fact the Tonalite is also termed as quartz –diorite then this unit will be grouped as Diorite. • These intrusives appear to cross-cut the volcano-sedimentary units in the Kukuluma terrain. • It is chloritized and carbonate altered. The carbonate alteration is evidenced by intense randomly oriented vein networks. • These intrusives form part of the Kukuluma Intrusive Complex (KIC).	6-115m
Felsic porphyry (FP)	**Granodiorite** • This is an intermediate coloured, porphyritic dyke. • Composed of plagioclase phenocrysts in a fine-grained groundmass. Rarely, biotites are visible within the unit. • This is the youngest intrusive unit in the area and cuts both the volcano-sedimentary units and the intrusive units.	2m

Table A2.1: Standardized nomenclature and descriptions for the volcano-sedimentary units and intrusive rocks found within the Kukuluma terrain, with comparisons to historical logging codes.

A2.1 Volcano-sedimentary units

The volcano-sedimentary rocks in the Kukuluma terrain comprise 5 units, which, from old to young include: black shale, ironstone, volcanoclastic sediment, intercalated chert-siltstone and massive siltstone (Fig. 2.2).

The stratigraphically lowermost unit in the sequence is black shale, variably logged as: black shale with arsenopyrite nodules (BSHAsP), graphitic black shale (BSHG), pyritic black shale nodules (BSHP), black shale with pyrrhotite nodules (BSHPr), carbonaceous pelite (CP), carbonaceous shales (CSH or SHC), graphitic shale (SHG), pyritic black shales (SHPN) and shale (SH) (Table A2.1). The unit reaches a maximum thickness of ~14m in drill core. The shale is generally only outcropping in areas that have been mined or have been cleared for drilling and in places next to, or within intrusive margins.

A well-bedded ironstone unit overlies the graphitic shale (Fig. 2.2). Historically this ironstone unit has been logged as Banded Iron Formation (BIF), BIF-chemical (BIFC), Oxide Facies BIF (BIFO), BIF undefined (BI) and some as the BIF-Sedimentary (BIFS) (Table A2.1). The ironstone package is widely distributed across the entire area (Fig. 1.3), and has a distinct magnetic signature on geophysical data sets. Within the unit logged as ironstone, lenses of intra-formational conglomerate are locally observed.

The ironstone unit is overlain by a volcaniclastic unit that reaches a maximum thickness of 66 m in drill core (Fig.A3.1c). Historically this unit has been logged as Acidic tuff (AT), Agglomerates (AG), Crystal tuff (CT), Intermediate tuff (IT), and Intermediate Undifferentiated rock (IM) and Lithic tuff (LT) (Table A2.1). All the historical logging in the database mentioned the tuffaceous nature of the rock.

In parts of Kukuluma pit, the ironstone unit transitions into an interbedded chert-siltstone unit consisting of chert layers interbedded with sandstone-siltstone beds that vary in thickness from 1.5 m to less than 10 cm thick (Fig. 3.8a). Historically, the chert-siltstone unit has been logged as Siltstones (ST), Meta-siltstones (MetaST), sandstone (SS) and mudstone (MSS). The maximum thickness of this unit in drill core is 30 m.

The intercalated chert-siltstone layers transitions into a massive siltstone Unit that reaches a maximum thickness of 190m in drill core. Historically this unit has been logged as BIF-Sedimentary (BIFS), Greywacke (GWAC), Meta-Sandstones (MetaSS), Meta-psammite (Metapsammite) and sandstones (SS). This unit may be a lateral equivalent of the volcanoclastic unit, and appears to be interlayered with volcanoclastic sediments; however, they have been logged as a distinct lithostratigraphic package. The Chert-Siltstone and

Siltstone Units are widely distributed in the area and occur as extremely weathered rock previously mapped as tuffaceous sediment.

A2.2 Intrusive units

Four main types of intrusives were identified in drill core within the Kukuluma terrain: diorite, monzonite, tonalite and granodiorite (see chapter 4 for details), however these units are hard to differentiate in drill core. Therefore, diorite is the adopted name in this study for the purpose of geological modeling. Units identified as diorite on geochemical grounds (see Chapter 4) were historically logged as Andesite (AN), Dacite (DA), Diorite (DI), Dolerite (DL), Intermediate Tuff (IT), Acidic tuff (AT), Intermediate undifferentiated (IM) and Sandstones (SS) (Table A2.1).

Granodiorite dykes form a distinct set of intrusives in the Kukuluma terrain, and have historically been logged as Felsic porphyry (FP) (Table A2.1).

Appendix 3. Descriptions of type sections from drill core

In this appendix, typical geological observations identified in drill core and used in 3-D modelling are presented. A full analysis of the deformation and intrusive history of the area as recognized in these drill holes, is presented in chapter 3. Summary diagrams of typical drill core intersections for each of the three major deposits are shown in figure A3.1. Each of these type sections from drill core are described below.

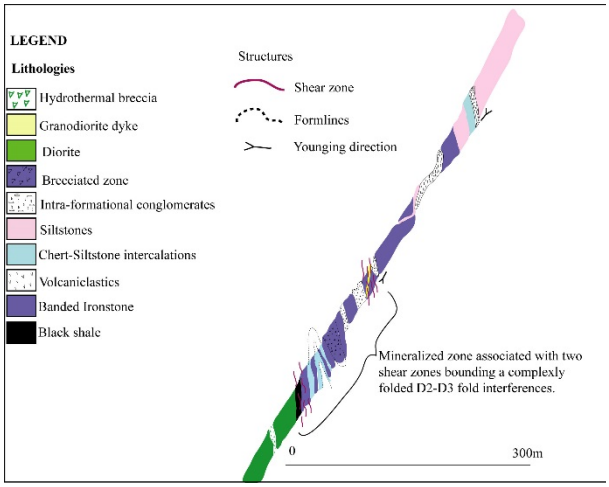

(a)

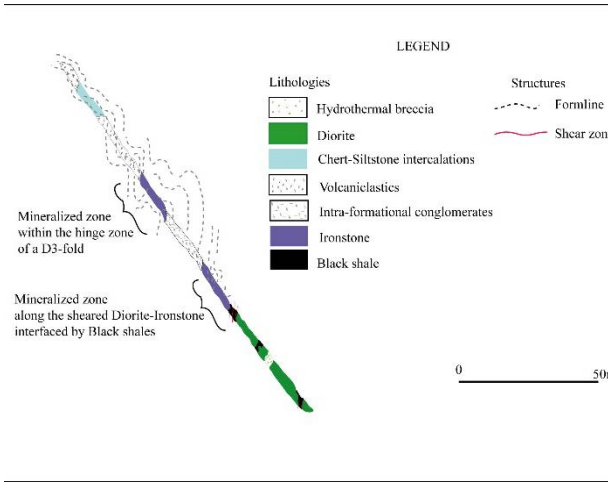

(b)

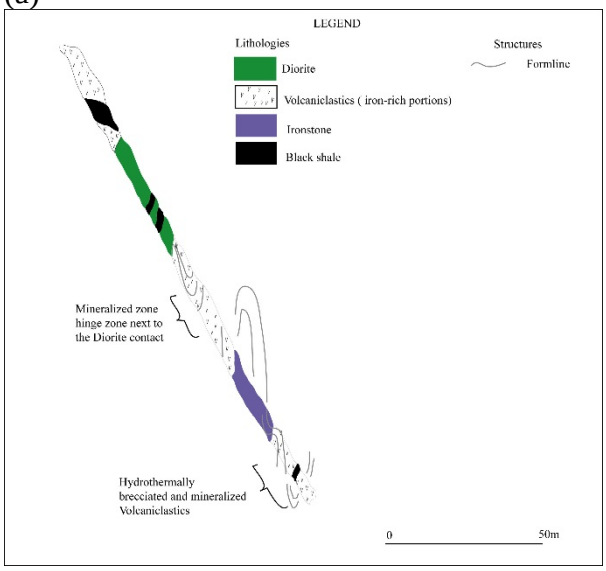

(c)

Fig. A3.1 Typical examples of relationships between lithologies, folds, shear zones, intrusions and mineralization as observed in drill core. (a) drill hole ID: MTRD0023 from Matandani pit; (b) drill hole ID: KKRD0002 from Kukuluma pit; (c) drill hole ID: AWDD0003 from Area 3 West pit.

All the drill hole sketches are projected in the right orientation with respect to the drilling azimuths in the respective pits. Both are drawn looking north with respect to the Kukuluma Mine Grid.

A3.1 Matandani type stratigraphy from drill core ID: MTRD0023

A total of seven lithological units were identified during the re-logging exercise of Matandani drill hole: MTRD0023 (Fig. A3.1a), which serves as a reference hole for the type

stratigraphy in the Matandani Pit. These units are black shale, ironstones, volcaniclastics, chert-siltstone intercalations, siltstones, diorites and granodiorite dyke.

From 495-605 m (~110m thick) ironstone is inter-bedded with both chert-siltstone and intra-formational conglomerate (Fig. A3.1a). In this interval the ironstone unit appears thicker (~30 m) in the hinge zone of a fold and progressively gets thinner (~10 m) towards the limb zones. The Intra-formational conglomerates are locally brecciated due to folding. These observations show that, there is considerable thickness variation in lithologies down-hole and possibly along strike depending on the position of the lithological unit in a fold system**.**

The drill core observation shows that, the diorite-ironstone contact is not intrusive. The interface between the diorite and ironstone is occupied by black shale between 606 m and 609 m. Over this interval, the black shale and the diorite are overprinted by a well-developed shear fabric dipping steeply to the northeast (Fig. A3.1a). The shear fabric can be traced for about 26 m into the diorite where it overprints early carbonate veins. Within the first 5 m from the contact, the quartz-carbonate-pyrrhotite veins are rotated into parallelism with the shear fabric. Assay results from the sheared diorite contact returned ~1 g/t Au. Intense hydrothermal brecciation was observed within the diorite at 681-686 m. The diorite fragments are randomly oriented in a carbonate dominated matrix. The carbonate matrix contains minor amounts of disseminated pyrrhotite and arsenopyrite. Assay results indicate 1.11g/t Au at 681.5m within this hydrothermally brecciated zone in the diorite.

The black shale unit is in contact with strongly brecciated ironstone composed of chert clasts in a black shale matrix with disseminated pyrrhotite. The clasts constitute 70% of the total rock mass. The bedded ironstone next to this brecciated zone is well-layered, and replacement of magnetite by pyrrhotite is common. Within the ironstone unit, a relatively weak shear fabric is observed. However, a complex network of fractures and veins which are in-filled by silica-pyrrhotite-arsenopyrite ± carbonate ± chlorite are observed. The assay results over this interval returned an average of ~ 2.5g/t Au. The higher gold values (> 3.0g/t Au) are found within ironstone that is highly fractured, intensely silicified, and where the magnetite is completely replaced by pyrrhotite. Intra-formational conglomerate, inter-layered with ironstone has low gold values < 0.5 g/t Au.

Apart from the main shear zone at the diorite-ironstone contact, a subordinate shear zone is developed through the hinge zones of a prominent fold observed in the drill core at 422-440 m (~ 18 m thick; Fig. A3.1a). This shear zone overprints the granodiorite dyke

which cuts through the folded sequence. The plagioclase phenocrysts and the groundmass of the granodiorite dyke show a preferred orientation which is parallel to the shear fabric. Where the shear zone cuts across ironstone and volcanoclastics a well-developed shear fabric is observed.

From 420 m to 600 m the hole contains a ~180 m thick mineralized zone bounded by two shear zones (Fig. A3.1a). However, gold mineralization is not uniformly distributed and most of the high grade gold is concentrated in ironstone layers while the chert-siltstone, volcaniclastic and intra-formational conglomerates units record low gold values (<0.5g/t Au).

A3.2 Kukuluma type stratigraphy from drill core ID: KKRD0002

Five rock units were identified in drill hole KKRD0002, which serves as a reference hole for the stratigraphy in Kukuluma pit, including: black shale, ironstone, volcanoclastics, chert-siltstone and diorite.

The diorite and ironstone units are never in direct contact in this hole. Instead they are everywhere separated by a thin layer of strongly sheared black shale. The shear fabric dips steeply northeast. The first 2 meters of diorite is also foliated (Fig. A3.1b). This shear zone is ~ 13 m thick down the hole and can be observed from 396-410 m. It is associated with intense carbonate alteration. Within the diorite, zones of hydrothermal breccia (example at 458 m) with a carbonate rich matrix can be found.

The ironstone that overlies the sheared black shale unit is only weakly sheared. In general the ironstone is well-layered with pyrrhotite replacing magnetite. An intense network of micro-fractures that are in-filled by pyrrhotite-carbonate veins is observed at 372-396 m. These micro-fracture networks are better observed in the chert layers where they are in-filled by pyrrhotite. The whole zone is intensely silicified. These micro-fractures indicate normal movement based on the displacement of the ironstone layers. Locally, within the ironstone unit the micro-fractures interconnect and form brecciated zones. It is within these intensely fractured zones that high gold values have been recorded.

Between 260-266m, a zone of moderately silicified and chloritized ironstone was observed. The ironstone preserves chert-magnetite layering. Minor amount of pyrrhotite has replaced the magnetite layers. The amount of micro-fracture development within this zone is minimal and the micro-fractures cut across the layering at right angles. These micro-fractures are in-filled with pyrrhotite. The gold grade within this zone is ~ 0.51g/t Au. This zone appears to be located within the hinge zone of a fold (Fig. A3.1b).

General observations from this drill core show that, high grade gold mineralization is localized in ironstones that are highly fractured and intensely silicified, carbonate altered and well supplied with disseminated pyrrhotite and arsenopyrite. Spatially, the ironstones appear to occur closely to the sheared diorite contact in a complexly folded pattern. The relatively lower grade gold values are found in ironstones within folded domains not linked to any clear shear zone or diorite contact, and in the chert-siltstones and volcanoclastics that appear to be spatially associated with the shear zone or the sheared diorite contact (Fig. A3.1b).

A3.3 Area 3 West type stratigraphy from drill core: AWDD0003

Four lithological units were identified during logging in drill hole AWDD0003, which is taken as a type section for the Area 3 West area. These are black shale, ironstones, volcaniclastics and diorite. The geology along the drill hole shows complex fold interferences as seen at 238-270 m (Fig. A3.1c). Within this folded zone, a volcaniclastic package (~32 m thick) intercalated with a relatively thin (~2 m thick) pyrrhotite-nodules-rich black shale is observed. Within the volcaniclastic unit, a ~22m thick, hydrothermal breccia zone was observed that spatially occurs along the hinge zone of the fold system. This observation shows that, there is a connection between the formation of breccia and the hinge zone of the fold system. These breccia zones appear to be steeply dipping at 80° to the west (Fig. A3.1c). Similar hydrothermal breccia zones were observed at 148-160 m within the hinge zone of a fold in volcaniclastics. This breccia zone shows volcaniclastic fragments in a quartz-carbonate matrix with disseminated pyrrhotite grains. The thickness of the volcanoclastic unit varies from the hinge zones where it is thicker to the the limb zone where it thins out.

The diorite-volcaniclastic contact is intrusive with the diorite truncating layering. This contact is overprinted by a weak foliation that dips ~ 75 - 80° west. The diorite is ~30 m thick; medium to fine grained and contains black shale xenoliths.

Gold mineralization is found within intensely brecciated material within the volcaniclastic unit (~24 m thick down the hole) with some mineralization along minor traces of steeper (~80° dipping towards W) foliations at 262 m that might possibly be local shear zones. Specifically, the mineralized zone is ~ 17 m thick from 241-258 m based on a cut-off grade of 0.5g/t Au. This volcaniclastic unit is intensely silificied and carbonate altered. The unit is composed of glassy-fragments of different shapes ranging from sub-rounded to ellipsoidal (example at 258 m depth) in a greenish coloured matrix. In places, these fragments are shattered by quartz-carbonate veins and in-filled by pyrrhotite veins. The entire

volcaniclastic unit within this zone is infiltrated by disseminated pyrrhotite and local arsenopyrite, which occur as clusters and some of them occur as fracture fill within the intensely fractured zones. Similar mineralization textures are observed with the volcaniclastic unit at 149-160 m. Within this zone, an intense hydrothermal breccia associated with intense carbonate ± chlorite alteration and disseminated pyrrhotite and some arsenopyrites are observed.

In general gold mineralization is linked to a ~20 m thick hydrothermally brecciated volcaniclastic unit that is associated with carbonate-chlorite-pyrrhotite ± arsenopyrite alteration. These hydrothermally brecciated zones occur along the hinge zones of folds (Fig. A3.1c). In addition, the hydrothermally brecciated zone at ~150 m depth is positioned in close proximity to the diorite contact.

Appendix 4. Cross sections used in 3-D modelling

A total of nine cross sections were constructed across the Matandani deposit, four across the Kukuluma deposit and three across Area 3 West (Fig. A4.1).

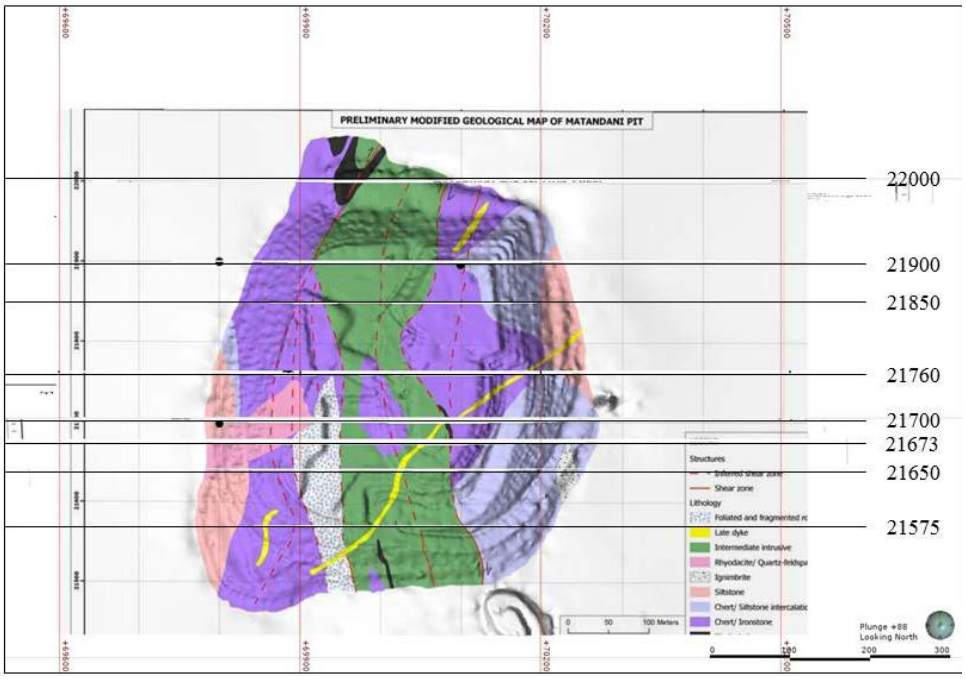

(a)

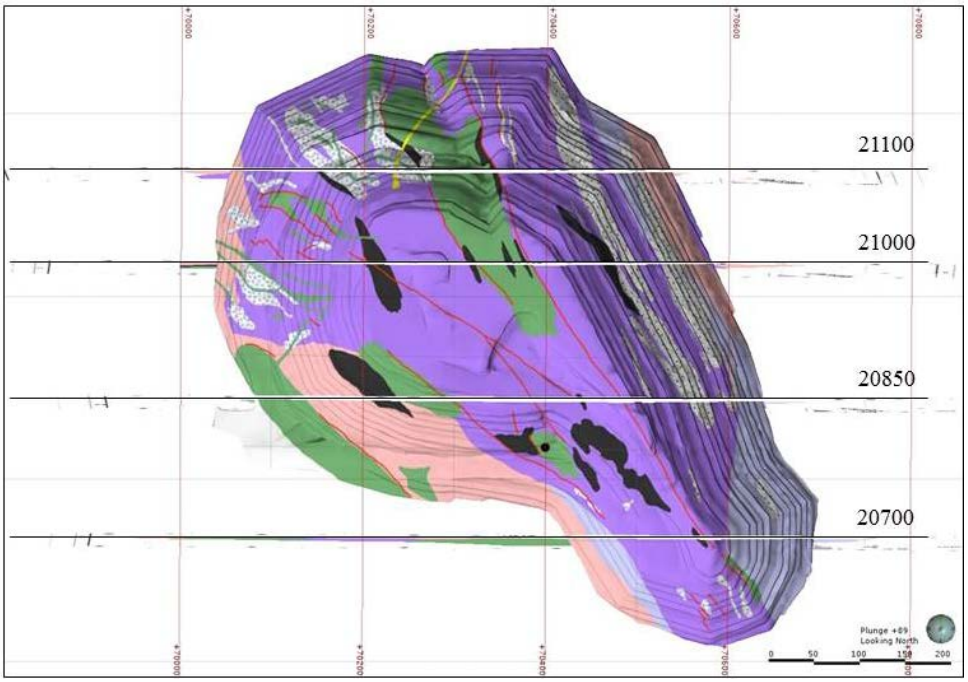

(b)

Figure A4.1. Geological maps showing the position of the section lines across the Matandani deposit (a), and Kukuluma deposit (b). The sections form the basis of 3-D models for the ore bodies. In both images the view is north with reference to the Kukuluma Local Mine Grid.

Sections were constructed by hand considering: bedding orientation, younging directions and folding. Examples of three sections are presented in figure A4.2. Results of the 3-D modelling for each of the ore bodies are shown in Figures A5.1, A5.2 and A5.3.

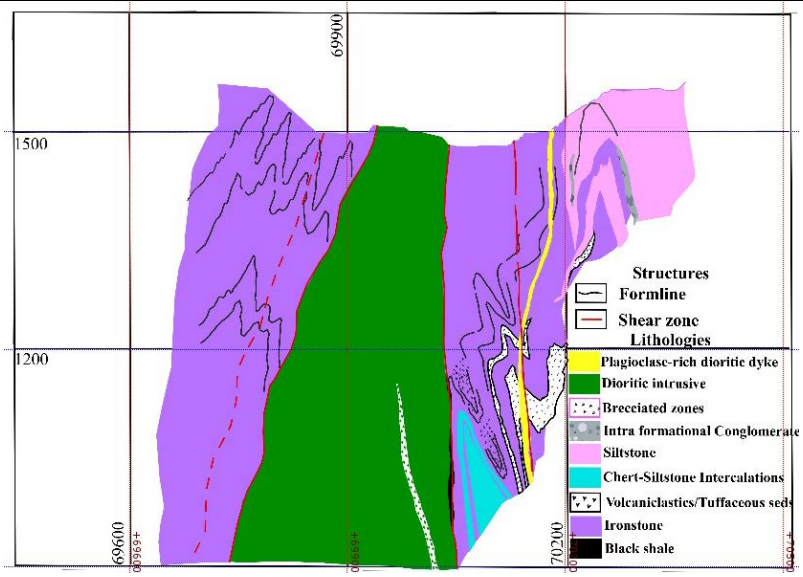

(a)

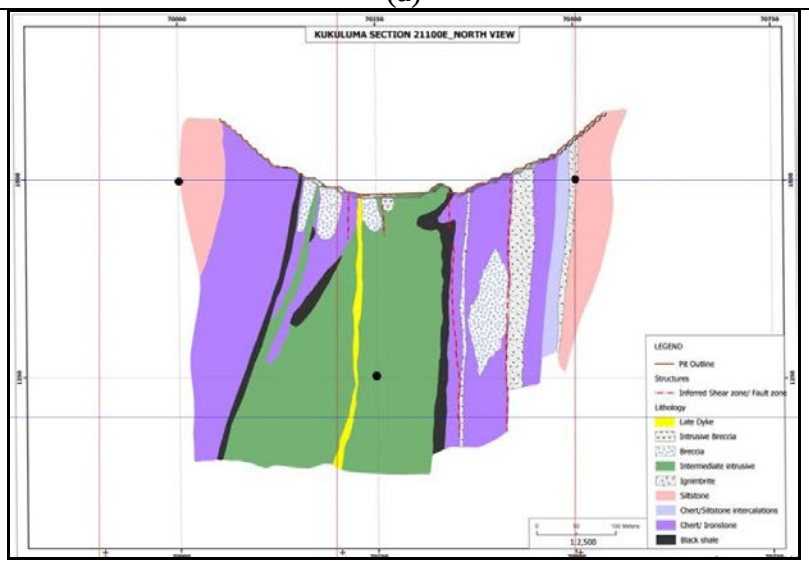

(b)

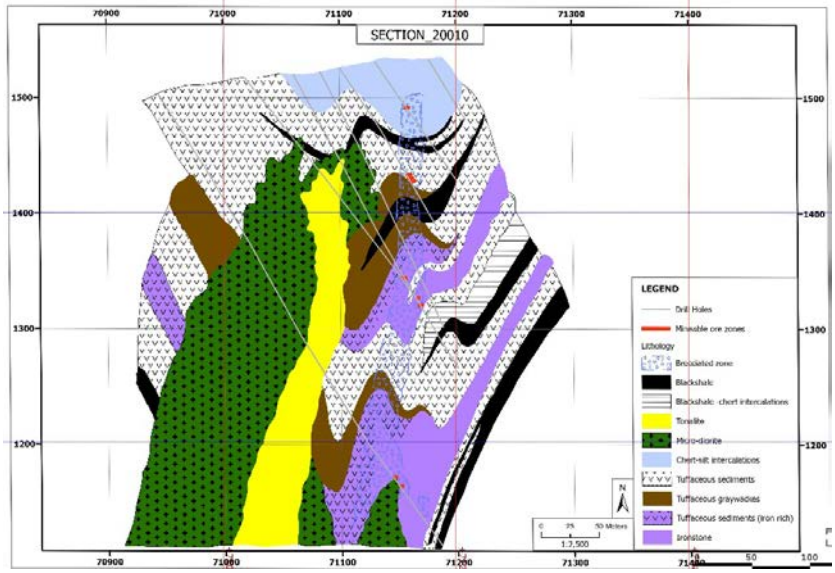

(c)

Figure A4.2. Examples of geological cross sections through the three deposits. (a) cross-section 21760 through the Matandani deposit; (b) cross-section through the Matandani deposit; (c) cross-section 20010 through the Area 3 West deposit. Sctions drawn with Leapfrog Geo software looking north with respect to the Kukuluma Mine Grid.

Appendix 5. Results from Leapfrog modeling

The key findings from the leapfrog modeling are described below; this information provides background information to the deformation scheme presented in Chapter 3.

A5.1 Matandani deposit

Geological cross-sections (e.g. Fig. A4.2) generated for this deposit from the 3-D geological model indicate that gold mineralization is spatially associated with shear zones that utilize the contact between the intrusive diorite and ironstone units.

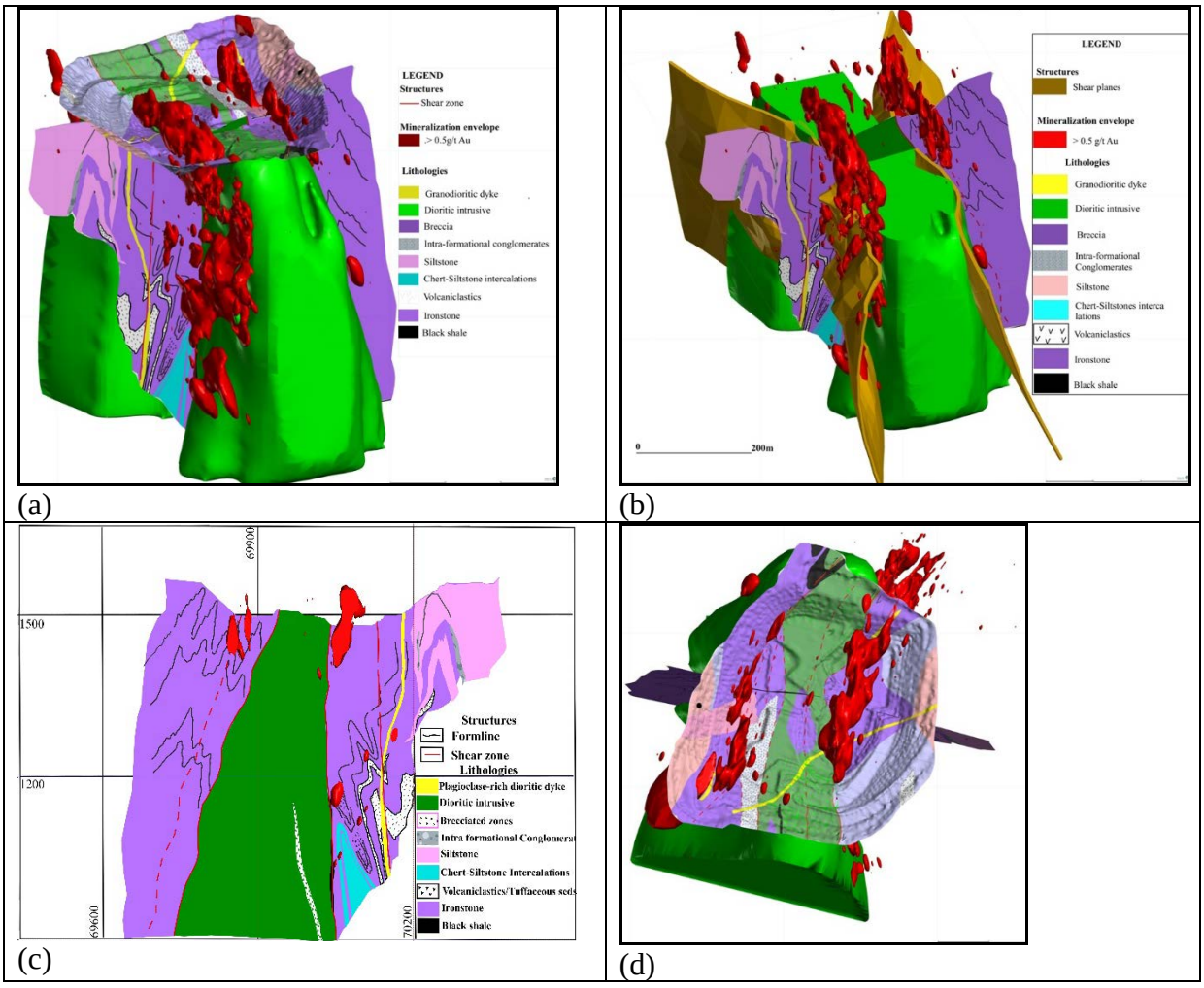

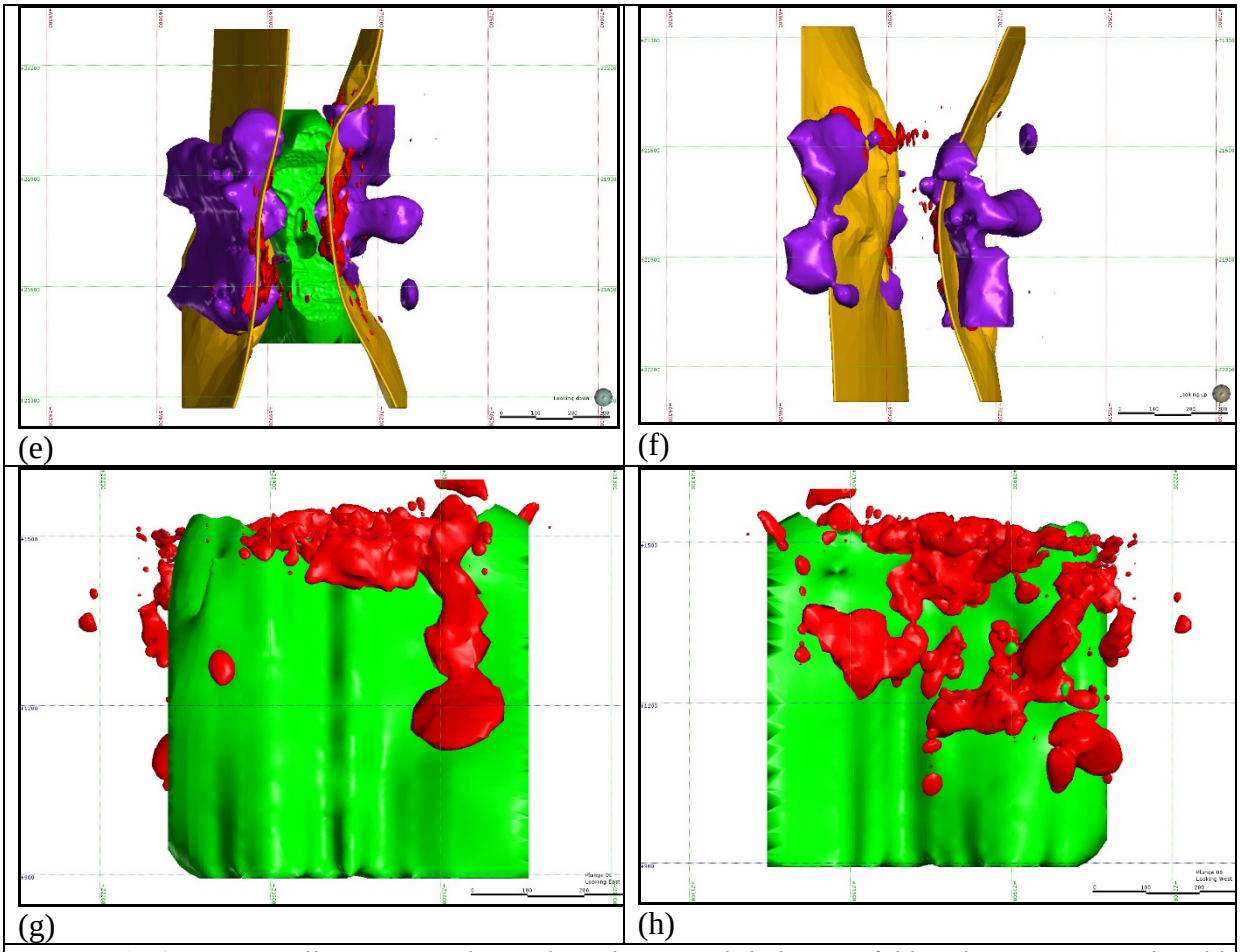

Figure A5.1. Images illustrating relationships between lithologies, folds, shear zones and gold mineralization for the Matandani deposit. (a) 3D model showing the mineralized sheared diorite-ironstone contact. The image was taken looking SW with respect to the local grid; (b) model showing the spatial relationship between the shear zone and mineralization envelope. The image was taken looking SW; (c) Geological cross-section 21760 showing the relationship between the diorite, ironstones with fold interference patterns, shear zone and mineralization envelope. The image was taken looking N; (d) Top view of the deposit showing the spatial relationship between the diorite and the poly-folded ironstones, the granodiorite dyke, the shear zone and mineralization envelope. The image was taken looking NE; (e) 3D model showing the relationship between the diorite, irregular shapes of ironstones, shear zones/planes and the ore envelopes. The image was taken looking N; (f) A view from the bottom of the 3D model showing the relationship between the ironstones being cut by the shear zone that are associated with gold mineralization;(g) Long section view of the Matandani deposit looking W; (h) Long section view of the Matandani deposit looking E

.

Along strike, the shapes of the diorite intrusion change in orientation from north-south to northeast trending defining a fold-like shape observable along the mid-western and eastern contacts between the diorite and ironstone units. The width of the ironstone unit along this folded portion of the eastern diorite-ironstone contact appears to widen (Fig.A5.1). Within this thickened zone of ironstone a wider (~113 m apparent thickness viewed from above) mineralized zone (ore envelope) is observed. A long section view along the eastern diorite–

ironstone contact shows a patchy ore envelope with some variable plunges towards south and north. This relationship spatially coincides with changes in the ironstone geometries down-dip (Fig.A5.1h), probably linked to folding.

Only a few diamond drill holes were drilled into the western diorite-ironstone contact zone. However, use was made of the available rock chip information together with the deposit`s surface geology to generate a geological model for this part of the deposit. The irregular orientation of the diorite-ironstone contact characterized by indentations, described for the eastern part of the deposit also occurs on the western side and towards the southwestern part of the deposit (Fig.A5.1g). Within these indentations along the diorite contact, a relatively greater thickness for the ironstone unit is found. The areas with thicker ironstone coincide with a widening of the ore envelope, spatially associated with a shear zone along the diorite-ironstone contact (Fig.A5.1d-e). A closer look along the southwestern diorite–ironstone contact shows patchy mineralization within the intra-formational conglomerate that is inter-banded with the ironstone unit (Fig.A5.1d). The patchy nature of the orebody within this unit occurs in places where the unit is cut by the shear zone.

The northwestern diorite ironstone contact shows some bending. However, these bends do not correlate with the shape of the orebody as the latter becomes progressively thinner and eventually become patchy towards the northnorthwest. Observations made from the long section view on the western diorite-ironstone contact show a consistent plunge to the southwest and patchy orebody shape towards the north (Fig.A5.1g).

A5.2 Kukuluma deposit

The results obtained for the Kukuluma deposit show two main, elongated, irregular lenses of Diorite that have a general northwest-southeast trend (relative to the Kukuluma Mine Grid). The shape of the eastern diorite lens is linear, whereas the western diorite lens appears to be more irregular in shape and associated with a number of folds that occur along its strike. The deposits show a spatial association with two lenses of ironstone units with a general northwest-southeast strike (Fig.A5.2a-b). The eastern ironstone unit appears to be linear and continuous both along strike and down dip, and has black shale associated with it. The linearity of the ironstones along strike is similar to that observed in the eastern diorite lens (Fig. A5.2a).

The western ironstone unit, which is bounded by two diorite bodies, is thicker on its northwestern part and thins towards its southern end (Fig. A5.2). This irregular shape fits

well with the irregular shape of the western diorite body observed in the deposit. The diorite-ironstone contacts are overprinted by late-stage shear zones.

The planar eastern, sheared diorite–ironstone contact shows a strong correlation with the orebody shape. Observations made from the long section view of the eastern diorite-ironstone contact show that, the shape of the orebody is 'patchy' down-dip without any definitive trend or plunge (Fig. A5.2c-d).

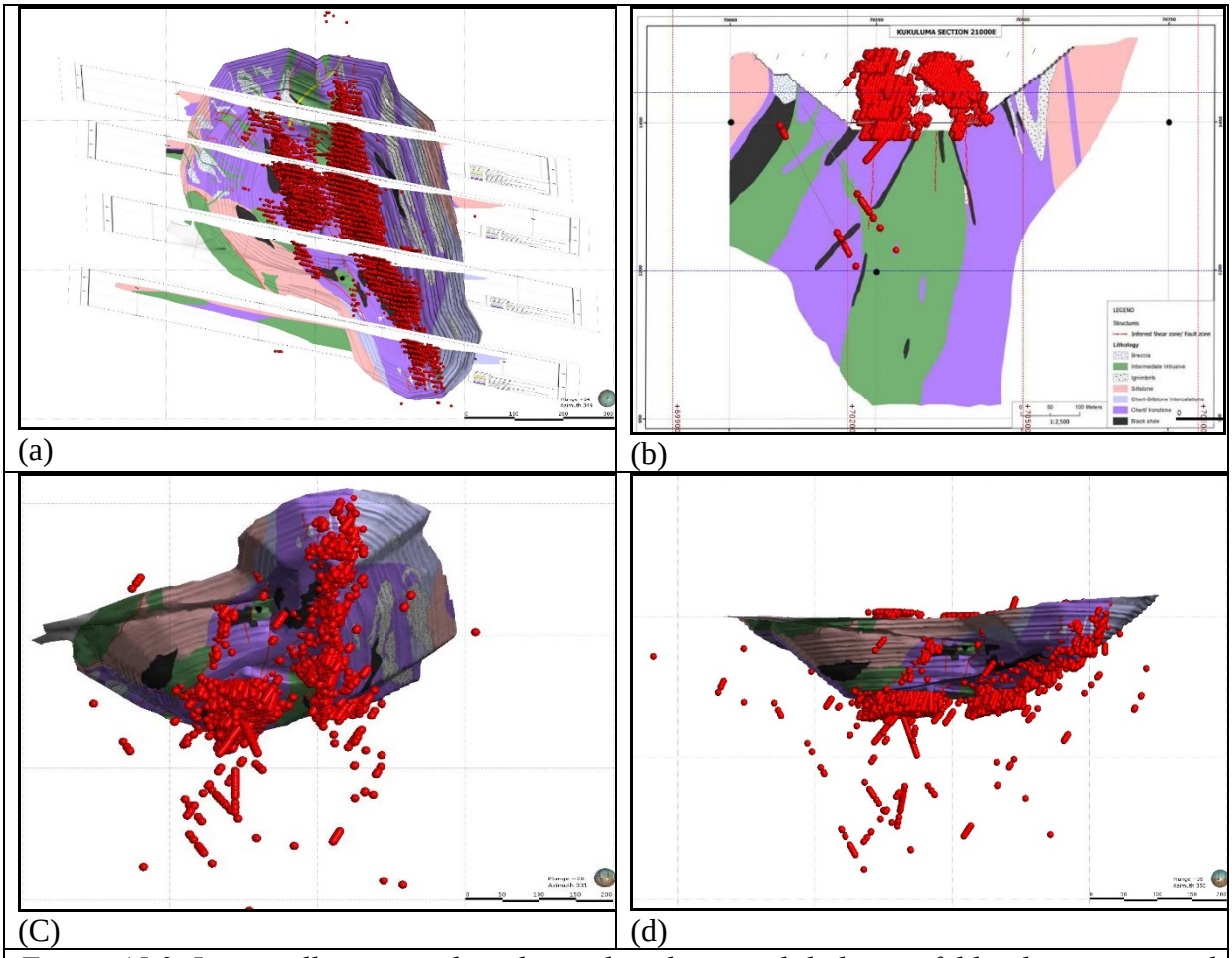

Figure A5.2. Images illustrating the relationships between lithologies, folds, shear zones and gold mineralization for the Kukuluma deposit. (a) Top view of the Kukuluma deposit showing cross-sections and two mineralized envelopes along the diorite-ironstone contacts in the E and a probable hinge zone of a fold in the W. Image was taken looking N; (b) Geological cross-section 21000 showing the relationship between the diorite, ironstones, shear zones and the mineralization envelope. The image was taken looking N; (c) N-directed view from below the Kukuluma deposit showing a circular to semi-circular cluster of mineralization in the west, and a linear mineralization trend in the E part of the deposit; (d) NNE view of the Kukuluma deposit showing mineralization trends. The mineralization envelope is represented by the red bodies.

Observations made along the western diorite–ironstone contact show an irregular shape of the orebody similar to the irregular shape of the diorite contact. Two sets of late-stage shear zones appear associated with mineralization along the western orebody: one along the diorite–ironstone contact; and a second within the ironstone unit. The western orebody appears to be circular towards the northern part of the deposit coincident with a widening of the ironstone unit between the two diorites and the trend of two shear zones that cut through the ironstones (Fig. A5.2b). Along strike towards the southern part of the deposit, the orebody shape gets progressively more planar as it coincides with the sheared diorite-ironstone contact. Observations made from a long section view of the western diorite-ironstone contact zones show that, there is possible plunge of the orebody towards the north on the northern part of the deposit.

A5.3 Area 3 West deposit

Results from the Area 3 West deposit show two main lenses of diorite with a general north-south strike (Fig. A5.3a). These diorite bodies are locally intruded by tonalite bodies with a general north-south orientation. The diorite bodies sandwich a complexly folded package of volcano-sedimentary rocks (Fig. A5.3b). Intense steeply dipping hydrothermal breccia zones have been observed along the hinges zones of the dominant folds.

Both individual geological cross-sections and 3-D view projections in Leapfrog demonstrate the strong spatial relationship between fold hinge zones and the planar, steeply dipping orebody shape along strike. A long section view of the mineralization within the Area 3 West deposit shows a plunge of the mineralization towards the south (Fig. A5.3c-d). The geological cross-sections show that the orebody is mainly located in the ironstone and volcaniclastic units.

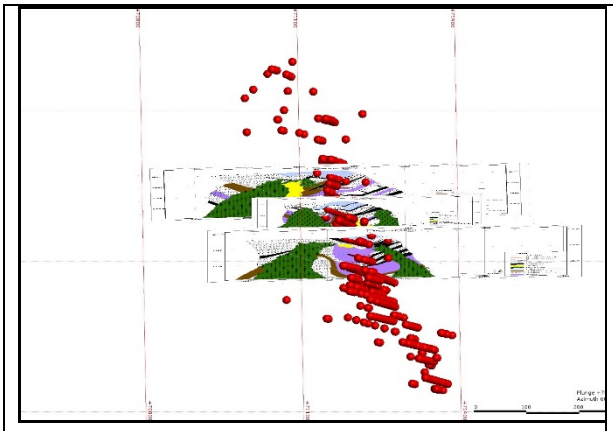

(a)

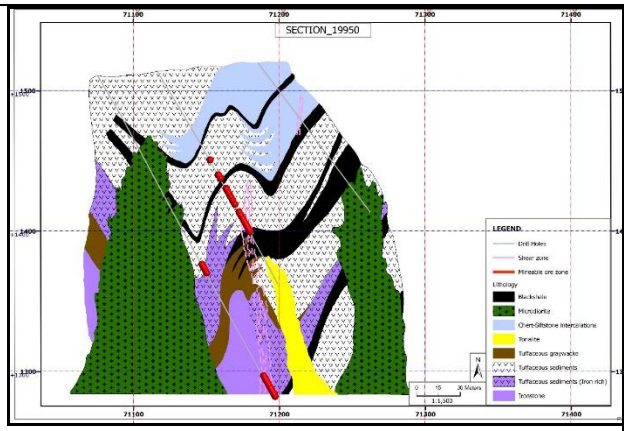

(b)

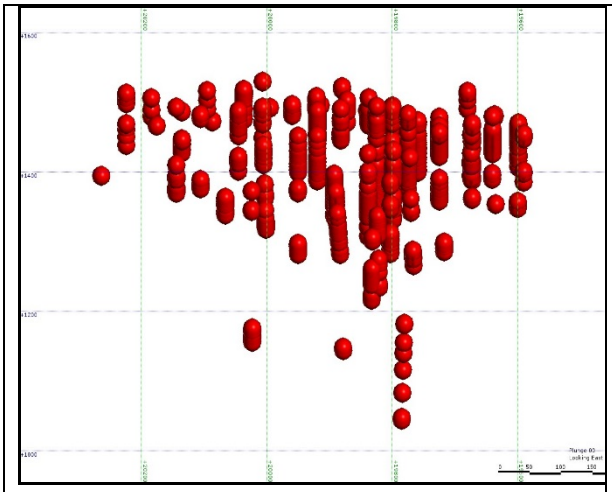

(c)

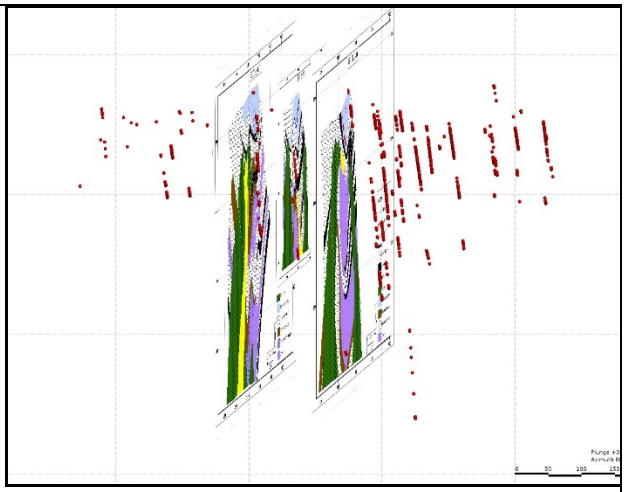

(d)

Figure A5.3. Images illustrating the relationships between lithologies, folds, shear zones and gold mineralization for the Area3 West deposit. (a) Top view of the Area 3 West deposit showing cross-sections and a mineralized envelope along the hinge zone of a fold. Image was taken looking north; (b) Geological cross-section 19950. The image was taken looking N; (c) A long section view of the Area 3 West ore zone, showing a possible south plunge. The image was taken looking east; (d) An oblique long section view towards east showing the relationship between the probable southern plunge of mineralization and the thicker ironstone in the hinge zone in the southernmost section of the deposit. The mineralization envelope is represented by the red coloured bodies.

Appendix 6. Relationship between host lithology and gold mineralization

This appendix provides a description of the data collected to establish the relationship between mineralization and lithology. A summary of this data is presented as part of chapter 3 (Fig. 3.12).

ID	E (UTM)	N (UTM)	Elevation	Length	Azimuth	Plunge	Deposit
MTDD0001	417969	9688963	1524	410.6	226	56	MATANDANI
MTDD0002	417832	9688702	1501	320.1	226	54	MATANDANI
MTDD0003	418112	9688653	1506	186.1	226	55	MATANDANI
MTDD0004	418006	9688500	1505	165.2	226	55	MATANDANI
MTDD0005	418006	9688500	1505	188.0	226	55	MATANDANI
MDD_205	418037	9688692	1542	200.0	225	50	MATANDANI
MTMT_1	418006	9688651	1543	161.1	226	75	MATANDANI
MTMT_2	417924	9688738	1536	150.0	226	90	MATANDANI
MTMT0005	418016	9688616	1477	79.8	226	90	MATANDANI
MTMT0006	418011	9688616	1477	148.7	46	77	MATANDANI
MTRC0007	417821	9688630	1540	150.0	270	49	MATANDANI
KKDD0001	418824	9688261	1461	306.6	226	55	KUKULUMA
KKDD0002	418681	9688166	1443	317.4	46	52	KUKULUMA
SRKKG_2	418619	9688112	1560	210.0	1	50	KUKULUMA
KKGT_1	418879	9688404	1574	60.0	147	65	KUKULUMA
KKGT_2	418869	9688347	1564	105.2	147	70	KUKULUMA
KKGT_3	418844	9688231	1553	95.0	327	70	KUKULUMA
KKGT_4	418837	9688200	1552	50.0	327	70	KUKULUMA
A1D_201	418764	9688316	1563	77.6	181	50	KUKULUMA
A1D_203	418865	9688316	1559	250.0	181	50	KUKULUMA
A1D_206	418790	9688291	1560	210.5	181	50	KUKULUMA
A1D_207	418903	9688290	1556	105.0	181	50	KUKULUMA
3WD_1	420085	9688066	1492	236.6	40	55	AREA 3 WEST
3WD_2	420174	9687991	1471	209.0	44	55	AREA 3 WEST
3WD_3	420118	9688017	1478	227.0	44	60	AREA 3 WEST
AWDD0001	420082	9687989	1473	329.6	41	57	AREA 3 WEST
AWDD0002	420024	9688027	1497	299.6	45	55	AREA 3 WEST
AWDD0003	419978	9688063	1510	269.8	45	60	AREA 3 WEST
AWDD0004	419929	9688092	1520	291.2	46	60	AREA 3 WEST
AWDD0005	420138	9687974	1459	284.0	46	50	AREA 3 WEST
Total				6093.6			

Table A6.1. List of drill holes used in the analysis of ore grade as a function of lithology. A total of 6094 m of core was examined from the Matandani, Kukuluma and Area 3 West deposits.

Field mapping and core logging indicate that there is a strong lithological control on gold distribution and gold grades in the Kukuluma terrain. Diamond drill holes were selected from the Matandani, Kukuluma and Area 3 West deposits (Table A6.1) to investigate the role of lithology on the distribution of gold mineralization.

The lithology of each hole was recorded and compared to the assay results extracted from the mine database. At Geita Gold Mine half of each diamond drill core is sampled every meter and assayed for gold (see section on assay procedures). Thus, a direct comparison between lithology and gold grades can be made. For the purpose of this exercise, all samples with gold grades above 0.1 ppm, above 0.5 ppm (the cut-off grade), above 1 ppm and above 5 ppm Au, were classified by lithological unit. The number of meters for each lithological unit falling into each of the four grade-categories was recorded, and the relative contribution of each lithology to the grade category, expressed as a percentage of total length, was calculated.

A6.1 Lithological groupings in drill core

In grouping the lithologies use was made of pre-existing core logs that were kept in the database at Geita Gold Mine. For each deposit 2-3 drill holes were re-logged, to check on the accuracy of the logging. It was noted that not all units were identified in the pre-existing logs with the same level of confidence, making it necessary to group units in the general categories listed here (Table A6.2). In all instances, ironstone units were easily identified because of their magnetic nature due to the abundance of magnetite (and pyrrhotite). Chert includes both massively banded chert and highly silicified, laminated lithologies of sedimentary origin. Many of the cherts are magnetic, and they are transitional to the ironstones. Black shales are graphite-rich and have been accurately logged. Volcanoclastic units comprise a range of lithologies including, agglomerate and breccia, fragmental tuff, ignimbritic units and tuff beds (see Appendix 2; Table A2.1). Sediments consist of alternating siltstone-shale units interpreted as greywackes with turbiditic characteristics, alternating with coarser-grained sandstone, grit and intra-formational conglomerate. The diorite unit comprises both monzonite, and diorite of the Kukuluma Intrusive Complex as discussed in chapter 4. In some logs, altered diorite may have been mis-identified as sediment; i.e. the relative contributions of sediment and diorite may vary slightly, compared to what is reported in Table A2.1. The granodiorite unit is distinct and has been logged accurately. This lithological grouping was later been matched with the standardized nomenclature for the rocks within the Kukuluma terrain proposed in this study (Table A2.1). Therefore, the nomenclature of the lithologies used in the descriptions below is the ones adopted in Table A2.1.

A6.2 Matandani deposit

From the Matandani deposit 11 diamond drill holes (Tables A6.1 and A6.2) were examined as part of this exercise, with a total of 2159.60 meters drilled. Nine of these holes were drilled towards the southwest, one was drilled towards the north east and one was drilled towards the west. Six holes were drilled at ~ 55° dip, two holes were drilled at ~75° dip and two holes were drilled vertically.

In the Matandani deposit all lithological units present within the drill core have been affected by low-grade mineralisation and record values above 0.1 ppm Au (Table A6.2; Fig.A6.1a). However, the lithological distribution is highly asymmetric with the chert (49%) and the well-bedded ironstone (28%) units recording ~80% of all gold above 0.1 ppm. The chert unit is the main host of gold for low grades, followed by ironstone, but as the grade increases the ironstone unit becomes the dominant host of gold. Other lithological units that are important hosts for low grade gold mineralization are the siltstones and the volcanoclastics. They host between 5 and 10% each of low grade mineralization. The remaining lithological units host less than 5% each of the mineralization. At values above 5 ppm Au the ironstone unit hosts 54% of the gold mineralization while the chert unit hosts only 27% of the gold. Other important lithological hosts for high grade mineralization are the volcanoclastics (~7%) and the diorite of the Kukuluma Igneous Complex (~11%). The most poorly mineralized units in the Matandani pit are the black shales and the granodiorites.

A6.3 Kukuluma deposit

From the Kukuluma deposit 11 diamond drill holes (Tables A6.1 and A6.2) were examined with a total of 1787.25 metres drilled. Four of these holes were drilled towards the south, two holes were drilled towards the northwest, two holes were drilled towards the southeast, one was drilled towards the northeast, one was drilled towards the north and one towards the southwest. Seven holes were drilled at ~50° dip, three holes were drilled at ~70° dip and one hole was drilled at ~65° dip.

The lithological controls on the gold grades in the Kukuluma deposit are similar to the Matandani deposit (Table A6.2; Fig. 3.12). For example, at gold values above 0.1 ppm the main host for gold is ironstone (41%) followed by chert (27%), with moderate contribution from sediments, volcanoclastics and diorite.

Using a cut-off grade of 0.5 ppm gold, the chert and the ironstone units' host similar amounts of gold (~36% each) followed by siltstone units (~17%). At higher grades the role of

ironstone as a host for gold decreases from ~25% (>1 ppm Au) to ~8% (>5 ppm Au), whilst the role of chert increases with ~47% (>1 ppm) and ~39% (>5 ppm Au) of the total respectively. At gold values over 1 ppm the sediments are important host rocks (~23%), which increases to ~30% for grades above 5 ppm. At low and moderate grades (<5 ppm Au), diorite contributes less than 5% of gold mineralisation, however, at grades over 5ppm gold, diorite is an important host rock accounting for ~21% of mineralisation. No mineralised granodiorites were identified in the Kukuluma deposit and the black shales host only minor amounts of gold.

A6.4 Area 3W deposit

From the Area 3 West deposit eight diamond drill holes were examined with a total of 2146.70 metres drilled (Tables A6.1 and A6.2). All holes were drilled towards the northeast at dips between 50 and 60°.

In the Area 3 West deposit, Ironstone Unit is the main host for mineralization at all gold grades, with a gradual increase in importance as a host rock for progressively higher grades: i.e. ironstone hosts 55% of the total core length at >0.1 ppm gold; 56% at >0.5 ppm gold; 63% at >1 ppm gold, and 67% at grades over 5 ppm gold. Chert units host ~25% of gold mineralization at all grades (Table A6.2; Fig. 3.12). Other rock units hosting significant gold mineralization are the volcanoclastics and diorite. Siltstone and black shale units host only low grade mineralization (< 0.5 ppm Au) and granodiorite host no significant mineralization.

Deposit	grade	Chert	Ironstone	Volc	Seds	Bshale	Diorite	Gran	Total
Matandani	>0.1 ppm Au (m)	533.44	300.49	112.01	69.35	30.24	31.49	5.19	1082.21
	>0.5 ppm Au (m)	287.65	208.38	32.76	29.04	5.45	15.60	2.54	581.42
	>1.0 ppm Au (m)	193.59	174.70	20.04	18.64	1.50	15.60	0.00	424.07
	>5.0 ppm Au (m)	33.28	65.17	9.00	1.00	0.00	13.00	0.00	121.45
Kukuluma	>0.1 ppm Au (m)	175.79	283.07	73.07	92.11	17.97	40.47	0.00	682.48
	>0.5 ppm Au (m)	111.30	111.41	16.20	52.89	4.00	8.30	0.00	304.10
	>1.0 ppm Au (m)	86.65	45.98	3.00	41.75	3.00	4.30	0.00	184.68
	>5.0 ppm Au (m)	21.00	4.45	1.00	15.98	0.00	11.00	0.00	53.43
Area 3 West	>0.1 ppm Au (m)	127.75	265.34	49.86	7.00	17.35	17.00	0.00	484.30
	>0.5 ppm Au (m)	60.11	128.50	27.00	1.00	2.50	10.00	0.00	229.11
	>1.0 ppm Au (m)	37.36	93.34	12.70	0.00	0.00	4.00	0.00	147.40
	>5.0 ppm Au (m)	10.21	28.44	2.00	0.00	0.00	2.00	0.00	42.65

(a)

Deposit	grade	Chert	Ironstone	Volc	Seds	Bshale	Diorite	Gran	Total
Matandani	>0.1 ppm Au (%)	49.29	27.77	10.35	6.41	2.79	2.91	0.48	100.00
	>0.5 ppm Au (%)	49.47	35.84	5.63	4.99	0.94	2.68	0.44	100.00
	>1.0 ppm Au (%)	45.65	41.20	4.73	4.40	0.35	3.68	0.00	100.00
	>5.0 ppm Au (%)	27.40	53.66	7.41	0.82	0.00	10.70	0.00	100.00
Kukuluma	>0.1 ppm Au (%)	25.76	41.48	10.71	13.50	2.63	5.93	0.00	100.00
	>0.5 ppm Au (%)	36.60	36.64	5.33	17.39	1.32	2.73	0.00	100.00
	>1.0 ppm Au (%)	46.92	24.90	1.62	22.61	1.62	2.33	0.00	100.00
	>5.0 ppm Au (%)	39.30	8.33	1.87	29.91	0.00	20.59	0.00	100.00
Area 3 West	>0.1 ppm Au (%)	26.38	54.79	10.30	1.45	3.58	3.51	0.00	100.00
	>0.5 ppm Au (%)	26.24	56.09	11.78	0.44	1.09	4.36	0.00	100.00
	>1.0 ppm Au (%)	25.35	63.32	8.62	0.00	0.00	2.71	0.00	100.00
	>5.0 ppm Au (%)	23.94	66.68	4.69	0.00	0.00	4.69	0.00	100.00

(b)

Table A6.2. (a) Length of logged drill core expressed in meters, listed by grade and rock type for the Matandani, Kukuluma and Area 3 West deposits. (b) Length of logged drill core expressed in % of total, listed by grade and rock type for the Matandani, Kukuluma and Area 3 West deposits. The lithological units listed comprise the following: Chert = massively banded chert and highly silicified laminated sedimentary units; Ironstone = well bedded, silicified, magnetite-rich units including BIF. Transitional with chert; Volc = volcanoclastic units including agglomerate, fragmental tuff and ignimbrite; Seds = sediments comprising alternating siltstone-shale units with layers of coarser-grained sandstone, grit and rare conglomerate. These units dominantly fall under the Siltstone group; Bshale = graphitic black shale; Diorite = monzonite and diorite of the and Gran = Granodiorite.

Appendix 7. Major and Trace element analyses

Element/Sample no.	KIC-01	KIC-02	KIC-03	KIC-04	KIC-05	KIC-06	KIC-07	KIC-08	KIC-09	KIC-10	KIC-11
SiO2	57.14	59.10	56.69	56.68	56.00	55.38	62.06	52.70	56.23	51.73	56.77
TiO2	0.46	0.42	0.47	0.51	0.52	0.51	0.42	0.58	0.49	0.56	0.46
Al_2O_3	16.33	14.49	16.08	16.12	16.52	15.97	16.50	14.44	16.32	14.92	15.05
FeO	3.09	3.78	5.88	6.14	5.44	5.54	3.97	7.11	5.89	9.03	6.90
MnO	0.05	0.07	0.10	0.05	0.08	0.07	0.05	0.09	0.07	0.07	0.08
MgO	2.53	3.55	2.94	3.61	3.00	3.40	2.58	5.53	3.47	5.62	2.77
CaO	6.23	5.85	5.29	4.09	4.50	4.39	3.96	6.98	3.78	4.51	5.26
Na_2O	6.64	4.97	6.17	4.49	5.69	6.22	6.61	4.46	5.63	4.50	6.27
K_2O	0.86	2.43	3.15	3.44	3.17	2.75	2.05	3.57	2.67	2.71	1.71
P2O5	0.50	0.40	0.36	0.44	0.47	0.45	0.35	0.86	0.43	0.83	0.46
LOI	4.58	3.97	1.88	4.53	3.78	3.58	0.92	3.14	4.54	4.13	4.86
Total	98.40	99.02	99.00	100.09	99.16	98.26	99.48	99.45	99.52	98.61	100.59
CaO+Na2O	12.87	10.82	11.46	8.58	10.19	10.61	10.58	11.44	9.41	9.01	11.53
Mg#	59.31	62.57	47.12	51.14	49.55	52.23	53.66	58.08	51.19	52.61	41.69
V	75.40	67.18	88.22	104.95	105.07	99.43	72.43	131.39	91.29	135.21	91.66
Cr	31.91	98.13	83.13	83.51	46.82	66.18	49.42	195.17	77.35	195.93	28.45
Ni	34.24	63.01	35.31	56.46	26.36	41.88	33.92	56.35	59.34	78.74	27.55
Rb	9.19	40.12	47.72	74.72	84.37	93.51	27.93	109.23	72.04	99.75	23.11
Sr	1446.78	1562.91	1534.81	1262.89	1245.08	1075.26	1135.55	855.53	674.15	1082.07	537.09
Y	15.22	13.15	20.86	14.56	16.05	15.00	11.83	28.13	11.21	29.96	13.73
Zr	185.55	149.11	238.28	138.60	173.40	170.01	151.97	274.58	131.85	284.22	187.15
Nb	6.00	4.61	9.40	5.53	6.04	5.80	5.09	9.74	5.62	9.82	5.39
Ba	237.37	1413.89	1898.63	1783.46	1600.76	1345.47	1722.08	2545.32	1385.58	749.87	149.30
La	121.78	68.59	102.61	81.02	82.68	80.94	57.01	166.15	77.27	184.12	78.90
Ce	235.18	142.95	212.18	163.65	169.19	167.96	116.12	353.66	158.17	379.51	161.82
Pr	25.95	17.15	24.48	18.69	19.48	19.36	13.28	42.13	18.30	44.78	18.43
Nd	96.49	69.46	95.99	72.82	75.62	75.68	52.45	172.62	71.57	177.99	74.67
Sm	13.96	11.14	15.46	11.17	11.85	11.29	8.25	26.47	10.25	28.78	11.76
Eu	2.80	2.77	3.73	2.65	3.01	2.71	2.05	6.53	2.28	6.67	2.54
Gd	7.17	6.57	9.21	6.35	6.99	6.66	5.15	15.35	5.42	16.27	6.61
Tb	0.79	0.66	1.04	0.70	0.78	0.70	0.57	1.64	0.51	1.55	0.64
Dy	3.34	3.34	4.73	3.31	3.60	3.18	2.74	6.87	2.64	7.39	3.27
Ho	0.52	0.48	0.73	0.52	0.57	0.52	0.46	1.04	0.42	1.08	0.51
Er	1.38	1.09	1.80	1.35	1.36	1.27	1.05	2.29	1.09	2.47	1.35
Tm	0.19	0.15	0.22	0.18	0.18	0.18	0.15	0.27	0.16	0.33	0.18
Yb	1.25	0.71	1.33	1.07	1.17	1.12	0.85	1.68	0.99	1.81	1.05
Lu	0.18	0.10	0.17	0.15	0.17	0.17	0.13	0.21	0.16	0.24	0.17
Hf	4.41	3.53	5.30	3.70	4.02	4.13	3.61	6.14	3.23	6.29	4.08
Th	20.30	12.00	18.25	11.55	16.89	17.06	11.95	31.58	17.52	32.83	16.22
U	3.75	3.95	4.59	4.59	4.26	4.09	3.47	7.40	8.36	7.78	5.24
Sr/Y	95.06	118.82	73.59	86.76	77.56	71.68	96.02	30.41	60.14	36.12	39.12

La/Yb	97.17	96.61	77.15	75.67	70.43	71.97	67.10	99.10	77.79	101.91	75.50
La/Ybn	66.01	65.63	52.41	51.40	47.84	48.89	45.58	67.32	52.85	69.23	51.29
Dy/Ybn	1.74	3.08	2.33	2.02	2.01	1.85	2.11	2.68	1.74	2.68	2.05
Zr/Hf	42.08	42.28	44.93	37.49	43.10	41.17	42.14	44.72	40.78	45.21	45.83
Zr/Sm	13.29	13.39	15.41	12.40	14.63	15.05	18.42	10.37	12.86	9.88	15.91
Nb/La	0.05	0.07	0.09	0.07	0.07	0.07	0.09	0.06	0.07	0.05	0.07
Th/U	5.41	3.04	3.97	2.52	3.96	4.17	3.44	4.27	2.10	4.22	3.10
Cr/Ni	0.93	1.56	2.35	1.48	1.78	1.58	1.46	3.46	1.30	2.49	1.03
Sr/Sr*	0.71	1.15	0.79	0.85	0.81	0.70	1.07	0.25	0.47	0.31	0.36

Table A7.1. Major and trace element analyses for the monzonite suite.

Element/Sample no.	**KIC-12**	**KIC-13**	**KIC-14**	**KIC-15**	**KIC-16**	**KIC-17**	**KIC-18**	**KIC-19**	**KIC-20**	**KIC-21**
SiO2	58.29	62.74	62.75	61.71	53.29	55.04	58.86	58.85	57.09	57.52
TiO2	0.39	0.32	0.33	0.58	0.67	0.64	0.51	0.59	0.61	0.51
Al_2O_3	15.81	14.88	14.40	16.70	16.82	16.33	15.96	16.76	17.07	16.21
FeO	7.49	2.83	3.02	6.98	7.82	7.00	6.91	6.78	7.33	7.71
MnO	0.04	0.04	0.05	0.07	0.10	0.13	0.12	0.09	0.06	0.08
MgO	2.04	2.61	2.70	2.97	4.16	3.46	2.70	3.07	3.17	2.15
CaO	2.92	3.46	4.20	3.13	6.26	6.55	4.38	4.71	3.65	6.59
Na_2O	5.11	5.17	5.61	3.62	3.56	3.79	3.36	4.79	3.84	3.14
K_2O	2.84	3.24	2.18	1.75	1.67	1.35	2.74	1.18	2.45	2.21
P_2O_5	0.15	0.21	0.20	0.21	0.24	0.27	0.20	0.20	0.31	0.18
LOI	3.38	3.24	3.92	1.72	5.24	5.55	4.16	2.43	1.44	3.32
Total	98.45	98.73	99.35	99.43	99.83	100.11	99.88	99.44	97.02	99.61
CaO+Na_2O	8.03	8.62	9.81	6.75	9.82	10.34	7.73	9.50	7.48	9.73
Mg#	32.68	62.17	61.48	43.12	48.65	46.87	41.10	44.69	43.50	33.15
V	75.17	62.49	56.28	175.05	162.55	158.14	112.83	135.19	149.50	114.20
Cr	63.84	96.59	98.49	81.82	97.60	87.08	49.50	89.57	87.43	84.63
Ni	36.76	61.37	57.92	57.86	60.24	66.02	76.78	30.00	59.29	23.80
Rb	98.78	60.84	52.48	72.66	62.47	48.33	87.85	43.04	94.59	65.72
Sr	797.59	1024.75	1062.38	978.06	773.78	679.84	800.15	778.44	876.08	572.36
Y	8.74	7.54	9.38	10.94	11.91	10.50	7.59	9.17	11.86	10.31
Zr	105.93	108.92	107.38	112.81	80.17	79.30	93.03	104.81	145.07	96.88
Nb	2.91	2.98	3.32	3.03	2.43	2.53	2.54	2.95	5.16	2.16
Ba	695.82	1477.81	1156.30	560.89	563.32	418.35	556.74	329.70	725.24	380.48
La	22.33	31.39	31.58	21.22	13.72	12.31	12.02	12.07	38.26	10.72
Ce	42.52	65.60	65.89	46.35	30.72	29.06	26.67	26.91	76.19	22.00
Pr	4.59	7.65	7.92	5.74	4.01	4.05	3.54	3.53	8.76	2.80
Nd	17.11	30.62	32.22	24.19	17.65	17.04	14.47	16.21	34.33	12.69
Sm	2.96	5.07	5.94	4.86	3.74	3.70	3.08	3.47	5.77	2.65
Eu	0.86	1.22	1.42	1.31	1.11	1.15	1.07	1.19	1.51	0.85
Gd	2.23	3.14	3.78	3.55	3.21	3.13	2.53	2.78	3.90	2.33

Tb	0.32	0.36	0.44	0.46	0.44	0.46	0.35	0.35	0.49	0.31
Dy	1.75	1.62	2.05	2.41	2.39	2.27	1.67	1.93	2.53	1.84
Ho	0.31	0.28	0.34	0.45	0.46	0.44	0.32	0.36	0.45	0.35
Er	0.86	0.61	0.88	1.19	1.27	1.08	0.76	0.99	1.29	0.94
Tm	0.14	0.09	0.12	0.18	0.19	0.16	0.12	0.14	0.18	0.14
Yb	0.94	0.50	0.61	1.04	1.19	0.94	0.66	0.79	1.09	0.75
Lu	0.14	0.08	0.08	0.17	0.18	0.15	0.11	0.12	0.16	0.10
Hf	3.05	2.83	2.91	2.99	2.27	2.31	2.53	2.88	3.73	2.54
Th	4.34	6.90	6.92	2.45	1.64	1.49	1.68	1.53	5.25	1.09
U	1.31	2.39	2.68	0.86	0.57	0.48	0.61	0.52	1.64	0.40
Sr/Y	91.26	135.97	113.22	89.40	64.97	64.75	105.42	84.89	73.87	55.52
La/Yb	23.88	63.08	51.91	20.40	11.53	13.10	18.21	15.28	35.10	14.29
La/Ybn	16.22	42.85	35.26	13.86	7.83	8.90	12.37	10.38	23.84	9.71
Dy/Ybn	1.22	2.14	2.20	1.52	1.31	1.58	1.66	1.60	1.52	1.61
Zr/Hf	34.69	38.49	36.90	37.73	35.32	34.33	36.77	36.39	38.89	38.14
Zr/Sm	35.79	21.50	18.08	23.21	21.44	21.43	30.20	30.20	25.14	36.56
Nb/La	0.13	0.09	0.11	0.14	0.18	0.21	0.21	0.24	0.13	0.20
Th/U	3.32	2.89	2.58	2.85	2.88	3.10	2.75	2.94	3.20	2.73
Cr/Ni	1.74	1.57	1.70	1.41	1.62	1.32	0.64	2.99	1.47	3.56
Sr/Sr*	2.17	1.68	1.69	2.15	2.44	2.24	2.99	2.74	1.26	2.52

Table A7.2. Major and trace element analyses for the diorite suite.

Element/Sample no.	**KIC-22**	**KIC-23**	**KIC-24**	**KIC-25**
SiO_2	62.90	62.76	62.20	62.15
TiO_2	0.55	0.56	0.55	0.56
Al_2O_3	15.74	15.94	15.56	15.53
FeO	4.83	5.04	4.81	4.87
MnO	0.08	0.08	0.08	0.08
MgO	1.87	1.93	1.88	1.89
CaO	3.78	3.11	3.88	4.09
Na2O	3.39	3.87	3.24	2.98
K2O	3.60	3.41	3.72	3.93
P2O5	0.17	0.17	0.16	0.17
LOI	3.66	3.15	3.23	3.70
Total	100.57	100.00	99.32	99.94
CaO+Na2O	7.16	6.98	7.12	7.07
Mg#	40.88	40.54	41.07	40.90
V	61.71	67.21	66.97	66.05
Cr	21.21	22.22	20.78	20.74
Ni	13.75	15.99	10.53	13.46
Rb	102.33	97.69	83.46	85.94
Sr	302.20	340.07	358.09	327.49

Y	16.88	16.54	16.30	15.93
Zr	132.42	128.70	132.30	130.04
Nb	5.70	6.04	5.90	5.73
Ba	584.53	520.77	507.52	545.58
La	24.26	23.89	23.69	23.52
Ce	52.25	50.96	50.99	49.37
Pr	6.15	5.79	5.89	5.79
Nd	23.64	22.66	22.88	22.49
Sm	4.45	4.21	4.36	4.31
Eu	0.96	0.86	1.05	1.15
Gd	3.61	3.70	3.63	3.46
Tb	0.50	0.49	0.52	0.48
Dy	3.17	3.08	2.46	2.86
Ho	0.57	0.55	0.62	0.56
Er	1.87	1.69	1.71	1.63
Tm	0.25	0.26	0.29	0.25
Yb	1.56	1.57	1.61	1.54
Lu	0.26	0.25	0.24	0.23
Hf	3.89	3.92	3.81	3.76
Th	8.30	8.12	8.10	7.67
U	2.82	2.76	2.83	2.62
Sr/Y	17.90	20.56	21.97	20.55
La/Yb	15.52	15.25	14.71	15.31
La/Ybn	10.54	10.36	10.00	10.40
Dy/Ybn	1.33	1.29	1.12	1.22
Zr/Hf	34.04	32.86	34.76	34.59
Zr/Sm	29.78	30.55	30.32	30.20
Nb/La	0.24	0.25	0.25	0.24
Th/U	2.95	2.94	2.86	2.93
Cr/Ni	1.54	1.39	1.97	1.54
Sr/Sr*	0.63	0.74	0.77	0.72

Table A7.3 Major and trace element analyses for the granodiorite suite.

Appendix 8. Data analyses of zircon standards used in geochronology

Analysis	$^{238}U/^{206}Pb$	Error (1σ)	$^{207}Pb/^{206}Pb$	Error (1σ)	$^{207}Pb/^{235}U$	Error (1σ)	$^{206}Pb/^{238}U$	Error (1σ)	Rho	Age (Ma) $^{207}Pb/^{206}Pb$	Error (1σ)	Age (Ma) $^{206}Pb/^{238}U$	Error (1σ)	Discordance (%)
GJ1-1	10.192	0.13	0.060	0.00	0.812	0.01	0.098	0.001	0.83	604	29	603	8	0
GJ1-2	10.165	0.14	0.060	0.00	0.818	0.02	0.098	0.001	0.57	615	49	605	8	2
GJ1-3	10.179	0.13	0.061	0.00	0.831	0.01	0.098	0.001	0.87	652	28	604	8	7
GJ1-4	10.238	0.13	0.062	0.00	0.828	0.02	0.098	0.001	0.66	657	40	601	7	9
GJ1-5	10.299	0.15	0.059	0.00	0.786	0.02	0.097	0.001	0.48	556	63	597	8	-7
GJ1-6	10.304	0.15	0.059	0.00	0.787	0.03	0.097	0.001	0.46	559	69	597	9	-7
GJ1-7	10.165	0.13	0.060	0.00	0.819	0.02	0.098	0.001	0.61	618	44	605	8	2
GJ1-8	10.183	0.13	0.060	0.00	0.810	0.01	0.098	0.001	0.74	597	35	604	8	-1
GJ1-9	10.285	0.14	0.062	0.00	0.826	0.02	0.097	0.001	0.56	663	49	598	8	10
GJ1-10	10.319	0.14	0.059	0.00	0.793	0.02	0.097	0.001	0.47	580	63	596	8	-3
GJ1-11	10.199	0.13	0.062	0.00	0.839	0.02	0.098	0.001	0.60	676	44	603	8	11
GJ1-12	10.116	0.13	0.059	0.00	0.807	0.02	0.099	0.001	0.59	574	46	608	7	-6
GJ1-13	10.203	0.13	0.061	0.00	0.823	0.02	0.098	0.001	0.58	636	45	603	7	5
GJ1-14	10.256	0.13	0.058	0.00	0.786	0.01	0.098	0.001	0.70	548	36	600	7	-10
GJ1-15	10.149	0.13	0.060	0.00	0.819	0.01	0.099	0.001	0.83	614	29	606	7	1
GJ1-16	10.251	0.13	0.061	0.00	0.815	0.01	0.098	0.001	0.83	625	29	600	7	4
GJ1-17	10.253	0.12	0.060	0.00	0.809	0.01	0.098	0.001	0.77	609	31	600	7	1
GJ1-18	10.299	0.14	0.062	0.00	0.826	0.02	0.097	0.001	0.67	666	40	597	8	10
GJ1-19	10.111	0.13	0.061	0.00	0.826	0.02	0.099	0.001	0.55	624	48	608	7	3
GJ1-20	10.180	0.13	0.059	0.00	0.804	0.01	0.098	0.001	0.68	581	38	604	7	-4
GJ1-21	10.093	0.13	0.060	0.00	0.820	0.02	0.099	0.001	0.57	606	47	609	7	0
GJ1-22	10.171	0.13	0.060	0.00	0.814	0.01	0.098	0.001	0.70	604	36	605	7	0
GJ1-23	10.310	0.13	0.060	0.00	0.802	0.01	0.097	0.001	0.75	603	33	597	7	1
GJ1-24	10.324	0.13	0.060	0.00	0.798	0.02	0.097	0.001	0.64	594	40	596	7	0
GJ1-25	10.316	0.13	0.060	0.00	0.801	0.01	0.097	0.001	0.84	601	28	597	7	1
GJ1-26	10.316	0.13	0.060	0.00	0.802	0.02	0.097	0.001	0.58	604	45	596	7	1
GJ1-27	10.126	0.13	0.060	0.00	0.816	0.01	0.099	0.001	0.72	601	35	607	7	-1
GJ1-28	10.179	0.13	0.060	0.00	0.807	0.01	0.098	0.001	0.79	587	31	604	7	-3

Table A8.1. U-Pb data for the GJ1 zircon standard.

Analysis	$^{238}U/^{206}Pb$	Error (1σ)	$^{207}Pb/^{206}Pb$	Error (1σ)	$^{207}Pb/^{235}U$	Error (1σ)	$^{206}Pb/^{238}U$	Error (1σ)	Rho	Age (Ma) $^{207}Pb/^{206}Pb$	Error (1σ)	Age (Ma) $^{206}Pb/^{238}U$	Error (1σ)	Discordance (%)
FC1-1	5.267	0.07	0.076	0.001	1.993	0.03	0.190	0.002	0.92	1098	23	1121	13	-2
FC1-2	5.384	0.07	0.076	0.001	1.950	0.03	0.186	0.002	0.91	1100	24	1098	13	0
FC1-3	5.525	0.08	0.076	0.002	1.901	0.04	0.181	0.003	0.63	1100	43	1072	14	2
FC1-4	5.041	0.07	0.076	0.001	2.085	0.04	0.198	0.003	0.79	1101	29	1167	14	-6
FC1-5	5.044	0.07	0.076	0.001	2.082	0.03	0.198	0.003	0.86	1100	26	1166	14	-6
FC1-6	5.132	0.07	0.076	0.001	2.046	0.03	0.195	0.003	0.89	1100	25	1148	14	-4
FC1-7	5.712	0.08	0.076	0.001	1.838	0.03	0.175	0.002	0.70	1100	35	1040	13	5
FC1-8	5.222	0.07	0.076	0.001	2.011	0.03	0.191	0.002	0.87	1100	25	1129	13	-3
FC1-9	4.913	0.06	0.076	0.001	2.138	0.03	0.204	0.002	0.75	1100	30	1194	13	-9
FC1-10	5.012	0.06	0.076	0.001	2.101	0.03	0.200	0.002	0.78	1105	28	1173	13	-6
FC1-11	5.221	0.06	0.076	0.001	2.013	0.03	0.192	0.002	0.81	1101	28	1130	13	-3
FC1-12	5.240	0.07	0.076	0.001	2.006	0.03	0.191	0.002	0.87	1102	25	1126	13	-2
FC1-13	5.212	0.06	0.076	0.001	2.015	0.03	0.192	0.002	0.79	1100	28	1131	12	-3
FC1-14	5.105	0.06	0.076	0.001	2.056	0.03	0.196	0.002	0.95	1099	22	1153	13	-5
FC1-15	5.206	0.06	0.076	0.001	2.017	0.03	0.192	0.002	0.89	1100	24	1133	13	-3
FC1-16	5.249	0.06	0.076	0.001	2.003	0.03	0.191	0.002	0.89	1102	24	1124	12	-2
FC1-17	5.224	0.06	0.076	0.001	2.011	0.03	0.191	0.002	0.94	1100	22	1129	13	-3
FC1-18	5.264	0.06	0.076	0.001	1.995	0.03	0.190	0.002	0.94	1100	22	1121	13	-2
FC1-19	5.043	0.06	0.076	0.001	2.083	0.03	0.198	0.002	0.83	1100	26	1166	13	-6
FC1-20	5.132	0.06	0.076	0.001	2.049	0.03	0.195	0.002	0.88	1102	24	1148	12	-4
FC1-21	5.239	0.06	0.076	0.001	2.005	0.03	0.191	0.002	0.78	1099	29	1126	12	-2
FC1-22	5.261	0.06	0.076	0.001	1.995	0.03	0.190	0.002	0.89	1099	24	1122	12	-2
FC1-23	5.224	0.06	0.076	0.001	2.011	0.03	0.191	0.002	0.94	1101	22	1129	13	-3
FC1-24	5.292	0.06	0.076	0.001	1.985	0.03	0.189	0.002	0.93	1100	22	1116	12	-1

Table A8.2. U-Pb data for the FC1 zircon standard.

Analysis	$^{238}U/^{206}Pb$	Error (1σ)	$^{207}Pb/^{206}Pb$	Error (1σ)	$^{207}Pb/^{235}U$	Error (1σ)	$^{206}Pb/^{238}U$	Error (1σ)	Rho	Age (Ma) $^{207}Pb/^{206}Pb$	Error (1σ)	Age (Ma) $^{206}Pb/^{238}U$	Error (1σ)	Discordance (%)
91500-1	5.597	0.08	0.074	0.00	1.827	0.06	0.179	0.003	0.47	1047	63	1060	15	-1
91500-2	5.591	0.08	0.072	0.00	1.778	0.05	0.179	0.003	0.52	990	53	1061	14	-7
91500-3	5.574	0.08	0.074	0.00	1.831	0.03	0.179	0.002	0.74	1042	33	1064	13	-2
91500-4	5.578	0.07	0.075	0.00	1.859	0.03	0.179	0.002	0.77	1075	31	1063	13	1
91500-5	5.564	0.08	0.078	0.00	1.926	0.04	0.180	0.002	0.71	1141	35	1065	13	7
91500-6	5.593	0.08	0.075	0.00	1.845	0.05	0.179	0.003	0.50	1066	57	1061	14	0
91500-7	5.583	0.07	0.075	0.00	1.856	0.04	0.179	0.002	0.61	1073	41	1062	13	1
91500-8	5.579	0.07	0.076	0.00	1.880	0.03	0.179	0.002	0.70	1098	33	1063	12	3
91500-9	5.588	0.07	0.075	0.00	1.839	0.03	0.179	0.002	0.68	1056	36	1061	13	0
91500-10	5.614	0.07	0.075	0.00	1.833	0.03	0.178	0.002	0.71	1059	34	1057	13	0
91500-11	5.600	0.07	0.075	0.00	1.838	0.04	0.179	0.002	0.66	1060	38	1059	13	0
91500-12	5.585	0.07	0.074	0.00	1.827	0.04	0.179	0.002	0.58	1042	43	1062	13	-2
91500-13	5.589	0.07	0.075	0.00	1.861	0.03	0.179	0.002	0.78	1081	30	1061	12	2
91500-14	5.587	0.07	0.075	0.00	1.853	0.04	0.179	0.002	0.69	1072	36	1061	13	1
91500-15	5.589	0.08	0.075	0.00	1.850	0.05	0.179	0.002	0.53	1069	51	1061	13	1
91500-16	5.592	0.07	0.075	0.00	1.845	0.04	0.179	0.002	0.56	1063	46	1061	13	0

Table A8.3. U-Pb data for the 91500 zircon standard.

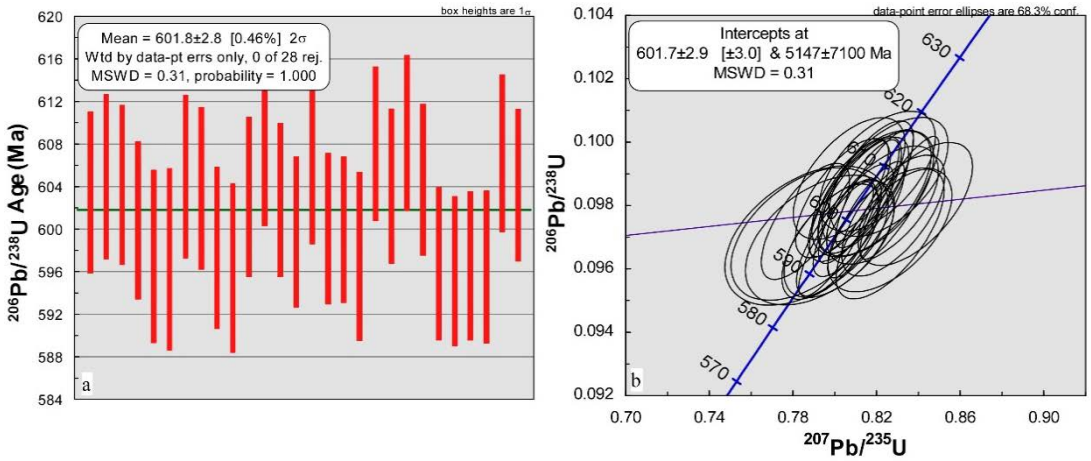

Fig. A8.1.The weighted average age and concordia age for the GJ1zircon standard.

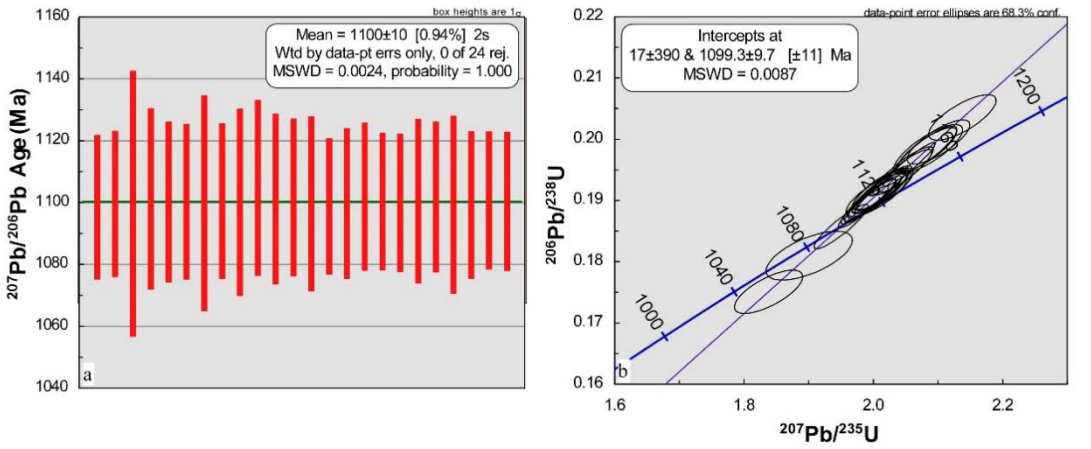

Fig. A8.2.The weighted average age and concordia age for the FC1 zircon standard.

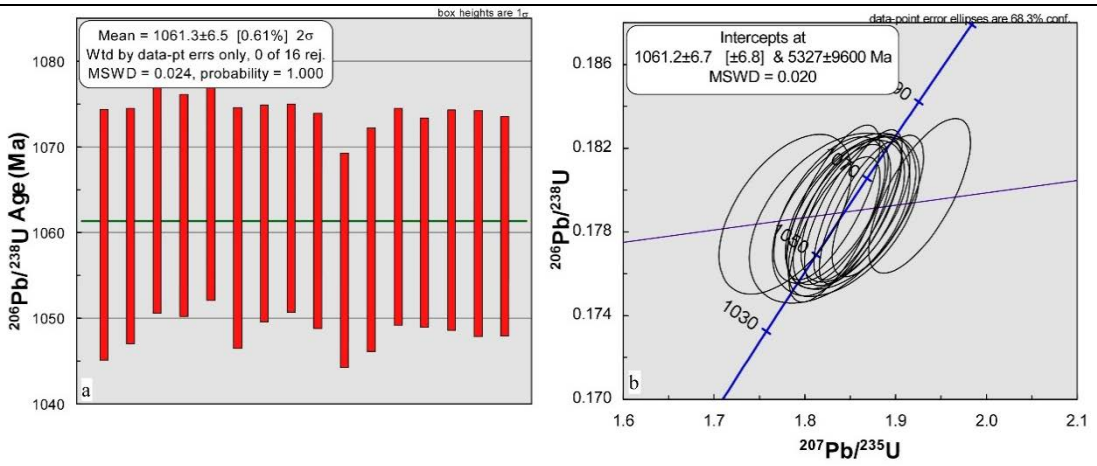

Fig. A8.3.Weighted average age and concordia age for the 91500 zircon standard.